Excitations and Criticality in Quantum Magnets

Philip Lloyd Herbert Merchant

Department of Physics and Astronomy

University College London

A thesis submitted for the Doctor of Philosophy

PhilosophiæDoctor (PhD)

February 2013

Declaration

I, Philip Lloyd Herbert Merchant, confirm that the work presented in this thesis is my own. Where information has been derived from other sources, I confirm that this has been indicated in the thesis.

Philip Lloyd Herbert Merchant, February 2013

Abstract

This thesis describes the neutron scattering studies of three model magnetic systems; the coupled spin dimer compound $TlCuCl_3$, the frustrated spin ladder material $BiCu_2PO_6$ and the impurity-doped spin ladder material $BiCu_{2(1-x)}Zn_{2x}PO_6$.

$TlCuCl_3$ is a realisation of a continuously tunable model magnet, where applied hydrostatic pressure can drive the system from a state of disorder into long-range magnetic order with the emergence of an excitation at the quantum critical point that corresponds to longitudinal fluctuations of the ordered moment. The study of the excitations in $TlCuCl_3$ is now extended to finite temperatures. The results are summarised in Chapter 4, where similarities are reported between the quantum phase and thermal phase transitions.

Spin ladder systems provide an exciting opportunity to study aspects of low-dimensional physics. With model magnets previously constrained to the limits of 'strong' exchange ($\sim$ 100 meV) in the cuprates and 'weak' exchange ($\sim$ 1 meV) in the metal-organics, the new spin ladder $BiCu_2PO_6$ offers the opportunity for study of spin ladder physics in the 'intermediate' exchange regime ($\sim$ 10 meV). Inelastic neutron scattering studies of this system are presented in Chapter 5, where the magnon dispersion, exchange geometry and anisotropy are deduced from analysis of the excitation energies.

Substitution of the Cu^{2+} sites in $BiCu_2PO_6$ with non-magnetic impurities Zn^{2+} results in the creation of $BiCu_{2(1-x)}Zn_{2x}PO_6$, where a single S = 1/2 moment is liberated for each impurity. These moments are shown to demonstrate long-range correlations and magnetic ordering below a characteristic temperature, T_N. Single crystal samples with $x = 0.01$, 0.03 and 0.05 have been investigated and structural studies of each are reported in Chapter 6. The field and temperature dependence of the observed long-range order is reported as well as a magnetic structure determination and studies of the impurity dependence of the coherence of the magnetic order.

Contents

Acknowledgements

First and foremost, I would like to thank my supervisors Prof. Des McMorrow and Dr. Christian Rüegg for the invaluable opportunity they have given me in making my thesis possible. Their continued support and advice constitutes the foundation on which my work was based, not only for general physics problems and quandaries, but in questions of instrument setup, experimental procedure, data analysis and the minutiae of scientific writing.

The experimental work was made significantly easier with the valued assistance of many people throughout the three and a half years of hard work. First, the measurements wouldn't have even been possible without high quality samples provided by my colleague, Shuang Wang at LDM, PSI. Her continued help during and between experiments was a huge asset and her support hugely appreciated.

Second, the on-hand support of the multiple instrument scientists at ILL and SINQ was invaluable, providing me with patient advice and assistance. With thanks to the high-pressure team at the ILL, Martin Böhm on IN14, Martin Mansson on TASP, Christof Niedermeyer on RITA-II and with a special thank you to Oksana Zaharko, whose patience I'm sure I tried multiple times during and after the TriCS experiment with support and advice on understanding the data and analysing it with Fullprof.

My many colleagues in and outside UCL have provided me with a wealth of experience, practical assistance and greatly valued support. Bruce Normand has helped enormously toward solving the questions of $TlCuCl_3$ with his theoretical contributions and strings of e-mails answering many of my questions; Simon Ward's expertise in Matlab helped with the streamlining of many lines of code; Michel Kenzelmann's guidance during experiments helped steer me in the right direction and Ross Springell's assistance with experimental work and guidance in scientific writing and research made the process far more enjoyable - to them all, thank you.

Although the fruits of my labour with them did not make it to the finished thesis, I would like to extend my gratitude to Mark Ellerby and Patricia Alireza at UCL who supported me through many, many hours of high-pressure magnetometry measurements, including the setup and calibration of some extremely fiddly instrumentation and the very stubborn ^{3}He fridge.

Finally, I would like to thank my parents, family and friends for their continued help during this time - in particular my partner Helen who has supported me with patience during the many long hours and multiple trips abroad.

List of Figures

List of Tables

1

Introduction

The documented history of magnetism and magnetic materials can be traced back many centuries to the observation of the naturally occurring material magnetite (commonly known as Lodestone)[1] that exhibited the remarkable property to attract metals such as iron without external influence. It was not until many years later that the origin of this property was explained, but the behaviour was no less remarkable for it - the macroscopic behaviour of classical magnetic materials is now understood to be the co-operative interaction of individual microscopic magnetic moments into a finite sized domain of parallel (ferromagnetic, FM) or antiparallel (antiferromagnetic, AFM) alignment below a 'critical' temperature.

It is below this temperature - the Curie temperature (T_c) in ferromagnets and the Néel temperature (T_N) in antiferromagnets - that the energy of the system is minimised by long-range alignment of magnetic moments. Above T_c, thermal fluctuations dominate and the system has no preferential order, existing in a state of paramagnetism. Crossing this boundary is an example of a type of phase transition, where the system undergoes a change in the state of magnetic order and a breaking of symmetry; in the paramagnetic phase the spin-space is 3D symmetric, and in the ordered state the symmetry is lost and the system has one preferential direction (Figure 1.1). Such phenomenology is not unique to magnetism, and the transition described is analagous to the breaking of a structural symmetry such as in the case of ice melting into water.

In some magnetic systems an ordered state is not observed even down to the lowest attainable temperatures, "$T = 0$ K". This is understood to be a direct consequence of the microscopic quantum nature of the ground state, where the magnetic moment of each electron μ_e is derived from its angular momentum which, when neglecting orbital contributions, is given by the intrinsic angular momentum operator $\hat{S}$, via

$$\hat{\mu_e} = -g\mu_B\hat{S}, \tag{1.1}$$

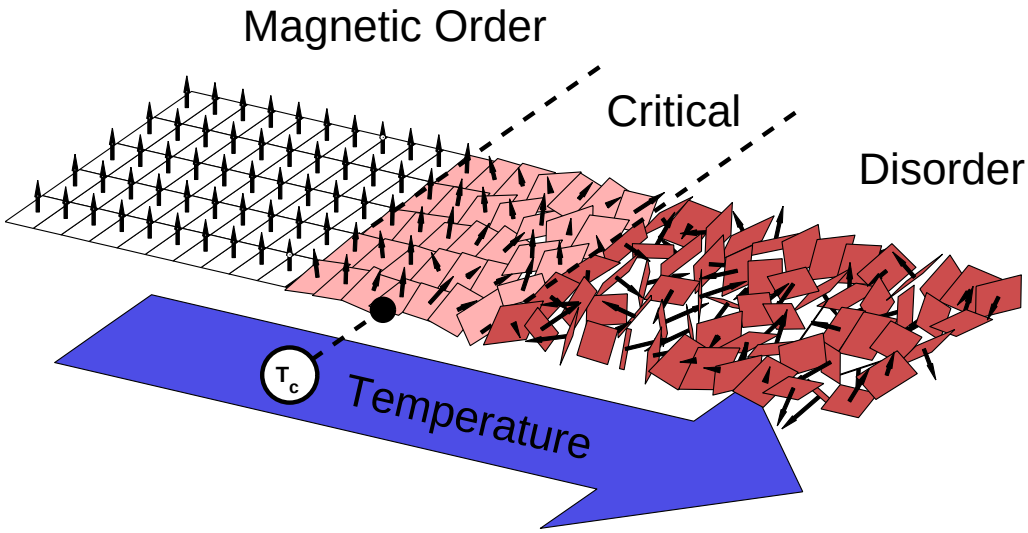

Figure 1.1: The destruction of ferromagnetic order upon heating. Below T_c the system is in a state of long-range order, represented by the co-alignment of the white squares; at and just above T_c, the energy k_BT of thermal fluctuations is on the order of the exchange energy and the ground state is critical. For $T > T_c$ there is no direction of preferred order and the system is paramagnetic.

where μ_B is the Bohr magneton and g is a coupling pre-factor that depends on the value of the spin quantum number of the particle, S. For electrons, $S = 1/2$ and $g \sim 2$.

The coupling of two spins obeys the quantum mechanical properties of *exchange symmetry*. The electrons are indistinguishable particles, and as fermions the overall wavefunction of two coupled electrons must be antisymmetric upon their exchange. The total wavefunction is made up of a product of a spatial wavefunction (ψ) and a spin wavefunction (χ). Therefore for the product to be antisymmetric, either the spatial component or the spin component of the overall wavefunction must be antisymmetric upon exchange of the two particles.

The spatial component of two spin $S = 1/2$ particles is given as either the symmetric wavefunction ψ_S, or the antisymmetric wavefunction ψ_{AS}. The corresponding spin wavefunctions are antisymmetric and symmetric, respectively, with the possible combined wavefunctions given as

$$\begin{aligned} \Psi_S &= \psi_S \frac{1}{\sqrt{2}}[|\uparrow\downarrow\rangle - |\downarrow\uparrow\rangle] \\ \Psi_{T0} &= \psi_{AS} \frac{1}{\sqrt{2}}[|\uparrow\downarrow\rangle + |\downarrow\uparrow\rangle] \\ \Psi_{T+} &= \psi_{AS}|\downarrow\downarrow\rangle \\ \Psi_{T-} &= \psi_{AS}|\uparrow\uparrow\rangle, \end{aligned} \tag{1.2}$$

where $\uparrow$ and $\downarrow$ describe the spin orientations of individual electrons, with the spin configuration of two electrons being given by one antisymmetric spin configuration (the

'singlet' state) or one of three degenerate symmetric spin configurations (the 'triplet' states). The energy of these states is determined by the spatial wavefunction, with contributions from the coulomb repulsion (quantified by the modulus of the wavefunction) and kinetic energy (quantified by the derivative of the wavefunction).

The possible overall wavefunctions therefore have different associated energies resulting from the correlation of electrons, with one specific arrangement being energetically preferable. Therefore the effects of exchange symmetry can be quantified by an interaction term J, denoted as the *exchange interaction* [2], and can be calculated via

$$J = \frac{1}{2}[\langle\Psi_S|\mathcal{H}|\Psi_S\rangle - \langle\Psi_T|\mathcal{H}|\Psi_T\rangle]. \tag{1.3}$$

where $\mathcal{H}$ is the effective Hamiltonian. For antiferromagnetic exchange ($J > 0$), the energetically preferable state for a pair of electrons is the singlet state, with the singlet spin wavefunction $\chi_S = \frac{1}{\sqrt{2}}[|\uparrow\downarrow\rangle - |\downarrow\uparrow\rangle]$ and $S = 0$. An electron pair coupled in this manner (i.e. via the exchange interaction) is referred to as a *spin dimer*, with a ground state given by the singlet state, and $S = 1$ excitations to the higher energy triplet states.

Extending to a many-electron system and focusing on the spin of the electrons only, one can consider a generic isotropic spin system with antiferromagnetic Heisenberg correlations, where the Hamiltonian is expressed in terms of spin operators $\hat{S}$ and given as $\mathcal{H} = \sum_{ij} J\hat{S}_i \cdot \hat{S}_j$, where i and j denote atomic sites. This Hamiltonian can be rewritten as

$$\mathcal{H} = \mathcal{H}_{zz} + \mathcal{H}_{\pm} = J\sum_{ij} S_i^z S_j^z + \frac{J}{2}\sum_{ij}(\hat{S}_i^+\hat{S}_j^- + \hat{S}_i^-\hat{S}_j^+) \tag{1.4}$$

where the Hamiltonian has been split into two terms. The first term $\mathcal{H}_{zz}$ is the Ising component and corresponds to correlations of spin direction along a specific quantisation axis (z in this case), and the second term $\mathcal{H}_{\pm}$ defines the 'spin-flip' components, where $\hat{S}^+$ and $\hat{S}^-$ are the raising and lowering operators. Considering a pair of electrons within the system, the preferred orientation is that of antiparallel alignment in a singlet state, with bond energy given by

$$\begin{aligned} E &= J\langle\hat{S}_i \cdot \hat{S}_j\rangle = J\langle(\hat{S}_i + \hat{S}_j)^2\rangle - \frac{J}{2}\langle\hat{S}_i{}^2 + \hat{S}_j{}^2\rangle \\ &= -JS(S+1) + \frac{J}{2}\langle(\hat{S}_i + \hat{S}_j)^2\rangle = -JS(S+1). \end{aligned} \tag{1.5}$$

with the last equality following from the property $|\hat{S}_i + \hat{S}_j| = 0$. This value is not obtained by merely allowing the two spins to be oriented antiparallel; such a case would give an interaction energy of $-JS^2$. The additional energy $-JS$ is a quantum

correction to the Ising eigenstate, and originates from allowing the variation of the moment from antiparallel alignment, accruing additional energy terms from the spin flip operators. This leads to the onset of *dimerisation* in a many-electron system, where pairs of electrons will preferentially couple into dimers each in a singlet ground state. Systems can be intrinsically dimerised, where dimers are formed between strongly coupled spins, or spontaneously dimerised where multiple pairs fluctuate over many possible dimer singlet configurations.

This is in contrast to the ferromagnetic case where the eigenstate corresponds to uniform alignment of spins and is identically that of the Ising eigenstate; the departure from this state in the antiferromagnetic case leads to the manifestation of *quantum fluctuations*, where the energy of the ground state can be minimised by the presence of the spin flip terms. These fluctuations occur with finite probability even down to $T = 0$ K as a consequence of Heisenberg's uncertainty principle, and when sufficiently strong they can prevent order entirely.

The strength of the quantum fluctuations can be quantised through the quantum correction, $-JS$, which in ratio to the classical energy $-JS^2$ results in quantum effects on the order $\sim 1/S$. Considering the general case of many spins correlated on a lattice, where the number of coupled spins is given by the co-ordination number z, this correction term is closer to $\sim 1/(Sz)$ [3].

This leads to an enhancement of the quantum fluctuations for systems with low co-ordination number z and low spin S. Minimum co-ordination number is found in systems with low values of dimensionality d, and it can be shown through the Mermin-Wagner theorem [4] that continuous symmetries cannot be broken at any temperature in systems where $d = 1$ or for systems at finite temperature for $d = 2$. While in any real model magnetic systems there will always be a finite three-dimensional exchange coupling, this can be significantly weaker than the 1 or 2 dimensional exchange terms, making them suitable approximations for experimental studies of low dimensional physics.

1.1 Quantum Magnetism

Even with high co-ordination number, long-range order can be prevented in some magnetic systems, typically in those where quantum effects are further enhanced by low spin quantum number S. Systems with $S \leq 1$ represent a class of materials of largest quantum effects and are thus referred to as 'quantum magnets'.

Much theoretical and experimental work has been dedicated to the study of quantum magnetic systems and their far-reaching impact on multiple fields of condensed

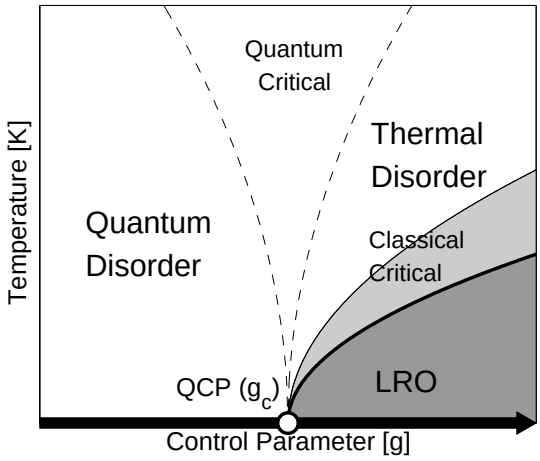

Figure 1.2: Phase diagram in the region of the QCP. The QPT is indicated by the black arrow and 'tuned' by a control parameter g. The QCP occurs at a critical value, g_c, and separates regions of quantum disorder (QD) from long-range order (LRO). The LRO extends to finite temperatures, with the classical critical regime separating LRO from thermal disorder.

matter physics, for example the questions of entanglement in many-body electron systems [5], the interplay of thermal fluctuations with pronounced quantum fluctuations [6], the application of 2-D S =1/2 antiferromagnetic models to understanding layered cuprate superconductors [7] and many more.

In particular, the existence of experimentally accessible $S = 1/2$ quantum disordered systems in the form of magnetic spin-gapped insulators leads to a fertile testing ground for quantum phase transitions and quantum critical phenomena.

With introduction of controlled perturbations, the quantum effects that preclude the existence of long-range order as described above can be continuously or discretely tuned across a phase boundary into an ordered state. The point separating these two phases is a *quantum critical point* (QCP) and the transition across it is a *quantum phase transition* (QPT). This is schematically shown in Figure 1.2 for a control parameter g, where g can be magnetic field, hydrostatic pressure or chemical doping and the strength of the quantum fluctuations scales as $1/g$ [5].

QPTs are a feature of many model systems, and experiments on a wide range of materials with different physical properties has led to a great deal of interest in quantum critical phenomena in multiple contexts. Examples include superconductivity through investigation of the cuprate superconductors and heavy fermion systems or the metal-insulator transition through studies of Mott insulators [8].

The physical properties of systems near the QCP are governed by the critical exponents; these are parameters which determine measurable quantities such as susceptibility, magnetisation or heat capacity under variation of the control parameter.

It is believed that these quantities might obey *universality*, where the value is independent of specific systems, depending only on the dimensionality of the system and order parameter, and on the nature of the constituent forces [2, 9]. This behaviour is known to occur for thermal phase transitions, but is as yet unconfirmed in the region of the QCP and is the focus of much current research.

Accompanying the stabilisation of order at the phase boundary is the emergence of coherent excitations of the ground state, shown by Goldstone to be a necessary consequence of spontaneous breaking of a continuous symmetry [10]. In the classically ordered example, the excitations are 'spin waves', describing transverse fluctuations of the ordered moment.

Beyond the QCP and within the quantum disordered regime, coherent excitations can persist; the ground state can be formed from the spontaneous formation of singlet dimer units, from which the principal excitations are those of triplet excitations located on the dimer, with any exchange coupling within correlated systems allowing for the propagation of triplets to neighbouring dimer units.

The dispersion of these triplets in reciprocal space can reveal information about the Hamiltonian; a summary of relevant theoretical models for application to experimental data will be presented in Chapter 3.

1.2 Model Magnetic Systems

The theoretical ideas of quantum magnetism can be tested experimentally through the investigation of model magnetic systems, which are physical realisations of model Hamiltonians in the form of crystalline lattices. The exchange geometry is dictated by the chemical composition of the compound and its symmetry, with correlations through the exchange interaction and various forms of superexchange mediated through intermediate atoms [11].

The coupled spin dimer system $TlCuCl_3$ provides a unique opportunity to study the evolution of elementary excitations across a QPT with unparalleled experimental flexibility. The system exists as a network of Cu^{2+} atoms, each possessing $S = 1/2$ and coupled into singlet dimers as illustrated in Figure 1.3. The ground state is non-magnetic, with bosonic quasi-particle $S = 1$ excitations above a spin gap energy $\Delta \sim 0.7$ meV. Through continuous tuning of hydrostatic pressure, the inter-dimer exchange interactions can be altered and a state of long-range magnetic order is stabilised. A very low critical pressure of $P = 1.07$ kbar allows for a systematic investigation of the evolution of elementary excitations across a quantum phase transition through high-pressure neutron scattering studies. Operating a method of continuous pressure

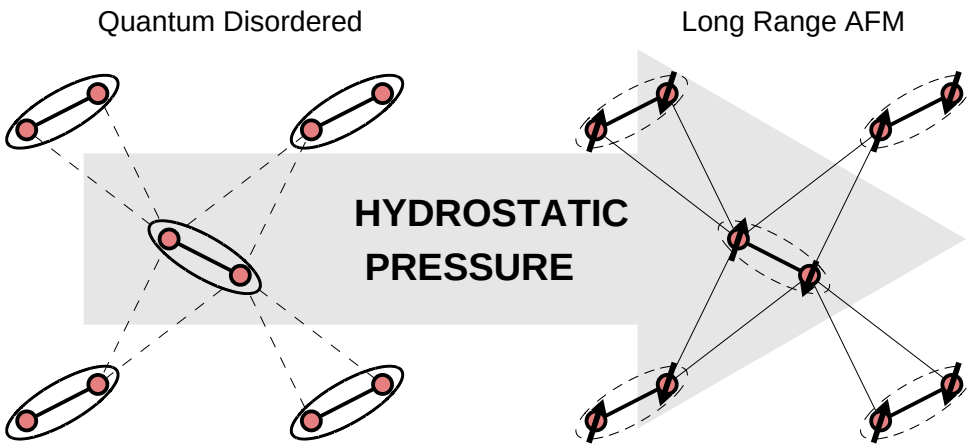

Figure 1.3: Stabilisation of magnetic order in $TlCuCl_3$ with applied hydrostatic pressure. The left picture indicates the weakly-correlated dimer units, with interdimer exchange given by the dashed lines. Increasing pressure alters these exchange interactions, increasing electron correlation and inducing magnetic order, illustrated by the right picture.

tuning and a cryostat with temperature regulation, the full evolution of excitations in the region around the QCP can be investigated, and is presented in Chapter 4.

Another kind of exchange geometry can be constructed by considering the case of a series of strongly coupled dimers. This is a 'spin ladder' geometry, so-called because the dominant exchange interaction scheme resembles that of a ladder, with the dimer units forming the 'rungs' and possessing exchange J_R, connected by interdimer exchange J_L in the manner of 'legs', as depicted in Figure 1.4 [a]. An example of such a geometry is the spin ladder compound $(C_5H_{12}N)_2CuBr_4$ [12], where the interladder exchange is significantly weaker than the intraladder exchange.

By considering the ratio of the rung to the leg coupling, the ground state can vary between an intrinsically dimerised case, as in $TlCuCl_3$, to a state of singlet bonds spontaneously forming on and fluctuating between many different pairs of magnetic atoms. This state is a 'resonant valence bond' (RVB) state, and can be used to describe the ground state of low-dimensional systems including that of the spin ladder.

In principle by strengthening the interladder exchange, the dimensionality of the exchange geometry increases and long-range order can be recovered. However, the inclusion of frustration on the lattice can prevent such order even for appreciably large inter-ladder exchange and higher dimensionality. Frustration effects within a spin ladder can be effected by including next-nearest-neighbour (NNN) exchange as is illustrated in Figure 1.4 [b], where the alignment of three spins to be mutually antiparallel is impossible and simultaneous bond-energy optimisation is once again prevented. A possible ground state could then correspond to an RVB state as given in Figure 1.4 [c].

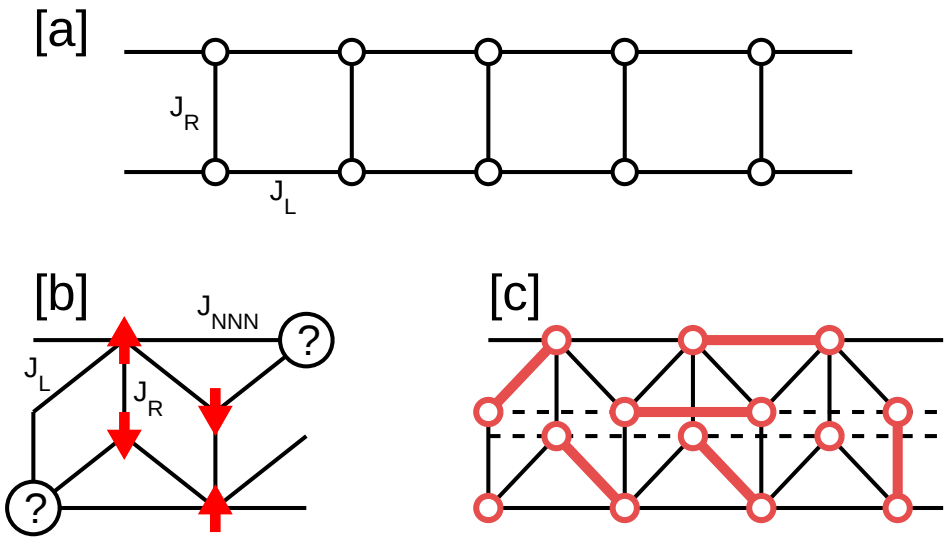

Figure 1.4: Spin ladder geometry. **[a]** The ladder is constructed from two coupled chains of spins, with the 'leg' exchange given by J_L and the 'rung' exchange given by J_R. **[b]** Illustration of how frustration prevents mutual antiparallel alignment of three coupled spins. **[c]** An example of the proposed 'RVB' ground state, with connected red circles indicating singlet states. The ground state is a rapid resonation of multiple singlets and exists as a superposition of many possible configurations.

The spin ladder compound $BiCu_2PO_6$ is a model magnetic system that is a practical realisation of the frustrated exchange geometry given in Figure 1.4 [c]. The system has been observed to exist in a quantum disordered ground state, with appreciable NNN exchange couplings that are thought to have significant effects on the dynamical properties. An investigation of the magnon dispersion energies and reciprocal space distribution will be outlined in Chapter 5.

As described for $TlCuCl_3$, a tuning of the Hamiltonian can be a method of recovering a form of long-range order. But a different kind of long-range order and QPT can be realised through the introduction of non-magnetic impurities onto a lattice that exhibits a quantum disordered ground state of dimers. This results in the liberation of a free spin on the site adjacent to the non-magnetic impurity. These impurity induced spins can then correlate with each other through an effective exchange interaction mediated through the connecting dimer sites. The realisation of such magnetic ordering is achieved through the substitution of Cu^{2+} ($S = 1/2$) with Zn^{2+} ($S = 0$) onto $BiCu_2PO_6$ and initial INS investigations of single crystals of this compound will be presented in Chapter 6.

Chapter 7 will follow, providing a short summary of the work conducted and an outlook.

2

Neutron Scattering

The dynamical and structural properties of model quantum magnets such as the ones introduced in the previous section are elucidated through investigation via neutron scattering, where neutrons are scattered elastically or inelastically from target samples, and a measurement of the scattered neutrons' energy and momentum is performed. The experimental data given in the chapters to follow were collected from several scattering experiments over the course of three and a half years, with multiple experiments on the beamlines located at the reactor source at the Institut-Laue-Langevin (ILL) in Grenoble, France, and beamlines from the spallation source (SINQ), at the Paul-Scherrer Institut (PSI) in Villigen, Switzerland.

The dynamical cross-section of neutrons for magnetic scattering is a derived mathematical quantity formulated from consideration of spin-spin correlations and as such experimental data yielded from scattering from solids can be directly and effectively applied to test theoretical models and ideas. In this chapter some of the basic theory of neutron scattering will be outlined, alongside an introduction of neutron diffraction and inelastic neutron scattering, with expressions for the cross-sections and the instrumentation used to measure them. The various sample environment options employed will also be presented and discussed.

2.1 Background

With the many applications to experimental investigations of modern physical problems, the technique of neutron scattering is an extremely powerful tool for physicists. It exists as a suitable probe to study solids and liquids, yielding structural information from interference effects that result from neutron wavelengths typically on the order of interatomic spacings.

"Thermal" neutrons are so-called due to their emission from a moderator near room temperature, and possess a Maxwellian distribution over the energy range 1-100 meV,

ideally suited for studying dynamical phenomena in materials. In addition, "cold" (0.1 - 10 meV) and "hot" (100 - 500 meV) neutrons are also produced through appropriate moderation at lower and higher temperatures respectively; the different ranges of incident neutrons thus allow experimental access across multiple energy regimes. As such, a combination of incident neutron energy and scattering geometry can be selected that is appropriate to the scattering system. The flexibility of neutron scattering energies and momenta allow for the systematic investigations at all relevant momentum and energy transfers.

There exist many texts that well describe the theoretical and practical principles of neutron scattering. Examples of more comprehensive treatments of scattering theory include those in the texts by G. L. Squires [13], Lovesey, [14, 15] and Shirane *et al.* [16] alongside many more. An abridged summary of the principal and relevant features is outlined below, but the reader is referred to the texts described above for a more thorough outlook. The ILL [17] and SINQ [18] websites are also excellent sources of information for available instrument setups and possible sample environments.

2.2 Basic Theory

The basic principle of neutron scattering is to project a beam of incident neutrons onto a sample that is to be investigated (the scattering system), from which they will scatter in all directions. The scattered neutrons and the scattering system obey standard laws of conservation of energy and momentum illustrated by Figure 2.1 and given by

$$\begin{aligned} \vec{Q} &= \vec{k}_i - \vec{k}_f \\ \hbar\omega = E_{\lambda_i} - E_{\lambda_f} &= \frac{\hbar}{2m_n}(k_i^2 - k_f^2) \end{aligned} \tag{2.1}$$

where m_n is the mass of the neutron, and ($\vec{Q}$, ω) correspond to the momentum and energy transferred to the scattering system through a scattering event. The quantities $\vec{k}_i$ and $\vec{k}_f$ are the initial and final wavevectors of the neutron and E_{λ_i} and E_{λ_f} are the initial and final energies of the scattering system. For crystalline systems, the momentum transferred to the crystal can be decomposed into a combination of the mode wavevector $\vec{q}$ and the reciprocal lattice wavevector $\vec{\tau}$, giving $\vec{Q} = \vec{q} + \vec{\tau}$.

2.2.1 Scattering Cross Section

In a scattering experiment, the measured quantity is the intensity of neutrons scattered. This is given by σ, the *scattering cross-section* and defined as the total number of

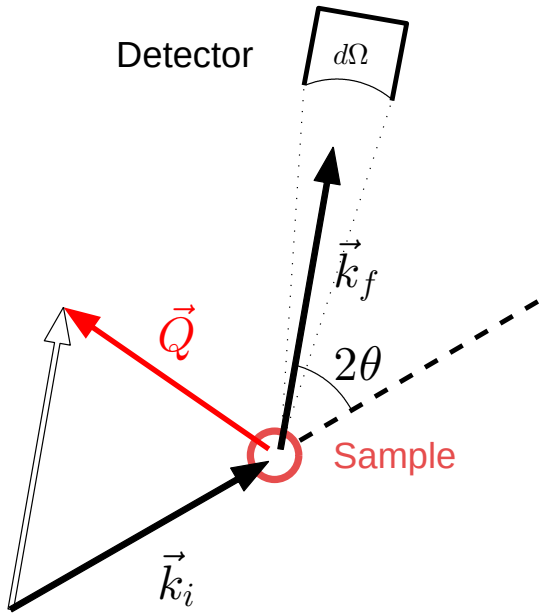

Figure 2.1: Illustration of generalised scattering geometry for neutrons of incident wavevector $\vec{k}_i$, final wavevector $\vec{k}_f$, and measured over solid angle $d\Omega$.

neutrons scattered per second, N_{tot}, divided by the total incident flux of neutrons Φ,

$$\sigma = \frac{N_{tot}}{\Phi}. \tag{2.2}$$

where by 'total', it is to be understood as the number scattered in all directions.

The neutrons are not scattered uniformly, and it is the angular distribution of scattered neutrons that yields information about the scattering system. This distribution is described by the *differential cross-section*, giving the total number of neutrons scattered into a small solid angle dΩ,

$$\left(\frac{d\sigma}{d\Omega}\right)_{\lambda_i \to \lambda_f} = \frac{k_f}{k_i}\left(\frac{m_n}{2\pi\hbar^2}\right)^2 |\langle \vec{k}_f \lambda_f | V | \vec{k}_i \lambda_i \rangle|^2, \tag{2.3}$$

and is derived from Fermi's Golden Rule [13]. λ_i and λ_f are the initial and final states of the scattering system and V is the real-space interaction potential, which determines the extent to which the incident neutrons interact with the scattering system. A calculation of the matrix elements yields the probability of a transition from the initial state to the final state of the combined momentum and energy of the neutron and scattering system.

The differential cross-section corresponds to an integration of scattering events over all final energies

$$\frac{d\sigma}{d\Omega} = \int_0^\infty \left(\frac{d^2\sigma}{d\Omega dE_f}\right) dE_f \tag{2.4}$$

where the integrand is defined as the *partial differential cross-section* and is the quantity defining the number of neutrons scattered within a finite energy range $E_f + dE_f$. For a neutron scattering event at the point $(\vec{Q}, \omega)$, it is given by

$$\left(\frac{d\sigma}{d\Omega dE_f}\right)_{\lambda_i \to \lambda_f} = \frac{k_f}{k_i}\left(\frac{m_n}{2\pi\hbar^2}\right)^2 |\langle \vec{k}_f \lambda_f | V | \vec{k}_i \lambda_i \rangle|^2 \delta(\hbar\omega + E_i - E_f). \tag{2.5}$$

In a scattering experiment the cross-section for specific transitions from one quantum state to another given by Equation 2.5 is not measured. Instead the observed scattered intensity is a measurement of the general partial differential cross-section $(d^2\sigma/d\Omega dE_f)$. This can be obtained by considering a summation over all final states λ_f and then average over the initial states λ_i. Following Ref. [13], one can calculate

$$\frac{d^2\sigma}{d\Omega dE_f} = \frac{k_f}{k_i}\frac{1}{2\pi\hbar}\sum_{jj'} b_j b_{j'} \int_{-\infty}^{\infty} \langle \exp\{-i\vec{Q}\cdot\vec{R_{j'}}(0)\}\exp\{i\vec{Q}\cdot\vec{R_j}(t)\}\rangle \times \exp(-i\omega t)dt. \tag{2.6}$$

where the interaction potential takes the form of the Fermi pseudo-potential with $V(\vec{x_j}) = (2\pi\hbar^2/m) b_j \delta(\vec{R}_j)$, and corresponds to neutrons scattering from the nuclei of the scattering system. $\vec{R}_j$ is the position vector of the jth nucleus, and the interaction strength is described by a 'scattering length', b_j. This value dictates the probability of a scattering event occuring and in contrast to the analagous quantity for X-ray scattering, varies in a manner largely independent of the atomic number.

2.2.2 Correlations

The cross-section of Equation 2.6 can be split into two components; the contribution from 'coherent' scattering and the contribution from 'incoherent' scattering, written as

$$\begin{aligned}
\left(\frac{d^2\sigma}{d\Omega dE_f}\right)_{coh} &= \frac{\sigma_{coh}}{4\pi}\frac{k_f}{k_i}\frac{1}{2\pi\hbar}\sum_{jj'}\int_{-\infty}^{\infty}\langle \exp\{-i\vec{Q}\cdot\vec{R_{j'}}(0)\}\exp\{i\vec{Q}\cdot\vec{R_j}(t)\}\rangle \times \exp(-i\omega t)dt \\
\left(\frac{d^2\sigma}{d\Omega dE_f}\right)_{inc} &= \frac{\sigma_{inc}}{4\pi}\frac{k_f}{k_i}\frac{1}{2\pi\hbar}\sum_{j}\int_{-\infty}^{\infty}\langle \exp\{-i\vec{Q}\cdot\vec{R_j}(0)\}\exp\{i\vec{Q}\cdot\vec{R_j}(t)\}\rangle \times \exp(-i\omega t)dt
\end{aligned} \tag{2.7}$$

where $\sigma_{coh} = 4\pi(\bar{b})^2$ and $\sigma_{inc} = 4\pi\{\bar{b^2} - (\bar{b})^2\}$, where $\bar{b}$ is the average value of the scattering length. The coherent cross-section refers to correlations between the positions of the same nucleus at different times, and on correlation between the positions of different nuclei at different times. The incoherent cross-section corresponds only to correlations between the same nucleus at different times.

The coherent cross-section therefore demonstrates interference effects, and it is through the observation of this term that structural and dynamical properties can be

observed. The incoherent scattering length varies across nuclei independent of the coherent scattering length, and is often observed as a finite background contribution on top of coherent intensity. The coherent expression given by Equation 2.7 can be considered in terms of the atomic correlations, and quantified by the correlation function $G(\vec{r},t)$

$$G(\vec{r},t) = \frac{1}{N(2\pi)^3}\sum_{jj'}\int \langle \exp\{-i\vec{Q}\cdot\vec{R_{j'}}(0)\}\exp\{i\vec{Q}\cdot\vec{R_j}(t)\}\rangle \times \exp(-i\vec{Q}\cdot\vec{r})d\vec{Q}, \tag{2.8}$$

and the scattering function $S(\vec{Q},\omega)$, given by

$$S(\vec{Q},t) = \frac{1}{2\pi\hbar}\int G(\vec{r},t)\exp\{i(\vec{Q}\cdot\vec{r}-\omega t)\}d\vec{r}dt, \tag{2.9}$$

where $S(\vec{Q},\omega)$ is closely related to the partial differential cross-section, given by

$$\left(\frac{d^2\sigma}{d\Omega dE_f}\right)_{coh} = \frac{\sigma_{coh}}{4\pi}\frac{k_f}{k_i}NS(\vec{Q},\omega). \tag{2.10}$$

Measurement of the partial differential cross-section is therefore a direct measurement of the Fourier transformed correlations of the atomic positions in space and time, with the Fourier transformed spatial component described by a vector $\vec{Q}$ in reciprocal space, and the Fourier transformed time described by energy ω.

Considering the cross-section for a Bravais crystal, where the atomic positions are described by the lattice vector $\vec{l}$, the scattering function becomes

$$S(\vec{Q},\omega) = \frac{N}{2\pi\hbar}\exp(-2W)\sum_{l}\exp(i\vec{Q}\cdot\vec{l})\int_{-\infty}^{\infty}\exp(-i\omega t)dt. \tag{2.11}$$

where N is the number of the nuclei in the crystal, and W the Debye-Waller factor originating from thermal motion of the nuclei. Rewriting the lattice sum over $\vec{l}$ as

$$\sum_{l}\exp(i\vec{Q}\cdot\vec{l}) = \frac{(2\pi)^3}{\nu_0}\sum_{\tau}\delta(\vec{Q}-\vec{\tau}), \tag{2.12}$$

where ν_0 is the volume of the unit cell of the crystal, the scattering function $S(\vec{Q},\omega)$ can be substituted into Equation 2.10. By performing the integral over energy, the differential cross-section is recovered as

$$\left(\frac{d\sigma}{d\Omega}\right)_{coh} = \frac{\sigma_{coh}}{4\pi}N\frac{2\pi}{\nu_0}\exp(-2W)\sum_{\tau}\delta(\vec{Q}-\vec{\tau}). \tag{2.13}$$

Scattering therefore only occurs for $\vec{Q} = \vec{\tau}$, which is a fulfillment of the Bragg condition with the observed angle of scattering as θ given by Bragg's Law

$$n\lambda = 2d\sin\theta. \tag{2.14}$$

Neutrons scattered as a result of the nuclear potential yield information about the nuclear arrangement of the scattering system, with elastic signal from the structural composition and inelastic signal from the vibrations of the nuclei (phonons). This kind of scattering intensity is referred to as 'nuclear scattering intensity'.

2.3 Magnetic Neutron Scattering

A second type of scattering occurs due to an interaction of the incident neutrons with any unpaired electrons in orbitals around the nucleus. The neutrons, with spin $S = 1/2$, have a finite magnetic moment that can interact with the local magnetic field produced by the unpaired spins. The intensity and reciprocal space distribution of neutrons scattering due to this interaction yield information about the electron correlation within the scattering system; this type of scattering is therefore referred to as 'magnetic scattering' .

The interaction potential V_m can be described by the coupling of the magnetic dipole moment of the neutron μ_N with the electron field B_e, giving $V_m = \mu_N \cdot B_e$ where the quantities are described by

$$\begin{aligned} \vec{\mu}_N =& -\gamma\mu_N\vec{\sigma_N} \\ \vec{B_e} =& \vec{B_S} + \vec{B_L} = \frac{\mu_0}{4\pi}\left\{\nabla \times \left(\frac{\vec{\mu_e} \times \hat{R}}{R^2}\right) - \frac{2\mu_B}{\hbar}\frac{\vec{p} \times \hat{R}}{R^2}\right\} \end{aligned} \tag{2.15}$$

with $\mu_N = (e\hbar/2m_p)$ is the nuclear magneton, $\vec{\sigma}_N$ the Pauli spin matrix, μ_B the Bohr magneton and γ = -1.913 the gyromagnetic ratio of the neutron. $\vec{\mu_e}$ is the magnetic dipole moment of the electron, $\vec{p}$ is the momentum of the electron and $\hat{R}$ is the unit vector of in the direction $\vec{R}$, a location at some point from the electron. The two terms in B_e are contributions from the intrinsic angular momentum (B_S) and from the orbital angular momentum (B_L). Considering this interaction, the double differential cross-section Equation 2.5 can be written as

$$\frac{d^2\sigma}{d\Omega dE_f} = (\gamma r_0)^2\frac{k_f}{k_i}|F_m(\vec{Q})|^2\exp(-2W)\sum_{\alpha,\beta}\left(\delta_{\alpha\beta} - \frac{Q_\alpha Q_\beta}{\vec{Q}^2}\right)S(\vec{Q},\omega). \tag{2.16}$$

with a notable difference when compared to the nuclear case given in Equation 2.10 being the inclusion of the *magnetic form factor*, $F_m(\vec{Q})$. This has the same origin as

the atomic form factor present in X-ray scattering, namely the electron cloud density $\rho(\vec{r})$. As the observed momentum transfer $\vec{Q}$ increases, the wavelength decreases to a scale on the order of the electron separation and interference effects attenuate the scattering amplitude.

Furthermore, an additional term, $\sum_{\alpha\beta}(\delta_{\alpha\beta}-\frac{\hat{Q}_\alpha\hat{Q}_\beta}{\vec{Q}^2})$, is also present. This arises from the projection of $\vec{Q}$ onto the plane orthogonal to the neutron scattering wavevector, a consequence of the evaluation of $\langle k|\nabla\times\left(\frac{\mathbf{s}\times\hat{\mathbf{R}}}{R^2}\right)|k\rangle$, and derived in Ref. [13]. It is to be noted that one consequence of this term is that contributions to the magnetic scattering intensity only occur for the scattering from spin components orthogonal to the scattering wavevector.

2.3.1 Elastic Magnetic Scattering

Considering the interaction potential due to the electron spin, the scattering function in Equation 2.16 is now dependent on the spin arrangements of the constituent atoms and not on the nuclear locations and as such is a different quantity to that given in Equation 2.11. Considering the matrix elements of Equation 2.5 for spin-spin correlations, the scattering function can then be calculated as

$$S(\vec{Q},\omega)=\sum_{i,j}\int_{-\infty}^{\infty}\langle e^{i\vec{Q}\cdot(\vec{R}_i-\vec{R}_j)}\rangle\langle S_i^\alpha(0)S_j^\beta(t)\rangle e^{-i\omega t}dt \tag{2.17}$$

where $\vec{R}_i$ corresponds to the location of the electron spin at the index i, and α,β corresponds to the spin component (i.e. x, y, z). Similar to the nuclear scattering function (Equation 2.9) being the Fourier transform in time and space of the correlations between positions of nuclei, the magnetic scattering function is the Fourier transform of time-dependent correlations of spins.

As $t\rightarrow\infty$, the correlation function $\langle S_i(0)S_j(t)\rangle$ becomes independent of time. Taking this limit and integrating the double differential cross-section over energy results in the equation

$$\left(\frac{d\sigma}{d\Omega}\right)_{el}=(\gamma r_0)^2N|F_m(\vec{Q})|^2\exp(-2W)\sum_{\alpha\beta}(\delta_{\alpha\beta}-\hat{Q}_\alpha\hat{Q}_\beta)\sum_l\exp(iQ\cdot l)\langle S_0^\alpha\rangle\langle S_l^\beta\rangle \tag{2.18}$$

The sum $\sum_l\exp(\vec{Q}\cdot\vec{l})$ can be shown to be equal to $\frac{2\pi}{\nu_0}\sum_{\tau_m}\delta(\vec{Q}-\vec{\tau}_m)$[13], where ν_0 is the unit cell sample volume and $\vec{\tau}_m$ is a reciprocal lattice vector in the magnetic unit cell. Similar to the nuclear elastic scattering, this results in elastic scattering occurring for scattering wavevectors $\vec{Q}=\vec{\tau}_m$, a fulfillment of the Bragg condition and leading to the observation of magnetic Bragg scattering at these wavevectors.

Figure 2.2: The neutron diffractometer TriCS (SINQ, PSI). The incident neutrons are selected from a white beam with a monochromator, which then scatter from the crystal sample. Intensity at a specific scattering wavevector is measured with the single tube detector or the area detector. A tilting geometry operates to allow for measurements across a wide range of reciprocal space. From Ref. [18]

Observation of elastic magnetic scattering (diffraction) can be achieved with any one of multiple available neutron instruments, such as the diffractometer TriCS, shown in Figure 2.2. In such an instrument, a fixed monochromator selects a specific wavevector that acts as the incident beam on the sample. A single detector or area detector is then utilised in a varying geometry beyond a rotateable sample to select a specific scattering wavevector for the same final energy.

2.3.2 Inelastic Magnetic Scattering

Returning now to consideration of scattering events at finite energy transfer, the scattering function is expressed in a general form

$$S^{\alpha\beta}(\vec{Q},\omega) = \sum_{i,j} \exp\left(i\vec{Q}\cdot(\vec{R}_i - \vec{R}_j)\right) \times \sum_{\lambda_i\lambda_f} \langle\lambda_i|\hat{S}_i^{\alpha}|\lambda_f\rangle\langle\lambda_f|\hat{S}_j^{\beta}|\lambda_i\rangle\delta(E_{\lambda_i} - E_{\lambda_f} + \hbar\omega) \tag{2.19}$$

where the spin term S_i^{α} denotes the spin component at the site $\vec{R}_i$ and λ_i and λ_f indicate the initial and final states of the scattering system. Thus, transitions between spin states of different energies contribute to the inelastic cross-section; measurement of the inelastic scattering intensity can therefore be used to infer information about the nature of these excitations.

Figure 2.3: A schematic showing the setup and instrumentation of a possible scattering geometry for the TASP (SINQ, PSI) triple-axis spectrometer, when the instrument is operated in a polarisation setup with flippers before and after the sample. From Ref. [18]

The analysis of inelastic neutron scattering intensity is a measurement of the double-differential cross-section where scattering contributions from finite energy transfers can be separated from those at zero energy transfer. This can be done with a great degree of accuracy with the triple-axis spectrometer (TAS).

The TAS is arguably the most versatile instrument available for neutron scattering studies, due to the ability to probe almost any coordinates in momentum-energy space in a precisely controlled fashion. Other spectrometers do have some advantages over the TAS, such as the time-of-flight spectrometers that allow for simultaneous data collection across a large area of reciprocal space, or back-scattering instruments that provide high resolution data, but it is the great flexibility of the TAS that sets it apart from other such instruments.

The three axes mentioned are the monochromator axis, the sample axis and the analyser axis. The monochromator operates through coherent Bragg scattering of a 'white' neutron beam, therefore defining the momentum and energy of the beam incident onto the sample. The analyser crystal operates in a similar fashion and selects a specified momentum and energy of the scattered beam. The sample rotation then allows for a variation of the momentum transfer within the region of reciprocal space

defined by the crystal.

Scans at and between specific points $(\vec{Q}, \omega)$ become possible, as well as the ability to distinguish the inelastic and elastic contributions to the cross-section. This is an intrinsic feature of the three-axis geometry, but to have an effective spectrometer many other components are necessary. These include but are not limited to monochromator/analyser crystals, collimators, detectors and energy filters. A possible setup of the cold neutron spectrometer TASP at SINQ, PSI is given in Figure 2.3.

The spectrometer can be adapted for a wide range of experimental methodologies through the ability to implement multiple sample environments. For example, polarisation analysis can be implemented with the installation of polarising devices, analysing devices and neutron flippers before and after the sample, or multiple analyser plates can be simultaneously operated to probe a broader range of reciprocal space.

2.3.3 Resolution Considerations

As with most experimental work, the precision of the data collection is restricted in no small part to the instrumental limitations. Due to the small scattering cross section of neutrons and with the limited neutron flux available, it is therefore necessary to perform measurements with finite beam divergences, and utilising monochromator and analyser crystals with significant mosaic widths. This results in the neutron beam, rather than being sharply focused at the desired energy momentum transfer $(\vec{Q_0}, \omega_0)$, having a finite width in energy and momentum. This distribution is referred to as the spectrometer resolution function, $R(\vec{Q} - \vec{Q_0}, \omega - \omega_0)$.

The volume and functional form for the resolution ellipsoid can be calculated via the Cooper-Nathans method [19]. This method takes into consideration the angular geometry of a triple axis spectrometer, but neglects the spatial effects (such as the size of the sample). The method given by M. Popovici[20] incorporates these elements, alongside the angular considerations included in Cooper-Nathans.

The measured scattering intensity can then be described as a convolution of the spectrometer resolution function and the scattering function $S(\vec{Q}, \omega)$, as illustrated in Figure 2.4. In this treatment, the scattering intensity observed by the analyser is the volume overlap of the resolution ellipsoid and the scattering function. When the ellipsoid $\vec{Q}$ value matches that of the minimum of a dispersion, scanning the spectrometer in energy results in overlap on the tails of the resolution with the dispersion branches on either side of the minimum. This results in a focusing effect, creating a 'wedge' shape in the scattering intensity.

The example in the figure is for one dimension, but the contribution to the scattering intensity is a full integration over the four dimensional $(\vec{Q}, \omega)$ space and results

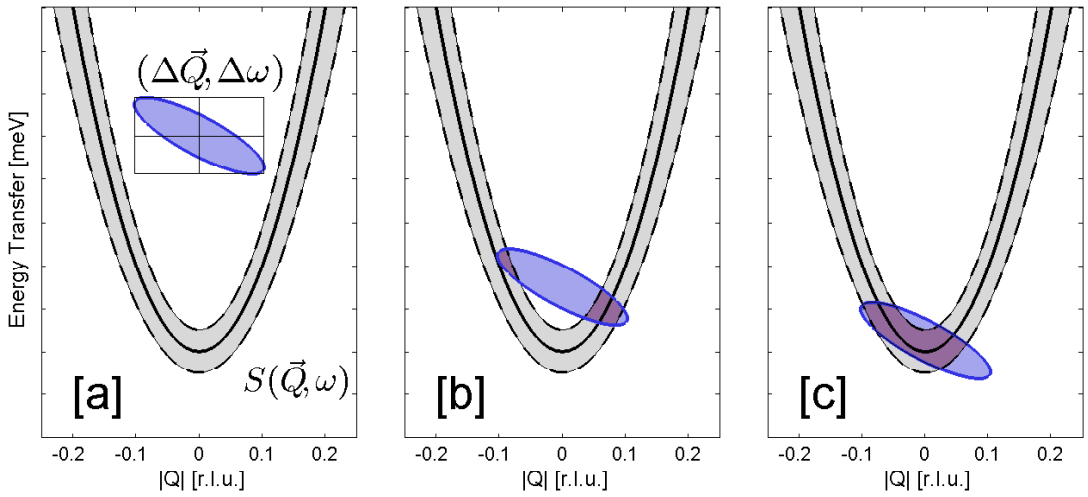

Figure 2.4: Neutron resolution convolution. **[a]** Illustrates a general magnon dispersion with a scattering function $S(\vec{Q}, \omega)$, with the grey shaded region as spectral width of the mode. The blue area is the resolution ellipsoid, $(\Delta\vec{Q}, \Delta\omega)$, with no overlap between the ellipsoid and the magnon dispersion. **[b]** The magnon dispersion and resolution ellipsoid with partial overlap. **[c]** The resolution ellipsoid and magnon dispersion with a large degree of overlap.

in a significant deviation from simpler lineshapes (e.g. Gaussian, Lorenzian). As such, this treatment is necessary to extract accurate spectral widths from the fitted scattering function. The resolution function has its peak at $(\vec{Q_0}, \omega_0)$, and decreases for deviations from that maximum, with the constant amplitude contours forming a set of nested ellipsoids in $(\vec{Q}, \omega)$ space. The functional form of the resolution function will depend only on $(\vec{Q_0}, \omega_0)$, given a specific instrumental orientation.

In the resolution convolution fitting process utilised in Chapter 4, the ellipsoid was calculated using the Popovici method using instrument parameters taken from the spectrometer used for the measurement - the cold neutron triple-axis spectrometer IN14 at the Institut Laue-Langevin (ILL), Grenoble.

2.4 Sample environment

A flexible sample environment within a neutron scattering experimental setup allows for extended investigations of external tuning parameters that can affect the properties of the scattering system under investigation. Sensitivity to temperature, pressure and magnetic field can all be measured with the application of a variety of commercially available or custom built instrumentation such as cryostats, cryofurnaces, cryomagnets or high pressure clamp or gas cells.

2.4.1 Cryogenics

Temperature is without doubt the key control parameter in the study of the properties of matter. Through the use of cryogenic liquids with low boiling points, specifically Nitrogen and Helium, a sample environment can be maintained and regulated that allows for the continuous variation of temperature. Magnetic behaviour is strongly temperature dependent, with magnetic properties emerging below a sample-dependent critical temperature T_c and the ability to continuously tune at a wide range of temperatures is crucial in the study of magnetic phenomena. Furthermore a rich variety of quantum critical phenomena occur as a consequence of quantum fluctuations, arising only when the effect of thermal fluctuations can be suppressed, namely when the system is at the lowest possible temperature, "$T = 0$ K".

The temperature range subject to study can be achieveable with more generic ^{4}He cryostats. These operate in a regime where the temperature of liquid ^{4}He with a boiling point of 4.2 K can be reduced to a base operating temperature of $\sim$ 1.5 K achieved through pumping. In some cases when lower temperatures are needed, use of ^{3}He is required. With pumping in the same fashion as the standard cryostat, ^{3}He fridges can be operated with a minimum temperature of 250 mK, below which further cooling cannot be achieved due to rapidly diminishing vapour pressure. However, even lower temperatures can be achieved with a dilution setup where liquid ^{3}He and superfluid ^{4}He coexist. Below 0.7 K these separate and the ^{4}He layer acts as a 'mechanical vacuum', resulting in significant cooling power [21] on the ^{3}He fluid. The upper operational limit of the dilution setup is the superfluid phase boundary of ^{4}He, occurring at 2.18 K.

Multiple cryostats are available for operation with neutron scattering environments, with variable sample spaces and wide scattering windows. The temperature is regulated through the monitoring of multiple thermometers, with the most accurate indication of the sample temperature given by a thermometer located at the bottom of a sample stick to which the sample is mounted. Comparing to the temperature read by a thermometer close to the source of generated heat, the temperature can be maintained through a prescribed set of parameters, the PID parameters, that adjust a heat load in proportion to the difference in temperature (P), a time-integral of the difference (I) and a time derivative of the difference (D). The parameters are chosen based on the temperature range, the heating power and the cryostat and are calibrated with a temperature controller. This results in an easy and reliable method of changing, maintaining and sweeping in temperature.

2.4.2 Magnetic Field

The application of magnetic fields is an indispensable tool for the elucidation of magnetic properties; the coupling of magnetic moments to external applied fields yields a finite energy term and result in phenomenological change in dynamic or structural properties - for example applied field can split degenerate excitations in a Zeeman-like fashion, or can result in a closing of a spin gap in a class of materials with Bose Einstein condensation.

The cryomagnets typically used in neutron scattering studies are commercially available units from companies such as *Oxford Instruments*, but pushing the upper limits on attainable sample environments is an active area of research [22]. In the design of a cryomagnet, there is always a trade-off to be made between the flexibility required by neutron scatterers (for example, variable sample space and configuration and a sufficiently large solid angle scattering window) and the limitations of the instrumentation (such as magnetic materials and electronics, cooling of the magnetic coils and sample and space restrictions).

The resulting vertical-field cryomagnets consist of split-pair coils in a Helmholtz configuration with the axis of the coils the vertical axis of the instrument. This allows for the loading of samples with relative ease, and a nearly 360° scattering window with the magnetic field maintained by a persistent current in the superconducting coils. The simultaneous application of cryogenic cooling methods is required to maintain the current below the critical value and prevent magnet quenching.

This upper limit is typically much lower than the highest magnetic fields attainable in bulk measurements, achieved with short duration pulsed magnetic fields; the persistent uniform magnetic fields with high uniformity required by neutron scattering have a maximum of ~ 15 T with current commercially available vertical cryomagnets.

2.4.3 High Pressure INS

High pressure is a powerful tool for experimental physicists. It allows for a continuous and reversible method of tuning the properties of a sample under investigation by directly altering the structure of the sample. This can result in a variety of other phenomena and phase transitions, sometimes as a result of only slight perturbations of the original structure. Specifically, the continuous tuning of applied hydrostatic pressure on a magnetic system mounted inside a cryostat at base temperature can be an experimental realisation of a quantum phase transition.

High-pressure instrumentation can exist for extreme pressure ranges up to many GPa with anvil cells, a miniaturised form of clamp cell, where crystal samples are placed

inside a gasket between two surfaces of hard material such as sapphire, moissanite or diamond. The hardest materials allow for the highest pressures, and in some circumstances diamond anvil cells can be effectively employed to reach 200 GPa, a pressure near that of the core of the earth.

However, while anvil cells have been adapted for use with experimental techniques such as heat transport, magnetometry and X-ray scattering, instrumental factors severely limit the range of allowed pressures for neutron scattering. Chief among these is the allowed sample size; the low relative flux of neutrons require large sample sizes that cannot be mounted inside generic anvil cells. While a larger anvil cell exists in the form of the Paris-Edinburgh cell [23, 24] with a range of applied pressure $P <$ 25 GPa, the lack of cooling power and limited sample sizes precludes the experimental conditions required for many investigations into quantum magnetic behaviour.

The range of pressures allowed for single crystal neutron spectroscopy is limited to a maximum of 15 kbar, through the use of a large clamp cell where single crystal samples of mass $\sim$ 1 g can be immersed in a pressure-transmitting medium such as Fluorinert and compressed between two large CuBe pistons. The attainable pressure is non-continuous in application; every pressure point requires a removal of the pressure cell from the instrument and a loading of pressure with an external ram. They are also non-reversible, with only an increase in pressure allowed. Furthermore, the higher pressures are only achievable with risk of strain and breakage of the sample.

For a continuous and reversible tuning of pressure, one can use the more flexible gas-loaded pressure cell, in which the sample is loaded into a chamber which is then filled with helium gas and pressurised, the apparatus for which is given in Figure 2.5 [a]. The pressure is maintained by an external compressor as the system is then cooled through the melting point. At the operating temperature $T \sim 1.5$ K, the sample is then encased in pressurised solid helium. Thorough investigations into the hydrostatic nature of the pressure through this loading technique have been performed through ruby fluorescence techniques, comparing Helium gas to that of other gas pressure mediums such as Xenon and Argon, and it was observed that solidified helium demonstrates a high hydrostaticity in the low temperature region [23].

The pressure must be loaded into the cell in the gaseous phase and then cooled into the solid phase, with pressure continuously applied throughout and after cooling through the phase transition, as illustrated in Figure 2.5 [b]. Therefore to ensure the correct pressure is loaded and to maintain a high level of hydrostaticity, before each pressure is loaded the system was heated to a point deep inside the gaseous phase (step (1)), before the pressure is increased (step (2)), before finally cooling through the transition (step (3)). Upon cooling through the phase boundary, a decrease in

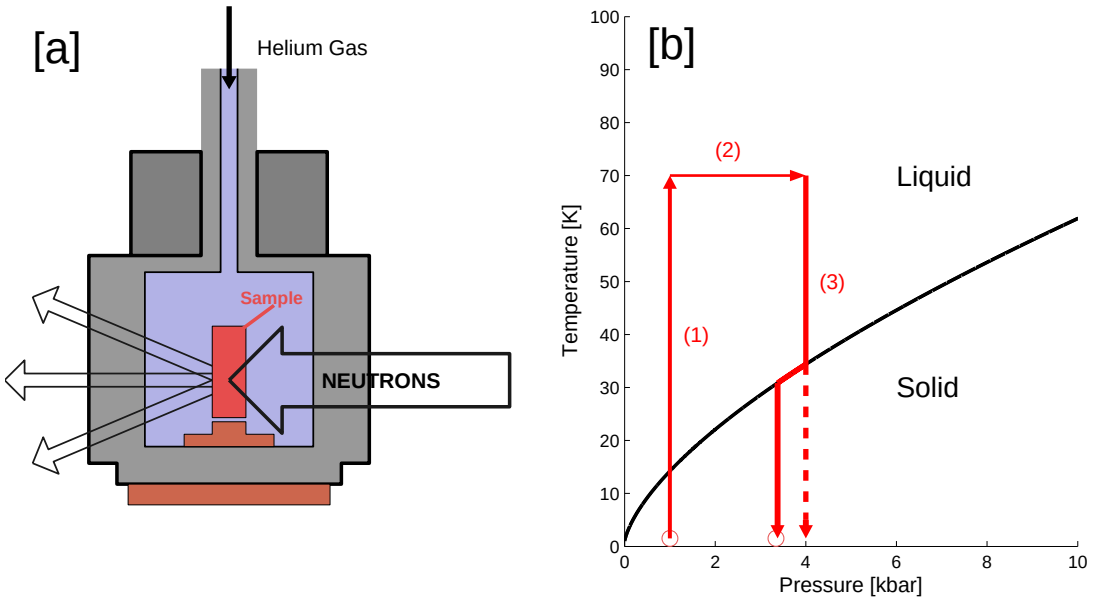

Figure 2.5: The high pressure INS setup. **[a]** The continuous loading gas pressure cell. The sample is loaded inside the cell and surrounded by ^{4}He gas, pumped in by an external compressor. Neutrons can pass through the cell and scatter from the sample inside. **[b]** The ^{4}He solid-liquid phase diagram for hydrostatic pressure and temperature of the operational pressure region. The red lines indicate the steps taken in loading a higher pressure.

pressure is possible because of the contraction of the helium volume, resulting in a final lower pressure as indicated. This effect is minimised through slow cool and correct calibration of the compressor that ensures a maintained hydrostatic pressure with cooling. This method is illustrated in Figure 2.5 [b], where liquid-solid phase boundary is shown by the black line and given by the Simon equation for Helium-4[25]; $P(\text{bar}) = 16.235[(\text{T}/0.992)^{1.5544} - 1]$.

3

Theory of Excitations

Any observed coherent inelastic neutron scattering intensity is a result of an excitation of the scattering system, in which energy and momentum is transferred from the neutron. The reciprocal space dependence of these excitation energies is the *dispersion*, and depends on the Hamiltonian of the scattering system.

To understand the observed dispersion from the INS data, theoretical models must be formulated against which it can be compared. This can be achieved through numerical calculation, where clusters of magnetic atoms are simulated for specific exchange geometries and the expected excitation energies calculated. However, this does not produce an analytical description and will only give calculated excitation energies for specified momentum transfers.

General analytical dispersion relations can be calculated from considering perturbative expansions around a strong coupling limit, where one visualises the exchange geometry existing as a network of interconnecting dimers, in which the intradimer term is stronger than the other exchange terms. The strong-coupling limit can also be modeled through the formulation of a bond-operator theory, where the Hamiltonian can be written as operators describing the different bonds between constituent atoms. These approaches have limitations, with the breakdown of the accuracy of the description once the ratio of interdimer terms to intradimer terms approaches unity [26].

The bond-operator approach has previously been shown to be very successful for the low temperature case of the spin dimer compound $TlCuCl_3$, and is proposed as a description of the dispersion of excitations in $BiCu_2PO_6$. The analytical descriptions of dispersions for both exchange geometries are considered below, with the case for $TlCuCl_3$ extended to finite temperatures and the case for $BiCu_2PO_6$ discussed in the context of extending a spin ladder treatment to include frustration from NNN interactions.

3.1 Bond Operator Theory

In a 'classical' magnetic phase transition, the breaking of symmetry is characterised by the emergence of long-range order in the crystal. In accordance with Goldstone's theorem, excitations emerge with the breaking of symmetry at the critical point [10]. The excitations, called 'Goldstone modes', in classical antiferromagnets simply describe transverse fluctuations of the ordered moment and are typically referred to as 'spin waves'. In the case of completely isotropic exchange interactions, these remain gapless with significant spectral intensity, and can be described with accuracy with Linear Spin Wave (LSW) theory, as is seen in the classical examples $RbMnF_3$ and MnF_2, [27, 28], with $S = (5/2)$.

In some cases of quantum magnetic systems, linear spin wave theory can be adjusted, such as for La_2CuO_4, which is a square-lattice Heisenberg $S = 1/2$ antiferromagnet, the ground state for which is widely accepted as long-range Néel order with a reduced sublattice magnetisation resulting from quantum fluctuations [29]. However, this quasi-classical picture of spin excitations fails when attempting to describe the spin-spin correlations of most quantum systems due to the bipartite model described by Néel order not being an eigenstate of the system. It is inappropriate to $TlCuCl_3$ in particular due to spin dimer exchange network not supporting such classical order.

It is possible to adopt a more robust theoretical framework based around the formation and excitation of individual bonds between and within pairs of spins, referred to as a *Bond Operator Theory*. Introduced by Sachdev and Bhatt [30] to describe the quantum ground state of spontaneous dimer formation on frustrated two dimensional S=1/2 antiferromagnets, more complete theories have been constructed with success for copper trichloride compounds [31, 32], and serve as a robust theoretical model for quantum systems evolving from the regimes of quantum disorder into the field and pressure-induced ordered phases for "T = 0K".

In the bond operator representation, through assuming the antiferromagnetic intradimer exchange is dominant, and choosing a quantisation axis defined by an external magnetic field, the $S = 1/2$ degrees of freedom on each dimer can be represented by the bond operators s, t_+, t_0 and t_- on the vacuum state $|0\rangle$

$$\begin{aligned} |s\rangle &= s^\dagger|0\rangle = \frac{1}{\sqrt{2}}(|\uparrow\downarrow\rangle - |\downarrow\uparrow\rangle) \\ |t_+\rangle &= t_+^\dagger|0\rangle = |\uparrow\uparrow\rangle \\ |t_0\rangle &= t_0^\dagger|0\rangle = \frac{1}{\sqrt{2}}(|\uparrow\downarrow\rangle + |\downarrow\uparrow\rangle) \\ |t_-\rangle &= t_-^\dagger|0\rangle = -|\downarrow\downarrow\rangle, \end{aligned} \tag{3.1}$$

Figure 3.1: Schematic representation of the interdimer and intradimer exchange interactions for $TlCuCl_3$. Left: *ac*-plane. Right: *bc*-plane. From Ref. [31].

where each spin operator $S^{\alpha}_{l,r}$ can be rewritten in this formalism as $S^{\alpha}_{l,r} = \pm\frac{1}{2}(s^{\dagger}t_{\alpha} + t^{\dagger}_{\alpha}s) - i\epsilon_{\alpha\beta\gamma}t^{\dagger}_{\beta}t_{\gamma}$, where $\{l, r\}$ indicates the left or right dimer site, and $\alpha = \{+, 0, -\}$. Hard-core bosonic statistics can be enforced through the double occupancy constraint on each dimer site i, given by

$$s^{\dagger}_{i}s_{i} + \sum_{\alpha=+,0,-} t^{\dagger}_{i,\alpha}t_{i,\alpha} = 1. \tag{3.2}$$

3.2 Finite temperature excitations in $TlCuCl_3$

The Bond Operator formalism has been used with great success to describe the elementary excitations of $TlCuCl_3$, introduced in §1.2. A full experimental background will be given in Chapter 4, and will detail the application of the bond operator theory that will be outlined in this subsection.

Quantitative calculations of superexchange interactions remain beyond the current understanding and computer power, but one is able to make qualitative arguments to construct a model for the network of pathways within $TlCuCl_3$. The full treatment is given in Ref. [31], resulting in a first estimate for the exchange through the consideration of the superexchange pathways mediated by Cl^{-} and Tl^{+} ions, and applying relevant bond angles, bond lengths and distances. A schematic representation of the exchange hierarchy is given in Figure 3.1.

With the bond operator representation in mind, the Hamiltonian can be rewritten using the spin operators, defined in the new representation as

$$\mathcal{H} = \mathcal{H}_0 + \mathcal{H}_1 + \mathcal{H}_1' + \mathcal{H}_1'' + \mathcal{H}_2 + \mathcal{H}_2' + \mathcal{H}_2'' + \mathcal{H}_3 + \mathcal{H}_3',$$

with each term as defined in Ref. [31]. Each term corresponds to triplet propagation and triplet pair creation across each of the different exchange pathways specified in the schematic diagram.

3.2.1 Disordered Phase

At zero pressure and zero magnetic field, as is the case for all fields and pressures below their respective critical values (H_c and P_c), the system is in a quantum disordered regime consisting of a condensate of singlets with a spin gap to excited triplet states on each dimer. This situation, typical of bond-operator theory, can be described by replacing the spin operator s_i with a c-number $\bar{s_i}$. This can be further reduced by the application of a mean-field approximation by considering the global average of the spin singlet density. In this case, $\langle s_i \rangle = \bar{s}$. The site-dependent chemical potential μ_i can be replaced by the global average $\bar{\mu}$; both are determined by a self-consistent minimisation of total fixed energy at fixed total boson number.

One can also treat the global constraint by replacing the singlet operator with the constraint itself,

$$s_i = s_i^\dagger = \sqrt{1 - \frac{1}{N} \sum_{i,\alpha=+,0,-} t_{i\alpha}^\dagger t_{i\alpha}}, \tag{3.3}$$

leading to the simultaneous elimination of the variable μ. This approximation, the Holstein-Primakoff (H-P) approximation, is equivalent to taking $\bar{s} = 1$ and $\mu = -\frac{3}{4}J$. This imposes the constraint that the condensate amplitude remains at unity and neglects the effect of quantum fluctuations entirely, in contrast to the previous approach in which they are retained in the triplet operators $t_{i\alpha}^\dagger$.

The substitution of the H-P constraint into the Hamiltonian, followed by the truncation at quadratic order and the diagonalisation of the result via a Bogoliubov transformation yields the dispersion relation E_k, where

$$E_k = \sqrt{(\frac{1}{4}J - \mu + \Lambda_k)^2 - \Lambda_k^2}; \tag{3.4}$$

$$\Lambda_k = \bar{s^2}\{(J_1 - \tfrac{1}{2}J_1')\cos k_x + J_1''\cos 2k_x - \tfrac{1}{2}[J_2\cos k_z + J_2'\cos(k_x + k_z) + J_2''\cos(2k_x + k_z)] + (J_3 - J_3')\cos(k_x + \tfrac{1}{2}k_z)\cos\tfrac{1}{2}k_y\}.$$

and $\vec{k} = (k_x, k_y, k_z)$ is a vector in recriprocal space. The self-consistent determination in the BO representation includes the quantum fluctuations within the $\bar{s}$ term, whereas the application of the H-P approach assumes this is equal to unity. The difference in the value of $\bar{s}$ in taking this approximation is 3%, imposing a maximal error of the same value. This implies that at zero temperature the H-P approach yields accurate expressions for $TlCuCl_3$, and has been used to great effect to analyse previous experimental data.

3.2.2 Pressure-induced order

The dispersion relations given by Equation 3.4 describe the excitations of the dispersive triplet modes in the disordered phase, and are sensitive to changes in the exchange interactions.

The effect of changing the ratio of inter-dimer and intra-dimer exchange interactions can be extracted directly from the equations and can be shown to have the effect of altering the band width and spin gap of the triplet excitations. A reduction of the energy (of the spin gap) to zero can be effected by a sufficient change in the exchange interaction ratios, resulting in triplet states with $S = 1$ becoming energetically favourable and LRO emerging with an ordering wavevector corresponding to the wavevector of the minimum excitation energy [33]

The effect of this ratio can be incorporated by including an explicit pressure dependence in exchange interaction terms in bond-operator theory. For simplicity, it is preferable to take a general model where the leading order pressure effects are contained in the exchange interactions J, J_2 and J_3, which consist of generalised representations of the dominant exchange interactions, where $J_3 = J_3 - J_3'$ and $J_2 = J_2''$. An ansatz for the effect of pressure can then be quantified by

$$\begin{aligned} J(P) &= -p(P)J \\ J_2(P) &= p(P)J_2 \\ J_3(P) &= p(P)J_3 \end{aligned} \tag{3.5}$$

where $p(P)$ is a dimensionless function of the real pressure P, with the case $p = 1$ being that of ambient pressure. For $(\vec{Q}, \omega)$ values near the excitation energy minimum, the changes in J_2 and J_3 describe the change of the band with pressure, and the change of J dictates the band centre. As such, the spin gap can be reduced to zero through an increase in $J(P)$, a decrease in $J_2(P)$ and $J_3(P)$, or a combination of these. The exact nature of the pressure-dependence of the exchange interactions will be discussed in Chapter 4.

The dispersion for the disordered, finite pressure phase is simply that given by Equation 3.4, inclusive of the substitution of the generalised pressure-dependent exchange interaction coefficients of Equation 3.5, resulting with the equation

$$E_k = \sqrt{(J^2 + 2J\epsilon_k)} \tag{3.6}$$

$$\epsilon_k = -\frac{1}{2}J_1 \cos k_x - \frac{1}{2}J_2(P)\cos(2k_x + k_z) + J_3(P)\cos(k_x + \frac{1}{2}k_z)\cos\frac{1}{2}k_y, \tag{3.7}$$

which gives a full magnon dispersion across reciprocal space in terms of the dimensionless pressure p. A QPT is realised when the magnon modes go soft at the excitation

energy minimum. The dimensionless critical pressure $p_c(P_c)$ corresponding to $E_Q = 0$ for the exchange interactions in $TlCuCl_3$ is

$$p_c = \frac{J - J_1}{J_2 + 2J_3} \simeq 1.108, \tag{3.8}$$

from which can be inferred that a very small value of p is required to bring the system into the quantum critical regime. This is consistent with the emergence of LRO at very low critical pressures observed in $TlCuCl_3$, as detailed in Chapter 4.

Increasing the pressure past p_c causes the degenerate triplet modes to mix with the singlet condensate. Redefining the bond operators to account for the mixing, the dispersion relation can again be calculated with a similar approach; again assuming the transformed singlet condensate (in this case, $\bar{a}$, with $a = us_i + \nu(fe^{i\vec{Q}\cdot\vec{r}_i}t_{i+}ge^{i\vec{Q}\cdot\vec{r}_i}t_{i-})$, with $\nu^2 + u^2 = 1$ and $f^2 + g^2 = 1$) has imposed on it the same global constraint as the disordered phase (i.e. $\bar{a} = 1$), the dispersion relation for the ordered phase can be defined as

$$E_{k\alpha} = \sqrt{\epsilon_{k\alpha}^2 - \Delta_{k\alpha}^2}, \tag{3.9}$$

with

$$\begin{aligned} \epsilon_{k+} &= J(u^2 - \nu^2) - 8\epsilon_Q u^2\nu^2 + (u^2 - \nu^2)^2\epsilon_k, \\ \epsilon_{k0} = \epsilon_{k-} &= Ju^2 - 4\epsilon_Q u^2\nu^2 + (u^2 - \nu^2)\epsilon_k \\ \Delta_{k+} &= (u^2 - \nu^2)^2\epsilon_{\mathbf{k}} \\ \Delta_{k0} &= -\Delta_{k-} = \epsilon_k \end{aligned} \tag{3.10}$$

where

$$u^2 = \frac{1}{2} + \frac{J}{(-4\epsilon_Q)}, \quad \nu^2 = \frac{1}{2} - \frac{J}{(-4\epsilon_Q)}, \tag{3.11}$$

and

$$\epsilon_Q = -\frac{1}{2}[J_1 + p(J_2 + 2J_3)] \tag{3.12}$$

The above choice of co-ordinates has resulted in the development of a staggered magnetic moment along the $\hat{x}$-axis in spin space, due to the transformed magnon operator $b_{\mathbf{k}+}$ being exactly that of t_x, but in principle any spatial direction can be chosen. The other two modes remain gapless at $\vec{Q}$ with a linear dispersion. These are the Goldstone modes, fluctuating in the plane perpendicular to the induced moment and acting as transverse phase modes. The final mode, $\mathrm{E}_{\mathbf{k}+}$ is the longitudinal mode, corresponding to amplitude fluctuations of the ordered moment and resulting from the non-commuting perturbed Hamiltonian.

The excitation gap from the amplitude mode can be written as

$$E_{k+} = \sqrt{4\epsilon_Q^2 - J^2}, \tag{3.13}$$

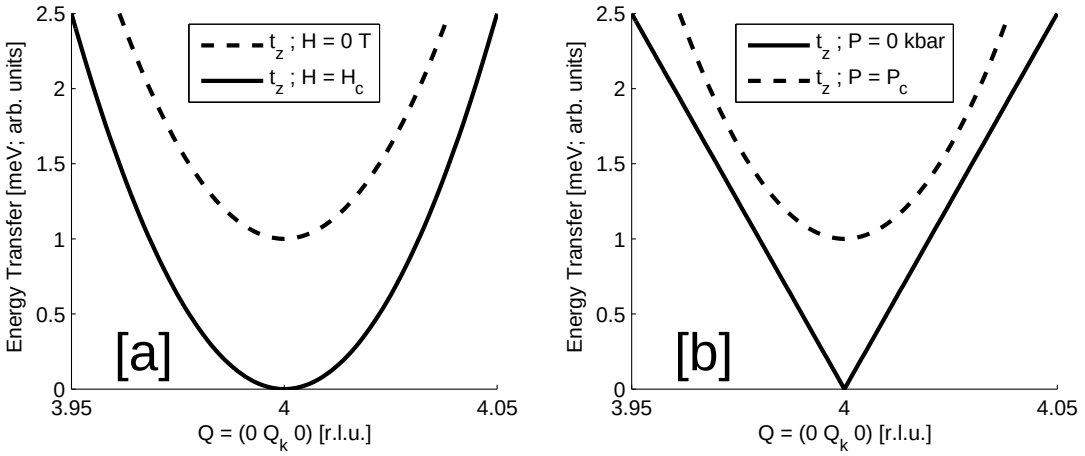

Figure 3.2: The change in the magnon dispersion in the vicinity of the ordering wavevector, for the pressure and field-induced phase transitions. [**a**] The lowering of the mode energy via the Zeeman term to reduce the S^z = -1 triplon to zero without altering the band dispersion, which is quadratic in nature for $0 < H < H_c$; [**b**] The change in the functional forms of all triplon branches under hydrostatic pressure; altering the ratio of interdimer to intradimer exchange broadens the band width, resulting in the reduction of the spin gap to zero, at which point the dispersion is linear in nature.

and increases with pressure, removing the degeneracy of the triplet modes. The other two triplet excitations remain gapless throughout the ordered phase.

The $t_{x,y,z}$ representation is preserved in the case of zero field, and the only triplet mixing with the condensate is that of the direction of the AFM spin moment, which can be resolved to be any one of the three triplets in a chosen theoretical framework. The other triplet modes describe the phase fluctuations and explicitly do not form a part of the condensate. As a result of the retained degeneracy, the magnon band at the QCP shows a departure from the quadratic functional form seen in the field-induced case [31]. Expanding Equation 3.6 around the $\vec{Q}$ dependent minimum, and substituting $\epsilon_{Q+\delta k} = \epsilon_Q + \delta\epsilon_k$, the resulting dispersion is

$$E_{Q+\delta k} \simeq \sqrt{E_Q^2 + 2J\delta\epsilon_k}. \tag{3.14}$$

Due to ϵ_k containing cosine terms in k which are minimal at $\vec{Q}$, $\delta\epsilon_k$ is quadratic in δk, and as such at the critical pressure (where $E_Q = 0$), E_k has a linear k dependence. For the field induced case, the degeneracy of the triplet modes are split, and the quadratic functional form of ϵ_k is retained as the spin gap is reduced to zero (Figure 3.2 [a]).

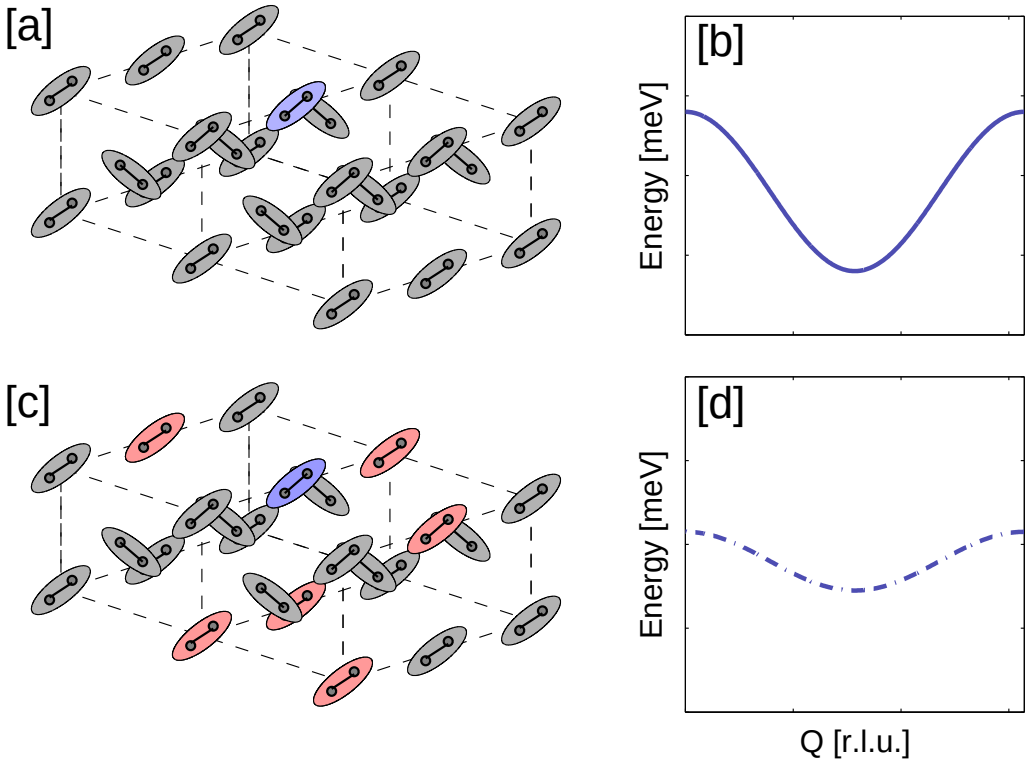

Figure 3.3: The effect of thermal population on excited triplet states. **[a]** Population of triplets at "$T = 0$ K", where the system is a condensate of singlets indicated by grey dimers. An excited triplet (blue dimer) can propagate across the lattice by hopping to other dimer sites. **[b]** Dispersion of triplet excitations at "T = 0 K". **[c]** Population of triplets for $T > 0$ K, where the system consists of a condensate of singlets with thermally populated triplet excited states (red dimers). An excited triplet (blue dimer) can not hop to dimer sites that are already populated by triplets. **[d]** Temperature renormalised dispersion.

3.2.3 Finite Temperatures - Effective Pressure

The above representations have all been calculated for a mean-field theory formulated at $T = 0$ K, and making the explicit assumption that $\bar{s} = 1$, and that the ground state is that of a condensate of singlet states. In heating to higher temperatures, the triplet excited states begin to become thermally populated and removing the validity of this assumption. An extension of the bond-operator theory is then required to account for finite temperatures. Such a treatment is given in Ref. [34], and is formulated from the inclusion of the thermal population factor $n(E_\alpha(\vec{Q}), \beta)$ into the Mean Field BO representations of $\bar{s}$ and μ, where E is the magnon energy, $\alpha = \{+, 0, -\}$ and $\beta = (k_B T)^{-1}$.

Qualitatively, the thermal population of states leads to 'thermal blocking', as illustrated in Figure 3.3. If sites are already occupied by thermally populated triplet

excitations, then there is a reduction in the mobility of any triplet excitations propagating between dimer sites, resulting in a band narrowing and an increased damping effect. The excitation spectrum is then dependent on the thermal population, which is in turn dependent on the excitation spectrum. The mean-field equations are then required to be solved self-consistently, with the ultimate effect of a renormalisation of the dispersion with increasing temperature.

An effective model for this dispersion must then be implemented such that the contribution to the scattering intensity from the excitations can be analysed. An appropriate choice of model is of significance when considering the convolution of the resolution ellipsoid with that of the magnon dispersion relation, as fitting the observed scattering intensity requires the implementation of an appropriate magnon dispersion to correctly account for all contributions to the scattering intensity.

A curvature in the vicinity of the ordering wavevector that is appropriate to the observed spin gap is paramaterised through an implementation of an *effective pressure*. This is the value of pressure that is required to reproduce the spin gap for the $T = 0$ K MFBO theory. As such, each point in the (P, T) phase diagram is mapped on to an appropriate value of pressure along the $T = 0$ line. In addition, this effective pressure value can then be allowed to vary to account for any variation of the local curvature in the vicinity of the dispersion minimum.

As such, the above paramaterisation allows one to provide a model for the resolution convolution to determine properties of the principal excitations. Unfortunately, because the chief effects of pressure and temperature on the band width are resolveable only through consideration of a wide energy range outside the experimental resolution, no properties of the system can be determined with the effective pressure parameter. A more detailed method of implementation is discussed in Chapter 4, alongside the inclusion of an additional broadening to the spectral lineshape to account for thermal damping effects.

3.3 Spin Ladder Dispersion

The bond operator formalism was first applied to the rungs of spin ladder systems by Gopalan *et al.* [35], further developed for unfrustrated coupled spin ladders at zero temperature [36, 37] and extended later to finite temperatures [26]. Similar MFBO treatments have been applied to the frustrated spin ladder Hamiltonian of which $BiCu_2PO_6$ is a realisation, and attention is now turned to the application of these and other strong-rung perturbative techniques for consideration in data analysis to follow in Chapter 5.

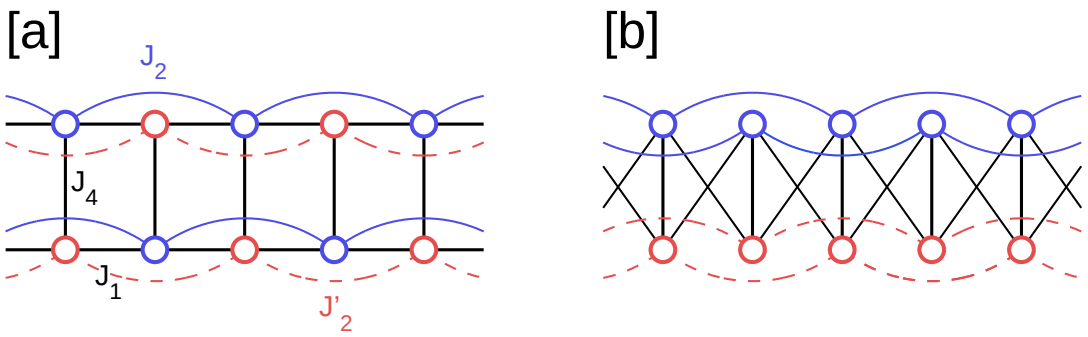

Figure 3.4: The exchange interactions in $BiCu_2PO_6$. **[a]** Generalised case of the 'classic' geometry with two inequivalent Cu sites and the two different NNN exchange interactions (J_2 and J_2'). **[b]** The topologically equivalent model described in Ref. [42], used to derive the dispersion of a singular mode across the Brillouin zone.

3.3.1 Onset of Incommensurability

The proposed exchange geometry of $BiCu_2PO_6$ is that of Figure 3.4 [a], created from the inclusion of NNN exchange interactions (J_2, J_2') in the classic spin ladder exchange geometry. For the case $J_2 = J_2'$ one can also consider this geometry to be that of the strong coupling of two alternating $J_1 - J_2$ spin chains, also possessing a spin liquid ground state for certain values of J_1/J_2 [38]. The Hamiltonian is given by

$$\mathcal{H} = \sum_{i,j} J_4 S_i \cdot S_j + \sum_{i,j} [J_1(S_i \cdot S_{i+1} + S_j \cdot S_{j+1}) + J_2 S_i \cdot S_{i+2} + J_2' S_j \cdot S_{j+2}], \quad (3.15)$$

with J_1, J_2, J_2' and J_4 as given in Figure 3.4. J_4 is the 'rung' exchange interaction and J_1 the 'leg' exchange interation.

The ground state of the spin ladder without the frustrating next-nearest neighbour interactions is a so-called 'rung-singlet' (RS) phase, the etymology of the term deriving from the strong-rung limit where singlet dimers are formed on the rungs. However, the correct physical picture allows for fluctuations between singlet dimers pinned on the rungs and other singlets formed between different pairs, resulting in a realisation of an RVB ground state, with the greatest extent of fluctuations occurring as the rung coupling is reduced.

With the inclusion of sufficiently strong NNN couplings and low rung exchange, a different ground state can be stabilised referred to as the 'columnar dimer' phase, where singlets are preferentially formed along the legs. The full characterisation of the ground state under variation of the exchange parameters J_1, J_4 and J_2 is a challenging theoretical problem, and has been achieved with exact diagonialisation and density matrix renormalisation group calculations [39] and summarised in Figure 3.5.

Figure 3.5: Phase diagram a spin ladder with frustrated exchange. The notation for the exchange interactions is that of Figure 3.4, but with $J_\perp = J_4$. The real-space correlation functions have an emerging incommensurability that create separated commensurate-incommensurate regimes as given by the green dashed line. The violet line is the conjectured phase boundary between the columnar dimer picture and the rung singlet picture. From Ref. [39]

The notable result is an onset of incommensurability in the spin-spin correlations that occur for appreciable J_2 values. This results in the manifestation of incommensurability in the magnon dispersion relations. Considering the strong rung-coupling regime, the problem can be treated through perturbative methods; by taking J_1 and J_2 as perturbations on a large rung exchange J_4, an analytical first order strong-rung perturbative (PSR) dispersion relation can be formulated [39]

$$\omega(k) = J_4 + J_1\cos(k) + J_2\cos(2k) + \frac{3(J_1^2 + J_N^2)}{4J_4} \tag{3.16}$$

where the frustration induced by the NNN coupling J_2 results in the $\cos(2k)$ harmonic and the onset of incommensurability for $J_2 \geq 0.25J_1$ in the magnon dispersion relation, with an incommensurate minimum given by

$$Q_{min} = \arccos\left(-\frac{J_1}{4J_2}\right) \tag{3.17}$$

which is exact for large J_4, but quantum fluctuations will strongly affect the value for the small J_4 regime.

3.3.2 Higher Order Perturbations for $BiCu_2PO_6$

The geometry considered above is a possible model for the case of the real material $BiCu_2PO_6$ (§1.2), which consists of a frustrated spin ladder geometry. However, the

Hamiltonian for this system must be generalised; the geometry of the lattice results in two rungs present per unit cell which are non-identical. In particular, this leads to the decoupling of the next-nearest-neighbour interaction into two values to be considered, J_2 and J_2', the interaction occurring between the two inequivalent Cu sites on each rung.

On a structural perspective, these two bonds are very similar and have an identical Cu-Cu connection vector between the inequivalent sites, $\vec{R}_{NNN} = [0\ 1\ 0]$. For this reason, the work by Koteswararao [40] and Mentré [41] was formulated on the assumption that $J_2' = J_2$. However, in the work presented in [42], it was observed that different J_2' and J_2 values are required to reproduce calculated density functional theory (DFT) calculations. In the reference, this assumption is discussed in relation to the available supersuperexchange channels available and is justified by the observation that the two exchanges occur between pairs of copper atoms inequivalent by symmetry and the Cu-O-O-Cu exchange channels are different.

Perturbative expansions to second order around the strong coupling limit (SO-PSR) have been performed for the proposed $J_2 \neq J_2'$ geometry of $BiCu_2PO_6$, and presented in Ref. [42]. A notable and important consequence of the two inequivalent rungs in the unit cell is the manifestation of two triplet dispersion bands. A full explanation is given in the reference, and a perturbative expansion calculation yields two excitation branches $E^{(2)}_{\alpha,\beta}(k) = A_k \pm |B_k|$, with

$$\begin{aligned} A_k = J_4 + \frac{12J_1^2 + 3(J_2 + J_2' - 4(J - J_2')^2}{16J_4} + \\ \left[\frac{J_2 + J_2'}{2} + \frac{(J_2 - J_2')^2 - 2J_1^2}{8J_4}\right]\cos(k) - \frac{(J_2 + J_2')^2}{16J_4}\cos(2k), \end{aligned} \tag{3.18}$$

$$B_k = \frac{J_1}{2}(1 + e^{-ik}) - \frac{J_1(J_2 + J_2')}{8J_4}(1 + e^{-ik} + eik + e^{-2ik}). \tag{3.19}$$

The expression over the Brillouin zone $0 < k < \pi/2b$ is given in Figure 3.6 [a], with a degeneracy of the two excitations at $Q = 2\pi/a$ that persists across the entire parameter space and is a consequence of the symmetry generators of the $Pnma$ structure. The single-mode contribution can be examined further by considering a topologically equivalent model described in Ref. [42] and shown in Figure 3.4 [b], where every second rung is flipped, and the model consists of identical rungs with half the unit cell periodicity. The calculation then yields

$$\begin{aligned} E(k) = J_4 + \frac{12J_1^2 + 3(J_2 + J_2') - 4(J_2 - J_2')^2}{16J_4} + \\ c_1\cos(k) + c_2\cos(2k) + c_3\cos(3k) + c_4\cos(4k), \end{aligned} \tag{3.20}$$

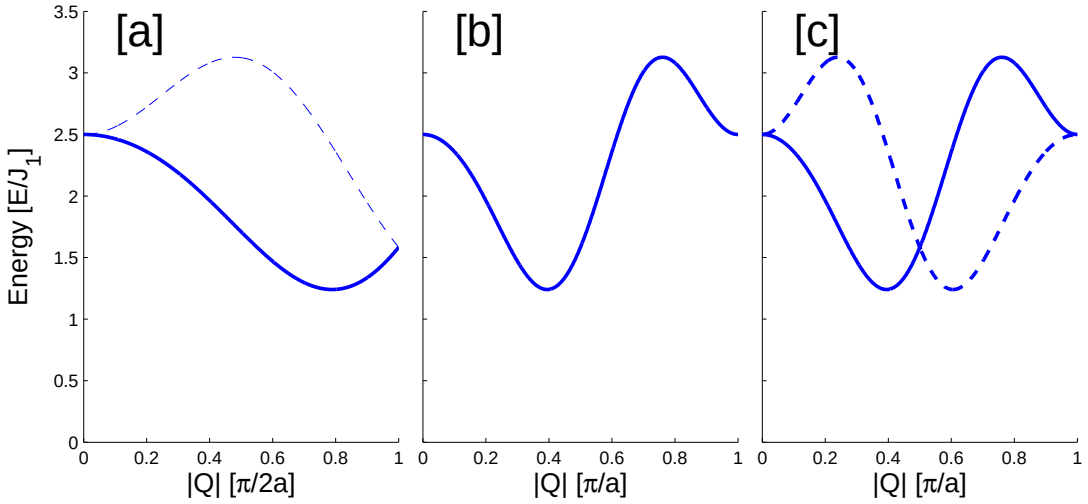

Figure 3.6: The triplet dispersion relations from second-order perturbation methods, outlined in Ref. [42]. **[a]** The two modes present from two non-identical rungs inside the unit cell. **[b]** Dispersion of the topologically equivalent model show in Figure 3.4. **[c]** Two modes are recovered when the dispersion in [b] is folded back through the Brillouin zone.

where $c_1 = -J_1 + \frac{J_1(J_2+J_2')}{4J_4}$, $c_2 = \frac{J_2+J_2'}{2} + \frac{(J_2-J_2')^2}{8J_4} - \frac{J_1^2}{4J_4}$, $c_3 = \frac{J_1(J_2+J_2')}{4J_4}$ and $c_4 = -\frac{(J_2+J_2')^2}{16J_4}$.

The resultant equation gives an expression for a single mode, and is plotted in Figure 3.6 [b]. The dispersion for the second branch can be recovered applying a π phase shift to fold $E(k)$ back through the Brillouin zone at [$-\pi/2a$, $\pi/2a$], with the dual dispersion identical to that in [a]. It is clear that the incommensurate nature is determined by the frustrated couplings, which appear to leading order in c_2 [42].

For comparative purposes, a full study of the magnetic excitations of an isolated ladder was performed by the same authors using exact diagonalisation (ED) techniques on finite spin clusters. Finite lattices of $N = 12$, 16, 20, 24, 32 and 36 sites were used, with periodic boundary conditions along the legs, assuming $J_1 \sim 12$ meV, $J_2 = J_1$, $J_2' = 0.5J_1$ and $J_4 = 0.75J_1$. This was found to reproduce the behaviour predicted by the analytical expressions above, but vastly overestimates the spin gap, which is a consequence of $J_4 < J_1$ and a departure from the strong-rung coupling limit.

3.3.3 Second order MFBO for $BiCu_2PO_6$

Remaining in the strong-rung coupling limit, the dispersion can be approached using a MFBO theory as presented in Ref. [39],and following Ref. [35]. The method is similar to that of §3.2, where the Hamiltonian is formulated by taking the triplet creation operators and transforming them under a Bogoliubov transformation and resulting in

a second order correction as

$$\omega(k) = J_R + J_1\cos(k) + J_2\cos(2k) + \frac{1}{4J_R}(J_1^2 + J_2^2) - \frac{1}{2J_R}[J_1\cos(k) + J_2\cos(2k)]^2 \quad (3.21)$$

where the difference in the next nearest neighbour terms J_2 and J_2' has not been taken into account. As such, this approach only predicts the emergence of a single mode due to the assumption of equivalence of the rung couplings, but is equivalent to that of a single mode derived from the expression in §3.3.2. This result requires a self-energy correction $0.7(J_1^2 + J_2^2)/J_4^2$ [35], the inclusion of which results in a good agreement with exact diagonalisation calculations for $J_4 = 3J_1$. The above formulaic expression is expected to be qualitatively valid as long as the system remains in the strong rung coupling limit. In the case for a typical spin ladder geometry, this validity remains for $J_4 > J_1$ [34], but the extent to which the inclusion of frustrating exchange interactions perturbs the system from the strong rung coupling regime is unclear.

In addition, by finding the solutions for the expression $\frac{d\omega}{dk} = 0$ derived for Equation 3.21, one can find expressions for the MFBO incommensurate minima/maxima Q_m, analagous to the equation given for the PSR expression by Equation 3.17. The MFBO expressions are

$$Q_m = \arccos\left(-\frac{J_1}{4J_2}\right); Q_m = \arccos\left(\frac{-J_1 \pm \sqrt{J_1^2 + 8J_2(J_2 + J_R)}}{4J_2}\right), \quad (3.22)$$

from which one can see that the first expression is identical to that of the PSR expression in Equation 3.17.

3.3.4 Summary and Application

In Chapter 5 a full application of the models outlined above to experimental data will be considered. Table 3.1 presents a summary of the frustrated spin ladder dispersion models detailed in this chapter, the reference from which they are derived, their dependent exchange parameters and the reference initialism used within this thesis.

Method	Frustration	Reference	Abbreviation
Perturbations from strong-rung limit (1st order)	$J_2 = J_2'$	[39]	PSR
Perturbations from strong-rung limit (2nd order)	$J_2 \neq J_2'$	[42]	SO-PSR
Second order MFBO	$J_2 = J_2'$	[39]	MFBO

Table 3.1: The multiple models for the dispersion relations in $BiCu_2PO_6$. Each model is summarised by the method used, the relation between J_2 and J_2', the reference from which it is obtained and the notation used within this thesis.

4

$TlCuCl_3$ - Evolution of Elementary Excitations Across the Pressure-Temperature Phase Diagram

In this chapter I present the experimental results of investigations in the vicinity of the quantum critical point in the spin dimer compound $TlCuCl_3$ introduced in §1.2. The QPT in $TlCuCl_3$ is realised by the application of hydrostatic pressure, with a region of long-range antiferromagnetic order separated from the region of quantum disorder by a QCP at the critical pressure $P_c = 1.07$ kbar.

The basic physical properties of $TlCuCl_3$ are summarised alongside the network of relevant exchange interactions. The points in pressure and temperature where INS spectra were collected are presented, followed by details of the analysis where the theoretical description given in Chapter 3 is applied. The characteristic properties of the excitations across the pressure and temperature phase diagram will be reported, with focus on the properties of the amplitude fluctuation of the ordered moment inside the ordered phase and its continuous evolution into a gapped triplet excitation under changes in hydrostatic pressure and temperature.

4.1 Background

The first synthesis of the $ACuX_3$ family of compounds, with X = Cl and Br, and A = K, Tl and NH_4, can be traced as far back as 1889 [43], but it was not until the 1960s that their magnetic properties and structure were first investigated, prompted by the unusual structure and magnetism of $LiCuCl_3 \cdot H_20$ [44, 45].

Figure 4.1: Susceptibility measurements for $TlCuCl_3$ and $KCuCl_3$. The left panel shows susceptibility curve for $TlCuCl_3$, taken from Ref. [49]. χ_1,χ_2 and χ_3 are as defined in the reference text. The right panel shows susceptibility curve for $KCuCl_3$, taken from Ref. [48]. χ_1, χ_2 and χ_3 are as defined in the reference text. The field direction is as defined in Ref. [48].

The existence of the gapped ground state in the A = Tl and K and X = Cl structures was elucidated early on from susceptibility data by Maass *et al.* (Ref. [46]), where the reciprocal molar susceptibility in $KCuCl_3$ was found to be inconsistent with that of the case for a monomer with $S = 1/2$ as the contributing magnetic species. Maass *et al.* attributed the broad maximum in their data to the formation of an antiferromagnetic dimer with strong exchange, resulting in a singlet ground state separated by an energy gap from the triplet excited state. The presence of a disordered ground state was evidenced through early NMR and EPR studies, demonstrating no long-range order down to 1.3 K [47].

Further work in the 1990s on the $KCuCl_3$ and $TlCuCl_3$ compounds was conducted to further investigate the gapped ground state. The observed susceptibility measurements on $KCuCl_3$ [48] and $TlCuCl_3$ [49] consisted of a broad maximum, separating a Curie-Weiss-like behaviour at high temperatures, and a exponential increase at the lowest temperatures, consistent with the result calculated by Troyer *et al*,

$$\chi(T) \propto \frac{1}{\sqrt{T}} \exp\left(-\frac{\Delta}{k_B T}\right), \tag{4.1}$$

where T is the temperature of the system, k_B is the Boltzmann factor and Δ the value of the spin gap [50].

From the data the values for the spin gap and the temperature at which the susceptibility is maximum, (Δ/k_B and T_{max}), were extracted for $KCuCl_3$ and $TlCuCl_3$ and are respectively (160 K, 30 K) and (22, 39 K), with Δ obtained using Equation 4.1 (Figure 4.1). There is uncertainty in the value extracted for the excitation gap, depending on the functional form used for fitting and the region of temperature sampled

T (K)	a (Å)	b (Å)	c (Å)	β ($^\circ$)
280	3.9728(2)	14.1509(4)	8.8660(3)	96.263(2)
2	3.9199(1)	14.0638(3)	8.7959(2)	95.521(2)

Table 4.1: Lattice parameters of $TlCuCl_3$, from neutron powder diffraction, from [52]

T (K)	a (Å)	b (Å)	c (Å)	β ($^\circ$)
280	4.0228(2)	13.7892(4)	8.7287(3)	97.040(2)
2	3.9625(1)	13.7096(2)	8.6594(2)	96.150(2)

Table 4.2: Lattice parameters of $KCuCl_3$, from neutron powder diffraction, from [52]

[49], but the spin gap can be reliably determined when combined with magnetisation measurements, which demonstrate the closing of the spin gap with applied fields of H = 23.1 T and 5.6 T for $KCuCl_3$ and $TlCuCl_3$, respectively [51]. When compared to $KCuCl_3$, $TlCuCl_3$ has a smaller excitation gap but a larger T_{max}. As such it can be seen that the contributions of the magnetic exchange to the susceptibility are different for the two systems. So while it is possible to determine the existence and magnitude of the spin gap, it is not possible to determine the exact exchange interactions for each system from susceptibility alone.

$TlCuCl_3$ and $KCuCl_3$ both crystallise in the $P2_1/c$ space group, with structural parameters given in Table 4.1 and Table 4.2. The structure consists of double chains of edge sharing octahedral $CuCl_6$ complexes, which are distorted by the Jahn-Teller effect resulting in complete quenching of orbital momentum [53]. The chain direction is along the a axis, as seen in Figure 4.2. The hole orbitals $d_{x^2-y^2}$ of the Cu^{2+} ions are shown alongside the relevant exchange interactions Cu^{2+}, which are realised to first approximaton by superexchange pathways through the 3p and 3s orbitals, located on the Cl^- ions [54]. Considering the configuration of the hole orbitals, parallels can be drawn to antiferromagnetic linear chains $CuCl_2{\cdot}2H_2O$ and $CuCl_2{\cdot}\ 2NC_5H_5$ [51, 55, 56, 57] and it can be deduced that J_1 and J_3 are antiferromagnetic. The 90° orientation of orbitals corresponding to J_2 mean that it could be either antiferromagnetic or ferromagnetic.

The exact exchange geometry cannot be determined from susceptibility alone; spin ladder, 2D and 3D dimer models, and alternating and zig-zag chain models can all be used to fit the data. A Haldane model was also suggested, in which the intradimer exchange is ferromagnetic and the system is described as an $S = 1$ chain.

However, a numerical modeling by Nakamura *et al.* (Ref. [58]) of the double spin chain system through the Quantum Monte Carlo method allowed for the comparison of multiple exchange geometries to experimental data of $KCuCl_3$. They found that intradimer exchange interaction is strongly antiferromagnetic, and therefore the Haldane chain picture does not adequately describe the susceptibility data, but rather strongly

Figure 4.2: The double chain structure of $TlCuCl_3$. The black circles indicate the Cu^{2+} ions, and the white circles the Cl^- ions. The hole orbitals and exchange interactions are shown. From Ref. [51]

supported the notion of a spin gap originating from a system described by the dimer model [59].

Triplets are $S = 1$ excitations, and as such energy and momentum resolved information can be extracted from the singlet-triplet transition matrix elements of the scattering function $S(\vec{Q}, \omega)$ in INS experiments. Experimental observation of the triplet wave dispersion across a dynamical $(\vec{Q}, \omega)$ range yields information about the dimensionality, strength and sign of the exchange interactions. Particular examples are $Cu(NO_3)_2 \cdot \frac{5}{2}D_2O$, an alternating chain compound where a spin ladder geometry was indistinguishable from susceptibility [60] but ruled out through INS; $(VO)_2P_2O_7$, an alternating chain compound in which the spin ladder geometry was deemed untenable due to the high levels of required anisotropy, and $Cu_2(C_5H_12N_2)_2Cl_4$ [61], revealed to be a frustrated three-dimensional quantum spin liquid, rather than the assumed spin-ladder geometry.

Extensive INS studies on $KCuCl_3$ [62, 63] and $TlCuCl_3$ [62, 64] on the dispersive low-lying excitation allowed the resolution of the question of the gap origin, through the observation of the dispersion curves of the magnetic excitations. The key results were (i) the observation of the spin gap manifesting as the lowest excitation energies at momentum wavevectors $\vec{Q} = (0\ 0\ -1)$ and $(1\ 0 \pm 1)$ r.l.u., an inconsistent result with

Figure 4.3: The crystal structure of $TlCuCl_3$. The $S = 1/2$ magnetic moments reside on the Cu^{2+} ions, with strong antiferromagnetic coupling forming dimers on Cu_2Cl_6 sites. Two stacking chains of dimers are present per unit cell, with strong inter-dimer exchange interactions. From Ref. [31]

that expected of the spin ladder geometry; (ii) a magnon bandwidth Ω in the **a*** and **c*** directions one order of magnitude larger than the spin gap, indicating strong inter-dimer exchange; (iii) significant dispersion along all three directions in reciprocal space, indicating a higher dimensionality of spin-spin correlations across the lattice despite possessing no long-range magnetic order [65]; and (iv) Momentum resolved dependence in the INS intensity that is incommensurate with the dispersion periodicity.

The Hamiltonian for the compounds $KCuCl_3$ and $TlCuCl_3$ is given by $\mathcal{H} = \mathcal{H}_0 + \mathcal{H}_1$, with

$$\begin{aligned} \mathcal{H}_0 &= -J \sum_i S_{i1} \cdot S_{i2} \\ \mathcal{H}_1 &= -\frac{1}{2} \sum_{ij,\mu\nu} J_{ij,\mu\nu} S_{i\mu} \cdot S_{i\nu}, \end{aligned} \tag{4.2}$$

where $\mathcal{H}_0$ is the case for an isolated dimer, with J as the intradimer exchange between Cu^{2+} sites on each dimer i, having spins S_{i1} and S_{i2}. The addition of $\mathcal{H}_1$ is essentially a perturbation from the dimer limit, and consists of the contributions of the inter-dimer couplings, with $J_{ij,\mu\nu}$ describing the interdimer exchange terms, between spins μ, ν of different dimer sites i and j. Figure 4.3 illustrates the proposed dominant exchange couplings in this interaction scheme, as presented in Ref. [31].

Figure 4.4: Magnon dispersion relations for **(a)** $TlCuCl_3$ and **(b)** $KCuCl_3$. The x-axis is labeled with reciprocal space points B = (0 2π 2π), C = (0 0 2π), D = (0 0 0), A = (π 0 0) and F = (π 0 2π). The points are experimental data from Refs. [53, 66]. The solid lines are fits to the first order perturbation theory outlined in Ref. [53], using the exchange parameters detailed in Table 4.3. From Ref. [31]

At first order, $\mathcal{H}_1$ results in Bloch-like triplet waves across reciprocal space, via propagation from dimer i to dimer j across the localised limit $|J|$, with the bandwidth and direction according to the specific coupling geometry and strength of the exchange interactions $J_{ij,\mu\nu}$.

It is to be noted that the energy scales for the two compounds are slightly different; $TlCuCl_3$ has a smaller spin gap $\Delta \approx 0.75$ meV, and a bandwidth $\Omega \approx 7.3$ meV [64], with $KCuCl_3$ characterised by $\Delta \approx 2.7$ meV, and $\Omega \approx 2.3$ meV. Despite this, the common formalism of the dispersion relation for both compounds is a strong suggestion that they share the same exchange interaction scheme. In both compounds, the energy gap corresponds to the lowest excitation energy, which is lowered from the intradimer coupling energy due to finite interdimer couplings. The higher spin gap and smaller bandwidth is indicative of the interladder couplings being weaker in the Potassium analogue, as is evidenced in Figure 4.4.

With this assumption, the exchange interaction terms have been extracted through a fit for each compound and are given in Table 4.3, with the exchange index corresponding to the labels in Figure 4.3. These extracted values confirm two previous conclusions - the strong AFM nature of the intradimer exchange, and the larger interdimer couplings of $TlCuCl_3$ compared to $KCuCl_3$. With these values for the exchange

J_{ij} [meV]	$R_{ij}[l.u.]$	$KCuCl_3$	$TlCuCl_3$
J_a	± (1 0 0)	0.210(5)	0.472(11)
J_{a2c}	± (2 0 1)	0.340(5)	1.430(8)
J_{abc}	± $(1 + \frac{1}{2}\frac{1}{2})$	-0.372(4)	-0.619(5)
	± $(1 + \frac{1}{2}\frac{1}{2})$		
J	± (0 0 0)	-4.287(4)	-5.424(11)

Table 4.3: Exchange interactions as presented in Figure 4.3 in $KCuCl_3$ and $TlCuCl_3$. From [64].

interactions, it is possible to formulate the magnon dispersion using the dispersion relations given in Chapter 3.

4.2 Quantum Phase Transitions

As summarised in the previous section, and shown experimentally, long-range magnetic order has not been found in the spin dimer compounds $TlCuCl_3$ and $KCuCl_3$ even when cooled to the lowest possible temperatures. At the lowest temperature, "$T = 0$K", such order is thought to be impossible due to the strong antiferromagnetic coupling present within the Cu_2Cl_6 dimer units. As such, these are magnetic insulators, consisting of intrinsic dimers with a ground state corresponding to a condensate of singlet states on each dimer across the crystal, and magnetic triplet excitations separated by a spin gap. However, it has been shown that long-range order can be achieved through the application of external control parameters.

Upon reduction of the spin gap to zero the energy of the triplet state goes to zero. Unconstrained by the Pauli exclusion principle these bosons can 'condense' in infinite number into the ground state. This can be achieved through both application of applied field and hydrostatic pressure, with the field-induced case being precisely the behaviour described by a class of transition called Bose Einstein Condensation, a phenomenon observed in the behaviour of liquid ^{4}He when cooled to a critical temperature of 2.17 K [67].

By mapping the case for AFM quantum spin systems to that of a Bose Einstein Condensate (BEC), it is possible to test critical behaviour in the vicinity of a QCP within a clean experimental window. Universality, critical exponents and the effect of dimensionality can be investigated through crystalline solids in this fashion, and the spin dimer magnetic insulators provide an unrivaled experimental testing ground for understanding quantum critical phenomena. BEC with LRO has been observed in a number of materials, including $BaCuSi_2O_6$[68], $Cs_3Cr_2Br_9$[69], $Cu(NO_3)_2{\cdot}2.5D_2O$[70] and $(CH)_3CHNH_3CuCl_3$[71], with the physics of the field-induced triplet condensation

remaining mostly unchanged due to the QCPs of all the above materials being in the same universality class [72].

The large interdimer coupling present in $TlCuCl_3$ places it in a unique position among such model magnets, due to its relatively small spin gap, allowing for a closing of the gap within realisable experimental conditions. Seminal studies by Ch. Rüegg *et al.* (Ref. [73]) have demonstrated the emergence of LRO from the closing of the spin gap through application of field, in which the energy of the triplets is lowered via a Zeeman term, and through hydrostatic pressure [33] which directly alters the Hamiltonian through structural changes altering the strength of the exchange interactions and results in a bandwidth broadening to lower the gap.

Susceptibility measurements on single crystals of $TlCuCl_3$ were performed in Ref. [74], conducted inside a clamp cell on a SQUID magnetometer. At $P = 0.74$ GPa (7.4 kbar), a kink in the magnetic susceptibility M/H shows a clear indication of the ordered state.

The observation of magnetic order in a low hydrostatic pressure showed that the QCP resides within the experimental range of the SQUID clamp cell ($P < 10$ kbar) and as such was suited to a more detailed study across the QPT through magnetisation measurements. This study is presented in Ref. [75], in which the reduction of the gap and emergence of magnetic order was determined to occur at $P = 0.42 \pm 0.05$ kbar, and in Ref. [74], where the critical pressure was deduced to be $P_c \sim 2$ kbar. The critical field H_c was observed to decrease with pressure, consistent with the conclusion that the pressure lowers the spin gap. Furthermore, in a clamp cell under applied field, Electron Spin Resonance (ESR) measurements showed the decrease of H_c with applied pressures $P = 0.5$ kbar and 1 bar, and a change in the g-factor of the absorption lines at these values [76].

The confirmed reduction of the spin gap through applied pressure is further investigated through inelastic neutron scattering measurements of the broadening of the band that results from a tuning of the ratio of intradimer to interdimer exchange. This powerful technique allows for experimental observation of the dispersion relation around the spin gap minimum, as detailed in the previous section. In combination with a ^{4}He gas cell as introduced in §2.4.3, the changing dispersion relation as a function of pressure can be measured across reciprocal space, and the results are presented in Ref. [33]. The experiment confirmed the emergence of long-range magnetic order at the QCP, occuring at $P_c = 1.07$ kbar, resulting from a reduction of the spin gap energy at the ordering wavevector $\vec{Q}_0 = (0\ 4\ 0)$ r.l.u.

A point of note is the discrepancy between the observed critical pressures of $P =$ 2 kbar, 0.42 kbar and 1.07 kbar, which is a consequence of the differet methods of

pressure application. The former two measurements were performed with clamp cells, the calibration of such is less accurate than in the case for the third measurement with the Helium gas loaded cell. $P_c = 1.07$ kbar can be taken to be the closest to the true value, having been successfully reproduced on multiple occasions [52].

In the cases for both field and pressure, the long-range magnetic order occurs at ordering wavevectors at which the spin-gap minimum occurs in the disordered phase, and from which it has been continuously reduced.

The previous sections have detailed the case for the exchange within the system being completely isotropic. However, ESR experiments [77] and INS studies [52] have shown that there exists a finite exchange anisotropy in the system. There exists a tiny anisotropy found in the ESR studies of 0.09 meV, and a larger 1% uniaxial anisotropy elucidated by INS studies. At the pressure-induced QCP this results in a gapped mode of ~ 0.4 meV.

4.3 Excitations - Experimental Case

The excitations of $TlCuCl_3$ are those introduced in Chapter 3, formulated from a MFBO theory with the singlet-triplet excitations of the disordered phase detailed in §3.2.1 and in the magnetic moment fluctuations of the ordered phase detailed in §3.2.2. For a classically ordered spin system, the fluctuations are constrained to those transverse to the ordered moment. Because of the quantum character of the 3D coupled spin dimer system, the ordered phase of $TlCuCl_3$ has a small magnetic moment per Cu^{2+} ion near the QCP. This results in sizeable amplitude fluctuations emerging at the QCP, detectable by INS and predicted by the MFBO theory, expressions for which are given in Chapter 3. The ordered phase can therefore be thought of as that of a phase of renormalised classical Néel Antiferromagnetic order (RC-AFM), with the renormalisation of the magnetic moment an effect of quantum fluctuations on the dimer bonds and the unique exchange coupling.

The predicted amplitude excitations have been experimentally verified through the use of INS studies, by Rüegg *et al.* in Ref. [33]. By following the evolution of the spin dynamics across the QPT, the continuous emergence of the gapped longitudinal mode across the phase boundary was experimentally observed. In addition to the amplitude mode, the two excitations perpendicular in spin-space were observed. One was gapless, but the other was gapped by ~ 0.4 meV as a result of a 1% uniaxial anisotropy in the exchange parameter. The longitudinal mode is a key feature of the quantum phase transition and is a direct consequence of the quantum character of the pressure-induced RC-AFM phase. Utilising the MFBO theory outlined in Chapter 3, the longitudinal

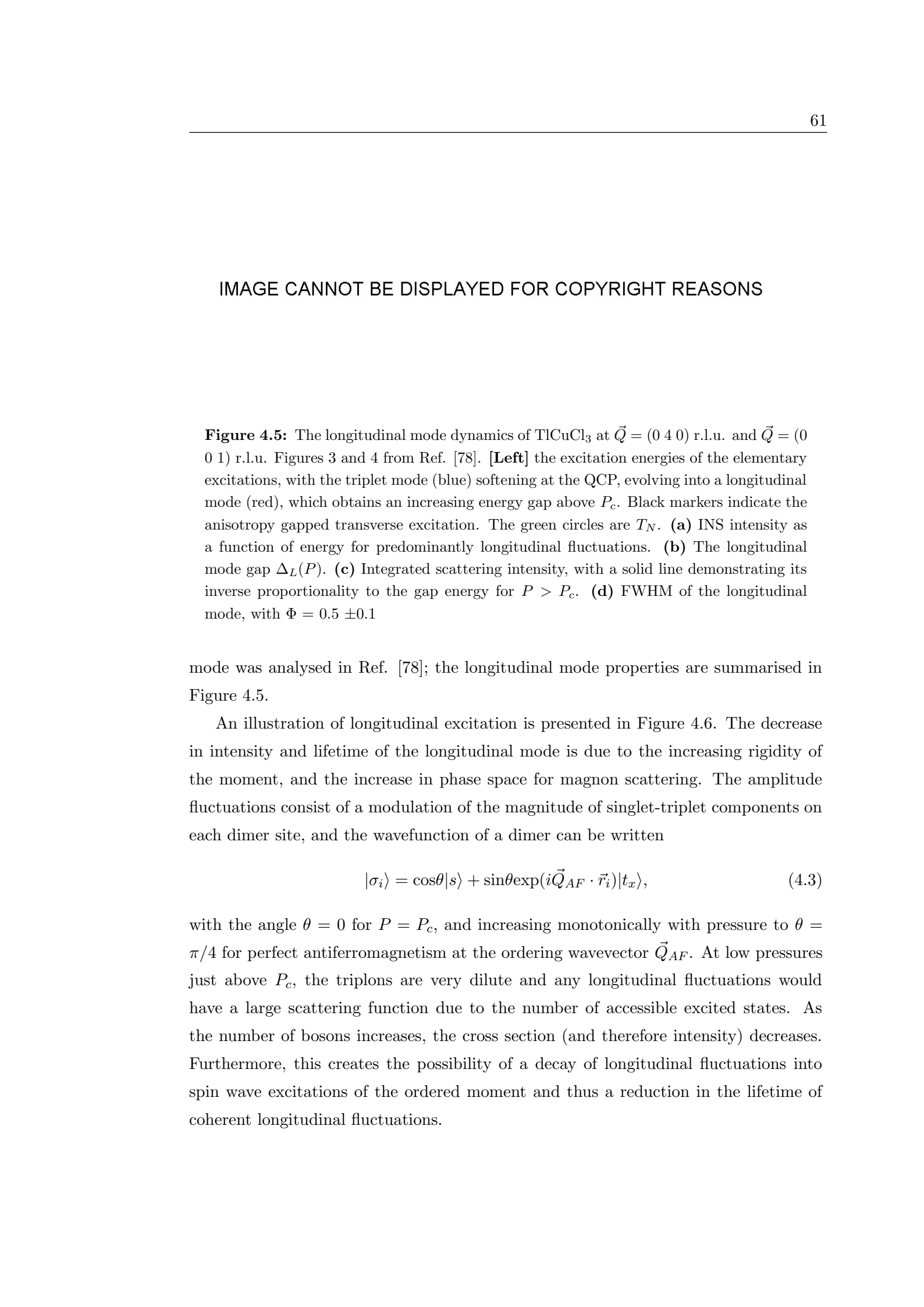

Figure 4.5: The longitudinal mode dynamics of $TlCuCl_3$ at $\vec{Q} = (0\ 4\ 0)$ r.l.u. and $\vec{Q} = (0\ 0\ 1)$ r.l.u. Figures 3 and 4 from Ref. [78]. **[Left]** the excitation energies of the elementary excitations, with the triplet mode (blue) softening at the QCP, evolving into a longitudinal mode (red), which obtains an increasing energy gap above P_c. Black markers indicate the anisotropy gapped transverse excitation. The green circles are T_N. **(a)** INS intensity as a function of energy for predominantly longitudinal fluctuations. **(b)** The longitudinal mode gap $\Delta_L(P)$. **(c)** Integrated scattering intensity, with a solid line demonstrating its inverse proportionality to the gap energy for $P > P_c$. **(d)** FWHM of the longitudinal mode, with $\Phi = 0.5 \pm 0.1$

mode was analysed in Ref. [78]; the longitudinal mode properties are summarised in Figure 4.5.

An illustration of longitudinal excitation is presented in Figure 4.6. The decrease in intensity and lifetime of the longitudinal mode is due to the increasing rigidity of the moment, and the increase in phase space for magnon scattering. The amplitude fluctuations consist of a modulation of the magnitude of singlet-triplet components on each dimer site, and the wavefunction of a dimer can be written

$$|\sigma_i\rangle = \cos\theta|s\rangle + \sin\theta\exp(i\vec{Q}_{AF} \cdot \vec{r}_i)|t_x\rangle, \tag{4.3}$$

with the angle $\theta = 0$ for $P = P_c$, and increasing monotonically with pressure to $\theta = \pi/4$ for perfect antiferromagnetism at the ordering wavevector $\vec{Q}_{AF}$. At low pressures just above P_c, the triplons are very dilute and any longitudinal fluctuations would have a large scattering function due to the number of accessible excited states. As the number of bosons increases, the cross section (and therefore intensity) decreases. Furthermore, this creates the possibility of a decay of longitudinal fluctuations into spin wave excitations of the ordered moment and thus a reduction in the lifetime of coherent longitudinal fluctuations.

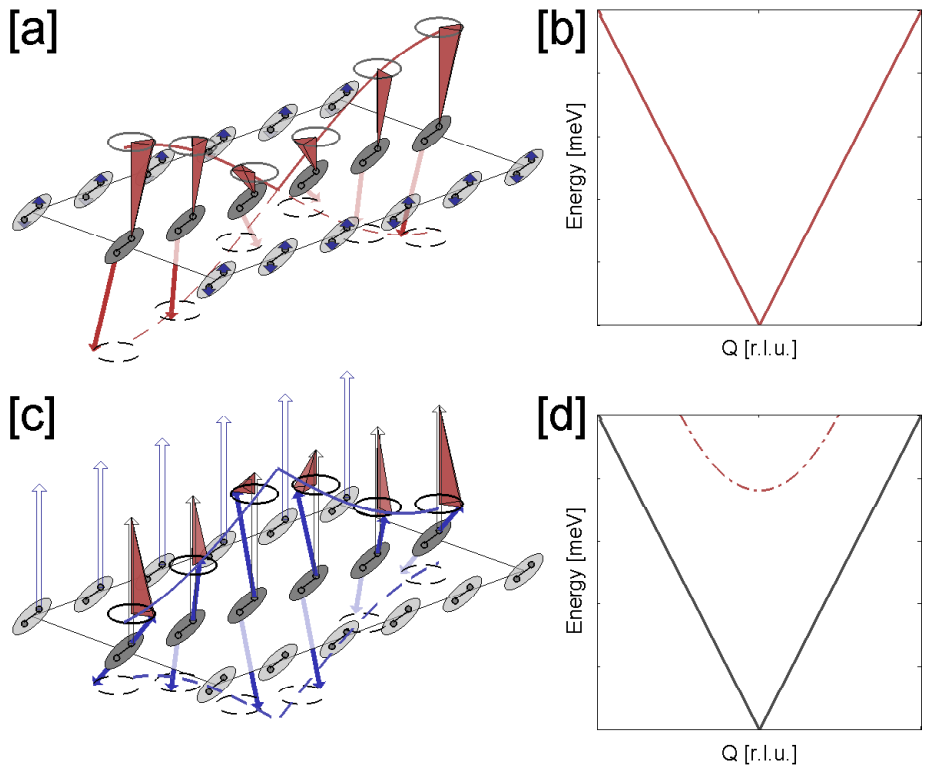

Figure 4.6: Longitudinal excitations at and above the QCP. **[a]** Schematic representation of the longitudinal excitation near the QCP. **[b]** Dispersion relation near $\vec{Q}$ = (0 4 0) r.l.u. for the excitations near the QCP. **[c]** Schematic representation of the longitudinal excitation in the RC-AFM phase. **[d]** Dispersion relation near $\vec{Q}$ = (0 4 0) r.l.u. in the ordered phase. For small pressures above P_c, the condensate still consists of a majority of singlets, with dilute triplet bosons. This results in a very small magnetic moment on the correlated dimer sites, given by the small blue arrows in [a]. A triplet excitation can propagate across the lattice by forming an amplitude oscillation of the magnitude of the sublattice magnetisation on each Cu^{2+} ion with minimal cost in energy due to the largely disordered nature of the adjacent dimers. This amplitude mode is represented by the vertical component of the red conal segment. The rotation across the lattice in a plane perpendicular to the amplitude fluctuation is representative of the transverse phase modulation. Both the longitudinal and transverse modes are gapless at $\vec{Q}$ = (0 4 0) r.l.u. as shown by the red line in [b]. For $P \gg P_c$, the triplet occupation on each dimer is high, and the system possesses long-range magnetic order with a much larger, rigid magnetic moment. Any excited longitudinal mode is one that deviates the lattice from this order, as presented in [c], with the amplitude mode in red, resulting in a transversely and longitudinally modulating mode represented in blue. The energy of this excitation is high due to the increased energy cost of varying the moment with respect to the highly ordered nature of the neighbouring dimers, and the lifetime becomes short due to the increased probability of decay into transverse excitations. In this picture, any amplitude fluctuations that occur are small and decay almost instantaneously, indicated by the high energy dashed red line in [d]. The transverse modes remain gapless.

4.4 Experiments across the Pressure-Temperature phase diagram

The scope of the current work is the extension of the scientific case detailed above to finite temperatures and the investigation of any resultant changes in properties of the elementary excitations, including the longitudinal mode. Furthermore, it seeks a comparison of the two methods of removing the order from the pressure induced RC-AFM phase - the case where it can occur through reversing the change of the exchange interactions by releasing the pressure on the system ('quantum melting'), or the second case realised through isobaric heating through the pressure-dependent Néel temperature ('thermal melting') without alteration of the exchange interactions.

In particular, it is of interest how thermal melting in $TlCuCl_3$ is a departure from the classical case, in which by heating across T_N the long-range order is removed through the thermal population of $S = 1$ excitations, which delocalise in the form of spin waves. The greater the occupation factor, the larger the reduction of the magnetic ordering. A continued increase in temperature results in continued reduction of magnetic moment until the order is lost entirely at the critical point, with gapless spin-wave excitations removed due to the restoration of spin symmetry. In an anisotropic 3D Heisenberg antiferromagnet, anisotropic terms in the Hamiltonian scale with the magnetisation [79] and the anisotropically gapped excitations demonstrate a downward shift in the excitation energy and signfiicant increase in damping as the temperature approaches T_N [80]; experimental examples include the antiferromagnets CoF_2 [81] and NiF_2 [82].

4.4.1 Experimental Setup

High-quality single crystals of $TlCuCl_3$ were grown by the Bridgeman method, and supplied by K. Krämer [83]. High-resolution INS studies were performed on the cold-neutron triple-axis spectrometer IN14 at the Institut Laue Langevin (ILL, Grenoble). The spectrometer was operated at a constant final wavevector of $\vec{k}_f = 1.15\ \mathring{A}^{-1}$, with a focusing pyrolytic graphite analyser, horizontal monochromator collimation open-60′-open-open, and a cooled Be filter positioned between the sample and analyzer.

The experiments were carried out using the ^{4}He gas pressure cell described in §2.4.3, mounted inside an orange cryostat. The pressure to be applied was calibrated with a pressure gauge, and the application of pressure was confirmed through checking strain readings from a sensor inside the cell. As detailed in §2.4.3, the final applied pressure can be different to the pressure calibrated on the gauge; to confirm the value, independent measurements of T_N are performed and compared to the previously calculated

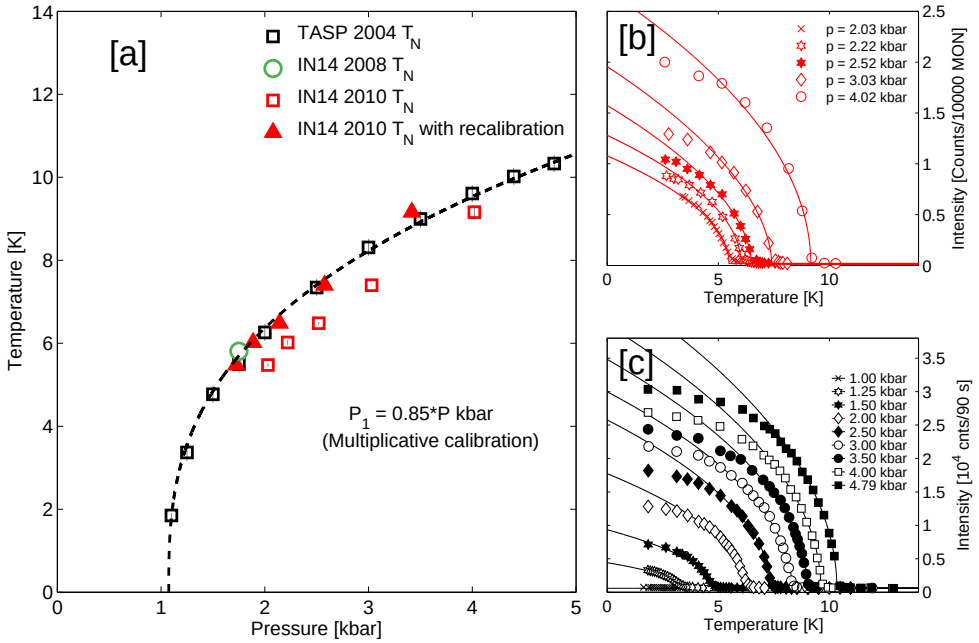

Figure 4.7: T_N values for measured pressure points. **[a]** $T_N(P)$ for different experimental data sets. **[b]** Fitted elastic scattering intensity for the 2010 data. **[c]** Fitted elastic scattering intensity for 2004 TASP data, from Ref. [52]. In [a], the $T_N(P)$ values for the 2004 TASP data are shown by the black squares, the $T_N(P = 1.75$ kbar) value IN14 2008 by the green circle, and the $T_N(P)$ values IN14 2010 data are shown by the red squares. The 2004 TASP data set is known to be consistent with previous experiments ([33, 52, 78]). The solid red triangles show $T_N(P)$ where the 2010 applied pressure values have been calibrated with a multiplicative prefactor as described in the text.

T_N values, measured on TASP in 2004 [52]. These values are known to be consistent with subsequent measurements [33, 78]. The T_N values were determined by monitoring scattering intensity of the Bragg peak at $\vec{Q} = (0\ 0\ 1)$ r.l.u. across the temperature-induced phase transition, for the values of applied pressure for which experiments were conducted on IN14 in 2008 and 2010.

Figure 4.7 details the determined T_N values for the values of applied pressure. The temperature-dependent magnetic Bragg peak intensity as measured on IN14 in 2010, and on TASP in 2004 are shown in Figure 4.7 panel [b] and panel [c] respectively. Panel [a] summarises the collected T_N values, demonstrating that the 2008 data is consistent with the previous value, but the data collected in 2010 has an offset from the expected values.

This offset can be corrected by applying a multiplicative prefactor Z to the applied pressure P to get a corrected pressure P_1 (i.e. $P_1 = ZP$). It was calculated that a prefactor of $Z = 0.85$ accurately reproduces $T_N(P)$ values that are consistent with previous measurements. The only effect this prefactor will have on the subsequent

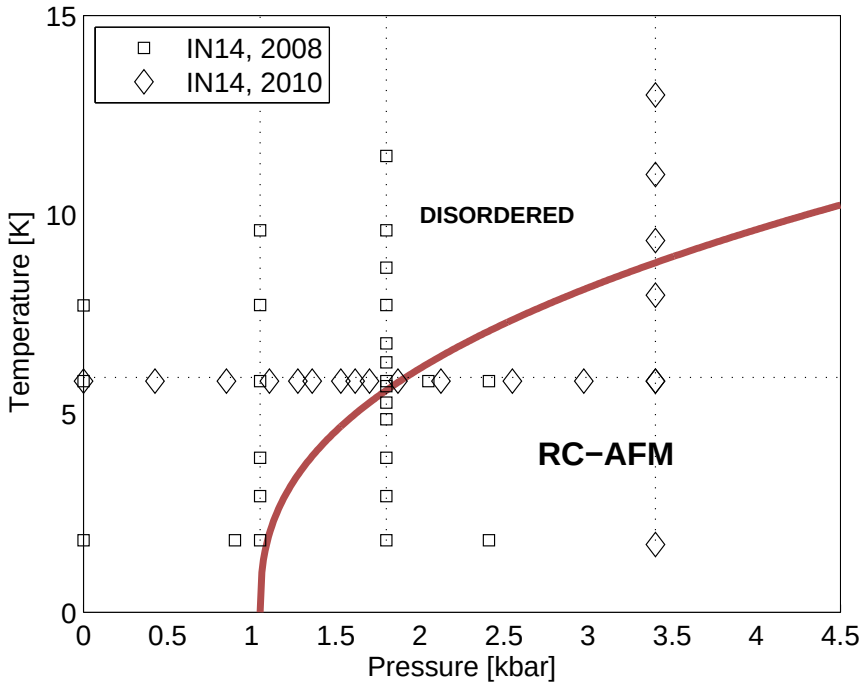

Figure 4.8: The points of data collection on IN14. The solid red line indicates the phase boundary separating the RC-AFM and QD phases of the (P,T) phase diagram. The open squares indicate the collected scans taken at selected pressure and temperature points on IN14 in September 2008. The open diamonds indicate the collected scans taken at selected pressure and temperature points on IN14 in November 2010.

discussion is on the attempts to quantify the dynamics as a function of pressure. In this case, the quantities are described by power laws and the calibration prefactor can be assimilated into the amplitude prefactor (e.g. for arbitrary properties X and B, $X = B(P-P_c)^{\alpha} = B(ZP-ZP_c)^{\alpha} = BZ^{\alpha}(P-P_c)^{\alpha}$), for which the absolute magnitude is not of significance.

The sample was loaded into the pressure cell such that the crystal was in the (**b***, **c***) scattering plane, and the elementary excitations measured at the same AFM zone centre as in previous experiments, at which point the elementary excitations occur at the minimum values and are driven gapless by applied pressure. The measured zone centre was $\vec{Q} = (0\ 4\ 0)$ r.l.u., chosen such as to remove all scattered intensity from the gapless Goldstone mode, and the system was therefore aligned and oriented such that the measured scattered neutrons at the energy-momentum points $(\vec{Q}, \Delta E)$, for $\Delta E =$ 0 to 1.8 meV. The lattice parameters of $TlCuCl_3$ change with pressure and therefore the single crystal was realigned after each pressure step.

The experiment was conducted such that INS scans were taken to systematically follow the evolution of the longitudinal and gapped anisotropic transverse excitations across any phase transition in the (P,T) phase diagram. Each (P,T) value for collected

data scans is presented in Figure 4.8.

Figure 4.9 demonstrates a selection of the data collected on IN14, ILL for the same crystal used for the study in Ref. [78]. It shows several scans for $0.2 < \Delta E < 1.8$ meV for a range of temperatures at the applied hydrostatic pressure $P = 1.75$ kbar, and compares these scans to scans at $T = 1.81$ K at finite pressure, presented as part of Ref. [78]. It is evident that in a manner similar to the case for increasing pressure to P_c at $T = 1.80$ K, the longitudinal mode undergoes a reduction in excitation energy as T_N is approached at $P = 1.75$ kbar. Intensity from the gapless transverse excitation does not contribute to the scattering intensity at this $\vec{Q}$ value.

Background subtraction was performed on all data (including that presented in Figure 4.9) to remove artifacts of the background, such as incoherent scattering. Background data was collected at $\vec{Q} = (0\ 3.5\ 0)$ r.l.u. for $\Delta E > 0.2$ meV and combined with a low energy ($\Delta E < 0.2$ meV) measurement at $\vec{Q} = (0\ 4\ 0)$ r.l.u. to account for contributions of the Bragg peak to the background at lower energies. A background scan is plotted in Figure 4.9 [b] by the grey squares.

The $P = 1.75$ kbar data is summarised as a contour plot in the context of the phase diagram in Figure 4.10.

Through the analysis of the collected data, it was possible to follow the evolution of the elementary excitations throughout the quantum critical phase diagram, and specifically across the phase boundary for the cases (i) $T = 0$ to $T = 11.47$ K for $P = 1.75$ kbar; (ii) $T = 0$ to $T = 13$ K for $P = 3.4$ kbar; (iii) $P = 0$ to $P = 3.4$ kbar for $T = 5.81$ K.

Throughout the RC-AFM phase of the (P, T) diagram given in Figure 4.8, the staggered magnetic moment is small. Table 4.4 gives the measured value for m, the magnetic moment per Cu^{2+} site, at $P = 14.8$ kbar and its reduction with increasing temperature, taken from the references given. The application of pressure beyond the critical value results in the increase of the staggered magnetic moment, M_{xy}, with $M_{xy} \propto \sqrt{P - P_c}$. While this relationship is formulated for the region close to the critical pressure [31], it does provide an upper limit on the value per Cu^{2+} site, and assuming the above relationship one might expect to observe values of $m \lesssim 0.28$ for $P \lesssim 3.4$ kbar.

4.4.2 Fitting

The experiments performed previously have been focused on the question of the 'low T' dynamics, and therefore on a region where the MFBO theory described in Chapter 3 remains accurate across the QPT. The fitting routine employed was one where the

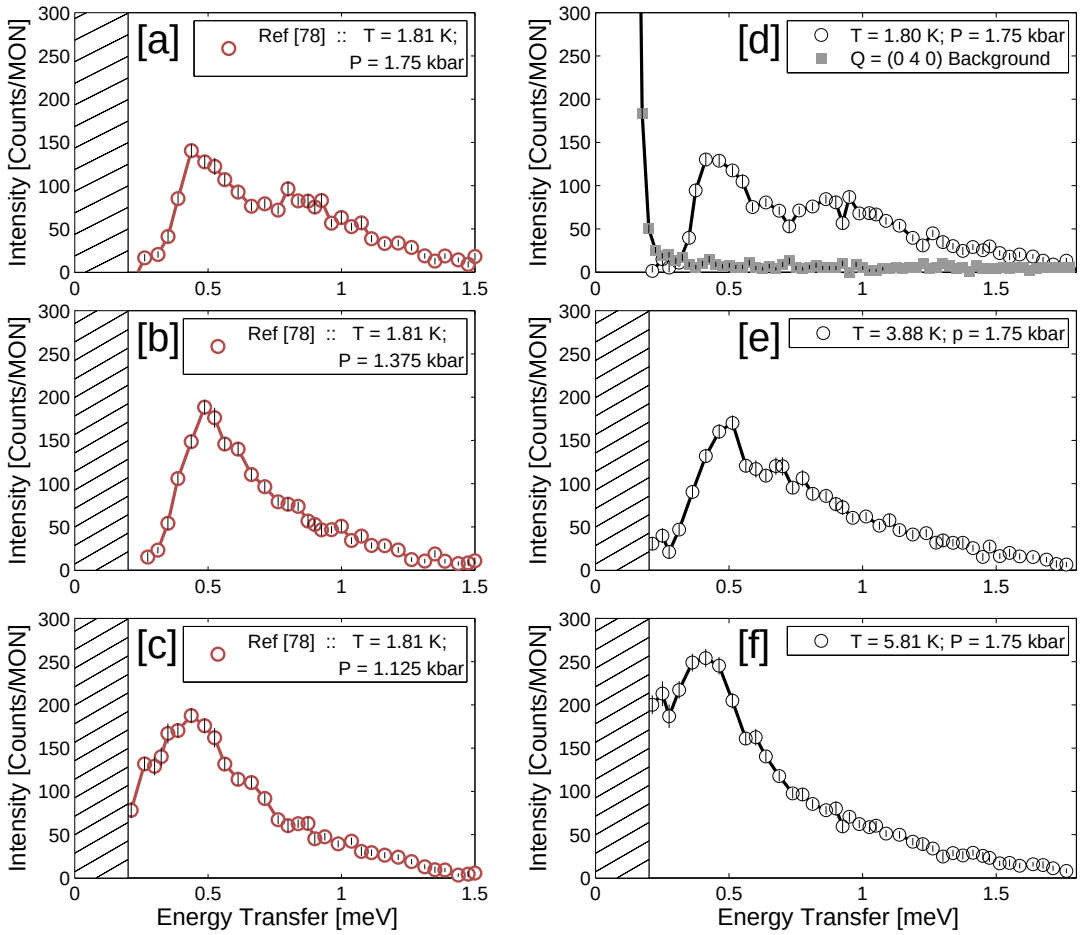

Figure 4.9: A comparison of softening of the longitudinal excitation at $\vec{Q} = (0\ 4\ 0)$ r.l.u. as a function of temperature renormalisation. **[a]** $T = 1.81$ K, $P = 1.75$ kbar. **[b]** $T = 1.81$ K, $P = 1.375$ kbar. **[c]** $T = 1.81$ K, $P = 1.125$ kbar. **[d]** $T = 1.80$ K, $P = 1.75$ kbar. **[e]** $T = 3.88$ K, $P = 1.75$ kbar. **[f]** $T = 5.81$ K, $P = 1.75$ kbar. The scans [a], [b] and [c] are the data presented as part of Ref. [78], collected on IN14 in 2005. From each scan a background has been subtracted, where the background is a combination of scans collected at $\vec{Q} = (0\ 4\ 0)$ r.l.u. and $(0\ 3.5\ 0)$ r.l.u. and plotted in [d]. The sharp rise in background intensity is the contribution from the Bragg peak, and necessitates the removal of all data for which $\Delta E < 0.2$ meV, resulting in the shaded region.

Ref	Pressure [kbar]	T_N [K]	T [K]	m [μ_B/Cu^{2+}]
[84]	14.8	16.9	1.5	0.70
[85]	14.8	16.9	4.0	0.64
			12.2	0.51

Table 4.4: Table describing the measured magnetisation per Cu^{2+} ion, taken from the references indicated.

calculated resolution ellipsoid was convolved with the MFBO equations without alteration, assuming a simple ansatz for the exchange interaction pressure-dependence. As

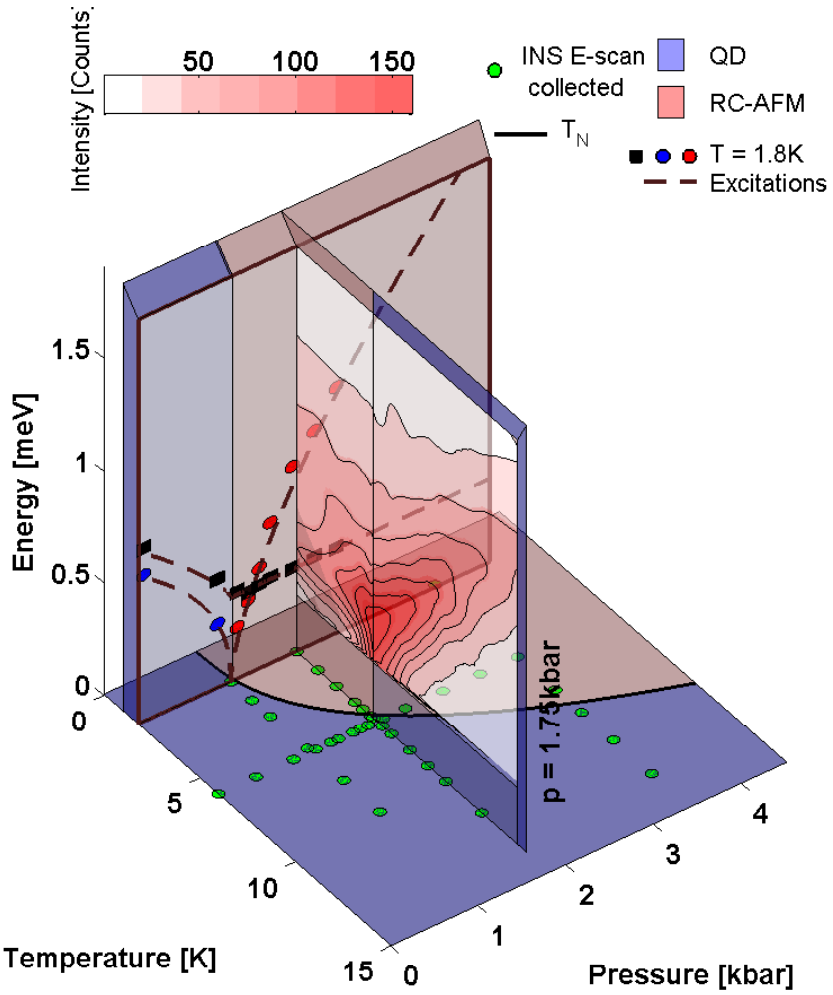

Figure 4.10: The INS data collected for $P = 1.75$ kbar for 1.8 K $< T <$ 11.47 K. The basal plane illustrates the phase diagram with T_N (solid black line) separating the RC-AFM phase and the QD phase. The green circles are the points of data collection summarised in Figure 4.8. The rear panel illustrates the fitted excitation energies presented in Figure 4.5. The contour colour indicates the counts for a defined monitor of scattered neutrons and therefore the mode intensity.

detailed in §3.2.3, increasing the temperature results in a renormalisation of the band, necessitating a modification of the MFBO theory to describe the data.

The temperature dependence of $S(\vec{Q},\omega)$ in dimer based compounds becomes increasingly significant as the pressure is increased due to the larger thermal population factor as the spin gap is continuously reduced to zero. The 'low' $T = 1.8$ K value represented a statistically insignificant level of thermal occupation, but for increasing T, thermal population becomes significant and thermal fluctuations are on a scale competing with the quantum fluctuations. In addition to affecting the magnitude of the spin gap, the change in temperature alters the bandwidth of the triplet excitations in an unknown fashion. Because the fitting of the scattering intensity is dependent on

the curvature of the band near the band minimum, the changes in bandwidth due to temperature must be accounted for.

A model for the band curvature can be effected through the implementation of the effective pressure parameter introduced in §3.2.3. In this model, a band curvature is determined from the value for the fitted spin gap by using the dispersion relations given in §3.2 and implementing a pressure value appropriate to reproduce that spin gap at '$T = 0$ K', i.e. an effective pressure.

The effective pressure values are then used to calculate the dimensionless pressure, which quantifies the change in interdimer exchange interactions and thus the band curvature. From assuming the reduced ansatz of Ref. [31], the dimensionless pressure is calculated by

$$p(P) - p_c = \beta_1(P - P_c) + \beta_2(P - P_c)^2, \tag{4.4}$$

The values for β_1 and β_2 can be determined through a known set of values for P and p. $p = 1$ for $P = 0$ kbar (i.e. ambient pressure), $p_c = 1.018$ at $P = 1.07$kbar, and $p = 1.4$ at $P = 14.8$kbar [31]. The latter comes from neutron diffraction studies which have yielded a total staggered magnetisation $M_{xy} = 60\%$ of the saturation value, applied to the assumed functional form for the staggered magnetisation $\langle M_{xy} \rangle \propto (p - p_c)^{1/2}$. This results in the values $\beta_1 = 0.017679$ kbar^{-1}, and $\beta_2 = 0.000738$ kbar^{-1}.

An effective pressure parameterisation of the change in the intradimer term J is not explicitly implemented, as the dominant effect of changes in J is the variation of the gap energy, which is included as a separate, fitted parameter. The dominant effect of the effective pressure parameter is then to alter the local curvature of the band minimum. Variations are only implemented to provide an effective model for the other fitting parameters to model the unknown effect of thermal fluctuations on the band curvature.

With an effective model for the local band curvature, an integrated scattering intensity is calculated from convolving the 4-dimensional $(\vec{Q}, \omega)$ resolution ellipsoid of the triple axis spectrometer with the dispersion, a process described in section §2.3.4, and fitting this resultant intensity to the experimentally measured intensity through a least squares fitting routine.

The integrated scattering is dependent on the excitation linewidth, which undergoes broadening upon heating. An appropriate choice for the lineshape function with the application of a bosonic occupation factor can be applied to account for this effect. For modes of infinite lifetime, $S(\vec{Q}, \omega)$ is a δ function in energy and the width in energy can be approximated to be on the order of the instrumental resolution at 'low' temperatures ($T = 1.8$ K). However, at higher temperatures, a finite damping term is necessary and

as a result of considering multiple models, the damped harmonic oscillator (DHO) lineshape used for phonon excitations [86, 87] was applied with success [34].

In modelling the magnon as a DHO, the scattering intensity is taken as a double Lorentzian lineshape

$$S(\vec{Q},\omega) = \frac{A[n(\omega)+1]4\Gamma_Q\epsilon_Q\omega}{[\omega^2-\epsilon_{DHO}(\vec{Q})^2]^2+4\Gamma_Q^2\omega^2}, \tag{4.5}$$

where $n(\omega)+1 = [1-\exp(\hbar\omega/k_BT)]^{-1}$ is the Bose factor for the thermal population. Here $\epsilon_{DHO}(\vec{Q})^2 = \epsilon_Q^2 + \Gamma_Q^2$ is the renormalized energy of the excitation, which is expressed in terms of the real excitation energy, ϵ_Q, and the line width of the scattered intensity, taken as the full width at half-maximum height, Γ_Q; thus the observed peak in the measured intensity does not correspond to the real excitation energy of the mode.

This lineshape, calculated for the appropriate temperature value, is then applied to the triplet band described by the fitted spin gap and the curvature parameterised by the effective pressure. This results in a model that can be effectively implemented in neutron resolution convolution analysis to produce a calculated scattering intensity for finite energy transfers. A line of best fit to the observed scattering intensity is created, determined from the fitting parameters: The spin gap (ϵ), the FWHM (Γ) and the intensity (I).

Care was taken to ensure an appropriate and consistent value of effective pressure was used for each of the determined spin gaps. Upon determination of a spin gap value with an appropriate effective pressure, the spin gap value was confirmed by allowing the relaxation of the effective pressure as a fitting parameter to obtain a new value and refitting the energy, FWHM and intensity. This method was performed near the phase boundary and in both the ordered and disordered phase. It was found that either the relaxed effective pressure parameter did not significantly vary from the calculated value, or the observed change on the extracted fitted parameters was minimal.

Comments on the formalism for magnetic excitations cannot be made without mention of phonon excitations and possible spin-phonon coupling. Previous work [52] on the spectrum in $TlCuCl_3$ above the elementary spinglet-triplet excitations has clearly identified phonon branches, the same as those reported in other studies [64, 88], along with others near the triplet mode energy. However, the focus of the current studies are around $\vec{Q}$ = (0 4 0) r.l.u., corresponding to a modest $|Q|$ value, and the higher momentum phonon scattering will therefore not affect the parametric investigation of quantum and thermal melting.

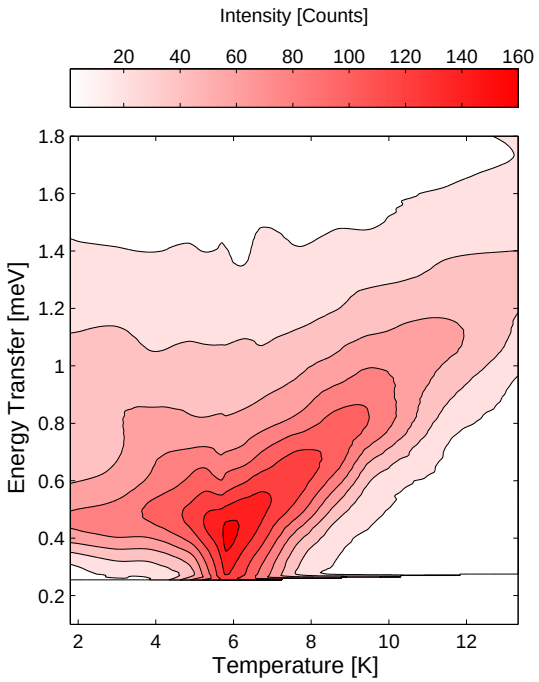

Figure 4.11: Contour plot showing the INS intensity at $\vec{Q} = (0\ 4\ 0)$ r.l.u. for $P = 1.75$ kbar as a function of temperature, where 1.8 K $< T <$ 11.47 K. The softening at $T = 5.81$ K can be seen in the low energy, high-intensity scattering at this point.

4.5 Data Analysis

In this section the results of the data analysis will be presented and the extracted excitation parameters summarised for the cases (1) Thermal melting at $P = 1.75$ kbar; (2) Quantum melting at $T = 5.81$ K; (3) Thermal melting at $P = 3.40$ kbar and (4) 'critical' scattering of the temperature dependent excitations at $P = 1.05$ kbar, near the critical pressure. The results will be discussed in the next section.

4.5.1 Thermal Melting, P = 1.75 kbar

At $P = 1.75$ kbar and $T = 0$ K, the system is in the RC-AFM phase. There is a damped but observeable longitudinal mode of significant spectral intensity alongside an anisotropy gapped transverse excitation of the ordered moment. As seen in Ref. [78], the act of lowering the pressure causes the softening of the longitudinal mode and its evolution into a gapped triplet state. This section details the work performed as a means of a comparative study to see the effect of temperature on the excitations of the system as it is heated through T_N.

In this case, the pressure is fixed at $P = 1.75$ kbar and the temperature controlled through thermal regulation on the cryostat. At this pressure, even the highest measured temperature will still be inside the solid helium phase. As such, while there

exists error in temperature determination, the pressure is required to be set only once and therefore the pressure at every point across the phase diagram will be the same; any error contained in the pressure determination is identically carried into each temperature point. Such error is thought to be small, as the measured T_N of the magnetic Bragg peak at $\vec{Q} = (0\ 0\ 1)$ r.l.u. is consistent with the previous results.

INS scans from 0.1 meV $< \Delta E <$ 1.8 meV were taken for temperature points from 1.8 K $< T <$ 11.47 K. Due to the presence of incoherent elastic scattering and contributions from the Bragg peak for energies close to zero, all data below $\Delta E = 0.2$ meV has been discounted. The remainder has been adjusted with suitable background measurements as described in §4.4.1. The raw data for these scans are summarised in Figure 4.11 by a contour plot. Each INS energy scan was fitted as outlined in §4.4.2. The fitted scattering intensity for a selection of T across the phase diagram is presented in Figure 4.12, illustrating the different contributions from each mode as temperature crosses the phase boundary.

A clear softening of the triplet excitations is observed, with $T_N = 5.81$ K, and demonstrating a significant damping and increase of spectral intensity. The lifetime broadening continues as the modes evolve into damped, gapped spin triplet excitations above T_N. The fitted damped harmonic oscillator energies (ϵ_{DHO}), real excitation energies(ϵ) and FWHM are summarised in Figure 4.13 for the longitudinal and transverse modes.

The FWHM for the longitudinal and transverse excitations are given in Figure 4.14 [b]. The Γ for the transverse mode remains small in the RC-AFM phase, indicating a long-lived, stable excitation, but for $T > T_N$, the width increases with temperature. The longitudinal mode has a larger FWHM at $T = 1.8$ K, and remains roughly constant for increasing T.

Figure 4.14 [a] illustrates the choice of effective pressure to model the dispersion across the phase transition. At $T = 1.8$ K, the effective pressure best describing the fitted dispersion is $P_{eff} = 1.6$ kbar, a departure from the pressure corresponding to the fitted spin gap ($P = 1.75$ kbar). With the given effective pressure, the energy gap is 0.8687 $\pm$ 0.013 meV. With the fitted effective pressure, the energy gap is 0.8701 $\pm$ 0.015 meV. This is an expected result given the relatively small changes in the quadratic nature of the dispersion far from the critical point, and justifies the model of the band curvature using an effective pressure.

4.5.2 Quantum Melting, T = 5.81 K

The longitudinal mode is a direct consequence of the quantum character of the system, but as shown in the previous subsection it remains observeable even upon heating to

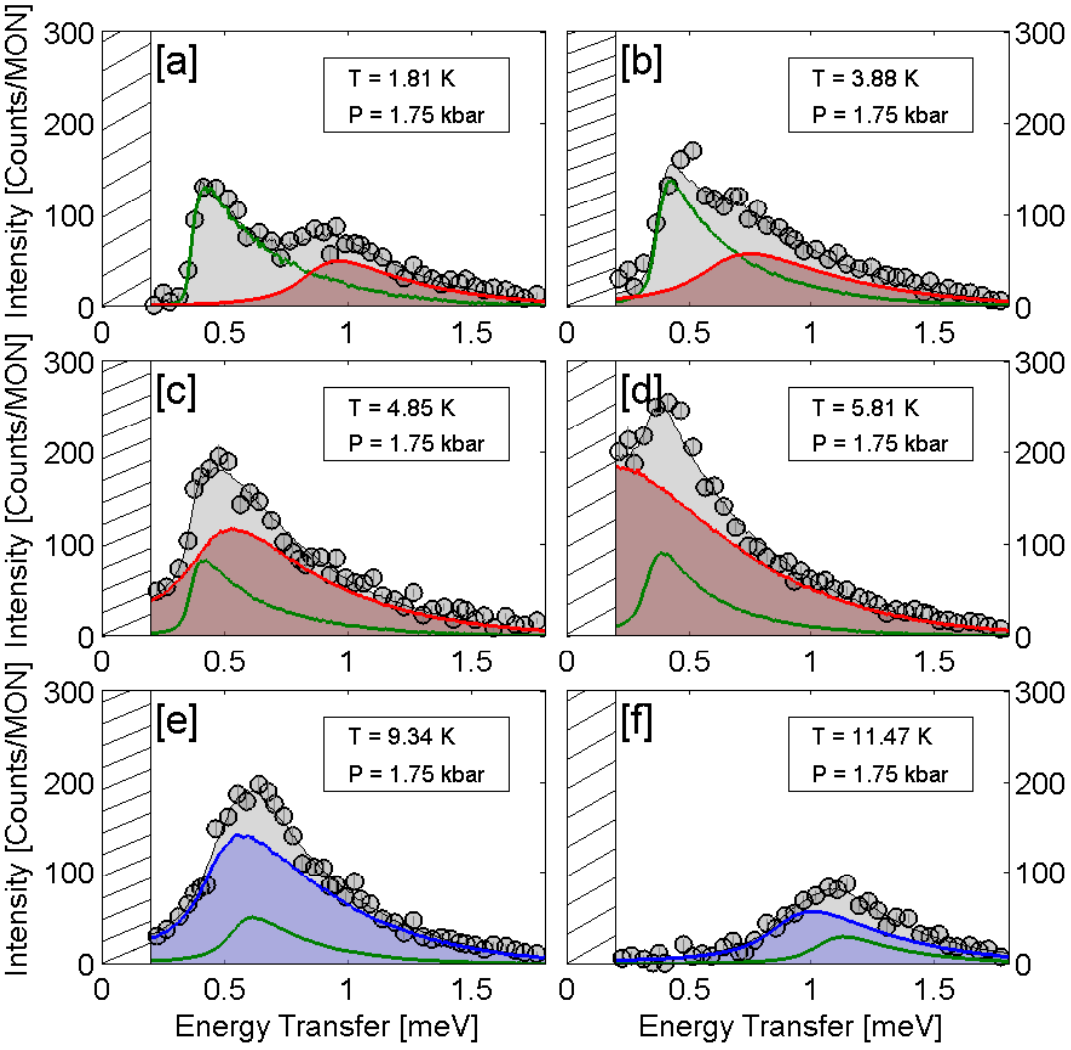

Figure 4.12: Fitted INS intensity at $\vec{Q}$ = (0 4 0) r.l.u. at $P = 1.75$ kbar for several temperature values. **[a]** $T = 1.81$ K. **[b]** $T = 3.88$ K. **[c]** $T = 4.85$ K. **[d]** $T = 5.81$ K. **[e]** $T = 9.34$ K. **[f]** $T = 11.47$ K. Panels [a] - [d] demonstrate the softening of the longitudinal excitation (denoted by the red shaded area) to $\Delta E = 0$ at $T = 5.81$ K, with a significant increase in the spectral intensity upon approach. The transverse excitation (green line) remains at $\Delta E \sim 0.4$ meV throughout the ordered phase. Panels [e] - [f] demonstrate the emergence of the singlet-triplet excitations for $T > T_N$, where both the longitudinal and transverse modes undergo significant thermal damping and upward shift in excitation energy.

finite T, only disappearing at the phase boundary where it evolves continuously into a triplet mode in a manner similar to the case for the QPT. In this section experimental data is presented that was collected as a means to compare the evolution of elementary excitations as a function of pressure at a finite temperature ($T = 5.81$ K) to determine the effect of temperature renormalisation upon the pressure-dependent dynamics.

At $P = 0$ kbar, $T = 5.81$ K the system is in a quantum disordered state described by

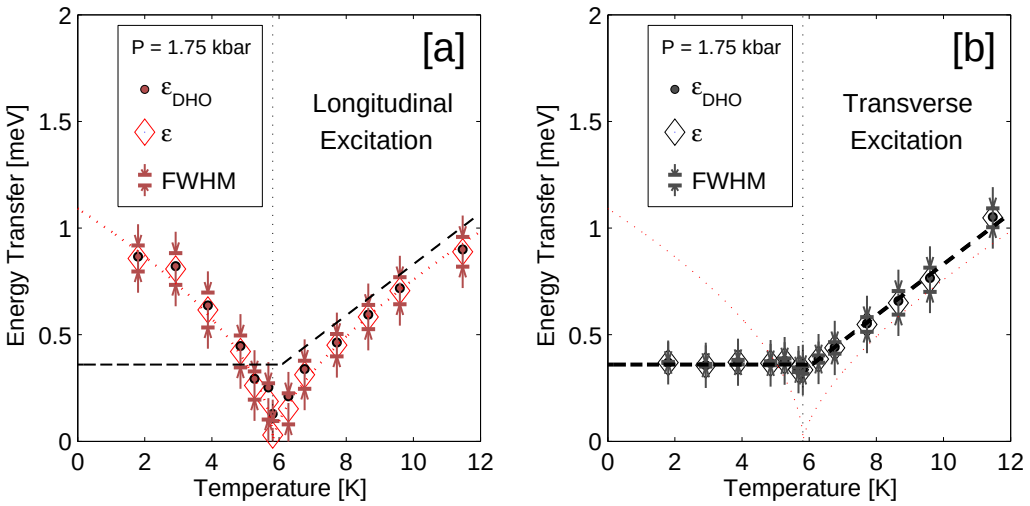

Figure 4.13: The excitation energies of the longitudinal and transverse excitations across the temperature-driven phase transition at finite pressure, $P = 1.75$ kbar. **[a]** The properties of the longitudinal excitation. **[b]** The properties of the transverse excitation. The damped harmonic oscillator energies (ϵ_{DHO}) are given by the small circles, the extracted real excitation energies (ϵ) given by the open diamonds, the FWHM (Γ) of the excitation given by the bounding arrows centered on ϵ. The red dashed line is a power law fit to the longitudinal mode energy, and the black dashed line is the fitted power law to the transverse excitation. The vertical dotted line indicates the phase boundary.

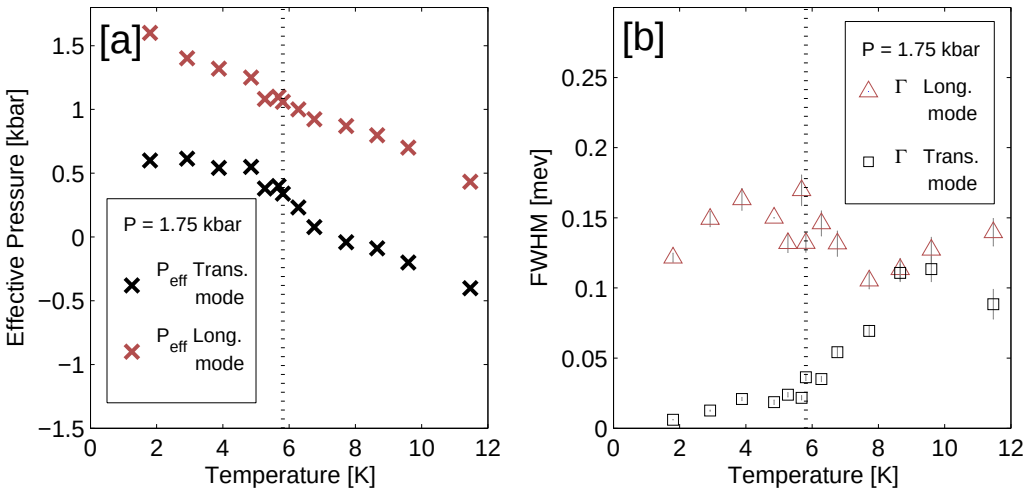

Figure 4.14: The effective pressure and FWHM of the longitudinal and transverse excitations across the temperature-induced phase transition at finite pressure, $P = 1.75$ kbar. **[a]** Effective pressure P_{eff} for longitudinal and transverse excitations. **[b]** FWHM (Γ) for longitudinal and transverse excitations.

.

spin dimers with a temperature-adjusted magnon dispersion. Increasing the pressure at this point is seen to have the same effect as in the low-temperature case, and reduces the spin gap continuously to zero. The INS scans are summarised in Figure 4.15, which

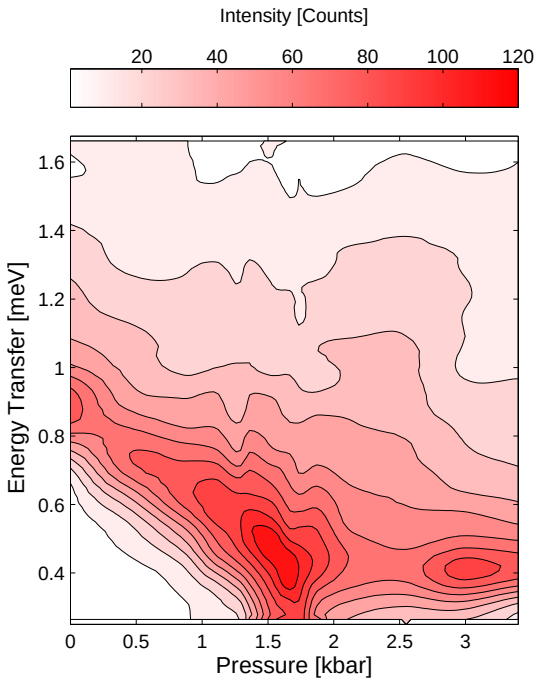

Figure 4.15: Contour plot showing the INS intensity for $T = 5.81$ K for 0 kbar $< P <$ 3.4 kbar. The softening at $P \sim 1.7$ kbar can be seen in the low energy, high-intensity scattering at this point.

presents the collected scans for 0 kbar $< P <$ 3.4 kbar for $0 < \Delta E < 1.8$ meV. As with the $P = 1.75$ kbar scans, the background has been subtracted, with low energy ($\Delta E < 0.2$ meV) data being discounted. Again, each INS energy scan was fitted as outlined in §4.4.2. The fitted scattering intensity for a selection of P across the phase diagram is presented in Figure 4.16, illustrating the different contributions from each mode as the pressure is increased through the critical pressure, $P_c(T = 5.81K) = 1.75$ kbar.

There are certain values of pressure and temperature for which the contributions to the scattering intensity from the two excitations substantially overlap. This can be seen, for example, in Figure 4.16[c]. This overlap can result in multiple combinations of the fitting parameters that provide local minima in the least-squares fitting routine; fitting the data *prima facie* may therefore result in multiple solutions. However, some of these solutions can be dismissed as incorrect by a lack of consistency with other measurements fitted with a more robust set of fitted parameter values. For example, a large discontinuity in the fitted transverse mode scattering intensity when considering the data at $P = 1.70$ kbar and $P = 1.275$ kbar would not be physical and thus be indicative of an incorrect solution.

To accurately fit such data, it is necessary to constrain the fit by contextualising the fitting parameters; this is done by considering other, more robust fitted parameters

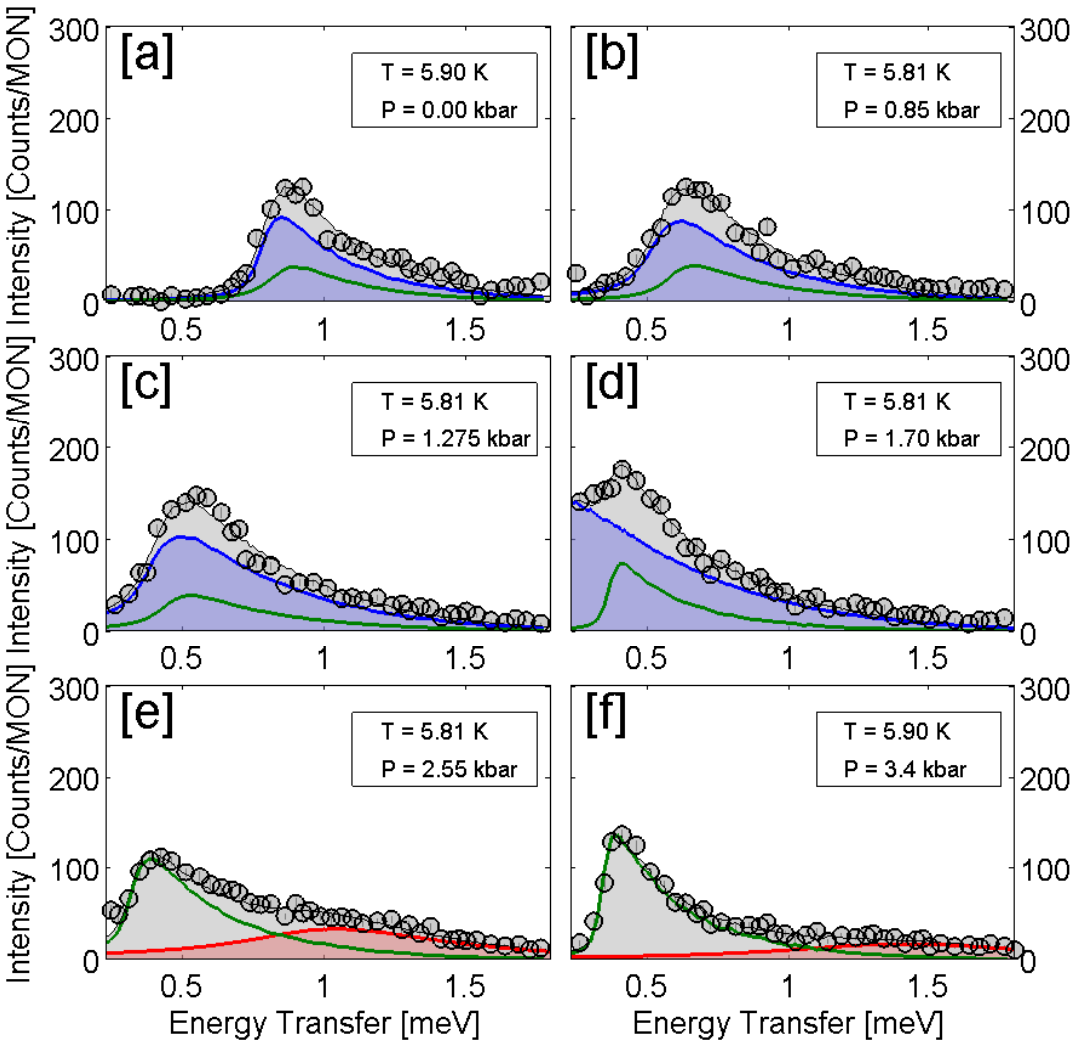

Figure 4.16: Fitted INS intensity at $\vec{Q}$ = (0 4 0) r.l.u. at $T = 5.81$ K for several values of applied pressure. **[a]** $P = 0$ kbar **[b]** $P = 0.85$ kbar **[c]** $P = 1.275$ kbar **[d]** $P = 1.70$ kbar **[e]** $P = 2.55$ kbar **[f]** $P = 3.4$ kbar. Panels [a] - [d] demonstrate the softening of the longitudinal triplet excitation (denoted by the blue shaded area) to $\Delta E \sim 0$ meV at $P = 1.70$ kbar, with a significant increase in the spectral intensity upon approach, as observed in thermal melting at $P = 1.75$ kbar. The transverse excitation (green line) also continuously reduces in energy, reaching $\Delta E \sim 0.4$ meV at the critical point, and remaining at that energy throughout the ordered phase. Panels [d] - [e] demonstrate the emergence of the longitudinal excitation for $P > P_c$, which becomes highly damped with reduced spectral weight with increasing pressure.

from other measurements. The initial values for fitting parameters are taken from the results yielded from other data sets with the closest P and T values to the data set being considered. The scattering intensities, excitation energies, and FWHM vaues are allowed independently vary before being uniformly relaxed to find the local minima.

The longitudinal mode is again seen to be experimentally observeable, albeit with

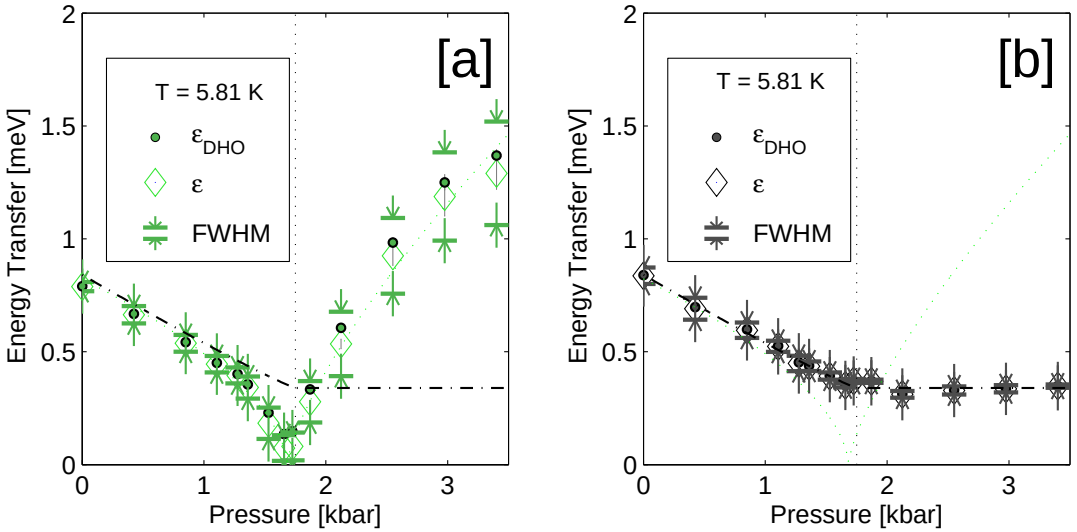

Figure 4.17: The excitation energies of the longitudinal and transverse excitations across the pressure-driven phase transition at finite temperature, $T = 5.81$ K. **[a]** The properties of the longitudinal excitation. **[b]** The properties of the transverse excitation. The damped harmonic oscillator energies (ϵ_{DHO}) are given by the small circles, the extracted real excitation energies (ϵ) given by the open diamonds, the FWHM of the excitation given by the bounding arrows centered on ϵ. The green dashed line is a power law fit to the real excitation energies, and the black dashed line is the fitted power law to the transverse excitation.

significant damping at the highest pressures. It is also seen to continuously reduce to zero in a manner similar to the previously reported cases; the fitted damped harmonic oscillator energies (ϵ_{DHO}), real excitation energies (ϵ) and FWHM are summarised in Figure 4.17 for the longitudinal and transverse modes.

The continuous reduction of the longitudinal mode to zero is a point of similarity to the temperature-induced phase transition, but it can be noted there is a difference in the behaviour of the FWHM as the pressure is increased, as evidenced by the longitudinal FWHM values plotted in Figure 4.18 [b] alongside the transverse FWHM values. The FWHM for the transverse and longitudinal triplet excitations are roughly equal for pressures below P_c, above which the longitudinal mode values begin to increase as the transverse values decrease, indicating as the ordered moment increases the transverse mode stablises and the longitudinal mode undergoes a reduction in lifetime.

Figure 4.18 [a] illustrates the choice of effective pressure to model the dispersion across the phase transition. There is a departure from linear behaviour which accounts for the effects of temperature on the dispersion at the band minimum; higher T begets a larger gap with smaller bandwidth, modeled by a lower effective pressure and is consistent with the values realised.

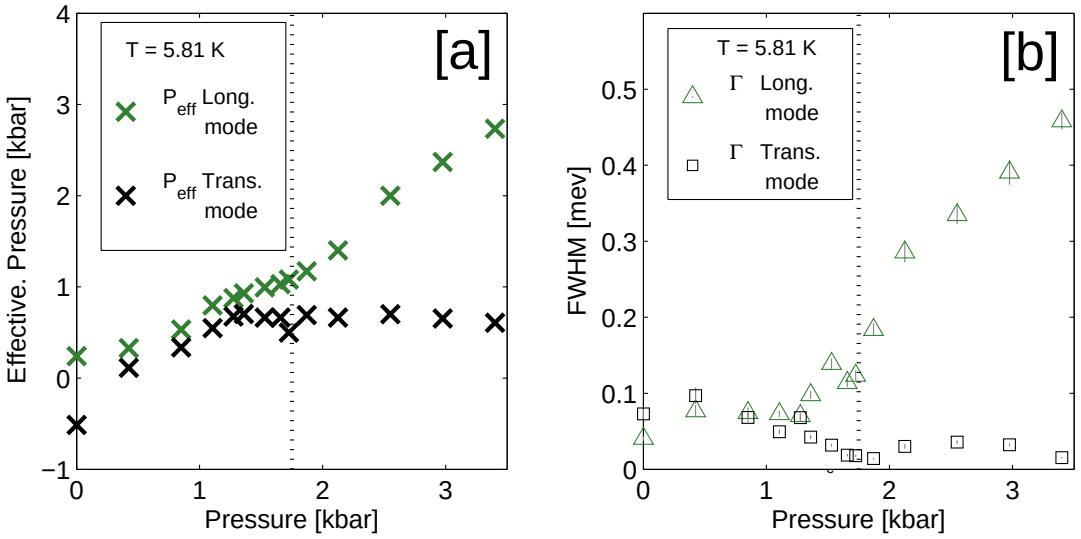

Figure 4.18: The effective pressure and FWHM of the longitudinal and transverse excitations across the pressure-induced phase transition at finite temperature, $T = 5.81$ K. **[a]** Effective pressure P_{eff} for longitudinal and transverse excitations. **[b]** FWHM (Γ) for longitudinal and transverse excitations.

4.5.3 Thermal Melting, P = 3.40 kbar

For $P = 14.8$ kbar, the magnetic moment per Cu^{2+} site is $m = 0.70\ \mu_B/Cu^{2+}$, reducing as the temperature increases (Table 4.4). Because of this large moment, any excitations in the form of amplitude fluctuations will be highly damped and at very high energy. In this regime it is unclear how any longitudinal fluctuations will evolve with temperature, and if they are observeable near the phase boundary due to the melting of the magnetic moment.

The pressures required to achieve such an ordered state are not possible inside the ^{4}He gas pressure cell, but it prompted investigation into the temperature-dependent dynamics near the higher ends of attainable pressures. The pressure point chosen for consideration was $P = 3.4$ kbar; at this pressure it was observed that the longitudinal mode intensity was greatly reduced with a significant FWHM while still being observeable. INS spectra were collected at this pressure across the temperature-induced phase transition with a motivation to understand the effect of increased staggered magnetisation on the longitudinal mode dynamics and for comparison to the case for a 'classical' Néel antiferromagnet.

The pressure is fixed at $P = 3.40$ kbar and the temperature is controlled through thermal regulation on the cryostat, with a fixed pressure that does not vary throughout the measurement, resulting in a fixed error as in the case for the lower pressure. The data for this thermal phase transition is summarised in Figure 4.19, in the form of a

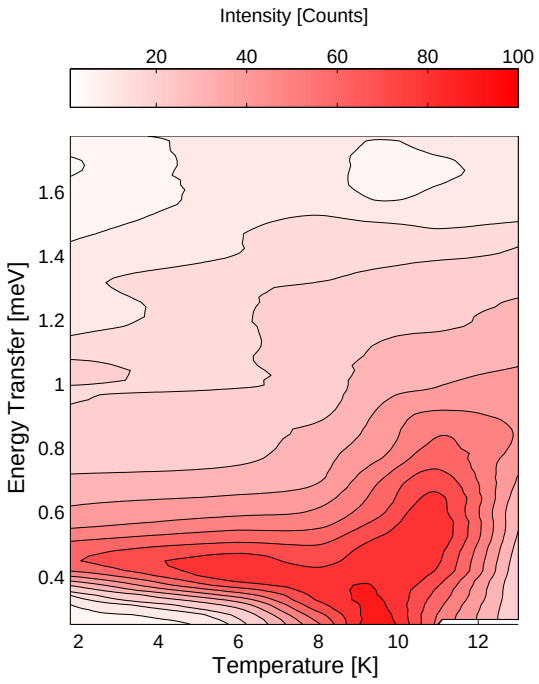

Figure 4.19: Contour plot showing the INS intensity for $P = 3.40$ kbar as a function of applied temperature, where 1.8 K $< T <$ 13.0 K. The softening at T $\sim$ 9.5 K can be seen in the low energy, high-intensity scattering at this point. There is weak scattering observeable from the longitudinal mode at higher energies for $T < T_N$.

contour plot for 1.8 K $< T <$ 13 K, for 0 meV $< \Delta E <$ 1.8 meV. As with previous scans, the background has been distracted and low energy data ($\Delta E <$ 0.2 meV) discounted. While not shown in the figure, the scan at $T = 1.8$ K extends up to ΔE = 2.5 meV due to the broad nature of the longitudinal mode. The fitted contributions to the scattering intensities from the elementary excitations are presented in Figure 4.20, with regions without measured data included in Figure 4.20 [c] and [e] to present the spectra on the same energy scale as the plot in [a].

The softening of the excitations at the critical point can be seen in the data presented in Figure 4.19, and the fitted contributions in Figure 4.20 reveal the softening of the longitudinal mode (red shaded area), before evolving into a gapped triplet state (blue shaded area) at $T > T_N$. There is a slight decrease in the transverse excitation (green solid line) as the phase boundary is approached.

The extracted mode energies are presented in Figure 4.21, the energy gap (ϵ, blue diamonds), DHO energy (ϵ_{DHO}, blue circles) and FWHM (blue bounding lines) for the transverse and longitudinal excitations across the phase transition. Here thermal effects are significant; the high levels of thermal damping leads to the increased FWHM and the significant difference in DHO and real excitation energies.

The changes in FWHM across the phase boundary are presented in Figure 4.22 [b]

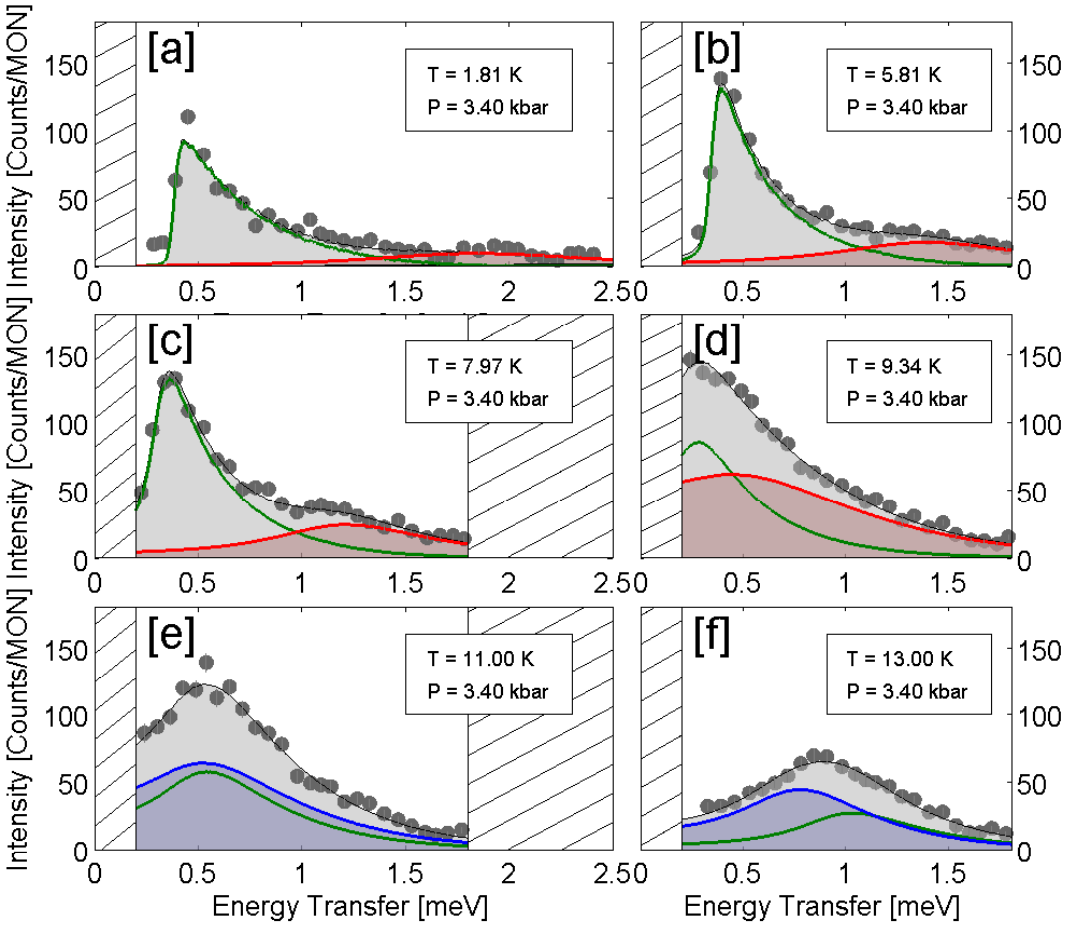

Figure 4.20: Fitted INS intensity at $\vec{Q}$ = (0 4 0) r.l.u. at P = 3.40 kbar for several temperature values. **[a]** T = 1.81 K, **[b]** T = 5.81 K, **[c]** T = 7.97 K, **[d]** T = 9.34 K, **[e]** = 11.00 K, **[f]** T = 13.00 K. Panels [a] - [d] demonstrate the reduction in energy of the longitudinal mode (denoted by the red shaded area), with a significant increase in the spectral intensity at T = 9.34 K. The transverse excitation (green line) remains gapped at $\Delta E \sim 0.4$ meV for low T, but demonstrates a slight reduction in energy as the temperature approaches T_N. Panels [d] - [e] demonstrate the emergence of the singlet-triplet excitations for $T > T_N$, where both the longitudinal (blue) and transverse (green) modes undergo significant thermal damping and upward shift in excitation energy.

for the longitudinal mode and the transverse mode as blue triangles and black squares respectively. The transverse mode, narrow in energy at low T, begins to broaden for temperatures just below the critical value. Conversely, the broad longitudinal mode narrows with increasing T. In Figure 4.22 [a] the effective pressure is included for completeness.

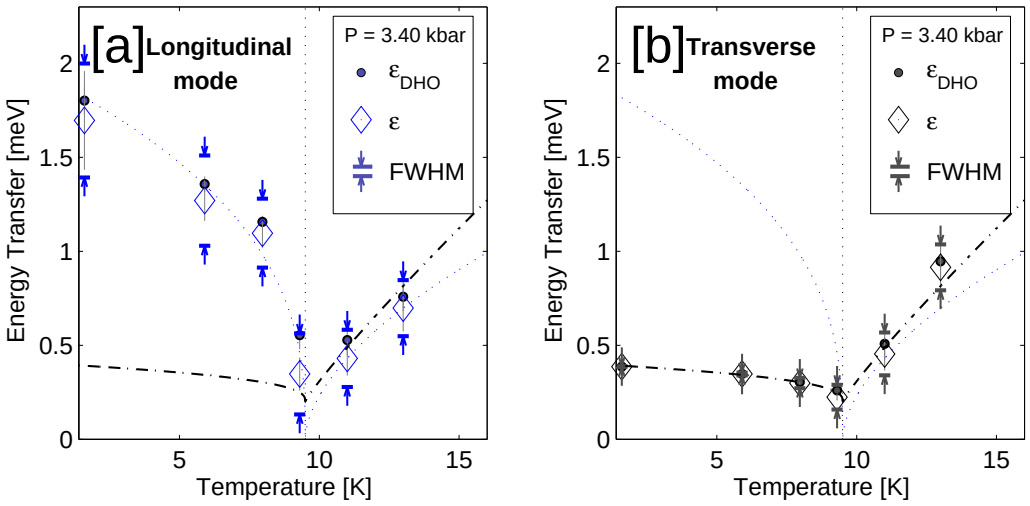

Figure 4.21: The excitation energies of the longitudinal and transverse excitations across the temperature-driven phase transition at finite pressure, $P = 3.40$ kbar. **[a]** The properties of the longitudinal excitation. **[b]** The properties of the transverse excitation. The damped harmonic oscillator energies (ϵ_{DHO}) given by the small circles, the extracted real excitation energies (ϵ) given by the open diamonds, the FWHM of the excitation given by the bounding arrows centered on ϵ. The blue dashed line is a power law fit to the real excitation energies, and the black dashed line is the fitted power law to the transverse excitation.

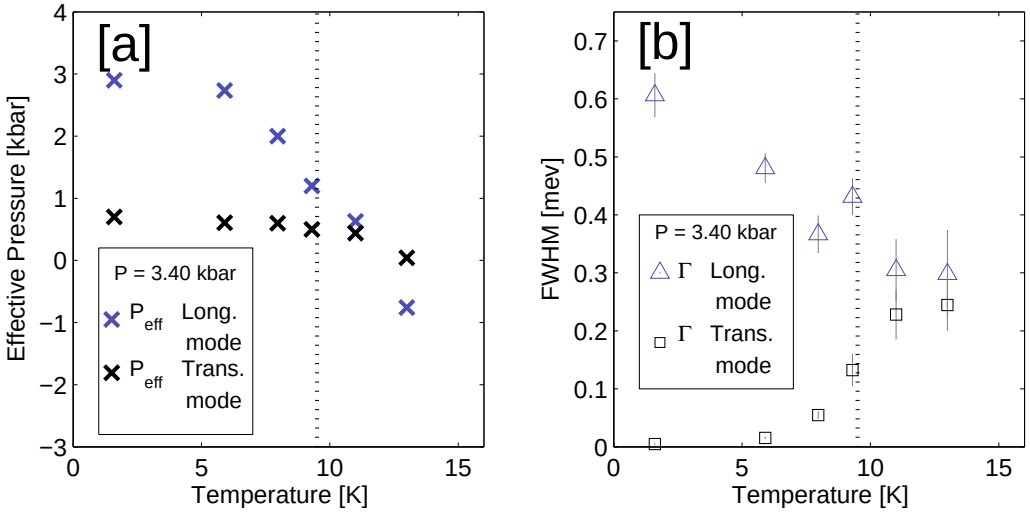

Figure 4.22: The effective pressure and FWHM of the longitudinal and transverse excitations across the temperature-driven phase transition at finite pressure $P = 3.40$ kbar. **[a]** Effective pressure P_{eff} for longitudinal and transverse excitations. **[b]** FWHM (Γ) for longitudinal and transverse excitations.

4.5.4 'Critical Scattering', P = 1.05 kbar

The evolution of the spin dynamics for finite T at $P = P_c$ was observed, where the system was fixed at the set pressure and the temperature was regulated with a cryostat.

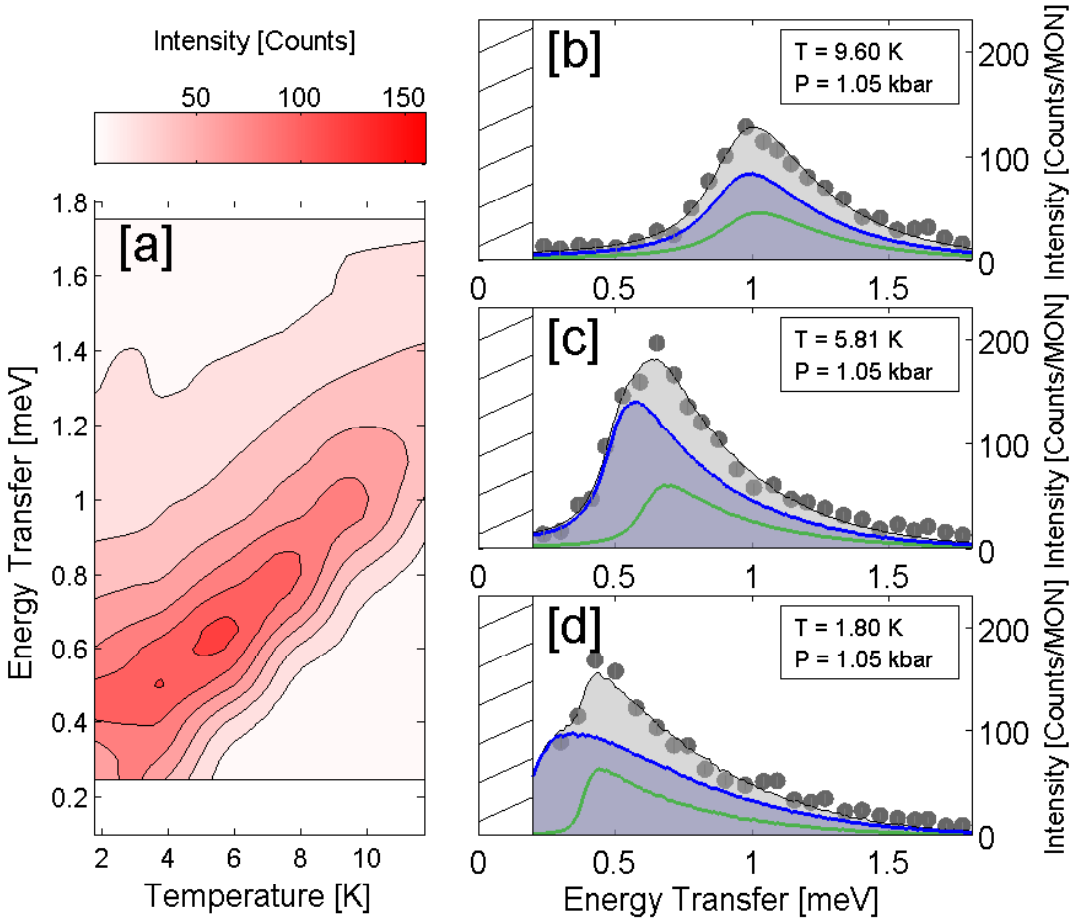

Figure 4.23: Properties of excitations at the critical point, $P = 1.05$ kbar, as a function of temperature. [**a**] Contour plot of the collected $P = 1.05$ kbar data. [**b**] Fitted INS data, for $T = 9.60$ K, [**c**] Fitted INS data, for $T = 5.81$ K, [**d**] Fitted INS data, for $T = 1.80$ K. Panels [b] - [d] illustrate the evolution of the gapped triplet mode in increasing temperature. The gap energy increases when heated as with the case for ambient pressure, also demonstrating an increase in FWHM with increasing temperature.

The data is given in Figure 4.23 [a].

In the picture of spin-spin correlations, the critical point can be described by a point of divergent correlations, and any fluctuations of the system can affect the static and dynamical properties at large length scales. For the case of 1-D systems, this survives up to finite temperature, resulting in the 'fan'-like quantum critical region in Figure 1.2. In the QD phase of $TlCuCl_3$ the quantum fluctuations are between coherent singlet and triplet states; due to low interdimer correlations the effect of a fluctuation on one dimer site on distant dimer sites is therefore negligible and the effects manifest only as coherent triplet exciations.

The QCP separates the QD phase with the RC-AFM phase of long-range order. It is at this QCP that the effect of quantum critical fluctuations are thought to be

greatest, and as such motivated the collection of high-resolution INS scans at this point to investigate the temperature behaviour of the excitations at the critical point and if this 3-D system remains gapless up to higher temperatures, exhibiting a quantum critical regime.

Figure 4.23 [a] shows the contour plot for the case of $P = 1.05$ kbar, which is within error of the critical pressure P_c. The data was collected up to 1.8 meV for 1.8 K $< T <$ 9.6 K. As with the other scans, background subtraction was performed and low energy data ($\Delta E < 0.2$ meV) was discounted. The fitted contributions from the dispersive triplet excitations are shown in Figure 4.23, panels [b] - [d], given by the blue shaded area and the solid green line. The data clearly demonstrates the reopening of the gap upon increase in temperature.

Figure 4.24 and Figure 4.25 give the extracted properties of the excitations for all measured T at $P = 1.05$ kbar. Figure 4.24 presents the longitudinal and transverse excitations. The excitation energy is observed to increase as the temperature increases, a result consistent with the results from lower pressure; the DHO renormalisation is small. The FWHM is also noted to increase as the temperature increases, as seen in Figure 4.25 [b]. The effective pressure is shown in Figure 4.24 [a] for completeness.

4.6 Excitations

4.6.1 Excitation Energies

An interesting result is the persistence of scattering intensity from amplitude fluctuations up to finite temperature. The collected evolution in temperature and pressure of this mode and the transverse mode are presented in Figure 4.26.

Figure 4.26 [a] shows the evolution of the mode gaps over the full range of pressures for $T = 1.8$ K, which represents the QPT (the data presented in Ref. [78] and summarised in 3.3.3), and for $T = 5.81$ K. The longitudinal mode of the ordered phase, represented in red, appears on the right, and soften with decreasing pressure until $P_c(T)$. The Goldstone mode in this regime is not visible due to the scattering geometry. At pressures below P_c, the (added) effect of quantum fluctuations is strong enough to "melt" the magnetic order, and all modes are gapped: the blue symbols represent the increasing gap of the lowest-lying excitation. The transverse mode shown by the black symbols is the anisotropic spin wave, whose gap remains at approximately 0.4 meV across the RC phase. The dashed lines are best fits to power laws, which will be discussed in the next section.

Figure 4.26 [b] shows the evolution of the mode gaps over the range of temperatures 1.8 K $< T <$ 14 K for pressures $P = 1.75$ kbar and $P = 3.4$ kbar. Here the ordered phase

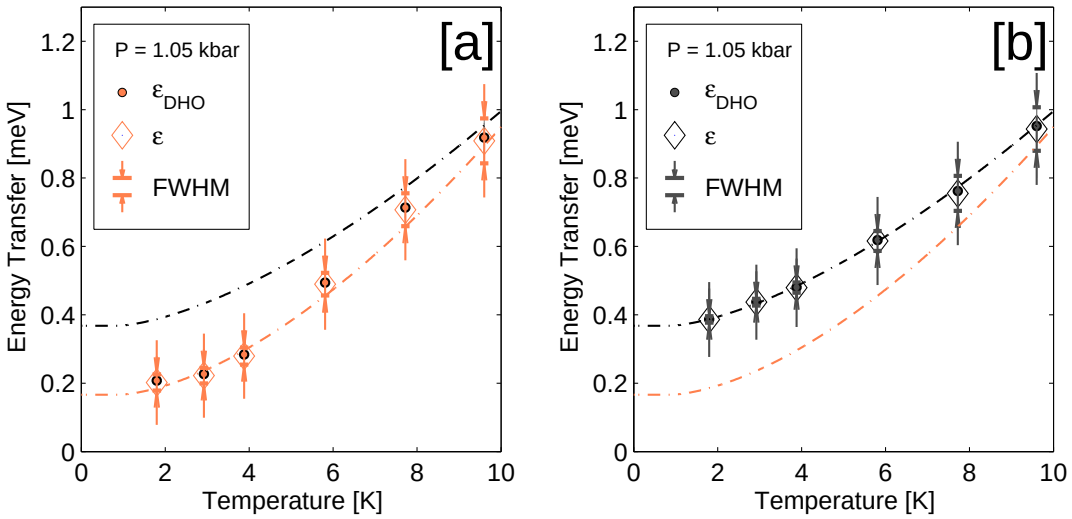

Figure 4.24: The excitation energies of the longitudinal and transverse spin excitations for increasing temperature at $P = 1.05$ kbar. **[a]** The properties of the longitudinal excitation. **[b]** The properties of the transverse excitation. The damped harmonic oscillator energies (ϵ_{DHO}) are given by the small circles, the extracted real excitation energies (ϵ) given by the open diamonds, the FWHM of the excitation given by the bounding arrows centered on ϵ. The orange dashed line is a power law fit to the real excitation energies, and the black dashed line is the fitted power law to the transverse excitation.

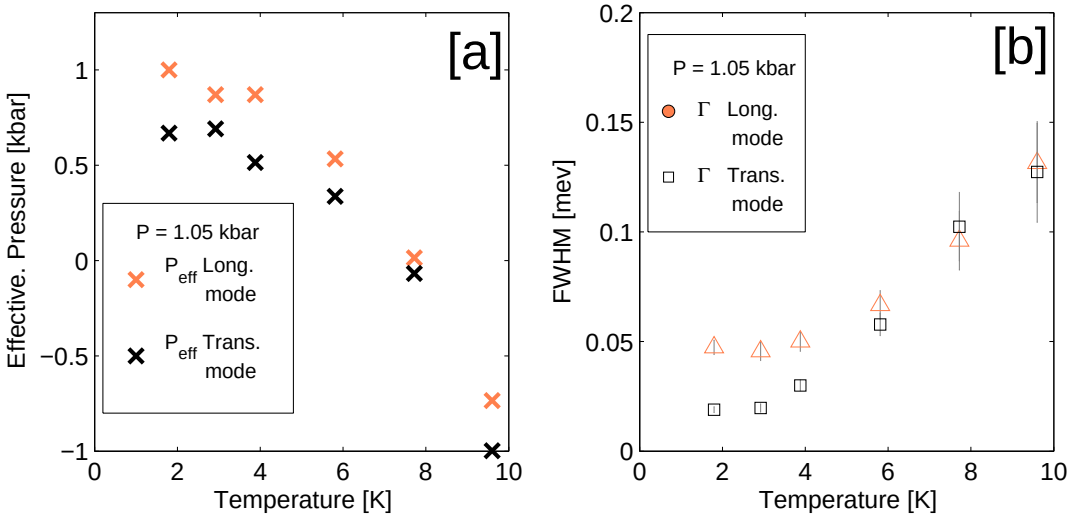

Figure 4.25: The effective pressure and FWHM of the longitudinal and transverse excitations for increasing temperature at $P = 1.05$ kbar. **[a]** Effective pressure P_{eff} for the transverse and longitudinal excitations. **[b]** The FWHM of the longitudinal and transverse excitations

is on the left, and the longitudinal mode, shown again in red, becomes soft at $T_N(P)$ determined by the applied pressure. Once again the Goldstone mode is not visible, and the black data points show the anisotropic spin wave, whose gap is essentially independent of temperature except for some small effects near T_N at $P = 3.4$ kbar.

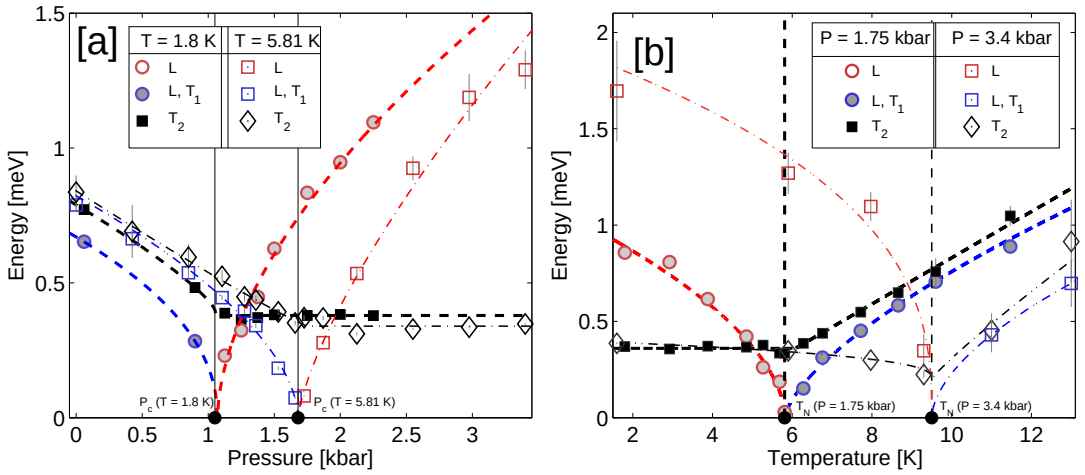

Figure 4.26: The excitation energies in $TlCuCl_3$ across pressure-driven and temperature-driven phase transitions. **[a]** The pressure-driven phase transition. **[b]** The temperature-driven phase transition. The energies of triplet excitations for two different temperatures ($T = 1.8$ K and $T = 5.81$ K) are shown in [a], as the system undergoes 'quantum melting' of magnetic order. Melting occurs from right to left: On the right is the ordered phase with one longitudinal mode, while at left is the disordered phase with three gapped modes (two shown). The energies for two different pressures ($P = 1.75$ kbar and 3.4 kbar) are shown in [b], as the system undergoes 'thermal melting' of magnetic order. Melting occurs from left to right: at left is the RC-phase while at right is the disordered, QD phase. Black squares and open diamonds give the energies of the transverse excitations, while circles and open squares show the longitudinal mode (red in the ordered phase, blue in the disordered one). Dashed lines are power law fits, as described in the text.

Although this has some parallels to the case of classical Néel order, where the spin wave energy is renormalised due to decreasing lifetime [89], the low energy scattering at this critical point remains dominated by the reduction of the longitudinal mode gap. Again, the longitudinal mode evolves continuously into one triplet excitation of the disordered phase, shown in blue, but here it is essential to note that the origin of the disorder lies in a combination of thermal and quantum fluctuations rather than quantum fluctuations alone. The dashed lines in this case are best fits to power laws, which will also be discussed in the next section.

4.6.2 Longitudinal Mode Dynamics

Further properties of the longitudinal mode can be deduced from information additional to its energy, as presented in §4.5 and summarised in Figure 4.27 and Figure 4.28.

Figure 4.27 illustrates the longitudinal mode spectral intensity as a function of pressure and temperature for the two types of phase transition. In this context in all cases the nature of the mode is identical; there is a large increase in spectral intensity

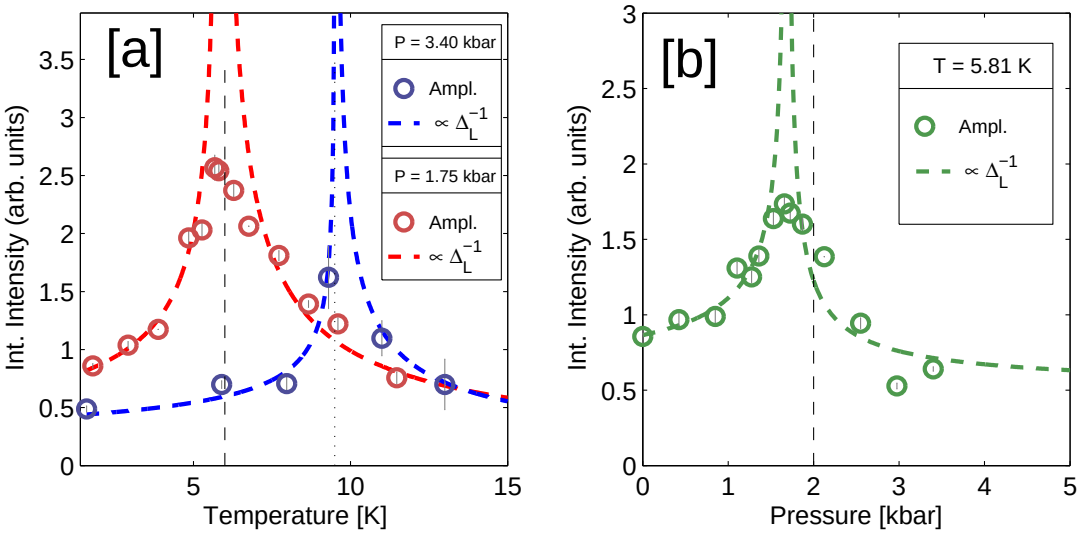

Figure 4.27: Integrated intensity of the longitudinal mode across the (P, T) phase diagram. **[a]** The integrated scattering intensity contribution of the longitudinal mode for the cases of 'thermal melting' at $P = 1.75$ kbar (red circles) and $P = 3.40$ kbar (blue circles). **[b]** The integrated scattering intensity for the case of finite T (= 5.81 K) 'quantum melting'. These factors are proportional to the inverse gap energy, which is plotted in each case as dashed lines to serve as a guide to the eye.

as the critical point is approached, indicating a large scattering cross-section at the critical point. This follows the same dependence on the gap energy as seen in the pressure-driven phase transition at $T = 1.81$ K, namely $I_N \propto 1/\epsilon$. This dependence is included in the figure for each case as dashed lines for a guide to the eye.

Figure 4.28 summarises the ratio of the FWHM to the excitation energy, $R = \Gamma/\epsilon_{DHO}$, and is presented to illustrate the stability of the longitudinal mode in the observed pressure-temperature region. $R_{[T=1.8K]}$ is the ratio for the excitation across the quantum phase transition, and is presented in Figure 4.28 [a] alongside the ratio for $T = 5.81$ K, $R_{[T=5.81K]}$. $R_{[T=1.8K]}$ possesses a small value for pressures $P < P_c$, with an increase to about 10% relative width above P_c with no divergence at the critical point. The FWHM and excitation energy reduce with exactly the same pressure dependence, barring a prefactor. As such, the mode is *critically damped* and it is well defined across the phase transition; the lack of divergence at the critical point indicates that critical fluctuations do not cause significant damping of the excitation.

The ratio $R_{[T=5.81K]}$, along with the ratios $R_{[P=1.75\text{kbar}]}$ and $R_{[P=3.40\text{kbar}]}$ presented in Figure 4.28 [b] do not share this behaviour. They all show a divergence as the critical point is approached, but settling to a constant value above/below the critical point. This indicates that as the energy approaches zero, there is significant damping and that they are therefore short-lived at the critical temperature $T_N \neq 0$. This is also

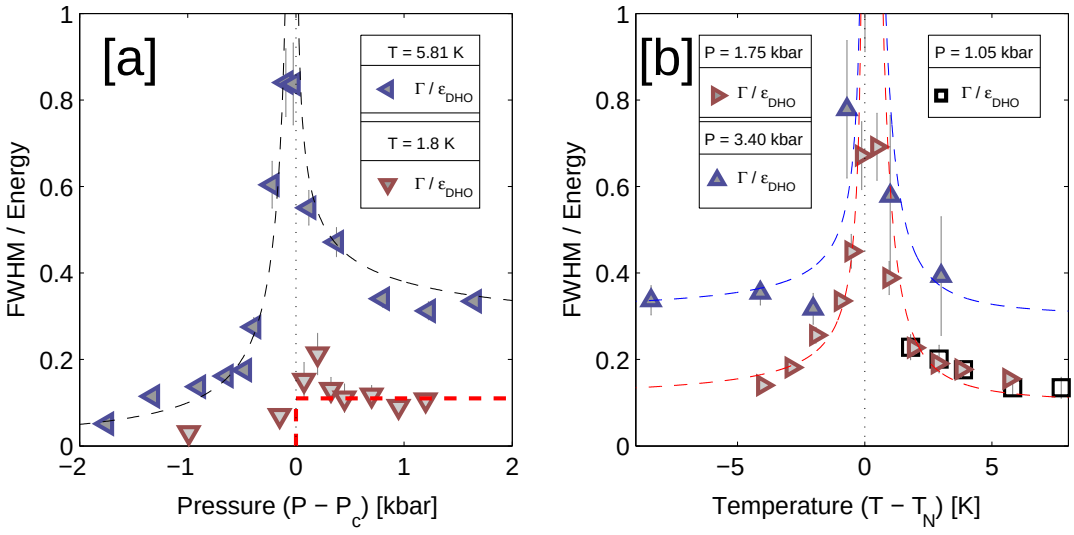

Figure 4.28: Relative linewidth (lifetime), $R = \Gamma/\epsilon_{DHO}$, of the longitudinal mode. **[a]** $R_{[T=1.8\text{K}]}$ (red triangles) and $R_{[T=5.81\text{K}]}$ (blue triangles). **[b]** $R_{[P=1.05\text{kbar}]}$ (black squares), $R_{[P=1.75\text{kbar}]}$ (red triangles) and $R_{[P=3.40\text{kbar}]}$ (blue triangles).

seen to be the case for 'quantum melting' at $T = 5.81$ K, as shown in Figure 4.28 [a] by the blue triangles; the divergence of $\Gamma_Q/\epsilon_{DHO}(Q)$ at P_c shows that the longitudinal mode is no longer well defined in the presence of thermal fluctuations.

4.7 Discussion

The following section discusses the key results of the experimental work. First, the longitudinal mode excitations across the phase boundary will be discussed in context of the fitted critical exponents, then the validity of the self-consistent mean field theory used to describe the zero pressure data [34] will be discussed for finite temperature, assuming different models for the pressure-dependent exchange interactions. Inferences are made about the nature of the longitudinal excitation, its stability up to higher temperatures and the role played by quantum and thermal fluctuations in the region near the QCP.

4.7.1 Excitations across the P-T phase boundary

The principal result is the continued observation of the longitudinal mode throughout the phase diagram. This was not a forgone conclusion; it was unclear from the low-T pressure-dependent experiments as to the temperature stability of this mode and its behaviour across T_N. Longitudinal modes have been observed in some quasi-one-dimensional (1D) quantum spin systems where the ordered ground state lies close to

a QCP, including the $S = 1/2$ chains $BaCu_2Si_2O_7$ [90] and $KCuF_3$ [91], and the $S = 1$ chains $RbNiCl_3$ [92] and $CsNiCl_3$ [93], and the stability of the mode has been called into question as it could decay into spin waves [78]. The observed longitudinal mode as a stable excitation to finite T throughout the RC-AFM phase is a unique result and indicative of the temperature dynamics of quantum spin dimer systems with three dimensional exchange geometry.

Some qualitative observations can be immediately made from behaviour of the excitation energies of the longitudinal and transverse modes presented in §4.5 and summarised in Figure 4.26. In the case of a 'classical' antiferromagnet, the melting of staggered order is due to thermal population of transverse spin waves, with a lack of any longitudinal excitation. It is possible that an approximation to the classical case can be achieved in $TlCuCl_3$ for very high pressures, where the intradimer terms are much greater greater than the interdimer terms and the moment is fully saturated. The large ordered moment means any kind of amplitude fluctuations require a large amount of energy, and have a short lifetime due to high probability of decay into spin waves and the mechanism for the phase transition would be that of the classical case. The phase diagram under consideration would then be an intermediary between the classical and quantum case where the nature of the excitations and phase transition are characterised by the amplitude fluctuations.

The observation of the continuous reduction of the longitudinal mode to zero energy is a significant result, as it implies that amplitude fluctuations play an important role up to finite temperatures and near the phase boundary, even in the case for applied pressure where the mode demonstrates a high level of damping. As such the thermal population of not only transverse spin waves (as in the classical case), but also of longitudinal (amplitude) fluctuations contribute to the melting of magnetic order at the phase boundary.

This is supported by the behaviour of the transverse excitation under application of temperature. If the phase transition were that of the classical picture and the ordered moment is reduced by population of transverse spin fluctuations only, an anisotropically gapped transverse mode would reduce in energy approaching the phase boundary. While a slight downward trend is observable for the higher pressure case $P = 3.4$ kbar, the phase transition is still dominated by the softening of the longitudinal triplet mode. As such we may conclude that the longitudinal fluctuations are key excitations within the system in the examined pressure-temperature range and are responsible for driving the phase transition through the melting of the magnetic order.

The longitudinal mode dynamics are summarised in Figure 4.29, with critical exponents extracted from fits to power laws, where a simultaneous fit was performed

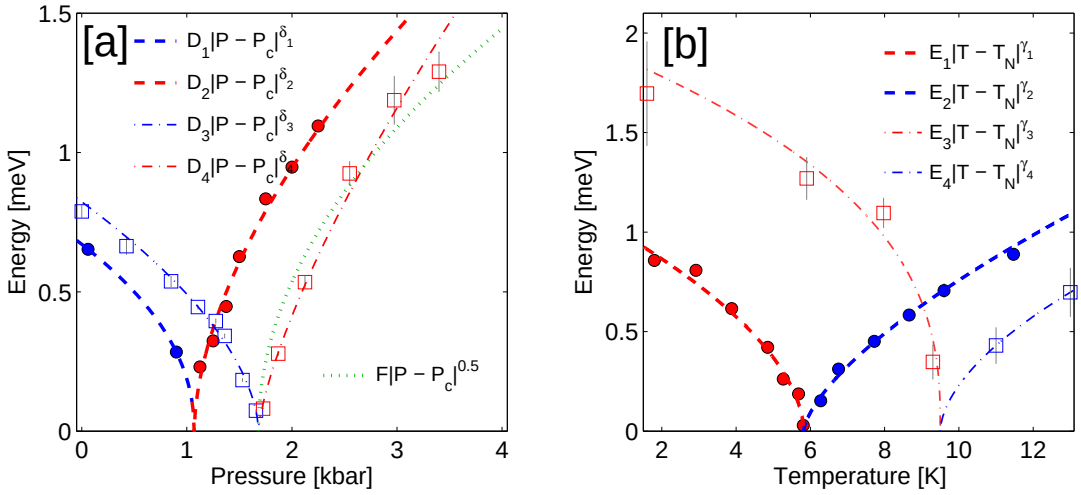

Figure 4.29: The longitudinal mode excitations presented in Figure 4.26, alongside fitted power laws. **[a]** The P-driven transitions for $T = 1.8$ K and $T = 5.81$ K, fitted to Energy = [prefactor]$(P - P_C)^{[\text{exponent}]}$. **[b]** The T-driven transitions for $P = 1.75$ kbar and $P = 3.40$ kbar, fitted to Energy = [prefactor]$(T - T_N)^{[\text{exponent}]}$. Prefactors and exponents are presented in Table 4.5

Parameter	Prefactor	Value	Exponent	Value
$P = 1.75$ kbar	E_1	0.4167 ± 0.0322	γ_1	0.5410 ± 0.0803
	E_2	0.2890 ± 0.0252	γ_2	0.6736 ± 0.0897
$P = 3.40$ kbar	E_3	0.8375 ± 0.1530	γ_3	0.3747 ± 0.1544
	E_4	$0.57 \pm$ N/A	γ_4	$0.34 \pm$ N/A
$T = 1.8$ K	D_1	0.6494 ± 0.018	δ_1	0.4675 ± 0.0575
	D_2	0.9849 ± 0.050	δ_2	0.5741 ± 0.0565
$T = 5.81$ K	D_3	0.5574 ± 0.0217	δ_3	0.5704 ± 0.0552
	D_4	0.8426 ± 0.0697	δ_4	0.7272 ± 0.0756

Table 4.5: Power-law exponents for the (P, T) phase transitions shown in Figure 4.29. There is no error quoted on the parameters E_4 and γ_4 as these parameters cannot be fitted due to insufficient datapoints. An estimate taken by observation has been included for completeness.

of the excitation energies above and below the critical temperature/pressure. The value of the critical temperature/pressure was also relaxed. The exponents and prefactors are as given in the figure and presented in Table 4.5. Assuming the case for independent quantum and thermal fluctuations, the power law description across the pressure-tuned phase transition should be independent of T. This is not seen to be the case, with the $T = 5.81$ K exponent $\delta_4 = 0.72 \pm 0.08 > \Phi = 0.5 \pm 0.1$ (where Φ is the value presented in Figure 4.5 and Ref. [78]). The dashed green line in Figure 4.29

[a] is an attempted fit of the $T = 5.81$ K data, constraining $\delta_4 = 0.5$. Furthermore, comparing the power law with $\Phi = 0.5$ (that describes the spin gap across the QPT) to the pressure dependence of the magnetisation, $M_{XY} \propto (P - P_c)^{0.5}$, the magnetisation dependence of the spin gap can be inferred to be approximately linear. Under temperature renormalisation, the spin gap would then be expected to follow Energy = [prefactor]$|T - T_N|^{\beta}$, where $\beta = 0.367$, that of a classical Heisenberg 3-D system [2]. The fitted exponent $\gamma_1 = 0.54 \pm 0.08$ does not match this value; indeed, it is much closer to the value expected from the result of a mean-field theory, $\beta = 0.5$. The mean-field exponent is one expected when the system is at or above the upper critical dimension. Thus the observed exponent is not expected for a classical system (where temperature lowers the dimensionality), but rather is expected from a system exhibiting quantum critical behaviour. Thus, the observation of the β (temperature) exponent having the mean-field value indicates that the interplay of quantum and thermal fluctuations is appreciable and significant.

4.7.2 MFBO at finite Pressure and Temperature

An adapted MFBO theory has been successfully implemented in §4.5, utilising a paramaterisation through effective pressure to simulate the triplet band at higher temperatures. The variation of the band width is contained in the effective pressure term, which can be varied independently of the spin gap. These two parameters combined contain all allowed variations of J, J_2, J_3 without a definitive analytical model specified for their variation beyond the reduced ansatz provided. It must be made clear that these parameters are varied in response to the data to reproduce the spin gap and ensure an accurate fit; the MFBO expressions are therefore an adaption of the current theory and in no way descriptive of the pressure dependent exchange parameters. The precise variation of J, J_2, J_3 in pressure is not implicit and multiple models can be realised that produce the observed phase transition.

It is desirable to formulate a model that reproduces the observed excitation energies extracted from the fitted data. The method for doing so is outlined in Ref. [34], where an effective partition function describing the thermal occupation of hard-core bosons can be obtained by enforcing the local constraint (Equation 3.2) at the global level. The comparison was made to INS data collected at $\vec{Q} = [0\ 0\ 1]$ and $[0\ 4\ 0]$ r.l.u. for the case of a conventional Bose occupation factor, and an ansatz formulated from Quantum Monte Carlo (QMC) and Quantum Transfer Methods (QTM) [50], referred

to as the Troyer-Tsunetsugu-Würtz (TTW) ansatz and given by

$$n(E_\alpha(\vec{Q}),\beta) = \frac{e^{-\beta E_\alpha(\vec{Q})}}{\frac{1}{N}\sum_{\vec{Q}}\sum_{\alpha} e^{-\beta E_\alpha(\vec{Q})}}, \tag{4.6}$$

where α denotes the triplet modes and β is the inverse temperature. It was found that the TTW ansatz reproduced the data with great success and succeeded in modeling the spin gap up to higher temperatures with a greater level of accuracy than the conventional occupation function. The extension to finite pressure once again requires the formulation of an ansatz for the pressure-dependence of the exchange interactions. The results from the assumption of different models are outlined below.

4.7.3 Pressure-dependence of the exchange interactions

Motivated by observations from magnetoelastic coupling [94], sound attenuation studies [95] and qualitative structural arguments, a model for the changing exchange interactions was taken in Ref. [78] such that the intradimer exchange J and the interdimer exchange J_2 change only, with

$$\begin{aligned} J(P) &= J(1 + A_0 P + B_0 P^2) \\ J_2(P) &= J_2(1 + A_2 P + B_2 P^2) \end{aligned} \tag{4.7}$$

where P is the hydrostatic pressure, $A_2 = -A_0 = 0.0066$ kbar^{-1} and $B_2 = -B_0 = 0.00109$ kbar^{-2} resulting in a scheme where $J(J_2)$ decreases(increases) with the same pressure dependence. This model reproduces the experimentally measured spin gap energies and the critical pressure at $T = 1.8$ K.

However, this formalism was taken without finite temperature data and while consistent with previous arguments on the exchange interaction pressure-dependence it is by no means unique. Multiple models for the pressure dependence of the exchange interactions for the minimal model given in Equation 4.7 can be effectively employed that (i) satisfy the condition that the longitudinal mode energy $\mathrm{E}_Q = 0$ (Equation 3.6) at $P = P_c = 1.07$ kbar and (ii) reproduce the pressure dependence of the longitudinal mode gap energies.

Taking the critical pressure, $P = P_c$, Equations 4.7 become $J(P_c) = J(1 + A_0 P_c + B_0 P_c^2)$ and $J_2(P_c) = J_2(1 + A_2 P_c + B_2 P_c)$, simplified to $J(P_c) = J(1 + C_0 P_c)$ and $J_2(P_c) = J(1 + C_2 P_c)$.

The pressure prefactors A and B can be derived for a more general model for $J(P)$ and $J_2(P)$ by considering the case $A_2/A_0 = B_2/B_0 = \alpha$. Substituting the $J(P)$

and $J_2(P)$ terms into Equation 3.6 with this constraint and solving for $E_Q = 0$, the prefactors can be calculated for a given P_c as

$$C_0(\alpha) = \frac{(J_2 + 2J_3 + J_1 - J)}{(J - \alpha J_2 P_c)}, \tag{4.8}$$

where $C_0 = A_0 + B_0 P_c = C_2/\alpha$ and the exchange parameters given are for $P = 0$ kbar. The C_0 values can be calculated in a straightforward manner as the zero pressure exchange interactions are known, but degenerate solutions exist for A_0 and B_0. A linear model can be taken such that the quadratic terms are ignored and $A_0 = C_0$. This model is found to accurately reproduce the spin gap behaviour for low energy values, but shows a divergence at higher energies that is corrected by the quadratic term.

The plurality of solutions for each α value of $A_0(\alpha)$ and $B_0(\alpha)$ can be reduced with fitting to the experimentally measured longitudinal mode energy at $T = 1.8$ K, $P > P_c$, and the resulting pressure prefactors are given in Figure 4.30. Figure 4.30 [a] and [b] demonstrate the dependence of the pressure prefactors C_0, C_2, A_0, B_0, A_2 and B_2 for different models of the pressure dependence of the exchange interaction, with specific cases highlighted in [c - e].

Every fitted parameterisation of the pressure-dependent exchange interaction results in an excellent description of the longitudinal gap energy and as such it is clear that the problem is underconstrained when considering low temperature data, as the phase transition is determined by the gap reducing to zero and has no dependence on the bandwidth. By considering the high temperature data, the spin gap becomes coupled to the bandwidth and therefore creates the possibility of constraining the problem.

The calculated $T_N(P)$ values yielded from the finite temperature MFBO theory for different values of α are plotted in Figure 4.31, alongside the experimentally measured values (denoted by the black squares). It can be seen that for all the possible models of spin gap reduction, the experimental data is not reproduced, with the theoretical calculations producing nearly identical T_N near P_c for all considered models and the problem remains underconstrained.

The origin of the deviation for $P > P_c$ in Figure 4.31 is not clear. It is possible that a correction to the calculations may be made through application of logarithmic corrections to the scaling parameters. This would seemingly be inconsistent with the result of Ref. [97], where a universal T_N behaviour was observed with a linear correlation with m_s. In this picture, the quantum and thermal fluctuations are independent and logarithmic corrections would be negligible. However, a consequence of such a regime would be that the temperature exponent would be pressure-independent and

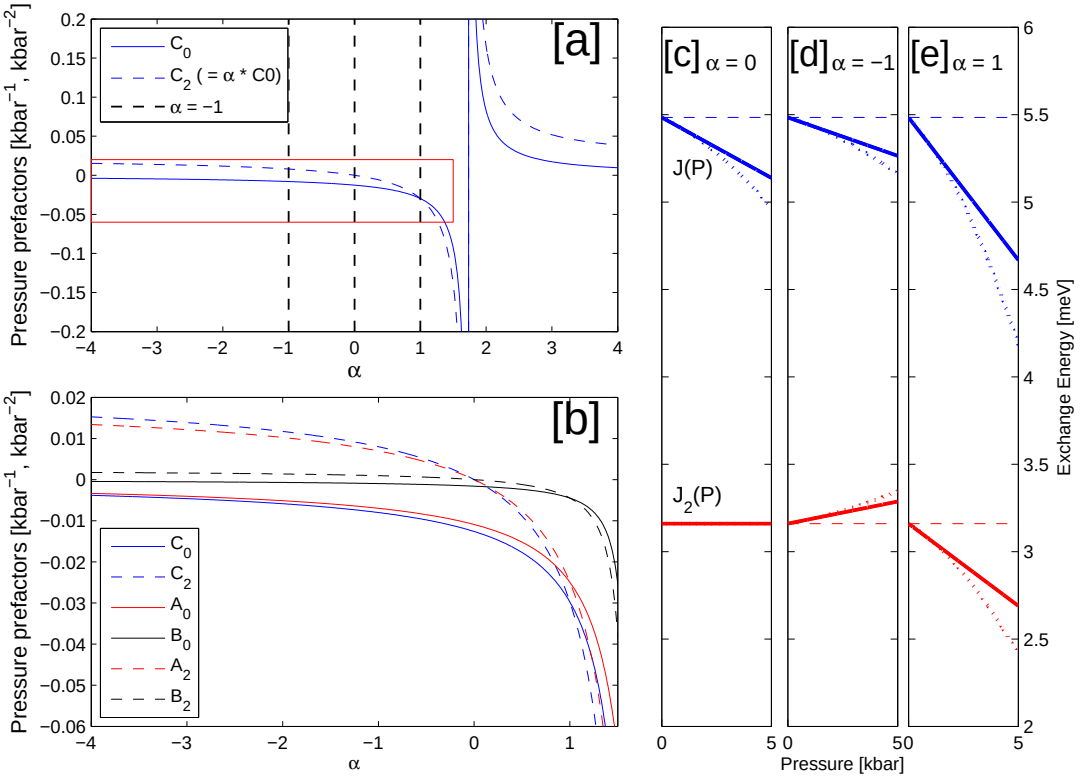

Figure 4.30: Models for exchange interaction pressure dependence. **[a]** Values for C_0 and C_2, where $C_2 = \alpha C_0$. **[b]** Expanded view of the red square in [a], showing the values for A_0, B_0, A_2 and B_2, calculated from fitting to the $T = 1.8$ K data. **[c]** $J(P)$ and $J_2(P)$ assuming $\alpha = 0$. **[d]** $J(P)$ and $J_2(P)$ assuming α = -1. **[e]** $J(P)$ and $J_2(P)$ assuming α = 2. In panels [c] - [e], dashed lines show the case for zero pressure dependence, the solid lines linear terms only and the dotted lines with quadratic terms included.

the pressure exponent would be temperature-independent. This is not observed, which would mean that either the data collected contradicts the result of Ref. [97], or that the extracted excitation energies are far from the region of criticality. The latter result would be a surprising occurrence, however, given the small magnetic moment in the region of the considered phase diagram and the persistence of the longitudinal mode. Further calculations and modeling on this system are therefore required to resolve this problem.

The importance of the interplay of quantum and thermal fluctuations can be inferred from the behaviour of the elementary excitations at the QCP and across the thermal phase transitions. In principle, the long-range correlations of the spins will diverge at the critical point, resulting in any fluctuations having significant long-range effects even up to finite temperature. Figure 4.28 [b] illustrates the small Γ/ϵ_{DHO} ratio for $P = 1.05$ kbar up to finite temperature. The value of this ratio does not suggest

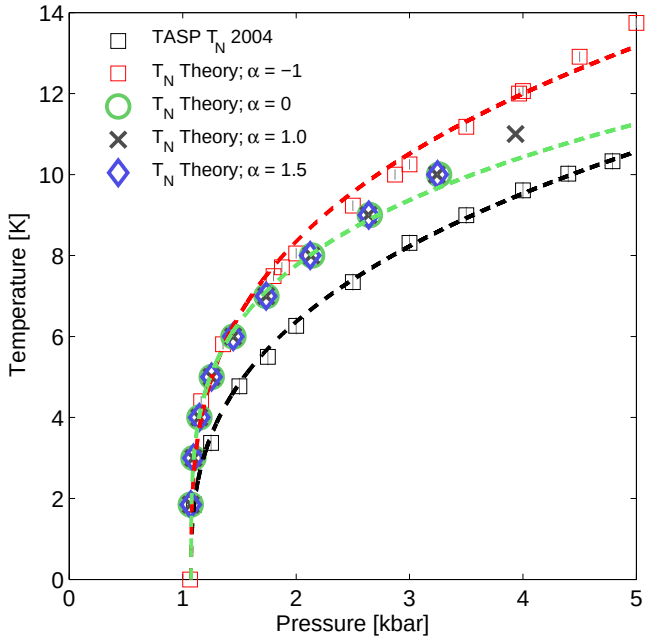

Figure 4.31: A comparison of the calculated T_N values, supplied by Ref. [96] utilising the finite temperature self-consistent MFBO for different models for the pressure dependence of the exchange interactions. The black squares are experimentally measured data from TASP, the rest are computational results as labeled.

any significant damping effects from the critical fluctuations and demonstrates the re-opening of the singlet-triplet gap. Coupled with the observation that the longitudinal mode is critically damped, this is suggestive that any present critical fluctuations do not significantly effect the dynamics of the system and if the quantum critical regime exists it would be confined to a narrow range around the phase boundary. While the system for $T > 0$ K, $P = P_c$ can be well described by the singlet-triplet picture, the contribution of increased quantum fluctuations could be manifest as log corrections to a temperature-adjusted mean field theory.

The effect of the inclusion of thermal fluctuations on the excitations is evidenced in the FWHM data presented in §4.5 and the ratios of FWHM to excitation energy shown in §4.6.2. For 'low' T (= 1.8 K), the ratio of the FWHM (Γ) to the excitation energy (ϵ_{DHO}) is a constant within the ordered phase, and remains so up to the critical point. For all other values of T, there is a divergence of the ratio at the phase boundary.

The critically damped nature survives up to higher temperature, but with an inclusion of a thermal damping term. As such, while for the highest pressure points the FWHM increases with the gap, the region near the critical point still possesses damping, leading to the divergence of $R_{[T=5.81\text{K}]}$ at T_N.

An effective field theory has been formulated by Kulik ad Sushkov [98] that well describes the longitudinal width for the quantum phase transition, demonstrating that

$\Gamma \propto \Delta_L$, through consideration of the mechanism of decay into fluctuations of the condensate field and transverse magnon fields. As such, the longitudinal mode is critically damped near the QCP in the pressure-induced ordered phase. The results given indicate a departure from this behaviour upon application of temperature, and the mode widths are seen to diverge upon approaching the phase transition. The dynamics of the longitudinal mode are therefore no longer well described by the result of the effective field theory.

This disparity is a consistent result, however. The Landau-Ginzburg (MF) theory is robust when the system lies in or above the upper critical dimension [99]; in this case, the effective field theory was formulated for a quantum system at "$T = 0$K", so the dimension of the system is $d = 3 + 1$ - three spatial dimensions plus the time dimension - which indeed equates to the upper critical dimension of $TlCuCl_3$. Upon the application of temperature, the dimensionality is reduced to $d = 3$ [99, 100], and the system therefore resides below the upper critical dimension. The results of the effective field theory no longer apply, and there is no reason to expect the longitudinal mode width to follow the same gap dependence in this case.

Despite its damped nature at higher temperatures near the phase boundary, the mode remains observeable within the RC-AFM phase. This is a result of unique structural and magnetic ordering features found in $TlCuCl_3$, such as the appreciable 3-D coupling leading to higher-dimensional spin correlations. Because of this high dimensionality, the system has an extended phase space, resulting in a smaller damping term as a consequence of quantum and thermal fluctuations.

The high dimensionality also contributes toward the restricted phase space for magnon scattering found in $TlCuCl_3$. The magnon-magnon interaction terms in the scattering cross section, which also create the two-magnon continuum, are appreciably small in $TlCuCl_3$. When the quasi-particle dispersion overlaps with two-particle continuum, there is destructive interference, resulting in a transfer of spectral weight and a decrease in the mode lifetime [101]. In $TlCuCl_3$, the continuum band is placed higher in energy than the low-lying single magnon excitations and their overlap is minimal; the effect on observed damping less significant than in lower-dimensional systems.

Furthermore, the coherence of a longitudinal mode is favoured by the collinearity of the spin order within $TlCuCl_3$. For non-collinear spins, a longitudinal excitation when viewed from the co-ordinate system of any adjacent spins will have a finite transverse component (entirely transverse for a spin oriented at 90° to the excitation). This results in an increased probability for decay into a transverse spin mode channel.

For a collinear system, however, a longitudinal excitation on one spin site would appear as a longitudinal fluctuation on all neighbouring spin sites and as such have a

smaller probability of decay into a transverse mode. The probability is further reduced by the large spectral weight observed in the transverse spin modes.

As such we can conclude that the longitudinal fluctuation within $TlCuCl_3$ exists as a critically damped but stable excitation of the system for 'low' T, observeable up to finite T and is a direct consequence of quantum critical dynamics.

Summary

$TlCuCl_3$ is a quantum spin dimer system that exhibits a pressure-driven phase transition into a region of renormalised classical antiferromagnetic order. The principal excitations of $TlCuCl_3$ have been investigated with inelastic neutron scattering techniques to compare the properties of the temperature-driven phase transition and the pressure-driven phase transition.

- Scattering intensity from the longitudinal excitation persists in the ordered phase for all investigated pressures and temperatures.
- Similarities are observed between the case of the pressure-driven phase transition and temperature-driven phase transition, notability the observation of a reduction of the longitudinal excitation energy and increased spectral weight at the phase boundary.
- The persistent reduction of the longitudinal mode energy implies that the temperature-driven phase transition is driven by population of both transverse and longitudinal excitations.
- The critical exponents for the temperature-driven phase transition deviate from that of a 3D Heisenberg antiferromagnet, indicating the importance of quantum effects.
- The longitudinal mode is a result of quantum effects, indicated lack of stability at the phase boundary, except for the region near the quantum critical point (i.e. at the lowest measured temperature $T = 1.8$ K).

Additional theoretical work is needed to effectively model the observed excitations and account for the phase boundary. In particular, a self-consistent mean-field bond operator theory or quantum corrections to the existing theory must be formulated to explain the interplay between thermal and quantum fluctuations in the vicinity of the quantum critical point.

5

$BiCu_2PO_6$ - Excitations and Interactions in a Frustrated Quantum Spin Ladder

This chapter will detail studies of the dynamical effects in the quasi-1-dimensional quantum spin ladder $BiCu_2PO_6$, as introduced in §1.2. The experimental work comprises the first neutron scattering experiments to be performed on single crystals of this compound. These are analysed in order to investigate the dynamical magnetic properties of the quantum disordered ground state and as such deduce the system Hamiltonian and exchange interactions.

The properties of $BiCu_2PO_6$ will be summarised, alongside a review of relevant background material. The experimental data for the INS studies will be summarised, fitted and presented alongside attempts to explain the dispersion with the theory of excitations presented in §3.3. Studies in applied magnetic field are also included in an attempt to distinguish the nature of individual excitations and exchange anisotropy, and discussion of the fitted excitations will be outlined alongside an outlook for future experimental work.

The work presented in this chapter presents a significant advance on the previous level of understanding of this frustrated spin ladder system. In particular, progress has been made toward understanding the magnetic excitations in the system, possible sources of aniosotropy and the nature of the exchange geometry. However, the studies and analysis presented do not constitute a complete solution to the questions and problems presented by this unique ladder system; results from the INS studies contain many features to which a final solution is and will continue to be a challenging problem.

This chapter therefore seeks to present possible solutions that best describe all the data collected in a consistent fashion in the context of current understanding that

serves as a guide to future experimental and theoretical work.

5.1 Background

The ground state of an isolated spin-1/2 Heisenberg two-leg ladder exhibits no long-range order due to the low dimensionality of the exchange geometry. This state exists with no classical analogue, and is a result of quantum fluctuations. The excitations from the quantum-disordered ground state correspond to spin fluctuations on the ladder geometry, with dispersion of the fluctuations dictated by the ratio of the leg and rung exchange terms, and the overall strength of intra- and inter-ladder coupling.

Considering the geometry for the typical two-leg spin ladder such as that seen in the proto-typical compound $(C_5H_{12}N)_2CuBr_4$ [102, 103], the ground state corresponds to the formation of short-range bonding of spin pairs into singlet states, which may fluctuate over nearby lattice sites. This is a realisation of a resonating valence bond (RVB) state [104], where the fluctuating singlet bonds can take multiple orientations [105], but are largely dictated by the relative strength of the leg and rung couplings. In the case for $J_R > J_L$, the singlet states are taken to predominantly form on the rungs, resulting in the formation of a 'rung singlet' (RS) state.

For negligible inter-ladder exchange, the correlations are confined within one ladder unit and the exchange geometry is that of spin dimer units coupled predominantly along one direction and can be considered as 'quasi-one-dimensional'. The coupling to additional dimer units across one or more 'leg' exchange interactions can extend the geometry up to multiple chains to form a ladder, with odd-leg ladders exhibiting a gapless spectrum and gapped spectrum for even-legged ladders [106]. The ladders then describe an intermediate geometry between the 1-D system described by a single chain and the 2-D square lattice geometry described by many such chains.

The excitations of the RS ground state of two-legged ladder systems correspond to triplet excitations of coupled spins, that can propagate within and between ladder structures. Taking this bond excitation approach, the spectrum can be described in a similar fashion to that of the correlated spin dimer case through the assumption of a singlet-triplet model within a bond-operator theory [26].

Such treatments of elementary excitations have contributed toward the understanding of magnetic excitations in model spin ladder systems, with a notable example being the recently synthesised organometallic spin ladder $(C_5H_{12}N)_2CuBr_4$, where the inter-ladder coupling is ~ 3 % of the characteristic ladder energy scale (which is on the order of ~ 1 meV). In this sense the system can be considered to be a realisation of a 1-D

Figure 5.1: The crystal structure of $BiCu_2PO_6$. Copper atoms are given by the light blue circles, the oxygen atoms by red circles, and the bismuth by grey circles. The Cu^{2+} zig-zag ladders are formed between two ribbons as shown by the dotted lines. Image from Ref. [110]

	a ($\AA$)	b ($\AA$)	c ($\AA$)	Volume ($\AA^3$)
$BiCu_2PO_6$	11.7768(1)	5.1729(0)	7.7900(1)	474.56

Table 5.1: Lattice parameters and unit cell volume of $BiCu_2PO_6$. From Ref. [114]

magnet, creating a rich testing ground for properties of low-dimensional magnetism [107].

The cuprate spin ladder compounds $(Sr,Ca,La)_{14}Cu_{24}O_{41}$ can be contrasted to the low-energy model system $(C_5H_{12}N)_2CuBr_4$, not only due to their significant characteristic ladder energy scale ($\sim$ 100 meV), but also due to the presence of additional interactions present in the Hamiltonian, most notably the four-spin cyclical exchange [108] which has considerable affect on the dynamical properties [109]. While these ladders are a departure from the 1-D physics well modelled by the coupled spin-chain model of the organometallic ladder, they have provided insight into the physics of low-dimensional quantum systems.

The spin ladder compound $BiCu_2PO_6$ (BCPO) presents an opportunity for study as

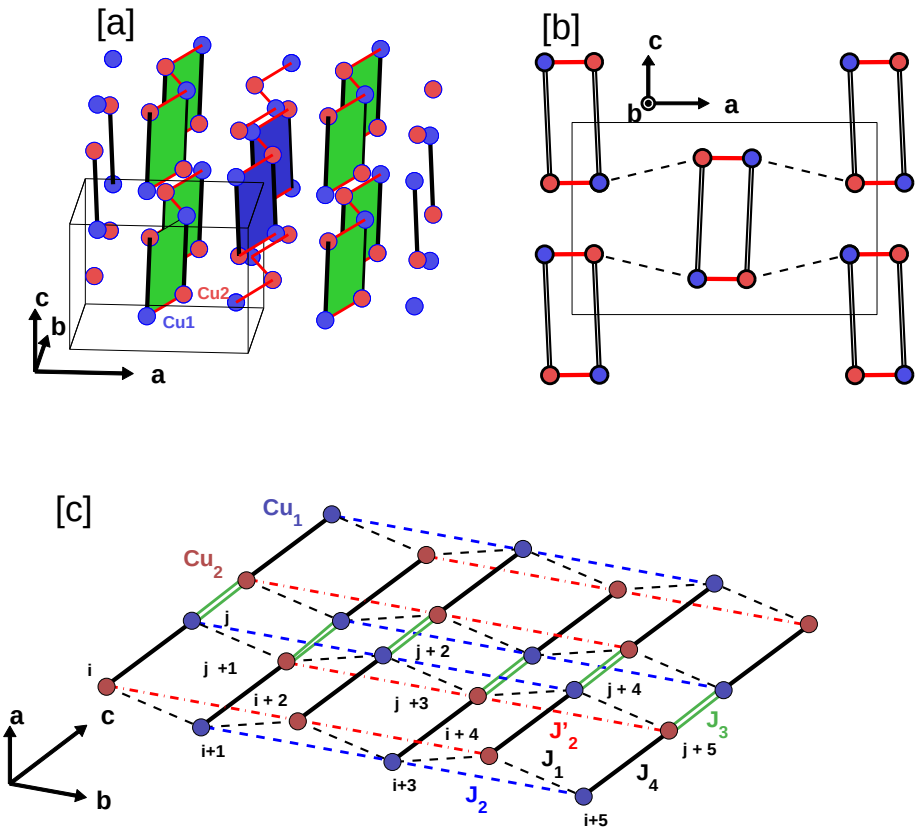

Figure 5.2: Schematic structure $BiCu_2PO_6$, indicating exchange interactions. [**a**] The 3-D structure with the crystallographic directions as indicated. The two crystallographically non-equivalent Cu atoms are shown by red and blue circles. [**b**] The projection onto the **a-c** plane. The dashed lines indicate the exchange between ladder units. [**c**] Exchange geometry within and between ladders in the **b-c** plane with the labels as indicated for the Hamiltonian in Equation 5.1, with the appropriate exchange parameters indicated.

a connecting case between these two 'extremes' of ladder geometry, notably possessing a characteristic energy scale on the order of $\sim$ 10 meV. The structure is shown in Figure 5.1, which depicts the formation of a 'zig-zag' ladder of Cu atoms formed by two Bi-Cu-O ribbons. $BiCu_2PO_6$ crystallises in the Pnma space group and has lattice parameters as given in Table 5.1

It has a proposed exchange interaction scheme similar to that of a coupled spin-chain geometry as seen in $(C_5H_12N)_2CuBr_4$, but with additional interaction terms J_2 and J_2' between the crystallographically non-equivalent copper sites Cu_1 and Cu_2. The exchange geometry is given in Figure 5.2 and for a single ladder unit is described by the Hamiltonian

$$\mathcal{H} = \sum_{i,j}[J_4 S_i \cdot S_j + \sum_{i,j} J_1(S_i \cdot S_{i+1} + S_j \cdot S_{j+1}) + J_2 S_i \cdot S_{i+2} + J_2' S_j \cdot S_{j+2}] \quad (5.1)$$

where J_1 and J_4 are the proposed 'leg' and 'rung' exchange terms respectively. J_2 and J_2' are the next-nearest-neighbour (NNN) terms. The dominant inter-ladder coupling between ladder units is given by J_3, as illustrated in Figure 5.2. The spin operators $S_{i,j}$ are those of the indicated ladder Cu sites i and j, as illustrated in Figure 5.2 [c].

The existence of the NNN terms J_2 and J_2' are predicted by the Muffin-tin orbital calculations [111], and supported by susceptibility data given in Ref. [40], which demonstrates a broad maximum at $T \sim 57$ K, lower than the predicted susceptibility for an isolated spin ladder or a 2D Heisenberg antiferromagnet. This is an effect typical of frustration and points to the importance of next-nearest-neighbour interactions along the legs.

It is also predicted to have finite interladder terms [41], with exchange J_3 connecting the ladders in the z-direction. This exchange is predicted to be weak relative to J_1, J_4 due to the associated Cu-O-Cu bond angle being close to 90°[41, 112], but considered significantly larger than the coupling along x, inferred to be negligible from DFT calculations [42].

The frustrated ladder geometry proposed is that of the case of two coupled $J_1 - J_2$ alternating chains. The isolated chain has been the subject of much study spanning the last four decades [113], and is known to exhibit a transition between a dimerised gapped state and a quasi-Néel-ordered state at a finite J_2/J_1 ratio [39]. Connecting two of these chains results in an alternating chain model that can describe the $BiCu_2PO_6$ geometry, and has been extensively studied using numerical methods [39].

The estimated exchange couplings for $BiCu_2PO_6$ place it well within the incommensurate rung-singlet phase. The excitation spectra within this phase can be treated as singlet-triplet excitations, with energy renormalisation from the frustrated couplings. Perturbative methods and bond operator theories have been presented in Ref. [39] and summarised in §3.3, assuming a strong-rung limit and the results of which indicate an incommensurate spin-gap minimum due to frustrated couplings.

Previous experimental work to elucidate the spin gap and possible magnetic dynamical effects have focused on neutron scattering and bulk measurements of powder samples, but no systematic experimental determination of the dynamical magnetic properties have been performed thus far on single crystal samples.

5.2 Inelastic Neutron Scattering Study of Magnon Dispersion of BCPO

With the recent availability of large-single crystal samples, the dispersion of magnetic excitations across reciprocal space can be investigated for the first time. With an esti-

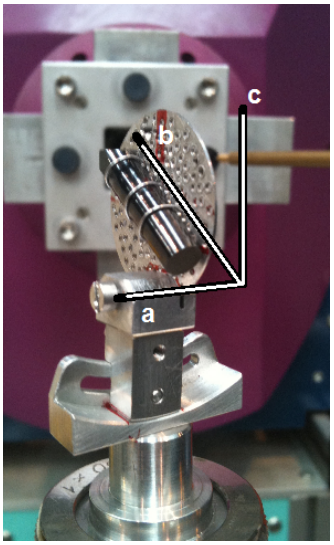

Figure 5.3: Single crystal of $BiCu_2PO_6$. The crystallographic **a**, **b** and **c** directions are indicated.

mated spin gap of $\Delta \sim 32$ K, the energy scale of the system is suited for investigation using thermal neutron scattering. By mounting the crystal sample in different scattering orientations with appropriate choice of k_f, the INS intensity can be systematically investigated for all three directions in recriprocal space up to energy transfer $\Delta E \sim 50$ meV.

5.2.1 Single Crystal Samples

The $BiCu_2PO_6$ single crystal samples used for the experiment were grown by S. Wang *et al.* [114], at the Laboratory for Development and Methods (LDM), at the Paul Scherrer Institut (PSI). They are high-quality single crystals grown through the Traveling Solvent Floating Zone (TSFZ) technique. Both the structural quality and the phase purity were studied via Riefveld refinement of diffraction data of X-ray powder. The morphology of the single crystal was checked through optical microscope observation and it was confirmed that the samples consisted of a single domain through observation of nuclear Bragg peaks, for example on MORPHEUS at SINQ (PSI).

The crystallographic orientation of the crystal used in INS measurements was analysed with X-ray and neutron Laue diffraction. Crystals were cut into samples approximately 5 mm diameter, 20 mm length, as shown in Figure 5.3 with the crystallographic (**a**, **b**, **c**) directions shown.

5.2.2 Experimental Setup

The experimental results to follow were obtained from work utilising the thermal triple-axis spectrometer IN22, located at the Institute Laue-Langevin (ILL) in Grenoble, France. The instrument is as outlined in §2.3.2.

The instrument was used in two separate investigations, carried out in June/July 2010 and June/July 2011. The same, unaltered crystal sample was used in both instances and the conditions were identical. The instrument was equipped with a standard orange cryostat operated in the temperature range 1.5 K - 200 K. A 360 degree scattering window allowed for the continuous rotation of the cryostat to investigate regions of allowed momentum transfer within the scattering plane.

The instrument was operated in constant final wavevector mode with $k_f = 1.97$, 2.662 or 3.84 Å^{-1} for an energy range of 0 meV $< \Delta E <$ 50 meV. A vertically focusing PG(002) monochromator was used in conjunction with a vertically fixed, horizontally focusing PG(002) analyser. A PG-filter was placed between the sample and the analyser. No collimation was used, and two sets of slits before and after the sample were optimised for background reduction.

The crystal was mounted in two orientations, first in the **b-c** scattering plane and then the **a-b** scattering plane, with the majority of experimental data collected in the former geometry.

Figure 5.4 indicates the points in reciprocal space for the **b-c** geometry where measurements were taken. The collected scans were taken in such a way as to allow for the analysis of the magnon dispersion as a function of (a) Q_k direction for $Q_l =$ 2 r.l.u., which corresponds to propagation vector along the ladder leg, and (b) the magnon dispersion in the Q_l direction for $Q_k = 0.50$; 0.55; 1.45 r.l.u., corresponding to propagation vectors along the ladder rungs.

Figure 5.5 [a] summarises the inelastic scattering intensity for $\vec{Q} = (0\ Q_k\ 2)$ r.l.u. for 0.4 r.l.u. $< Q_k <$ 1.9 r.l.u. for ΔE from 0 meV to 20 meV. As predicted by theoretical models, the gap minimum is not located at $Q_k = 0.50$, but rather at the larger momentum transfer $Q_k \sim 0.60$. From this it can be immediately deduced that the magnon excitation spectrum is indeed incommensurate with the lattice. Data is presented in Figure 5.5 [b], illustrating the difference in the INS intensity at these two points. The magnetic origin of the modes is confirmed through comparison to the higher temperature data, plotted as the red markers in panel [b]; there is no remaining scattering intensity upon heating to 30 K.

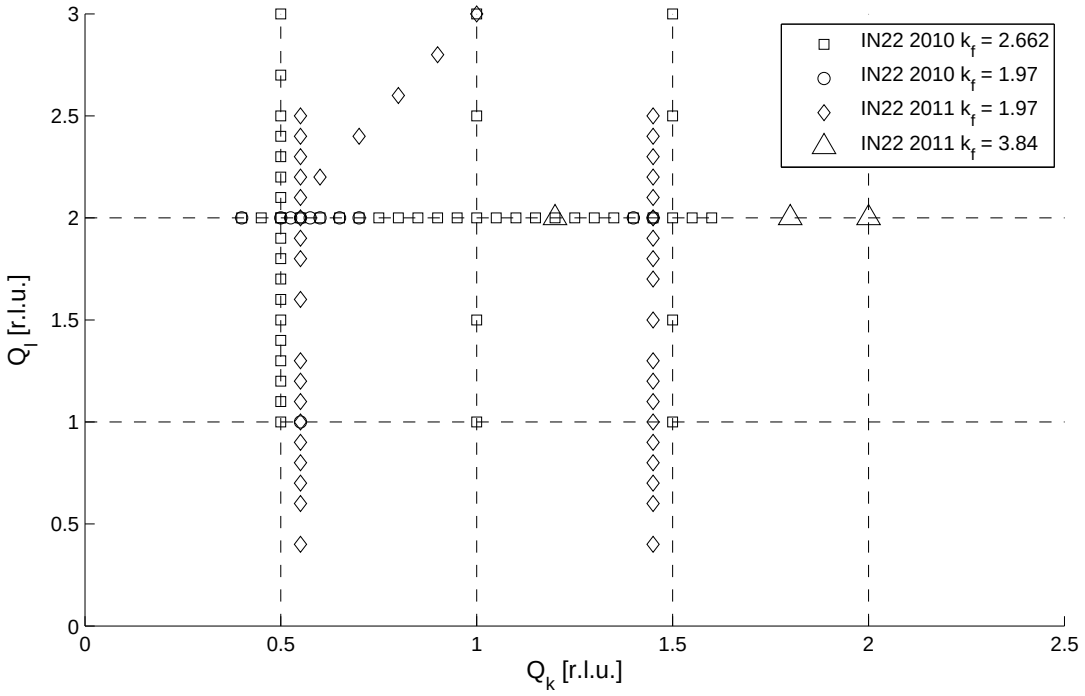

Figure 5.4: Reciprocal lattice vectors indicating where measurements were performed on IN22. Each marker indicates a scan in energy transfer, with the absolute values varying between each scan. The squares indicate measured points taken in 2010 with $k_f = 2.662$ Å^{-1}, with the key observations the evolution of the dispersion in Q_k at $Q_l = 2$ r.l.u., and in Q_l at $Q_k = 0.5$. The circles indicate higher resolution measurements with $k_f = 1.97$ Å^{-1} taken in the same experiment. The diamonds illustrate the additional scans taken in 2011 at $k_f = 1.97$ Å^{-1}, and the triangles the high-energy, low-resolution scans taken at $k_f = 3.84$ $\AA^{-1}$.

5.3 Fitting the data

It is evident even on a qualitative level that there are multiple magnon excitations extending up to higher energies. Separation of these modes is possible through a quantitative analysis of the INS scattering intensities by application of a fitting routine that identifies the contribution from separate magnetic excitations and simultaneously fits the added contributions to the total scattering intensity. This was done at all measured momentum transfers via a least-squares fitting routine. As such it is possible to fit the excitation energy, integrated scattering intensity and the energy FWHM of the excitation.

However, to successfully and satisfactorily replicate the observed energy dependence of the scattering intensity, an adjusted energy lineshape was taken. This was a necessity due to the presence of strong focusing effects within the observed scattering, a direct consequence of convolving a finite-width resolution ellipsoid (shown in Figure

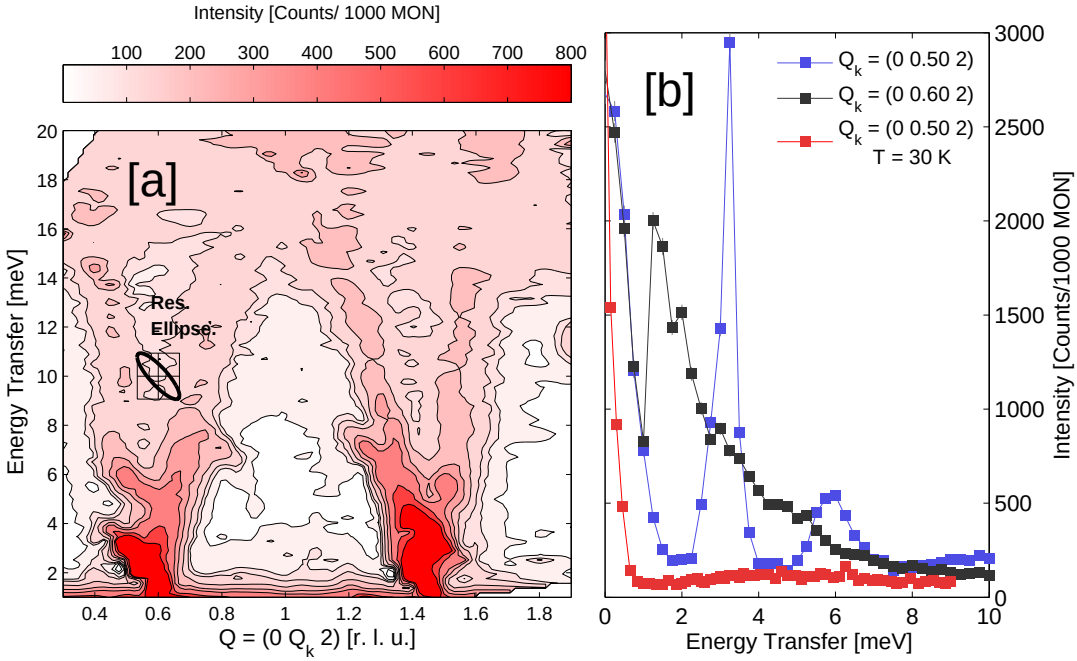

Figure 5.5: Magnetic exctiations in $BiCu_2PO_6$, along the ladder direction $\vec{Q} = (0\ Q_k\ 2)$ r.l.u., **[a]** Contour plot summarising the INS intensity for 0.3 r.l.u. $< Q_k <$ 1.9 r.l.u. **[b]** INS scans near the dispersion minima, with $Q_k = 0.6$ r.l.u. given by the black squares. $Q_k = 0.50$ r.l.u. is given by the blue squares (T = 1.5 K) and the red squares (T = 30 K). The resolution ellipsoid $(\vec{Q}, \omega)$ is shown in [a]. The plotted contours and the colourmap have been chosen to emphasise the high energy scattering at $\Delta E > 5$ meV, which is significantly lower in intensity than that measured at the spin gap $\Delta \sim 1.8$ meV. The dispersion minima occur near $Q_k = 0.60$ r.l.u. and 1.40 r.l.u., indicating that the magnon dispersion is incommensurate with the lattice.

5.5 [a]) with a band minimum of comparable width in $\vec{Q}$. Given the significant change in the dispersion over the measured 0.05 r.l.u. increments, the occurrence of resolution effects are expected and can only be avoided through observation with a higher resolution instrument.

Without information on the general 3-D dispersion of the system, a neutron resolution convolution analysis as detailed in §2.3.3 is not possible. However, a first estimate for the magnon dispersion can be attained from fitting the data through an adaption of an asymmetric Gaussian lineshape to account for the focusing effect. In this functional form, the FWHM above and below the peak centre are taken to be fixed to a determined ratio which can be chosen by inspection and refined as a fitting parameter.

Examples of the fitted scattering intensity are given in Figure 5.6, for two points near the focusing condition, $\vec{Q} = (0\ 0.55\ 2)$ r.l.u. and $\vec{Q} = (0\ 1.45\ 2)$ r.l.u., both achieved through fitting to the asymmetric Gaussian lineshape. They demonstrate

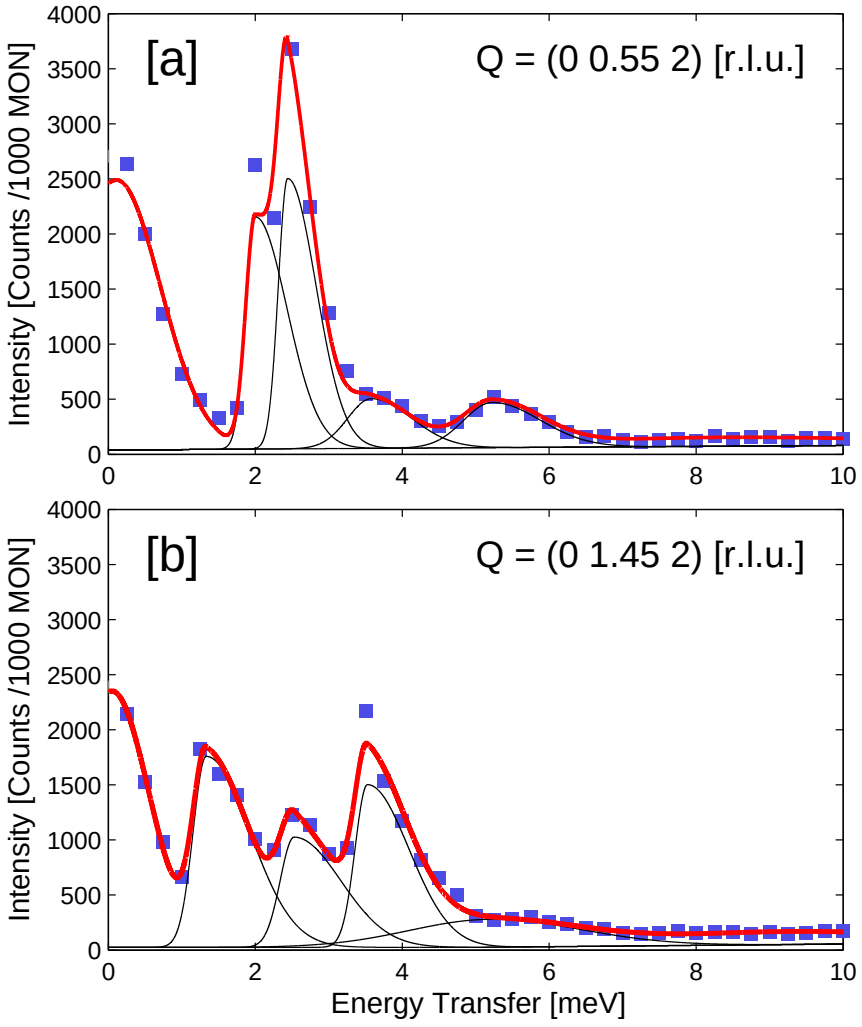

Figure 5.6: Examples of the fitted INS spectra. **[a]** Intensity for $\vec{Q}$ = (0 0.55 2) r.l.u. **[b]** Intensity for $\vec{Q}$ = (0 1.45 2) r.l.u. In both cases, the solid red lines are the lines of best fit assuming the asymmetric Gaussian lineshape described in the text.

also a plurality of modes present in the magnon dispersion.

The same treatment was performed across all measured INS data given in Figure 5.4, and summarised in Figure 5.7 for the four directions in reciprocal space where the transfer energy momentum dependence can be analysed systematically; [a] 0.35 r.l.u. $< Q_k <$ 1.9 r.l.u. at Q_l = 2 r.l.u. for $\Delta E <$ 20 meV; [b] 1 r.l.u. $< Q_l <$ 3 r.l.u. at Q_k = 0.5 r.l.u. for $\Delta E <$ 9 meV; [c] 0.4 r.l.u. $< Q_l <$ 2.5 r.l.u. at Q_k = 0.55 r.l.u. for $\Delta E <$ 8 meV; [d] 0.4 r.l.u. $< Q_l <$ 2.5 r.l.u. at Q_k = 1.45 r.l.u. for $\Delta E <$ 8 meV. The fitted excitation energies (open black squares) are plotted on top of contour plots summarising the data.

To measure the Q_h wavevector dependence, the crystal was mounted such that scattering was possible within the **a-b** plane. INS spectra were collected for -2 meV $<$

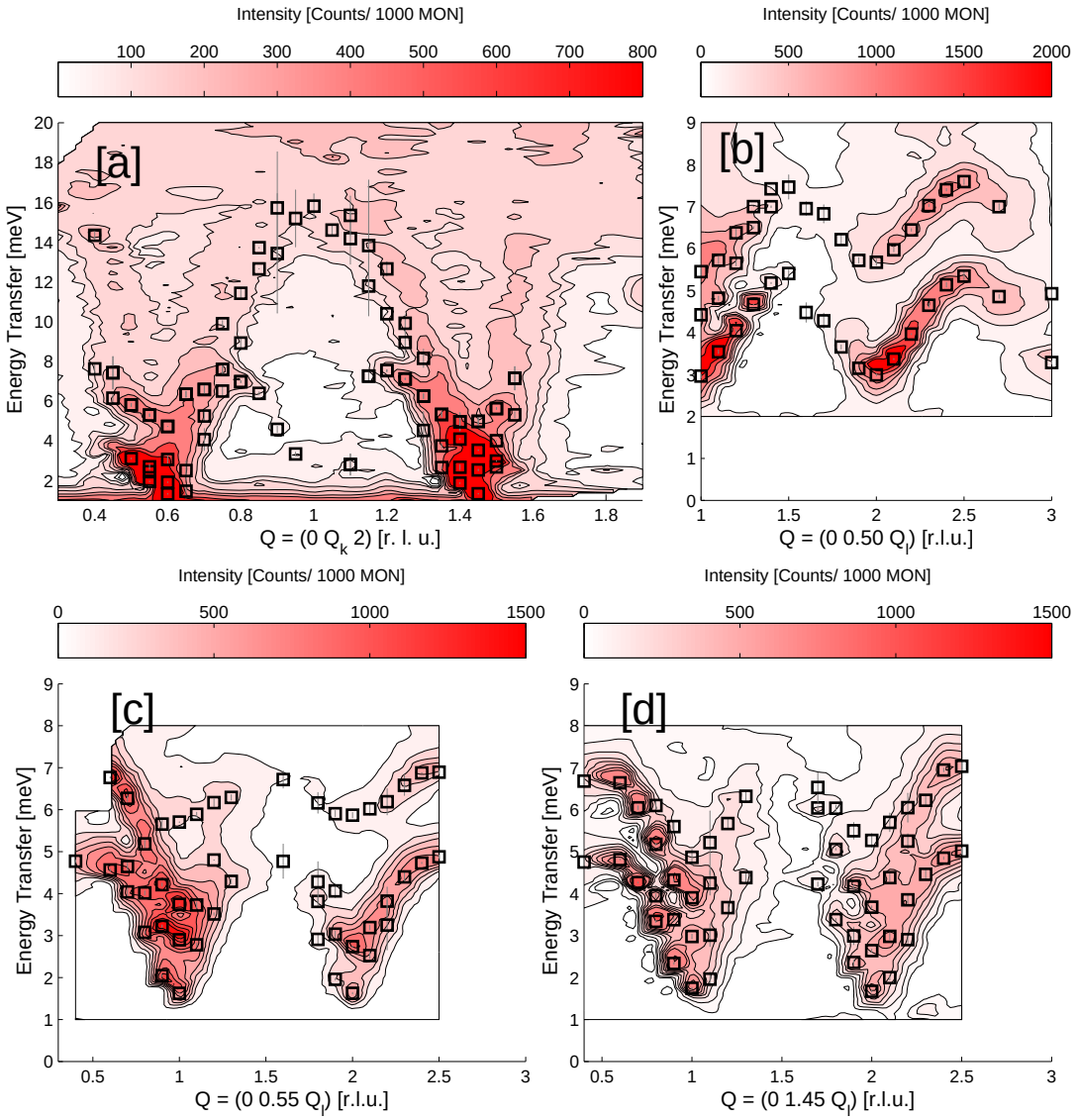

Figure 5.7: Fitted excitation energies in BCPO, along the measured reciprocal space directions. **[a]** $\vec{Q} = (0\ Q_k\ 2)$ r.l.u.; $k_f = 2.66$ Å^{-1} **[b]** $\vec{Q} = (0\ 0.50\ Q_l)$ r.l.u.; $k_f = 2.66$ Å^{-1} **[c]** $\vec{Q} = (0\ 0.55\ Q_l)$ r.l.u.; $k_f = 1.97$ Å^{-1} and **[d]** $\vec{Q} = (0\ 1.45\ Q_l)$ r.l.u.; $k_f = 1.97$ Å^{-1}. Each fitted mode is described by an open black square plotted atop contour plots summarising the scattering intensity.

$\Delta E < 10$ meV for $Q_l = 1.5$ r.l.u., and -2 r.l.u. $< Q_h < 0$ r.l.u. The data is summarised as a contour plot in Figure 5.8. The magnon excitation energy remains constant, from which it can be inferred that there is no dispersion along the Q_h direction, and is indicative of weak coupling between ladders along this direction.

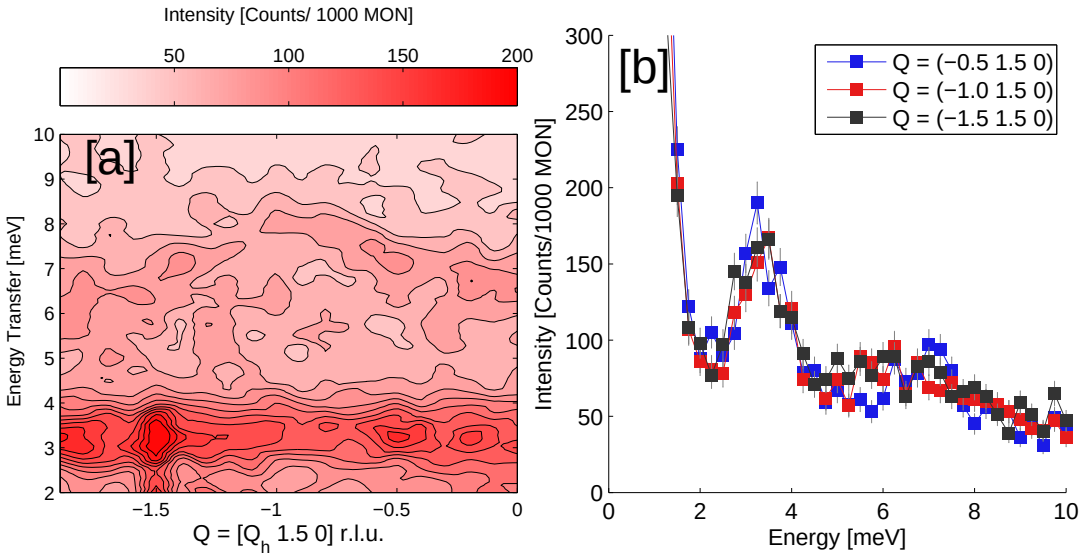

Figure 5.8: Inelastic intensity for $\vec{Q} = (Q_h\ 1.5\ 0)$ r.l.u. **[a]** Contour plot of inelsatic scans taken for -1.9 r.l.u. $< Q_h < 0$ r.l.u. **[b]** Scans taken at Q_h = (-0.5 1.5 0) r.l.u., (-1 1.5 0) r.l.u. and (-1.5 1.5 0) r.l.u. The measurements were taken with the crystal mounted in the **a-b** scattering plane.

5.3.1 High Resolution INS

The multiplicity of modes in the low energy region is hard to precisely resolve with the setup on IN22; it is clear that multiple modes exist and they can be isolated but systematic error in their relative weights and excitation energies are introduced due to the experimental resolution available.

Further experiments to investigate the nature of the low-lying excitation modes were conducted by high-resolution INS, performed on the cold neutron triple axis spectrometers IN14 (ILL, Grenoble, FR) and TASP (PSI, Villigen, CH). The higher resolution results from the low incident energy of the neutrons used in these spectrometers, albeit with constraints from instrument geometry that prevent a study up to high energy transfers.

IN14 is located on the cold beam guide H53 at the ILL. It has a vertically focusing PG (002) monochromator, and a horizontally focusing PG(002) analyser. A cooled Be-filter was placed between the sample and the analyser, and the instrument was operated in constant k_f mode with $k_f = 1.3$ Å^{-1}. The collimation was set to open-60′-open-open and two slits before and after the sample were optimised for maximum background reduction.

TASP is located at the end of the cold neutron guide 1RNR14 at SINQ, PSI. In a similar setup to IN14, it has a vertically focusing PG monochromator and a horizontally

focusing analyser. A cooled Be-filter was placed between the sample and analyser and the instrument was operated with constant $k_f = 1.3$ Å^{-1} and $k_f = 1.5$ Å^{-1} . No collimation was used, but slits were optimised for maximum background reduction.

One set of data was collected on IN14 in a single day of beam time in July 2010 for the same crystal sample as used for IN22, mounted in a **b-c** scattering geometry inside a standard orange cryostat. The operational temperature range was between $T = 1.5$ K and $T = 200$ K. Due to constraints on the accessible regions of reciprocal space for the required energy transfer, the excitation minima $\vec{Q} = (0\ 0.56\ 2)$ r.l.u. and (0 1.44 2) r.l.u. were not accessible. Therefore, studies were performed on the minima at $\vec{Q} =$ (0 0.56 1) r.l.u., which can be seen to be similar from Figure 5.7 [b] - [d], albeit with the addition of an excitation at $\Delta E = 4$ meV.

The same crystal was mounted in TASP inside a vertical 9 T cryomagnet, and operated in a temperature range between $T = 1.5$ K and $T = 200$ K. As a necessity of the design of the cryomagnet, the scattering window is reduced due to the presence of the split coils, leading to roughly half the scattering intensity measured. This, coupled with the lower incident flux of TASP relative to IN14 resulted in a greatly reduced measured intensity and the counting times were adjusted accordingly such as to measure equivalent scattering intensity. The same reciprocal points were measured on TASP as on IN14.

The comparison for the low-energy high resolution data for TASP and IN14 are presented in Figure 5.9 [a] and [b] respectively, where the presented scans from TASP are those where the cryomagnet was set at $H = 0$ T.

The higher energy transfer on TASP was achievable due to instrument geometry and a choice of higher final wavevector and as such the 6 meV excitation is observable. The occurrence of multiple modes is clear here, with four independent modes identified and significant spectral intensity in a highly-focused Q range.

5.3.2 Applied Magnetic Field

Principally, an $S = 1$ triplet excitation is triply degenerate with each state identified by different S^z eigenvalues, taking the values of 0, $\pm$ 1. The degeneracy can be lifted in presence of anisotropy in the system, resulting in three modes with different excitation energies in reciprocal space.

The low-E modes of $BiCu_2PO_6$ can thus be explained through identifying and ascribing S_z values to each excitation. A high-field cryomagnet was employed in both the TASP and IN14 experiments described above, with the former investigated for H = 0 T and 6 T, and the latter for 0 T $< H < 14.9T$. The Zeeman interaction energy,

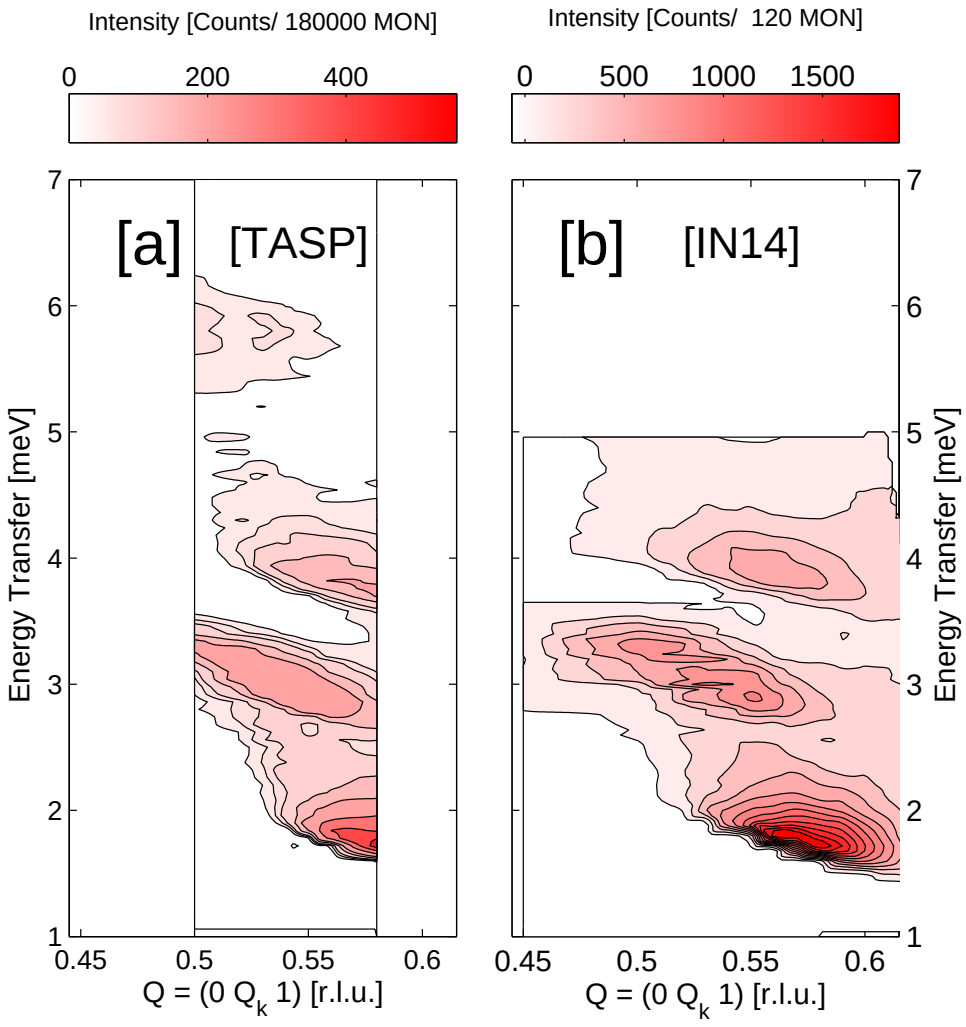

Figure 5.9: Zero-field high resolution INS scans, taken on TASP, SINQ and IN14, ILL for $\vec{Q} = (0\ Q_k\ 1)$ r.l.u. **[a]** Contour plot of the INS scans taken on TASP, with 0.5 r.l.u. $< Q_k <$ 0.58 r.l.u. **[b]** Contour plot of the INS scans taken on IN14, with 0.45 r.l.u. $< Q_k <$ 0.62 r.l.u. The higher energy range shown in the TASP figure is a result of different scattering conditions from the instrument geometry.

which is proportional to $\vec{H} \cdot \vec{S}$, will split modes with different S_z values with increasing field.

Figure 5.10 illustrates this effect; panel [a] shows the fitted excitation energies for the case of zero field for the data presented in Figure 5.9 [a] utilising the asymmetric Gaussian lineshape as described above. The fitted energies are identified by the square markers. Figure 5.10 [b] shows the same region of data collection for the applied field oriented in the direction $H \parallel \mathbf{a}$, with $H = 6$ T, with the fitted excitation energies identified by both the diamond and triangular markers.

Two key observations can be drawn from the fitted energies. First, the modes

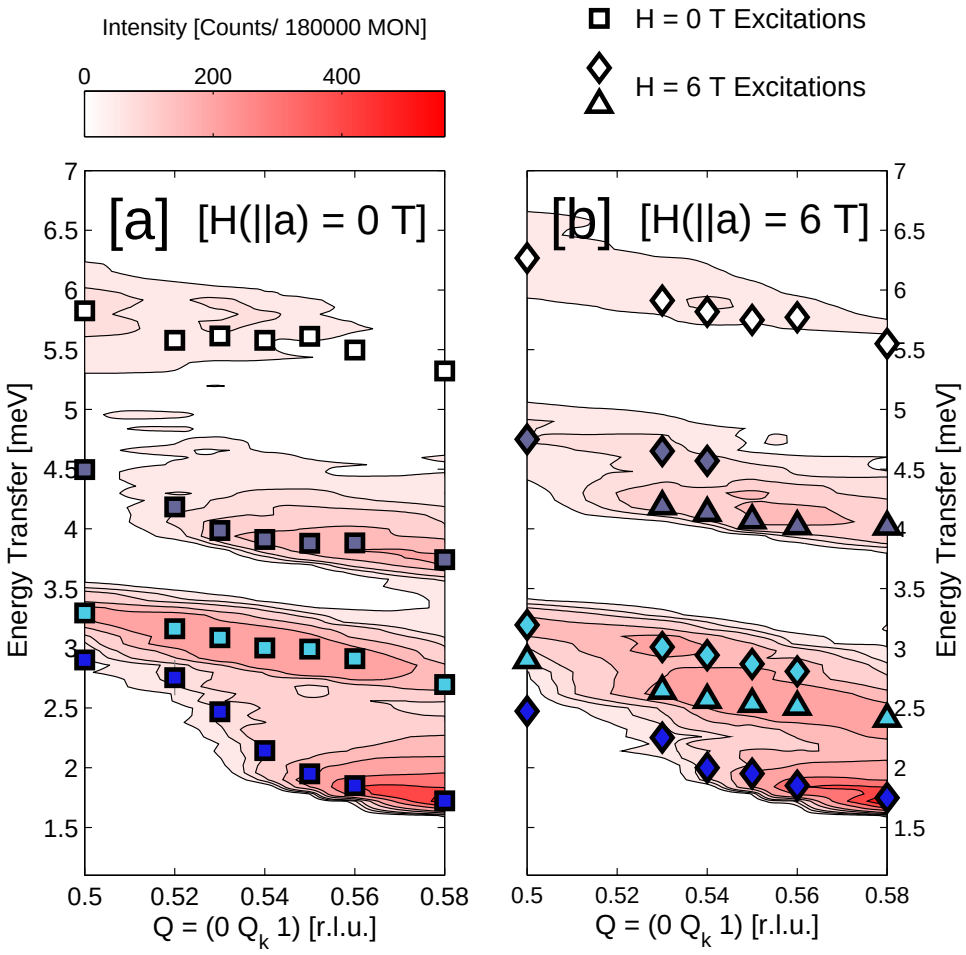

Figure 5.10: Fitted INS intensity for $Q = (0\ Q_k\ 1)$ r.l.u., measured on TASP. **[a]** Contour plot of the INS intensity for $H = 0$ T, with square markers indicating the fitted excitation energies. **[b]** Contour plot of the INS intensity for $H = 6$ T, with the diamond and triangular markers indicating the fitted excitation energies.

exhibit a field dependence, with the lowest-lying mode demonstrating no change in energy, the second mode ($\Delta_{H=0T} \sim 3$ meV) renormalises downwards and both the third and fourth modes ($\Delta_{H=0T} \sim 4$ meV; $\Delta_{H=0T} \sim 6$ meV) renormalise upward with applied magnetic field.

The second observation is the field-induced splitting of the higher energy modes. At $H = 6$ T, up to 6 excitations are experimentally resolvable and the fitted energies are given in Figure 5.10 [b]. Figure 5.11 shows the fitted INS spectra for $\vec{Q} = (0\ 0.53\ 1)$ r.l.u. for [a] $H = 0$ T and [b] $H = 6$ T. The solid red line in both cases illustrates the fitted scattering intensity, with the individual modes highlighted in [b] with the dashed black lines. The blue dotted line in panel [b] denotes the fit to the $H = 0$ T data shown in panel [a], and is included for comparison.

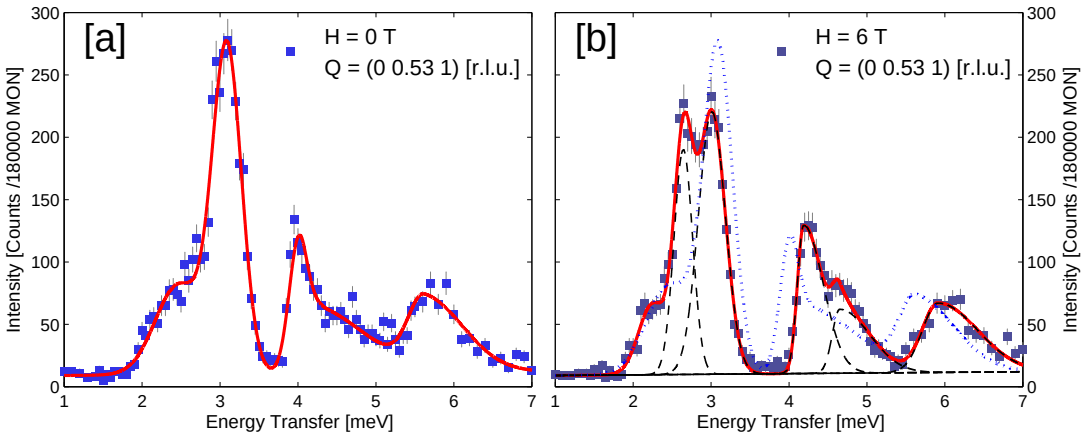

Figure 5.11: Splitting of the triplet modes in BCPO by a magnetic field, at $\vec{Q} = (0\ 0.53\ 1)$ r.l.u. **[a]** $H = 0$ T. The blue squares indicate the measured INS intensity, and the solid red line the line of best fit. **[b]** $H = 6$ T. The blue squares indicate the measured INS intensity, and the solid red line the line of best fit. The black dashed lined indicate the fitted contributions from individual modes, and the dashed blue line is the line of best fit for for $H = 0$ T, included for comparison.

For $Q_k = 0.53$ r.l.u. the observed shifts in energy from lowest to highest, are $\Delta E =$ (0, -0.079, -0.4457, + 0.1997, +0.6616, + 0.2921) meV. The value for a classical Zeeman interaction term ($E = g\mu_B \mathbf{S} \cdot \mathbf{H} = 0.696$ meV, for a g-factor $g = 2$) is not consistent with these results. This disagreement, along with the multiple modes present, point to further spin-spin interactions that change the nature of the field interaction term. A notation is therefore introduced to identify these modes; from lowest to highest energy the modes observed at $H = 6$ T are denoted as E_0, E_{11}, E_{12}, E_{21}, E_{22} and E_3.

A more comprehensive study of the field-dependent excitations was conducted by performing a second experiment on IN14, taking place in July 2011. The setup was identical to that previously used, with the same crystal loaded into an Oxford Instruments 15 T cryomagnet similar to that used on TASP previously.

The excitations were measured for comparison to the TASP data for applied fields 0 T $< H <$ 14.9 T. For $\vec{Q} = (0\ Q_k\ 1)$ r.l.u., with 0.5 r.l.u. $< Q_k <$ 0.6 r.l.u., the measured INS spectra are summarised in Figure 5.12 for $H = 13.5$ T and $H = 14.9$ T. The extent and nature of the splitting can be identified on a qualitative level; the lowest lying mode remains constant in energy with applied field, but the excitation at $\Delta_{H=0T} \sim 3$ meV has split into two resolvable parts, denoted by the previously introduced notation as E_{12} and E_{11} for the higher and lower energy modes respectively and E_0 for the lowest lying, field-independent mode. The excitations are observed to occur at $\Delta(E_{11}) = 1.5$ meV and $\Delta(E_{12}) = 2.8$ meV at $H = 14.9$ T, with E_{11} overlapping with E_0 mode at $H = 13$ T.

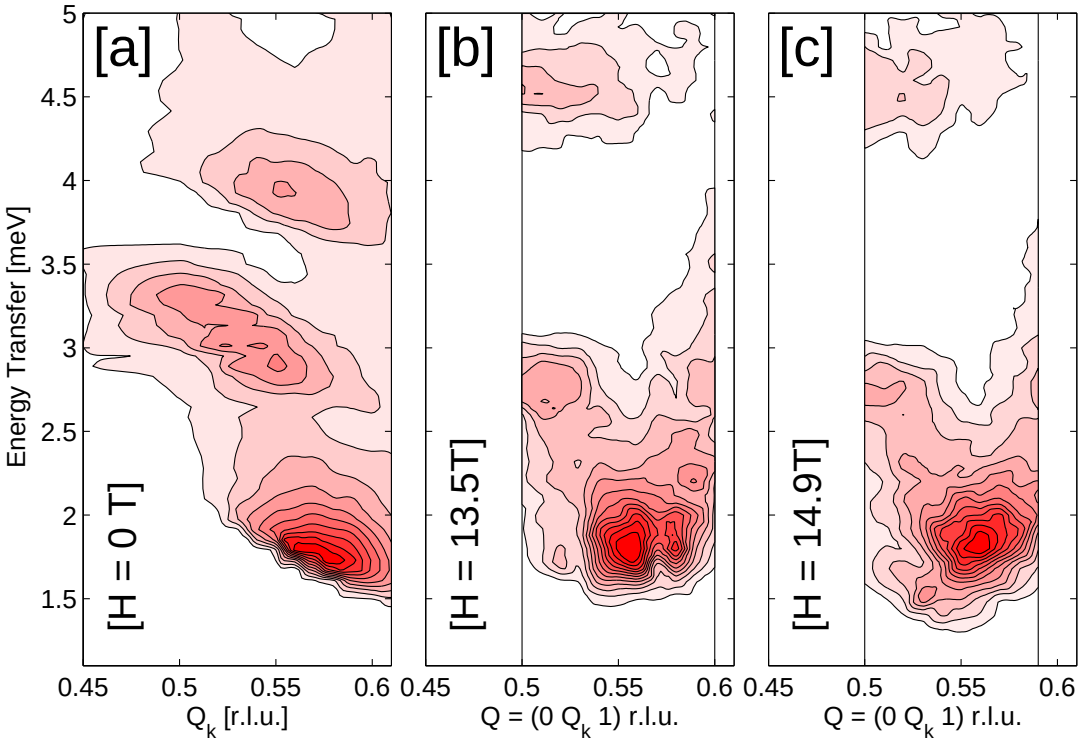

Figure 5.12: Splitting of the triplet modes in BCPO for $\vec{Q} = (0\ Q_k\ 1)$ r.l.u. and H || **a** (IN14, ILL). [**a**] $H = 0$ T, [**b**] $H = 13.5$ T and [**c**] $H = 14.9$ T. The contours indicate the INS intensity. The E_0 mode shows no field dependence, with the higher energy modes splitting into multiple resolveable parts, with the E_{11} mode energy lowered below E_0 for $H > 13.5$ T.

The two contributions to the scattering intensity of the excitations for $\Delta E < 4$ meV are wavevector-dependent; at $Q_k = 0.56$ r.l.u. there is minimal intensity from the E_{12} mode, but significant contributions from both E_{11} mode and the E_0 mode, the field-independent mode. At $Q_k = 0.53$ r.l.u., the dominant contribution to the scattering intensity is that of the E_{11} mode, with a weak intensity from E_{12} and the E_0 modes identified. At $Q_k = 0.51$ r.l.u. only the contribution from E_{12} and E_{11} can be measured. These three wavevectors $\vec{Q} = (0\ 0.56\ 1)$ r.l.u., $(0\ 0.53\ 1)$ r.l.u. and $(0\ 0.51\ 1)$ r.l.u. are therefore identified for regions where the field-dependence of the magnetic excitations can be elucidated. Data for the field dependence of the excitations at these points in reciprocal space are shown in Figure 5.13.

First, a discussion of the possible anisotropy terms will be presented, followed by a discussion of the dispersion as a whole.

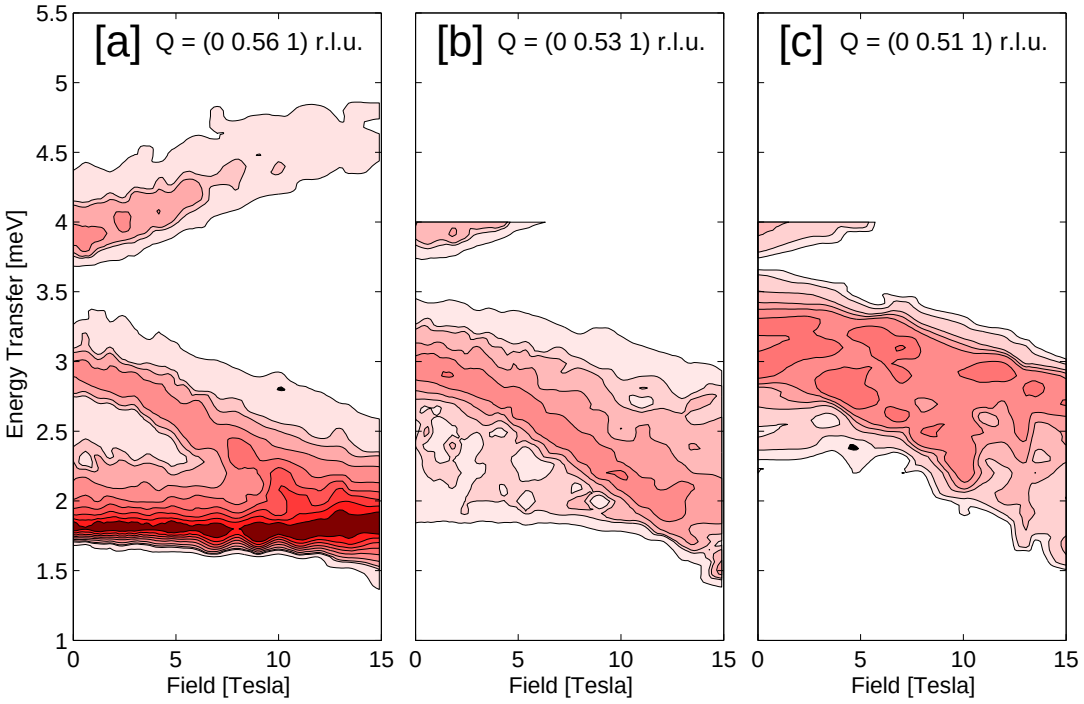

Figure 5.13: Momentum and field dependence of excitation energies for 0 T $< H <$ 14.9 T, where H || **a** (IN14, ILL). [**a**] Contour plot of INS intensity for $\vec{Q}$ = (0 0.56 1) r.l.u. [**b**] Contour plot of INS intensity for $\vec{Q}$ = (0 0.53 1) r.l.u. and [**c**] Contour plot of INS intensity for $\vec{Q}$ = (0 0.51 1) r.l.u.

5.4 Anisotropic Interactions

In addition to the observation of a field-independent $S_z = 0$ mode, the data presented in the previous section show two main features upon the application of magnetic field; a lifting of the degeneracy of $S_z = \pm 1$ into multiple excitations and different non-linear field-dependence of the spin gap of each of these split modes. A simple model of strongly coupled dimers does not exhibit these properties. The observed splitting is therefore inferred to be a result of the additional terms in the Hamiltonian of $BiCu_2PO_6$.

For a gapped spin system with spatially isotropic exchange interactions, the principal excitations are triplet modes that couple identically with the field and exhibit linear field-dependence, with a Zeeman energy term

$$E = g\mu_B \sum_i \mathbf{H} \cdot \mathbf{S}_i \tag{5.2}$$

where $\mathbf{H}$ is the applied field and $\mathbf{S}_i$ denotes the spin at site i.

The field-dependent magnetisation of pure $BiCu_2PO_6$ samples has been investigated for high magnetic fields 0 T $< H <$ 60 T, where a pulsed field is applied to

powder samples [42]. The resultant magnetisation was observed to increase linearly up to the critical field H_c, beyond which it exhibits a steep linear increase. However, for an ideal, defect-free SU(2) invariant gapped system there is no finite magnetisation below H_c. Impurities can result in a finite magnetisation contribution, but it is argued that for the low temperatures measured these would saturate at $H = 5$ T, far below the critical field. The authors of Ref. [42] propose the finite slope is a result of Dzyaloshinskii-Moriya (DM) anisotropic interactions in the system.

The DM interaction is given by

$$\mathcal{H}_{DM} = \mathbf{D}_{ij} \cdot (\mathbf{S_i} \times \mathbf{S_j}), \tag{5.3}$$

where $\mathbf{D}_{ij}$ is the DM vector for interaction between spins located at sites i and j. It is possible for a DM term to be present for atomic bonds that possess no inversion symmetry around their centre (i.e. the bond is not invariant under the transformation $(x, y, z) \rightarrow (-x, -y, -z)$). In $BiCu_2PO_6$ two such bonds can be identified and are those mediated by the rung and leg exchange, with respective connection vectors $\mathbf{R}_{rung}$ and $\mathbf{R}_{leg}$.

The effect of DM interaction on the magnetisation of an isolated dimer is presented in Ref. [115]. The presence of a DM interaction between the coupled spins mixes triplet excitations into the singlet ground state, resulting in a uniform magnetisation response $\mathbf{m_u} \propto \mathbf{D} \times (\mathbf{D} \times \mathbf{B})$ and a staggered response $\mathbf{m_s} \propto \mathbf{D} \times \mathbf{B}$, even below the critical field. This has been observed in the spin ladder compound $Cu_2(C_5H_12N_2)_2Cl_4$ [115] and it is concluded that the observed magnetisation below the critical field in $BiCu_2PO_6$ may also be a result of finite DM terms.

As such, the mixing of singlet and triplet states that result from the presence of DM terms in $BiCu_2PO_6$ can be identified as a likely candidate mechanism for the behaviour at finite fields of the $S = 1$ excitations.

5.4.1 Eigenstates of a 4-spin cluster model

The change in excitation energy of the system from an anisotropy can be approximated by the excitation spectrum of an isolated cluster of 4 Cu atoms shown in Figure 5.14 [a]. In the picture of a singlet condensate with triplet excitations on the cluster, the energy eigenstates can be taken as an approximation of the excitation spectrum of the ladder. While the isolated nature results in excitation energies independent of momentum transfer, information can still be extracted from the excitation energies to discern the nature of the mixing of energy eigenstates via anisotropic interactions.

The model is formed by the arrangement of ideal SU(2) spin-1/2 particles located on each of the four sites, with the spin operators defined as $S_i^{\{x,y,z\}}$, with i denoting

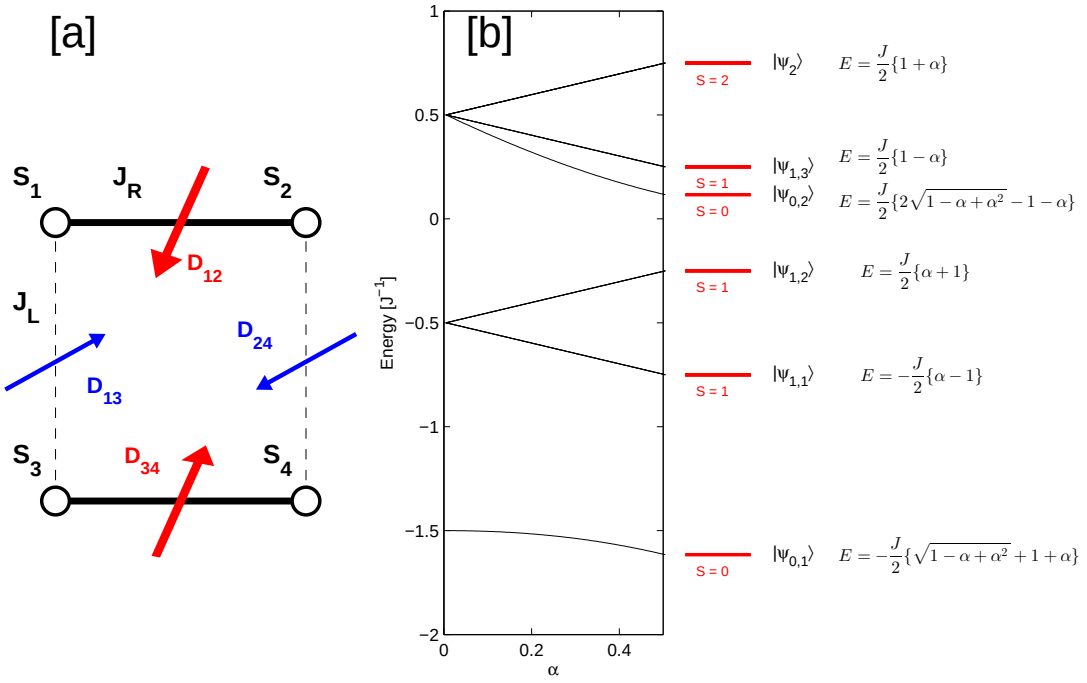

Figure 5.14: Structural schematic and excitation energies of a four-spin cluster. **[a]** Schematic of the four spin cluster with each circle indicating a spin site and the solid and dashed lines the exchange interactions. General DM vectors are given by the red and blue arrows. **[b]** The multiple excitations of the four-spin cluster with no anisotropy terms or applied field, for rung exchange interaction $J_r = J$, and leg exchange $J_l = \alpha J_r$. The energy level equations are as in Ref. [116].

the lattice site. Each spin operator is constructed by a product of N SU(2) matrices through the operation

$$S_i^{\{x,y,z\}} = \prod_1^{i-1} \left[\begin{pmatrix} 1 & 0 \\ 0 & 1 \end{pmatrix} \otimes \right] \sigma^{\{x,y,z\}} \prod_{i+1}^{N} \left[\otimes \begin{pmatrix} 1 & 0 \\ 0 & 1 \end{pmatrix} \right] \tag{5.4}$$

where $\otimes$ is the Kronecker (outer) product, and $\sigma^{x,y,z}$ are the Pauli spin matrices, given by

$$\sigma^x = \frac{\hbar}{2} \begin{pmatrix} 0 & 1 \\ 1 & 0 \end{pmatrix} \quad \sigma^y = \frac{\hbar}{2} \begin{pmatrix} 0 & -i \\ i & 0 \end{pmatrix} \sigma^z = \frac{\hbar}{2} \begin{pmatrix} 1 & 0 \\ 0 & -1 \end{pmatrix}. \tag{5.5}$$

The evaluation of Equation 5.4 results in spin operators for each site $\mathbf{S_i} = (S_i^x, S_i^y, S_i^z)$ of dimension $(2^N, 2^N)$, formulated in the S^z basis. The interaction between the spins can then be freely represented by products of the operators. Neglecting anisotropy terms, the energy spectrum of the four-spin cluster is represented by the eigenvalues

of the Hamiltonian $\mathcal{H}_0$

$$\mathcal{H}_0 = J_R\left(\mathbf{S_1}\cdot\mathbf{S_2}+\mathbf{S_3}\cdot\mathbf{S_4}\right)+J_L\left(\mathbf{S_1}\cdot\mathbf{S_3}+\mathbf{S_2}\cdot\mathbf{S_3}\right). \tag{5.6}$$

The eigenvalues are the energies required to form an excitation within the cluster. The two-leg spin ladder of $BiCu_2PO_6$ is constructed by linking many of the clusters described above, where the effect of constructing a geometry in a long-range periodic fashion is to allow dispersion of the excitations from site to site. This results in a Q-dependence of the excitation and in the observed spin gap occurring for a lower energy. This feature is not reproduced for the isolated four spin system. However, the essential features of the excited modes are still dictated by the exchange within the unit cell which can be modeled on a simple level by the cluster detailed above and presented in Figure 5.14.

The eigenvalue and eigenvectors were extracted through calculations carried out in the MATLAB software package through use of its 'eig.m' routine, designed to extract eigenvalues and eigenvectors of a specified matrix.

Taking the model $J_L = \alpha J_R$, the eigenstates of the Hamiltonian correspond to 16 states; two $S = 0$ states, 9 $S = 1$ states (three sets of three degenerate states) and 5 $S = 2$ states. The energy dependence of the rung and leg coupling is given in Figure 5.14 [b]. The α-dependence of the energies are consistent with the formulae given in Ref. [116], calculated for an identical arrangement of $S = 1/2$ atoms and quoted in Figure 5.14.

The observed dispersion in reciprocal space is known to have a periodicity equal to that of the lattice in the Q_l direction, and double that of the lattice in the Q_k direction, indicative of coupling between excitations on lattice sites with half-unit cell separation in Q_k and single unit-cell separation in Q_l. This, combined with the results observed later in this chapter of the fitted magnon dispersion (§5.5) and the structure factor analysis (§5.6) indicate that the system is in a regime where the magnon dispersion is dominated by excitations of the rung units. As an approximation, the four-spin cluster is therefore examined in the regime of strong rung coupling ($J_R \gg J_L$) by taking $\alpha = 0$.

The excitations can be characterised through an analysis of the eigenvectors of the system. Extracting the eigenvectors of the $\mathcal{H}_0$ matrix yields the eigenstates within the S^z basis. It is useful to consider these eigenstates in the basis of two rung dimers formed on the tetramer, $|(12)(34)\rangle$. The individual dimer states are given in Table 5.2. It is to be noted that the S^x and S^z bases can be identically represented by the Pauli

Dimer state (12)	(x-axis quantisation)	Dimer state (34)	(x-axis quantisation)
$\|\kappa_S\rangle$	$\frac{1}{\sqrt{2}}(\|\uparrow\downarrow\rangle - \|\downarrow\uparrow\rangle)_{12}$	$\|\sigma_S\rangle$	$\frac{1}{\sqrt{2}}(\|\uparrow\downarrow\rangle - \|\downarrow\uparrow\rangle)_{34}$
$\|\kappa_+\rangle$	$\|\uparrow\uparrow\rangle_{12}$	$\|\sigma_+\rangle$	$\|\uparrow\uparrow\rangle_{34}$
$\|\kappa_-\rangle$	$\|\downarrow\downarrow\rangle_{12}$	$\|\sigma_-\rangle$	$\|\downarrow\downarrow\rangle_{34}$
$\|\kappa_0\rangle$	$\frac{1}{\sqrt{2}}(\|\uparrow\downarrow\rangle + \|\downarrow\uparrow\rangle)_{12}$	$\|\sigma_0\rangle$	$\frac{1}{\sqrt{2}}(\|\uparrow\downarrow\rangle + \|\downarrow\uparrow\rangle)_{34}$

Table 5.2: The single-dimer excited states expressed for the two dimer-basis $|(12)(34)\rangle$ introduced in the text, in the condition of strong rung coupling ($J_R \gg J_L$).

$\|\psi\rangle$	Eigenstate (x-axis quantisation)	Eigenstate (two-dimer basis)
$\|\psi\rangle_{0,1}$	$\|\uparrow\downarrow\downarrow\uparrow\rangle - \|\uparrow\downarrow\uparrow\downarrow\rangle - \|\downarrow\uparrow\downarrow\uparrow\rangle + \|\downarrow\uparrow\uparrow\downarrow\rangle$	$\|\kappa_S\rangle \otimes \|\sigma_S\rangle$
$\|\psi\rangle_{1,1}$	$\frac{1}{2}(\|\downarrow\uparrow\downarrow\downarrow\rangle - \|\uparrow\downarrow\downarrow\downarrow\rangle + \|\downarrow\downarrow\uparrow\downarrow\rangle - \|\downarrow\downarrow\downarrow\uparrow\rangle)$	$[\|\kappa_S\rangle \otimes \|\sigma_-\rangle] - [\|\kappa_-\rangle \otimes \|\sigma_S\rangle]$
	$\frac{1}{\sqrt{2}}(\|\uparrow\downarrow\downarrow\uparrow\rangle - \|\downarrow\uparrow\uparrow\downarrow\rangle)$	$[\|\kappa_S\rangle \otimes \|\sigma_0\rangle] - [\|\kappa_0\rangle \otimes \|\sigma_S\rangle]$
	$\frac{1}{2}(\|\uparrow\uparrow\downarrow\uparrow\rangle - \|\uparrow\uparrow\uparrow\downarrow\rangle + \|\uparrow\downarrow\uparrow\uparrow\rangle - \|\downarrow\uparrow\uparrow\uparrow\rangle)$	$[\|\kappa_S\rangle \otimes \|\sigma_+\rangle] - [\|\kappa_+\rangle \otimes \|\sigma_S\rangle]$
$\|\psi\rangle_{1,2}$	$\frac{1}{2}(\|\downarrow\uparrow\downarrow\downarrow\rangle - \|\uparrow\downarrow\downarrow\downarrow\rangle + \|\downarrow\downarrow\downarrow\uparrow\rangle - \|\downarrow\downarrow\uparrow\downarrow\rangle)$	$[\|\kappa_S\rangle \otimes \|\sigma_-\rangle] + [\|\kappa_-\rangle \otimes \|\sigma_S\rangle]$
	$\frac{1}{\sqrt{2}}(\|\uparrow\downarrow\uparrow\downarrow\rangle - \|\downarrow\uparrow\downarrow\uparrow\rangle)$	$[\|\kappa_S\rangle \otimes \|\sigma_0\rangle] + [\|\kappa_0\rangle \otimes \|\sigma_S\rangle]$
	$\frac{1}{2}(\|\uparrow\uparrow\downarrow\uparrow\rangle - \|\uparrow\uparrow\uparrow\downarrow\rangle + \|\downarrow\uparrow\uparrow\uparrow\rangle - \|\uparrow\downarrow\uparrow\uparrow\rangle)$	$[\|\kappa_S\rangle \otimes \|\sigma_+\rangle] + [\|\kappa_+\rangle \otimes \|\sigma_S\rangle]$
$\|\psi\rangle_{1,3}$	$\frac{1}{2}(\|\downarrow\uparrow\downarrow\downarrow\rangle + \|\uparrow\downarrow\downarrow\downarrow\rangle - \|\downarrow\downarrow\downarrow\uparrow\rangle - \|\downarrow\downarrow\uparrow\downarrow\rangle)$	$[\|\kappa_0\rangle \otimes \|\sigma_-\rangle] - [\|\kappa_-\rangle \otimes \|\sigma_0\rangle]$
	$\frac{1}{\sqrt{2}}(\|\uparrow\uparrow\downarrow\downarrow\rangle - \|\downarrow\downarrow\uparrow\uparrow\rangle)$	$[\|\kappa_+\rangle \otimes \|\sigma_-\rangle] - [\|\kappa_-\rangle \otimes \|\sigma_+\rangle]$
	$\frac{1}{2}(\|\downarrow\uparrow\uparrow\uparrow\rangle + \|\uparrow\downarrow\uparrow\uparrow\rangle - \|\uparrow\uparrow\downarrow\uparrow\rangle - \|\uparrow\uparrow\uparrow\downarrow\rangle)$	$[\|\kappa_0\rangle \otimes \|\sigma_+\rangle] - [\|\kappa_+\rangle \otimes \|\sigma_0\rangle]$

Table 5.3: The calculated eigenvectors of the ground state and the nine $S = 1$ excitations, using the notation of the two dimer basis given in Table 5.2. The $|\psi_{1,1}\rangle$ and $|\psi_{1,2}\rangle$ correspond to triplet rung excitations, with $|\psi_{1,3}\rangle$ corresponding to a two-particle boundstate.

matrices shown in Equation 5.5 through an appropriate transformation vector. The S^x basis is chosen for convenience as it lies along the direction of applied field.

Table 5.3 gives the eigenstates of the Hamiltonian $\mathcal{H}_0$ in the prescribed basis for the groundstate and the $\Delta S = 1$ excitations. The first column details the state in the notation of Figure 5.14, the second the calculated eigenstate with x direction taken as the quantisation axis, and the third the eigenstate in the two-dimer picture.

The ground state is described by two singlet states on the rungs, and it can be seen that the two lowest lying excitations correspond to triplet excitations, and the highest lying corresponding to two-magnon excitations. The two triplet excitations are formed by the superposition of the two possible arrangements of the product of a singlet state and a triplet state on either dimer, with the two types of $S = 1$ wavefunction distinguishable by the phase difference between the constituent triplet-singlet product excitations. The triplet excitations are degenerate at $\alpha = 0$, but the mentioned difference in phase implies different correlations between the rungs, which can be seen in the removal of the degeneracy as α is increased.

Remaining at $J_R \gg J_L$, the effect of inclusion of anisotropic terms in the Hamiltonian can be parameterised upon the application of magnetic field. Extending the Heisenberg Hamiltonian $\mathcal{H}_0$ results in

$$\mathcal{H} = \mathcal{H}_0 + \mathcal{H}_{ANI} + \mu_B \sum_i^4 \mathbf{H} \cdot \mathbf{S}_i, \tag{5.7}$$

where $\mathbf{H} = (H^x, H^y, H^z)$, $\mathbf{S}_i = (S_i^x, S_i^y, S_i^z)$ and $\mathcal{H}_{ANI}$ is the contribution to the Hamiltonian from anisotropic terms. The applied field is that of the x-direction, thus $H_y = H_z = 0$, and the split eigenstates are those with the x-axis as the quantisation axis. Without the anisotropic term, the field splitting is the classical Zeeman-type, demonstrating a linear dependence, with the splitting prefactor determined by the quantum number m, where m takes the values from $-|S| \rightarrow +|S|$.

Inclusion of anisotropic terms perturbs the linear field-dependence and leads to zero-field splitting. A general modeling of the anisotropy is possible through the application of single-ion (SI) anisotropy, where the spin on an atom is coupled in some fashion to the local crystal field surrounding it. The strength and direction vary between systems and its existence is not implicit to the $BiCu_2PO_6$, but nevertheless it is a useful method to parameterise the extent of unknown aniostropic interactions within a system. The single-ion term $\mathcal{H}_{SI}$ is typically parameterised with the easy axis term D and the axial term E,

$$\begin{aligned} \mathcal{H}_{SI} =& D\left\{(S_1^x + S_2^x)^2 + (S_3^x + S_4^x)^2\right\} \\ &+ E(\left\{(S_1^y + S_2^y)^2 + (S_3^y + S_4^y)^2\right\} - \left\{(S_1^z + S_2^z)^2 + (S_3^z + S_4^z)^2\right\}), \end{aligned} \tag{5.8}$$

where the anisotropy is taken to be located on a dimer unit, requiring the addition of the spin operators of the spins on each dimer site. The single-ion term has the effect of creating an easy-axis in the spin space, and creating a field-independent splitting between the different states described by the m quantum number. The D^x term creates a matrix that is diagonal, and uniformly splits the $m = \pm 1$ states from the initially degenerate $m = 0$ state. The E term specifies a non-diagonal anti-symmetric matrix that mixes the $m = \pm 1$ states. Therefore m no longer becomes a good quantum number and the eigenstates of the system exhibit non-linear field-splitting.

The direction of the single-ion anisotropy vector results from the coupling of the magnetic moment of the dimer to the local crystal field. Therefore the term must obey the symmetry operations of the $BiCu_2PO_6$ lattice. The (D, E) anisotropy term is therefore generalised as a vector in cartesian form as $E = (E^x \;\; E^y \;\; E^z)$, centred on the rung connection vectors, where the E notation has been chosen to avoid confusion with the DM vectors in the analysis to follow. Considering the operation of a symmetry

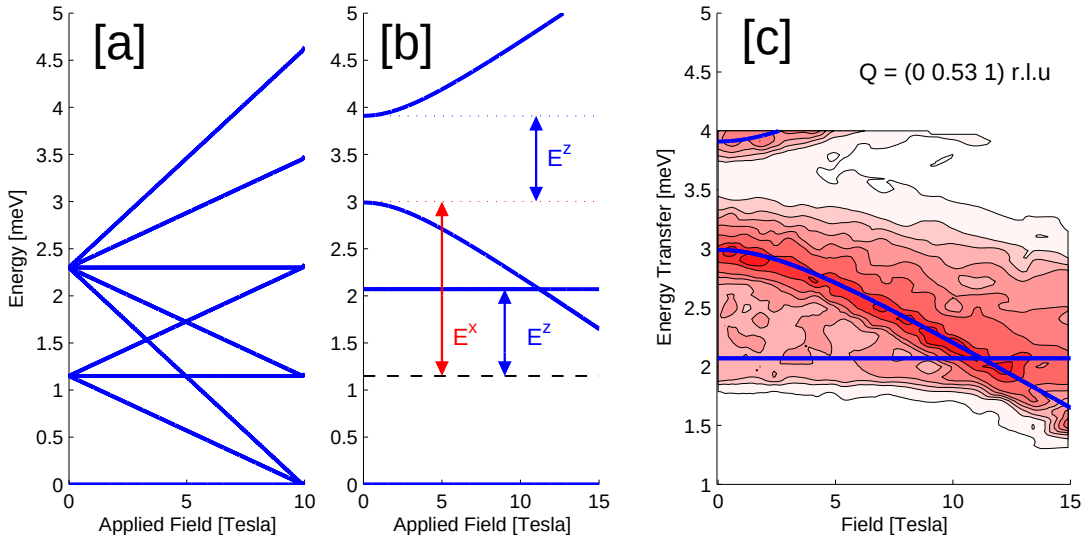

Figure 5.15: Effect of single-ion anisotropy on the excitation energies. **[a]** Excitation energy field-dependence without anisotropy terms; **[b]** Excitation energy field dependence with E^x and E^z single-ion anisotropy terms; **[c]** Excitation energy field dependence as given in [b], plotted against a contour plot of collected data.

element that maps a rung to itself, e.g. $[x, \frac{1}{2}$ - $y, z]$, the transformation results in $(E^x\ E^y\ E^z) = (E^x\ -E^y\ E^z)$, implying $E^y = 0$ and constraining the vector to be located in an easy plane orthogonal to the crystallographic **b** direction.

The effect of applying the SI anisotropy to the Hamiltonian in Equation 5.7 is given in Figure 5.15 [a] and [b]. By careful choice of E^x and E^z terms, field-dependent excitation energies that reproduce the observed behaviour can be extracted. The resulting field-dependent energies for the triplet modes are shown in Figure 5.15 [c]. The parameters selected to reproduce this behaviour are $E^x = 1.6J_R$ and $E^z = 0.8J_R$; $J_R = 1.15$ meV.

The non-linear field dependence is well reproduced, but the single-ion term does not account for the observation of more than two $S = 1$ excitations. The single-ion term mixes the excitations described by different S_z within each $S = 1$ excitation but without any cross-terms between different $S = 1$ excitations. As such $E_{11} = E_{12}$ and $E_{21} = E_{22}$ for all values of applied field.

Further mixing of the excitation states can occur through consideration of the Dzyaloshinskii-Moriya (DM) interaction as given by Equation 5.3. Neither the rung nor the leg connection vectors possess inversion symmetry and therefore are identified as possible sources of DM interactions.

However, while the symmetry of the leg and rung connections do not prevent the possibility of DM interactions, the *Pnma* symmetry of the lattice does constrain the

Symmetry Element (T)	$T(\mathbf{R}_I)$	$T(\mathbf{L}_I)$	$\mathbf{D}'$(rung)	$\mathbf{D}'$(leg)
(x,y,z)	(12)	(24)	D^x_R, D^y_R, D^z_R	D^x_L, D^y_L, D^z_L
(x, $\frac{1}{2}-y$, z)	(12)	[24]	$-D^x_R, D^y_R, -D^z_R$	$-D^x_L, D^y_L, -D^z_L$
(-x, $\frac{1}{2}+y$, -z)	(43)	[31]	$-D^x_R, D^y_R, -D^z_R$	$-D^x_L, D^y_L, -D^z_L$
($\frac{1}{2}-x$, $\frac{1}{2}+y$, $\frac{1}{2}+z$)	(78)	[86]	$D^x_R, -D^y_R, -D^z_R$	$D^x_L, -D^y_L, -D^z_L$
($\frac{1}{2}+x$, $\frac{1}{2}-y$, $\frac{1}{2}-z$)	(65)	[57]	$D^x_R, -D^y_R, -D^z_R$	$D^x_L, -D^y_L, -D^z_L$
($\frac{1}{2}+x$, y, $\frac{1}{2}-z$)	(65)	(57)	$-D^x_R, -D^y_R, D^z_R$	$-D^x_L, -D^y_L, D^z_L$
($\frac{1}{2}-x$, $-y$, $\frac{1}{2}+z$)	(78)	(86)	$-D^x_R, -D^y_R, D^z_R$	$-D^x_L, -D^y_L, D^z_L$
($-x$, $-y$, $-z$)	(43)	(31)	D^x_R, D^y_R, D^z_R	D^x_L, D^y_L, D^z_L

Table 5.4: The Dzyaloshinskii-Moriya vectors under the applied symmetry operations for *Pnma*. Following the notation of Figure 5.16, the initial rung and leg connections are $\mathbf{R}_I$ = (12) and $\mathbf{L}_I$ = (24), with DM vectors $\mathbf{D}_{rung}$ = (D^x_R, D^y_R, D^z_R) and $\mathbf{D}_{leg}$ = (D^x_L, D^y_L, D^z_L) respectively. T gives the symmetry element under consideration, and the final rung and leg vectors under this operation are given in the second and third columns, where square brackets indicate that the connection vector is across two unit cells. The DM vectors for each transformed rung and leg are given in the fourth and fifth column respectively.

orientation of the two vectors, similar to the case for the single-ion term. Table 5.4 details the transformed DM vectors $\mathbf{D}'$, where $\mathbf{D}'_{ij} = \det(T)T(\mathbf{D}_{ij})$ for each symmetry element R, and accounting for the pseudovector nature of the DM interaction with a determinant prefactor.

Figure 5.16 illustrates the possible DM vectors present on the lattice, and summarising the possible orientations of each {x,y,z} component. The DM interaction on the rung is constrained to be oriented along the y direction, due the symmetry of the lattice requiring (D^x, D^y, D^z) = (-D^x, D^y, -D^z) on each rung site, yielding the result $D^x = D^z = 0$. The leg DM interaction has no such constraint and retains all three {xyz} components.

The Hamiltonian resulting from the addition of the DM interaction into Equation 5.7 can be diagonalised in the same fashion as for the single-ion anisotropy. The resulting eigenvalues are the excitation energies of the cluster, and are produced for the range of fields 0 T $< H <$ 15 T.

Figure 5.17 illustrates the effect of adding DM interactions on the rungs (panel [b]) and on the legs (panel [c]), to be compared with the zero field results presented in panel [a]. Like the single-ion anisotropy, application of the rung DM interaction does not result in a splitting of the $|\psi\rangle_{1,1}$ and $|\psi\rangle_{1,2}$ states, because the rung term does not mix these two states; instead the mixing occurs only within the singlet and triplet eigenstates of each rung. This results in three sets of two degenerate modes exhibiting non-linear field dependence. In contrast, the application of a leg DM interaction causes

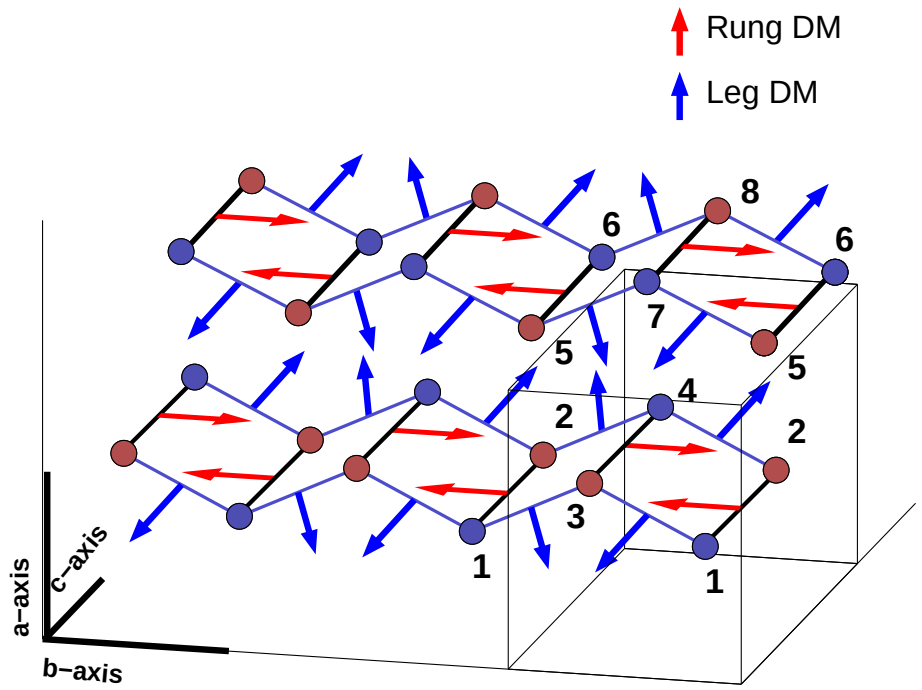

Figure 5.16: Schematic illustration of allowable Dzyaloshinskii-Moriya vectors for anisotropic spin couplings present in $BiCu_2PO_6$. The rung DM vector is given by $\mathbf{D}_R$ = (0 D_y 0), and the leg by $\mathbf{D}_L = (D'_x \;\; D'_y \;\; D'_z)$. The symmetry operations between the rungs constrain the $\mathbf{D}_R$ vector to the y-direction, as illustrated by the red arrows. The same symmetry operations applied to the legs do not constrain the $\mathbf{D}_L$ vector in any one crystallographic direction, but do dictate the relative directions of each leg DM term, as given by the blue arrows.

mixing between $|\psi\rangle_{1,1}$ and $|\psi\rangle_{1,2}$. This results in the splitting of $|\psi\rangle_{1,1}$ and $|\psi\rangle_{1,2}$ into five substates, as observed in panel [c].

The combination of single-ion terms and Dzyaloshinksii-Moriya terms for the case of [a] Rung DM and [b] Leg DM are presented in Figure 5.18, with parameters chosen by inspection that suitably reproduce the observed field dependence. Figure 5.18 [a] illustrates the comparison of raw data to the extracted eigenvalues for a Hamiltonian incorporating rung DM terms and a single-ion E^x term, included by necessity to separate the triplet modes, with magnitudes $E^x = 0.7J_R$, $\mathbf{D}_{rung} = 1.8\ J_R$ (0 1 0) and $J_R = 1.45$ meV. The Rung DM term acts in a similar way to the E^z term and splits the field-dependent modes, reproducing the data behaviour at the lower field values, but beginning to diverge at higher applied fields as the states engage in appreciable mixing.

Figure 5.18 [b] illustrates the extracted energy eigenvalues for $\mathbf{D}_{leg} = 0.55^* J_R$[0 1 0] with $J_R = 2$ meV. A single ion term $E^x/J_R = 1.4$ has been included to reproduce

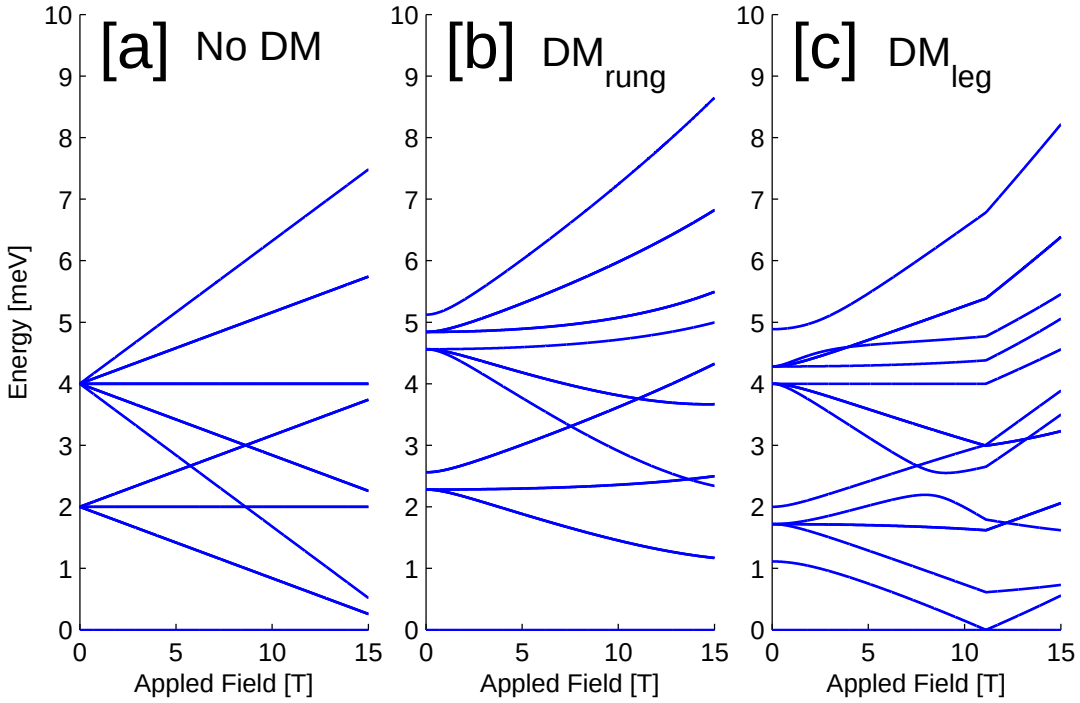

Figure 5.17: Field dependence of excitation energies, calculated from a four spin cluster and considering DM interaction terms. [**a**] Excitation energy field dependence with no DM terms, with $J_R = 2$ meV. [**b**] Excitation energy field dependence, including a rung DM term [**c**] Excitation energy field dependence, including a leg DM term. Upon addition of DM terms a non-linear field dependence results, albeit with different mixing of triplet states occurring depending on whether rung or leg terms are included.

the triplet-mode separation, but $E^z = 0$ and $\mathbf{D}_{rung} = 0$. The non-linear field dependence is reproduced, but there are several higher lying excitation energies that do not correspond to observation. By considering the single ion terms E^x, E^z alongside a leg DM vector, $\mathbf{D}_{leg}$ and a rung DM vector $\mathbf{D}_{rung}$ the field dependence of two downward trending excitations can be qualitatively reproduced, as shown in Figure 5.18 [c]. The parameters for the curves here are $J_R = 1.15$ meV, $\mathbf{D}_{leg} = J_R[0\ 1\ 0]$, $\mathbf{D}_{rung} = 2J_R[0\ 1\ 0]$, $E^x/J_R = 1.4$ and $E^z/J_R = 0.7$.

The implementation of a wide parameter space is illustrative of the complex nature of anisotropic interactions within $BiCu_2PO_6$. The data can be qualitatively reproduced through consideration of a combination of allowed anisotropies within the system. It is to be noted, however, that the splitting of the zero-field excitation is a phenomenon only reproduced when considering anisotropic interactions between rung units and therefore mixing the different $S = 1$ excitations.

While it is clear that the multiple modes observed on TASP and IN14 originate

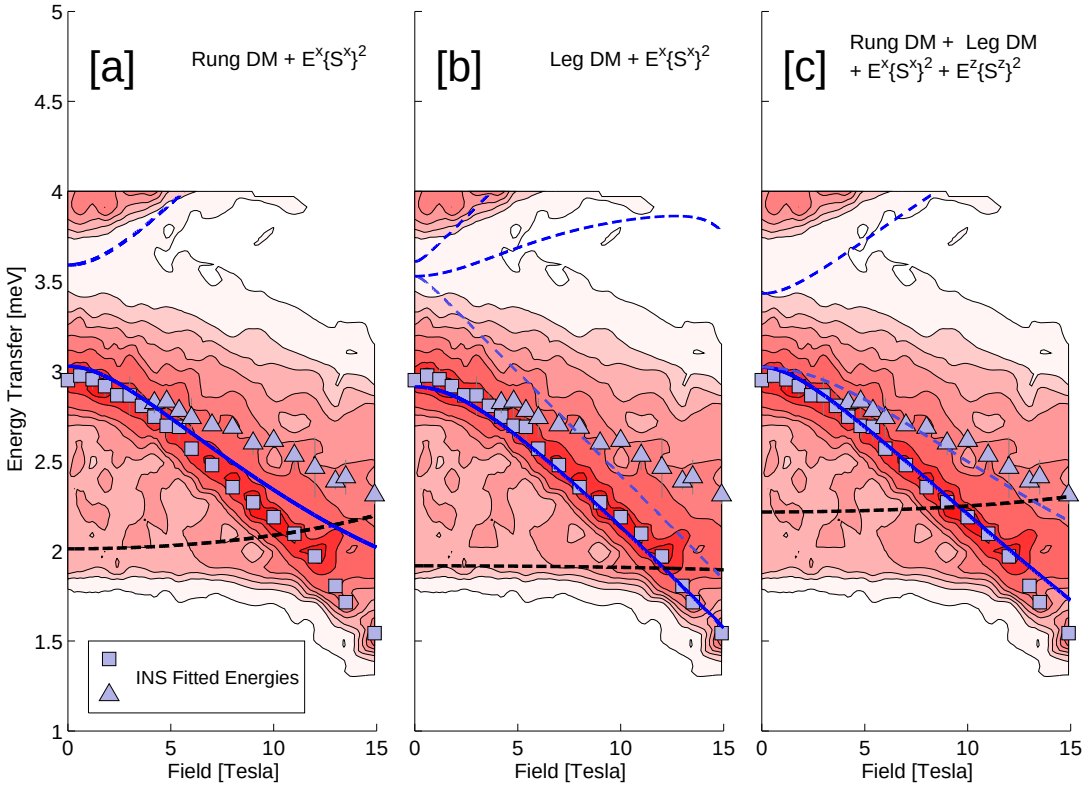

Figure 5.18: A comparison of excitation energy field dependence modeled using the four spin cluster to experimental data for $\vec{Q}$ = (0 0.53 1) r.l.u. as presented in Figure 5.13 [b]. **[a]** Excitation energy field dependence modeled from a rung DM term and a single ion E^x term. **[b]** Excitation energy field dependence modeled from a leg DM term and a single ion E^x term. **[c]** Excitation energy field dependence modeled from a rung DM term and single ion E^x and E^z terms. The intensity of the INS data is represented by the contour plot, and the light blue squares and triangles indicate the excitation energies fitted to the data.

from some form of anisotropic terms in the Hamiltonian, the treatment as given above does not comprehensively reproduce the multiple observed modes. In particular, the origin of the higher lying mode E_3 is not clear.

From observation of the TASP data, this mode is known to exhibit field dependence (see Figure 5.10) and therefore has a finite field-interaction term, necessitating a finite S_z value. It could be identified as one of the split triplet modes; this may be possible, as the higher energy modes E_{21} and E_{22} have not been as thoroughly investigated as the lowest lying excitations E_0, E_{11} and E_{12} and the full field dependence not yet elucidated. It is possible that E_3 is a fourth $S = 1$ mode rather than E_{22}, with the discrepancy in the zero-field splitting explainable by a $\vec{Q}$-dependence - this phenomenon has been evidenced in quantum systems possessing DM interactions, for example $SrCu_2BO_2$ [117].

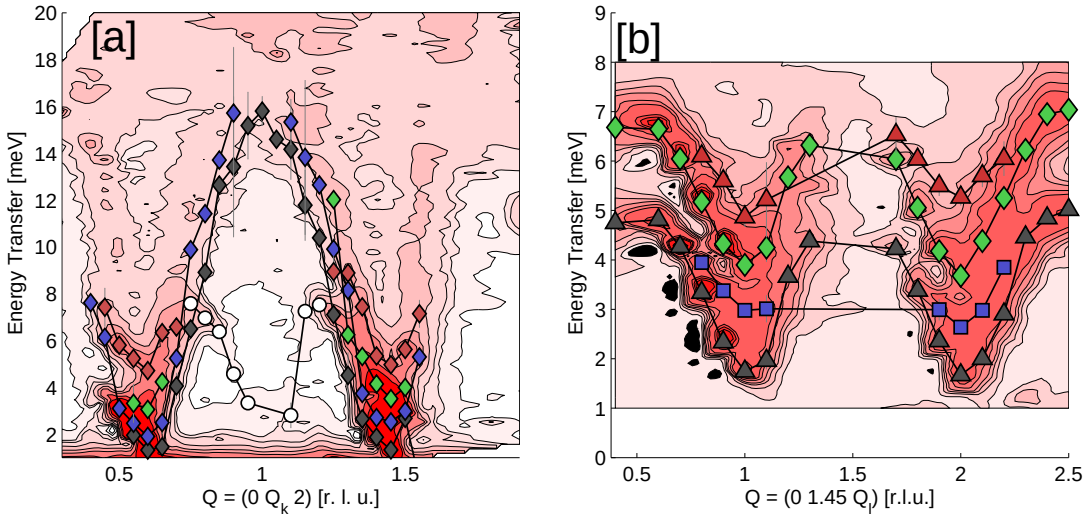

Figure 5.19: The assignment of the fitted excitation energies shown in Figure 5.7 into dispersion branches. **[a]** Mode assignment for $\vec{Q} = (0\ Q_k\ 2)$ r.l.u.; **[b]** Mode assignment for $\vec{Q} = (0\ 1.45\ Q_l)$ r.l.u. The $Q_k = 0.55$ and 0.5 datasets have mode assignments identical to that shown, with ascending energy assigned by colour.

Alternatively, the higher lying mode could have some other origin as yet unidentified. More thorough high-resolution investigations of the dispersion for higher energy transfers ($\Delta E > 4$ meV) are necessary to fully answer this question.

5.5 Magnon Dispersion and Exchange Geometry

Motivated by the observation that the observed multiple modes in BCPO originate from anisotropic splitting of an $S = 1$ mode, the excitation energies extracted from fitting the INS data can be assigned into magnon branches, where each magnon branch can be attributed to an $S = 1$ excitation split from anisotropic effects, with the assumption that the extent of the splitting is Q-independent. The mode assignment is shown in Figure 5.19 for [a] $\vec{Q} = (0\ Q_k\ 2)$ r.l.u. and [b] $\vec{Q} = (0\ 1.45\ Q_l)$ r.l.u. The black markers describe the lowest-lying field independent mode, with the blue, green and red circles assigned in order of increasing energy and each correspond to modes that undergo field splitting as seen in the previous section. The white circles will be discussed in the context of two-particle boundstates in §5.6.2.

As demonstrated in §5.3, the Q_h-dependent inter-ladder correlations are minimal, resulting in a flat magnon band. The excitations are then taken to have no dispersion in this direction. This reduces the problem to a 2-dimensional exchange geometry given in Figure 5.2 [c], considering magnon dispersion within the (Q_k, Q_l) directions in reciprocal space that, due to the unique geometry of $BiCu_2PO_6$, correspond to

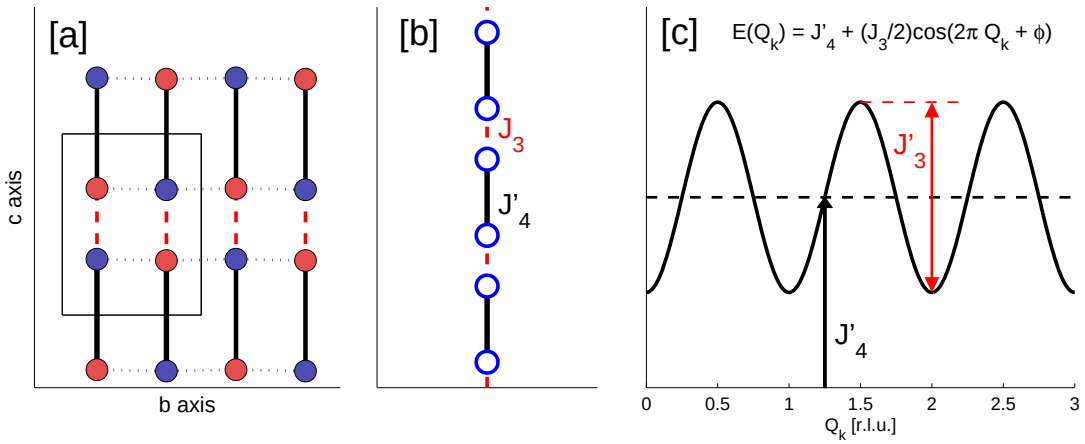

Figure 5.20: Modeling of $BiCu_2PO_6$, by approximating dispersion in the Q_l direction as that of a coupled dimer system. **[a]** Schematic of the coupled ladders in $BiCu_2PO_6$. **[b]** The coupled dimer model, showing the effective dimer exchange J_4' and the interladder coupling J_3. **[c]** The dispersion relation of the coupled dimer model of [b]. The average spin gap given is by J_4' and the bandwidth by J_3.

intra-ladder and inter-ladder dispersion respectively. Therefore these reciprocal lattice directions can be considered separately in terms of intra-ladder spin correlations and inter-ladder spin correlations.

The Q_k magnon dispersion is an incommensurate dispersion that has double the lattice periodicity, and can be analysed considering the dispersion relations outlined in §3.3. The Q_l dispersion is propagation between the ladders, and is described by a sinusoidal function sharing the lattice periodicity, with minima in the excitation energy commensurate with the lattice. Quantitative analysis of the extracted excitation energies are to follow.

5.5.1 Inter-ladder (Q_l) dispersion

The dominant coupling between ladders is contained in the exchange interaction J_3, which is in the direction of the the Cu-Cu vectors $\vec{R}$ = [0.0176 0 0.3708] and [-0.0176 0 0.3708] (given in f.l.c., fractional lattice co-ordinates). The main contribution of the exchange in the Q_l direction is a consequence of the inter-ladder coupling, and the intra-ladder exchange can be separated as a constant energy value when considering dispersion in this direction. This is supported by the commensurate nature of the excitations as shown in Figure 5.7.

The momentum-dependence of the inter-ladder dispersion is a result of the inter-ladder exchange term J_3. The presence of this inter-ladder exchange term allows for the propagation of any triplet excitations ocurring within a ladder structure. By taking

J_3 as the dominant inter-ladder exchange interaction, the dispersion in the Q_l direction can be effectively modelled in a coupled-dimer picture presented in Figure 5.20. The coupled ladder shown in Figure 5.20[a] can be approximated by coupled dimers as shown by Figure 5.20 [b], resulting in the dispersion plotted in Figure 5.20 [c], the dispersion given by

$$E(Q_k) = J_4' + \frac{J_3}{2}\cos(2\pi Q_k + \phi), \tag{5.9}$$

with a dimer exchange coupling described by $J_4'(Q_k)$, a value that corresponds to the energy required to excite a triplet on the frustrated isolated ladder, dependent on the intra-ladder momentum transfer. J_3 is the interdimer coupling, and ϕ a phase value.

The extracted excitation energies for all Q_l directions presented in Figure 5.7 have been fitted simultaneously to Equation 5.9 with a uniform bandwidth and phase ($\phi = \pi$). The resultant dispersions are given in Figure 5.21, with fits to Equation 5.9 given by the solid lines. The red markers for $Q_k = 0.55$ and 1.45 r.l.u. cannot simultaneously be described by a single uniformly shifted mode. It is to be noted that this mode corresponds to the E_3 excitation discussed in the previous section, the origin of which is unclear.

As a result of fitting the data to the above described formalism, the inter-dimer exchange $J_3 = 3.1 \pm 0.06$ meV; effective dimer exchange $J_4' = 3.492 \pm 0.037$ meV, and energy splitting between the branches are fitted, and the latter defined as the difference in energy between the lowest energy excitation and the higher energy modes (blue, $\Delta_1 = 0.882$ ($\pm$ 0.0927) meV and green, $\Delta_2 = (1.9479 \pm 0.0622$) meV.

5.5.2 Intra-ladder (Q_k) dispersion

It is clear from inspection of the data presented in Figure 5.19 that the calculated dispersion relations for typical Heisenberg two-leg spin-ladders cannot be used to describe the excitations in $BiCu_2PO_6$, where an onset of incommensurate dispersion is clearly evidenced. The additional next-nearest-neighbour interactions are then significant in the exchange geometry and a model with their inclusion must be considered for a quantitative analysis.

The theoretical approaches outlined in §3.3 , while formulated for an isolated ladder, can be used as a model for the magnon dispersion in $BiCu_2PO_6$ by considering the Q_k direction only, and treating the inter-ladder term J_3 as a Q_k independent modulation to the observed dispersion. This is justified due to the geometry of the system where intra-ladder dynamics are contained solely within one crystallographic direction.

Each of these branches can be independently fitted to the magnon dispersions presented in §3.3, summarised in Table 3.1 and given by Equations 3.16, 3.20 and

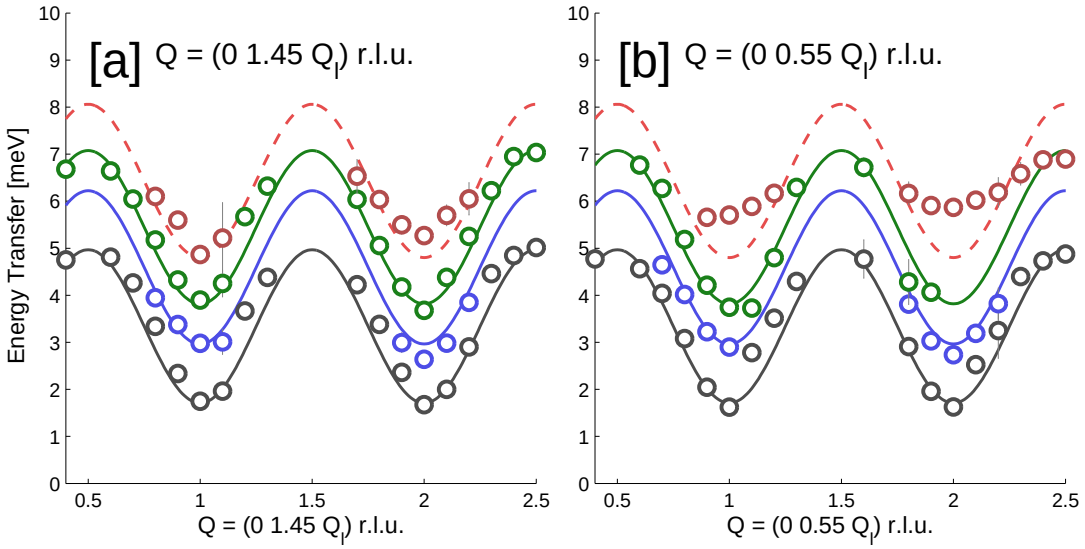

Figure 5.21: Dispersion along Q_l in BCPO, with fitted coupled dimer dispersion. **[a]** $\vec{Q}$ = (0 1.45 Q_l) r.l.u. **[b]** $\vec{Q}$ = (0 0.55 Q_l) r.l.u. The solid lines give the lines of best fit assuming a sinusoidal dispersion relation as described in the text. The fitted values are J_4' = 3.492 ± 0.037 meV, J_3 = 1.539 ± 0.033 meV and the energy splitting values between the modes are $\Delta_{1,2}$ = [0.882 (± 0.0927) , (1.9479 ± 0.0622)] meV.

3.21. A triplet mode, described by the blue diamonds in Figure 5.19 will be taken for illustrative purposes, but in the analysis to follow all three modes are simultaneously fitted assuming a uniform shift between them due to anisotropy.

First, the description formulated from second-order perturbations from the strong rung limit (SO-PSR) is considered, where $J_2 \neq J_2'$. Figure 5.22 demonstrates the efforts to fit the expression in Equation 3.20 through variation of multiple parameters within the expression. The solid blue line is utilising the SO-PSR parameters outlined in Ref. [42], given as $[J_1,\ J_2,\ J_2',\ J_4] = J_1[1\ 1\ 0.5\ 0.75]$, with $J_1 \sim 12$ meV. This parameterisation vastly overestimates the spin gap by an amount $\sim J_1$.

Accounting for any discrepancy in the dispersion along the ladder direction, one can take higher dimensional terms that correspond to inter-ladder coupling. Given the lack of dispersion along the Q_h direction, the entire interladder interaction resides in the Q_l direction considered in the previous section and shown to possess a dispersion bandwidth of $J_3/2 = 1.56$ meV resulting in a Q_k-independent shift $\Delta_k = (J_3/2)\cos(2\pi Q_l)$. This is not sufficient to account for the observed discrepancy. By taking this value, a dispersion can be 'fitted' by allowing J_1 to vary with the other parameters constrained to the established values. This results in a triplet dispersion that reproduces the spin gap but fails to reproduce the band width. The result of this method is given by the dashed blue line in Figure 5.22, and corresponds to a value of

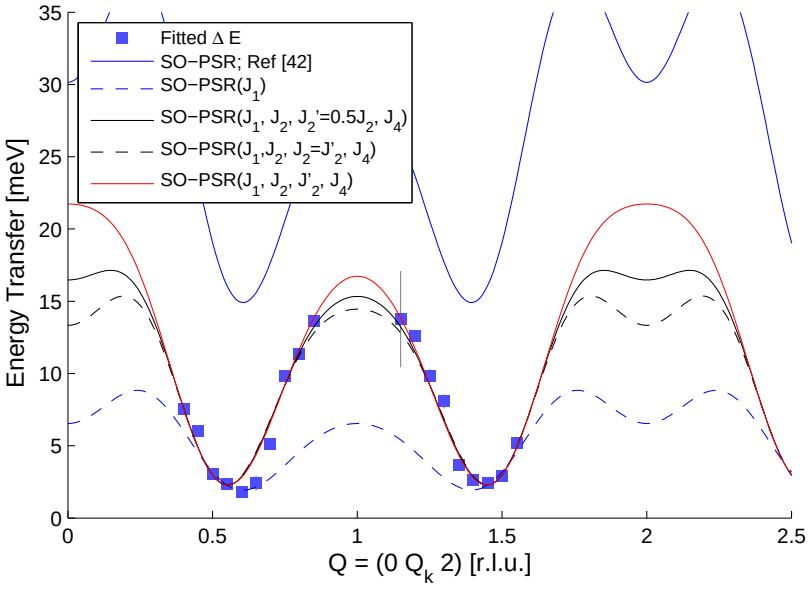

Figure 5.22: Dispersion assuming the SO-PSR expression given in §3.3 (Equation 3.20), fitted to the data presented in Fig. 5.19. The blue line is the dispersion for the parameters given in Ref. [42], the remaining lines are as described in the text. The blue dashed line is a fit allowing J_1 to vary. The black line, black dashed line and red line indicate fits when allowing J_1, J_2 and J_4 to vary given different values of J_2'. The fitted parameters are given in Table 5.5.

	J_1 (meV)	J_2/J_1	J_2'/J_2	J_4/J_1
Black solid line	5.5 ± 0.5	2.5 ± 0.2	0	2.4 ± 0.2
Red line	4.6 ± 0.25	2.0 ± 0.1	0.5	1.6 ± 0.3
Black dashed line	3.9 ± 0.5	1.6 ± 0.1	1.0	1.3 ± 0.7

Table 5.5: Fitted exchange parameters for $BiCu_2PO_6$ from the SO-PSR expression, with the first column denoting lines given in Figure 5.22.

$J_1 = 3.64$ meV.

Fits to the SO-PSR description can be made by removing constraints on one or all of the exchange parameters. The solid black line, the dashed black line and the red line in Figure 5.22 are the resultant dispersions with freely fitted J_1, J_2 and J_4, with $J_2' = 0.5J_2$, $J_2' = J_2$ and $J_2' = 0$ respectively. The three sets of parameters are given in Table 5.5.

It is clear there are multiple solutions to the presented data for consideration of different J_2 and J_2' values and further data is required to distinguish the cases in the SO-PSR formalism. Absence of data at the zone boundary is restricting the quality of the fit.

Now the dispersion relations formulated assuming $J_2 = J_2'$ are considered, using the

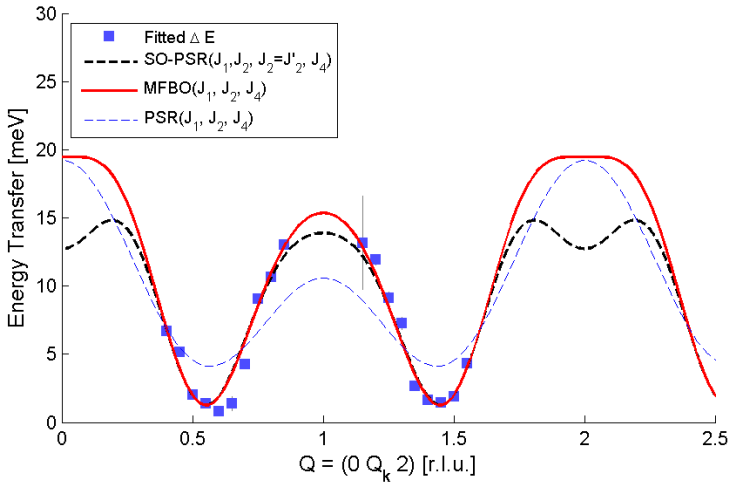

Figure 5.23: Q_k dispersion fitted to the data presented in Fig. 5.19, for PSR, SO-PSR and MFBO expressions. The black dashed line is the SO-PSR expression for $J_2 = J_2'$, as shown in Figure 5.22, compared to the second-order MFBO expression given by the red line and the PSR given by the dashed blue line.

expressions formulated from a first-order expansion in the strong-coupling limit (PSR) and the second-order mean field bond-operator method (MFBO). Both expressions are now fitted to the data and shown in Figure 5.23, allowing a free variation of J_1, J_2 and J_4 and assuming a uniform shift of $J_3/2$. These are plotted alongside the SO-PSR fit constraining $J_2 = J_2'$. The PSR and MFBO expressions are fitted with a self-energy correction $0.7(J_1^2 + J_2^2)/J_4^2$ [35].

It can be seen that the dispersion and spin gap are not well reproduced by fitting to the PSR expansion. While the second-order MFBO was not found to reproduce the gap produced by ED calculations in Ref. [39], it is shown in Figure 5.23 to both accurately reproduce the gap and the measured dispersion from the given INS results for the fitted parameters in Table 5.6. The fitted values result in a small J_1/J_4, placing the system closer to the strong coupling regime and the self-energy correction is small. Furthermore, inputting the fitted value $J_2/J_1 = 1.535$ into the first expression in Equation 3.22 results in a value for the incommensurate minimum $Q_m = 0.55$ r.l.u., close to that observed in the data. Due to the second order nature of the MFBO expression, two maxima are actually present near the values $Q_k = 0, 2$ r.l.u., similar to those observed in the SO-PSR dispersion in Figure 5.23. These are not easily discernable in the figure, but by putting the fitted values of Table 5.6 into the second expression of Equation 3.22, one can obtain the value for these maxima as $Q_m = \pm$ 0.04 r.l.u.

	J_1 (meV)	J_2/J_1	J_4/J_1
Red solid line	5.3 ± 0.5	1.5 ± 0.1	2.4 ± 0.2

Table 5.6: Fitted exchange parameters for $BiCu_2PO_6$ from the MFBO expression as plotted in Figure 5.23.

5.5.3 Scattering for $E > 15$ meV

The limited range of the experimental data presented above does not allow for a conclusive analysis of the dispersion. The multiple solutions from the different dispersion models provide a range of parameters that depend on the ratio of exchange interactions, and the nature of the ratio J_2/J_2'. In this sense the fit is underconstrained and a range of multiple parameters can qualitatively describe the data so far presented.

Additional high energy INS scans were measured to investigate the full extent of the bandwidth, near the region $Q_k = 2$ and for high energy transfer values $\Delta E > 15$ meV. To resolve the excitations in this region, IN22 was operated in an identical setup as described in §5.2.2, but at $k_f = 3.84$ Å^{-1}. This wavevector, while allowing access to high energy transfers $E \leq 50$ meV, does result in a coarser resolution with an energy resolution extending over 1-2 meV.

Energy-dependent scans were taken at $\vec{Q} = (0\ 1\ 2)$ r.l.u., $(0\ 1.2\ 2)$ r.l.u., $(0\ 1.8\ 2)$ r.l.u. and $(0\ 2\ 2)$ r.l.u., for energy transfers $\Delta E < 50$ meV in order to observe higher energy scattering and provide additional information to constrain the model. Figure 5.24 shows the collected data for the high energy scans. Multiple peaks in the intensity are observed for $\Delta E < 20$ meV, and across all values of observed momentum transfer a large, broad intensity peak is observed for $\Delta E > 20$ meV centred around ~ 25 meV.

The magnetic nature of an excitation can be elucidated through a comparison to data collected at higher temperatures. At momentum transfer $\vec{Q} = (0\ 2\ 2)$ r.l.u., that data for $T = 1.8$ K and $T = 200$ K are compared in Figure 5.24 [b]. The excitations remaining at high T can be identified as phonons, and the absence of the broad maximum confirms its magnetic nature.

The measured data is limited by the resolution, and observed scattered intensity is determined by the extent of the focusing condition. The convolution of an ellipsoid of finite width with a dispersion containing a steep energy gradient, as seen in the region of $Q_k \sim 1.7$ r.l.u., will result in an unavoidable instrumental broadening. Identifying the excitation modes for this region of reciprocal space requires the measurement of intensity via Q-scans at finite fixed energy transfer.

Such scans are performed for $\Delta E = 12$, 15, 20, 22.5 and 25 meV. Figure 5.25 summarises the extracted excitation energies from these Q_k-scans performed with the

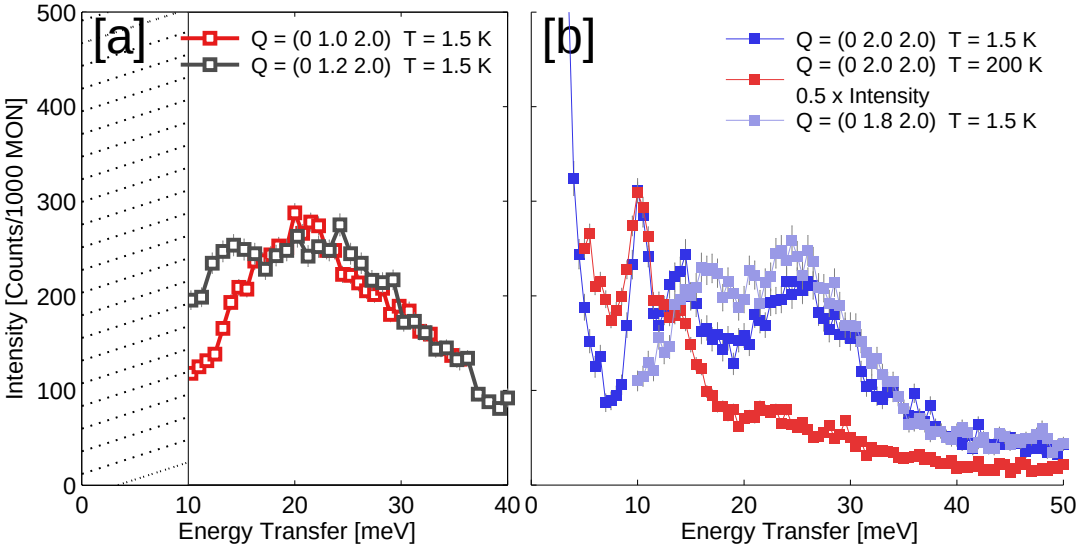

Figure 5.24: High Energy INS scans collected with $k_f = 3.84$ Å^{-1}. **[a]** $\vec{Q} = (0\ 1\ 2)$ r.l.u. and (0 1.2 2) r.l.u. **[b]** $\vec{Q} = (0\ 1.8\ 2)$ r.l.u. and (0 2 2) r.l.u. The red markers in [b] gives the intensity measured at $\vec{Q} = (0\ 2\ 2)$ r.l.u. for $T = 200$ K. All other scans are at base temperature ($T = 1.5$ K)

same $k_f = 3.84$ Å^{-1}. Panels [a] and [b] illustrate example Q-scans with the fitted intensity assuming a Gaussian lineshape in Q_k for the magnetic intensity. The peaks identified at $\Delta = 25$ meV have a smaller signal to noise ratio than those at lower energies. The scattering intensity at $Q_k = 2$ for the scans at $\Delta E = 12$ meV can be identified as non-magnetic in nature from the persistent intensity at $T = 200$ K.

A summary of all fitted intensities is presented in Figure 5.25 [c]. The black bordered white squares are peaks in scattering intensity that have been shown to be magnetic or have not been shown to be non-magnetic, and are plotted alongside a single peak extracted from the higher energy scans shown in Figure 5.24 and denoted by the black bordered white diamond. The blue bordered white diamonds and circles are peaks shown to be non-magnetic in nature and are included in this plot for completeness. It is to be noted that while non-magnetic intensity is idenfitied in these regions, it does not preclude the existence of coherent magnetic excitations, merely make them hard to resolve. The solid blue line and the dashed blue line are the SO-PSR and MFBO dispersions presented in Figure 5.23.

The scattering across the region of $Q_k = 1$ r.l.u. between 20 meV and 25 meV is broad with minimal features. This can be understood to be the result of a broad maximum in reciprocal space, either from continuum or from a flat band maximum that is convolved with the instrumental resolution, shown in [c] by the blue bordered ellipse.

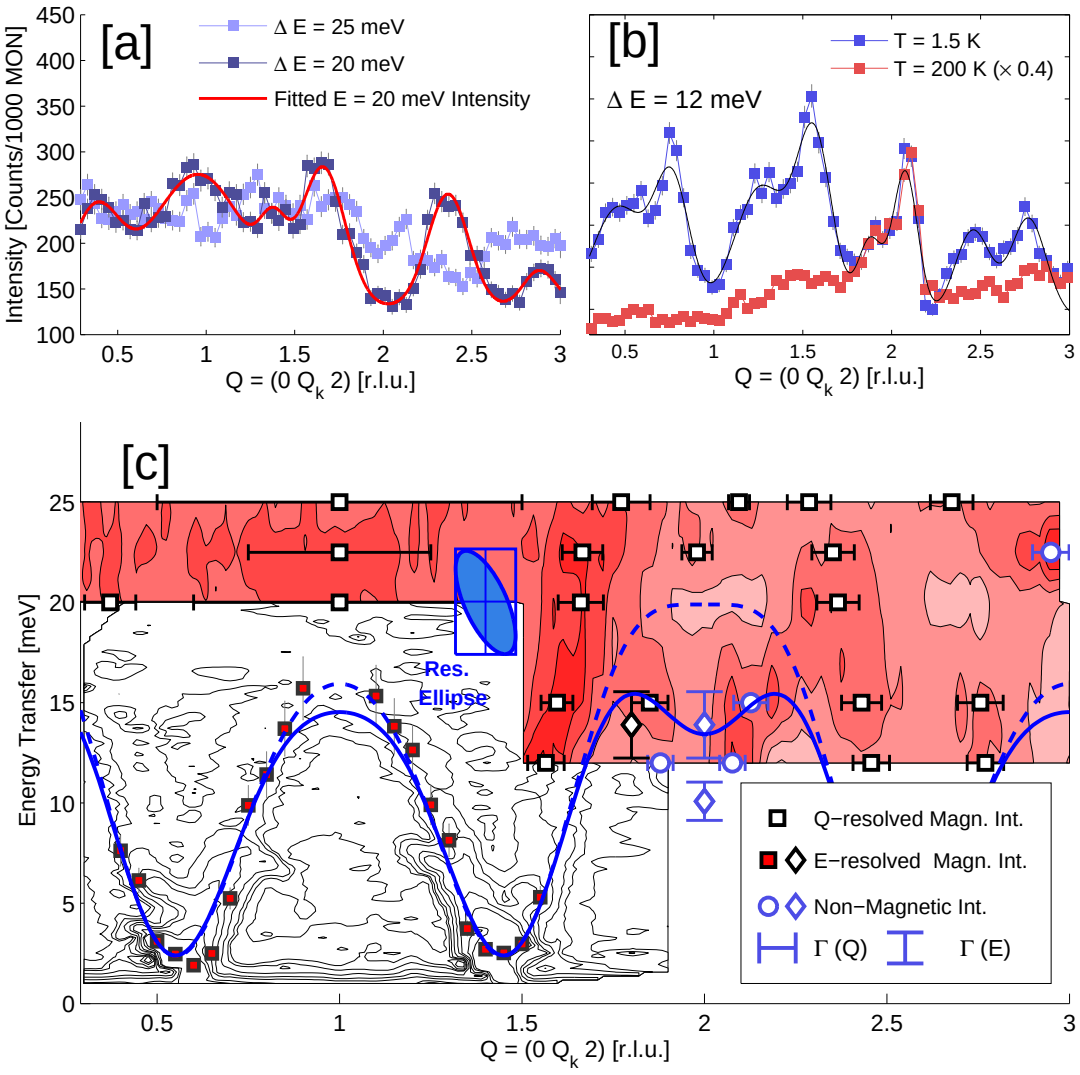

Figure 5.25: Summary of high energy excitations extracted from Q-scans and E-scans. **[a]** Fitted momentum resolved intensity for $\Delta E = 20$ meV alongside the raw data for $\Delta E = 25$ meV. **[b]** Fitted momentum-resolved intensity for $\Delta E = 12$ meV for $T = 1.5$ K alongside an identical scan conducted at $T = 200$ K, which has had a uniform scaling prefactor applied to allow for comparison. The intensity near $Q_k = 2$ r.l.u. is of non-magnetic origin, and is consistent with the intensity shown in Fig. 5.24. **[c]** The extracted excitations from the collated data; The fitted E-resolved excitation energies shown in Figure 5.19 are given by the red squares, with the additional unidentified mode at $Q_k = 1.8$ shown in Figure 5.24 given as a black diamond. The momentum-resolved modes are given by the black bordered squares. The modes known to be non-magnetic in origin are given by the blue bordered symbols. The bounding bars are indications of the FWHM, resolved in $\vec{Q}$ or E as is appropriate. The resolution ellipsoid at this k_f is as given, and the blue solid and dashed lines are the fits to the data as shown in Figure 5.23 for the SO-PSR and MFBO descriptions respectively. The black contours show the data previous presented in Figure 5.5, and the filled red contours show the high-energy data.

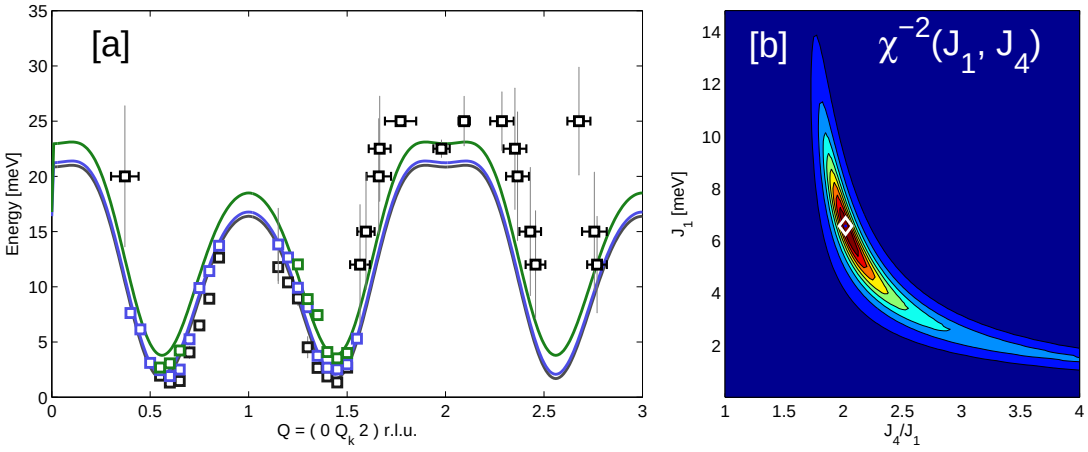

Figure 5.26: Best fit of MFBO theory to combined data including Q-resolved excitations. **[a]** The line of best fit described by the parameters in Table 5.7; **[b]** The inverse χ^2 from fitting the data to MFBO theory assuming multiple J_1 and J_4 parameters.

All observed Q-resolved peaks occur on a background that increases with energy, but does show some Q-dependent features, most notably in Figure 5.25[a], where the dark blue squares indicate the intensity at $\Delta E = 20$ meV at $Q_k = 1$ r.l.u. distributed over a width of ~ 1 r.l.u. while measuring minimal intensity at $Q_k = 2$ r.l.u. This and the observed 25 meV maximum in the high energy scan at $Q = (0\ 2\ 2)$ r.l.u. are magnetic and significantly broader than the known $(\vec{Q}, \omega)$ resolution of the instrument. These features cannot be attributed to coherent scattering and can instead be understood to be given by a broad two-magnon continuum. This will be addressed in §5.6.1.

The presence of the band maximum at $Q_k = 2$ is supportive of the dispersion being described by MFBO theory. The additional modes were incorporated into the fit of the dispersion relation where all magnon branches in Q_k and Q_l were fitted simultaneously to the second-order MFBO expression. The dispersion branches were assumed to be split uniformly in $\vec{Q}$ as in §5.5.1, with the magnitude of the splitting from the lowest energy excitation given by Δ_1 (first branch) and Δ_2 (second branch). The resulting fits are given in Figure 5.26 [a]. The accuracy of the fit is seen in [b], which gives a contour plot of χ^{-2} for J_1 and J_4, with a value of J_2 fixed by solving the equation

$$\left(\frac{d\omega(k)}{dk}\right)_{k=Q_m} = 0 = -[J_1 + 4J_2\cos(Q_m)]\left(1 - \frac{1}{J_4}[J_1\cos(Q_m) + J_2\cos(2Q_m)]\right) \tag{5.10}$$

for the assumed minimum $Q_m = 0.56$. The extracted parameters with associated error are given in Table 5.7.

	J_1 (meV)	J_2/J_1	J_3/J_1	J_4/J_1	Δ_1	Δ_2
Fitted Value	6.5	1.33	0.50	2.0	0.33	2.1
Fitted Error	0.20	N/A	0.02	0.02	0.13	0.05

Table 5.7: Fitted exchange parameters for $BiCu_2PO_6$ from consideration of all fitted excitation energies, assuming the MFBO expression.

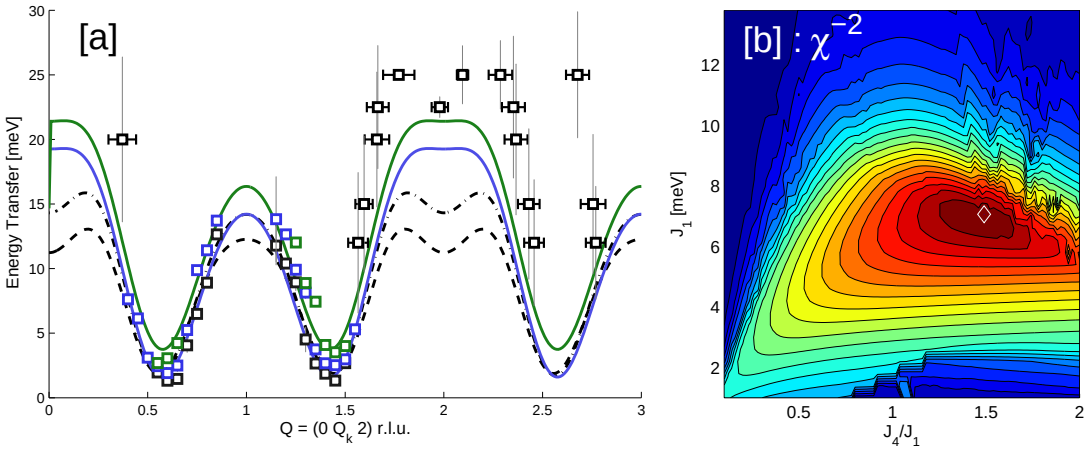

Figure 5.27: Best fit of the SO-PSR model to combined data including Q-resolved excitations. **[a]** The lines of best fit described by parameters in Table 5.8; **[b]** The inverse χ^2 from fitting the SO-PSR model for a range of J_4 and J_1 values. The dashed lines in [a] describe the fitted dispersion when $J_2 = 0.5$ and $J_2 = 0.25J_2$.

	J_1 (meV)	J_2/J_1	J_2'/J_1	J_3/J_1	J_4/J_1	Δ_1	Δ_2
Fitted Value	7.0	1.8	0.00	0.40	1.5	0.41	2.1
Fitted Error	0.40	0.10	0.10	0.03	0.20	0.18	0.08

Table 5.8: Fitted exchange parameters for the description using the SO-PSR model, from consideration of all fitted excitation energies.

This can be compared to a fit to the SO-PSR expression - considering all the extracted excitation energies in both reciprocal space directions, the dispersion was fitted to the SO-PSR theory allowing free variation of J_1, J_2, J_2', J_3 and J_4. The resulting fit is given in Figure 5.27 alongside a χ^2 plot of dispersions fitted for a range of J_1, J_4 values. The extracted parameters are given with errors in Table 5.8, including Δ_1 and Δ_2 as defined in the MFBO case.

The best solution is that of $J_2' = 0$, giving a J_2 value that is approximately twice that of J_1. The other parameters indicate a dominant rung coupling regime and are close to those of the MFBO result. Currently there is not enough information present to accurately fit the dispersion utilising the SO-PSR theory without constraining a specific ratio of J_2'/J_2, as can be seen in the χ^{-2} plot. Even under these constraints,

it is seen that $J_2' > 0$ cannot reproduce the band maximum at 25 meV, with examples for the best fits assuming $J_2' = 0.5J_2$ and $J_2' = 0.25J_2$ plotted by the dashed lines in Figure 5.27.

The result of the above analysis is that within current theoretical description, $BiCu_2PO_6$ exists in a regime dominated by rung coupling, with a dispersion described by MFBO with the MFBO parameters given in Table 5.7, or described by the SO-PSR theory with the parameters given in Table 5.8.

5.6 Magnetic Structure Factor

Considering now the scattering function defined in Equation 2.19, and the basis-appropriate spin operators given by $\mathbf{S}_i^+$, $\mathbf{S}_i^0$, $\mathbf{S}_i^-$ for the spin at site i, $S^{\alpha\alpha}(\vec{Q},\omega)$ can be rewritten for the singlet-triplet excitation basis. The scattering function for the triplet excitations are S^{++}, S^{00}, S^{--}, with one triplet excitation S^{++} given by

$$S^{++}(\vec{Q},\omega) = \sum_{i,j} e^{i\vec{Q}\cdot(\mathbf{R_i}-\mathbf{R_j})} \sum_{\lambda_i\lambda_f} \langle\lambda_i|\mathbf{S}_i^+|\lambda_f\rangle\langle\lambda_f|\mathbf{S}_j^+|\lambda_i\rangle\delta(E_{\lambda_i} - E_{\lambda_f} + \hbar\omega), \qquad (5.11)$$

where $|\lambda_i\rangle$ and $|\lambda_f\rangle$ are the initial and final states respectively and can be taken as singlet and triplet excitations $|s\rangle$, $|t^0\rangle$, $|t^+\rangle$ and $|t^-\rangle$. The S^{--} and S^{00} scattering functions are identical, due to the equality yielded from the summation over spin correlation functions.

The structure factor for interacting dimer systems can be formulated utilising the random phase approximation (RPA) and has been evaluated in Ref. [118, 119] in the context of the spin-dimer compound $Cs_3Cr_2Br_9$, and is formulated from a model including interactions between and within identical dimers on two different sublattices. The cross-section calculation considers finite exchange correlations within and between the sublattices and accounts for the two different excitations. It is given by

$$\frac{d^2\sigma(\vec{\kappa},\omega)}{d\Omega d\omega} \propto J[1-\cos(\vec{\kappa}\cdot\vec{R})]\left[\frac{\delta(\omega-\omega_A(\vec{q}))}{w_A(\vec{q})}[1+\cos(\vec{\rho}\cdot\vec{\tau}+\phi)] + \frac{\delta(\omega-\omega_O(\vec{q}))}{w_O(\vec{q})}[1-\cos(\vec{\rho}\cdot\vec{\tau}+\phi)]\right] \qquad (5.12)$$

where $\omega_{O,A}$ are the two mode energies, denoted as 'acoustic' and 'optical', ρ is the vector connecting the sublattices, τ is the reciprocal lattice vector and ϕ is the relative phase of the Fourier sum of the interactions between the sublattices. The $[1-\cos(\vec{\kappa}\cdot\vec{R})]$ term is typical of the INS cross-section of spin dimer systems and results from the interference of scattered neutrons from the two magnetic moments on the dimer. The

$[1 \pm \cos(\vec{\rho} \cdot \vec{\tau} + \phi)]$ terms are interference terms present due to the occurrence of two dimers within the unit cell, with the $\pm$ terms corresponding to the 'acoustic' and 'optical' branches. The sign difference in the interference term originates from the relative phase shift of π between the excitations.

The same RPA approach can be applied to interacting dimer systems with similar exchange geometry, and expressions for the dynamic structure factor have been formulated for the 3-D coupled dimer system $TlCuCl_3$ [64] and the weakly coupled ladder $(Hpip)_2CuBr_4$ [12] as

$$S^{\alpha\alpha}_{\pm}(\vec{Q},\omega) = \frac{J_r}{w_{\pm}(\vec{Q})}\left(\frac{1}{2}\sin\left(\frac{\vec{Q}\cdot\vec{K}_1}{2}\right) \pm \frac{1}{2}\sin\left(\frac{\vec{Q}\cdot\vec{K}_2}{2}\right)\right)^2 \cdot \delta(\hbar\omega - \omega_{\pm}(\vec{Q})) \quad (5.13)$$

with $\vec{K}_1$ and $\vec{K}_2$ as the two non-equal rung connection vectors of the contributing dimer units. The $\pm$ term results in two modes from the possible phase discrepancies between the spin correlations on each contributing dimer and correspond to the acoustic and optical states of Equation 5.12 as previously discussed.

Generalising further to $BiCu_2PO_6$, there are an increased number of possible excitations that can occur because of the four dimers present per unit cell, comprised of two ladders with two rungs each (Figure 5.2). The presence of two additional dimers in the unit cell does not require the extension of the RPA treatment from that used previously, as the Fourier transformed exchange interactions for two rungs within the same ladder are identical. However, the presence of a second, non-equivalent rung in each ladder results in a relative phase difference in relation to the exchange geometry.

As presented in §3.3 and shown in Ref. [42], there exists two excitation branches that result from the two non-equivalent rungs per unit cell, with a π phase shift between the two cases, consistent with a translation of half a reciprocal lattice vector between rungs.

This also manifests as a π phase shift between the Fourier transformed exchange interactions, which when applied to the structure factor calculations as in Equation 5.12, yields two results for the scattering function $S(\vec{Q},\omega)$, with $\phi_1 = 0$ and $\phi_2 = \pi$ for each respective excitation branch. As such the excitations are described by two 'acoustic' branches and two 'optical' branches, with the structure factor for each given

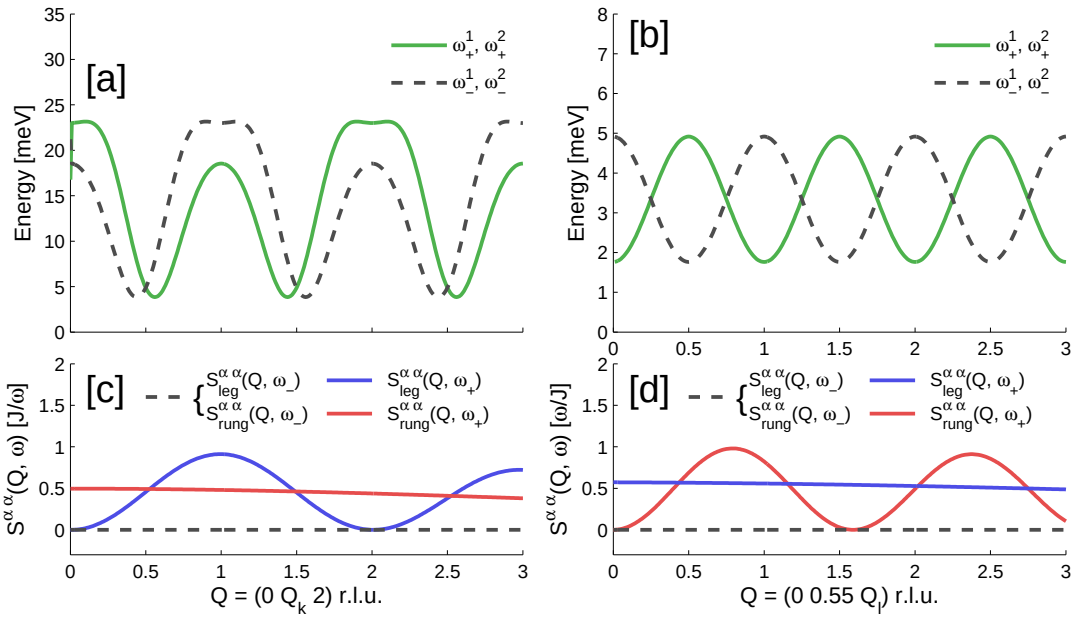

Figure 5.28: The dispersion relations and calculated structure factors for $\omega_{\pm}^{1}$ and $\omega_{\pm}^{2}$ along the leg and rung directions.**[a]** Dispersion for $Q = (0\ Q_k\ 2)$ r.l.u. **[b]** Dispersion for $Q = (0\ 0.55\ Q_l)$ r.l.u. **[c]** The calculated structure factor for $Q = (0\ Q_k\ 2)$ r.l.u. **[d]** The calculated structure factor for $Q = (0\ 0.55\ Q_l)$ r.l.u. The contribution from the legs has no modulation in Q_l, and the contribution from the rungs no modulation in Q_k.

as

$$
\begin{aligned}
S_{+}^{\alpha\alpha}(\vec{Q},\omega_{+}^{1}) = S_{+}^{\alpha\alpha}(\vec{Q},\omega_{+}^{2}) &= \frac{J_r}{w_{+}^{1}(\vec{Q})}\left(\frac{1}{2}\sin\left(\frac{\vec{Q}\cdot\vec{K}_1}{2}\right) + \frac{1}{2}\sin\left(\frac{\vec{Q}\cdot\vec{K}_2}{2}\right)\right)^2 \\
&\quad \cdot\,\delta(\hbar\omega - \omega_{+}^{1}(\vec{Q})) \\
S_{-}^{\alpha\alpha}(\vec{Q},\omega_{-}^{1}) = S_{-}^{\alpha\alpha}(\vec{Q},\omega_{-}^{2}) &= \frac{J_r}{w_{-}^{2}(\vec{Q})}\left(\frac{1}{2}\sin\left(\frac{\vec{Q}\cdot\vec{K}_1}{2}\right) - \frac{1}{2}\sin\left(\frac{\vec{Q}\cdot\vec{K}_2}{2}\right)\right)^2 \\
&\quad \cdot\,\delta(\hbar\omega - \omega_{-}^{2}(\vec{Q})).
\end{aligned}
\tag{5.14}
$$

where the dispersions for ω_{+}^{1} and ω_{+}^{2} are degenerate, and the dispersions for ω_{-}^{1} and ω_{-}^{2} are degenerate.

The correlations that contribute to the structure factor originate from a triplet excitation on a bond that then propagates to neighbouring sites, mediated by the intra-ladder and inter-ladder exchange interactions. The possible contributions to the structure factor can then be calculated with Equation 5.14 by considering correlations from both the leg and rung exchange interactions, J_{rung} and J_{leg} with connection vectors $\mathbf{K}_{rung} = [\pm 0.0176\ 0.000\ 0.6292]$ f.l.c., $\mathbf{K}_{leg} = [0.1620\ 0.500\ \pm 0.0020]$ f.l.c. The different structure factors are given in Figure 5.28 for two of the measured directions in reciprocal space.

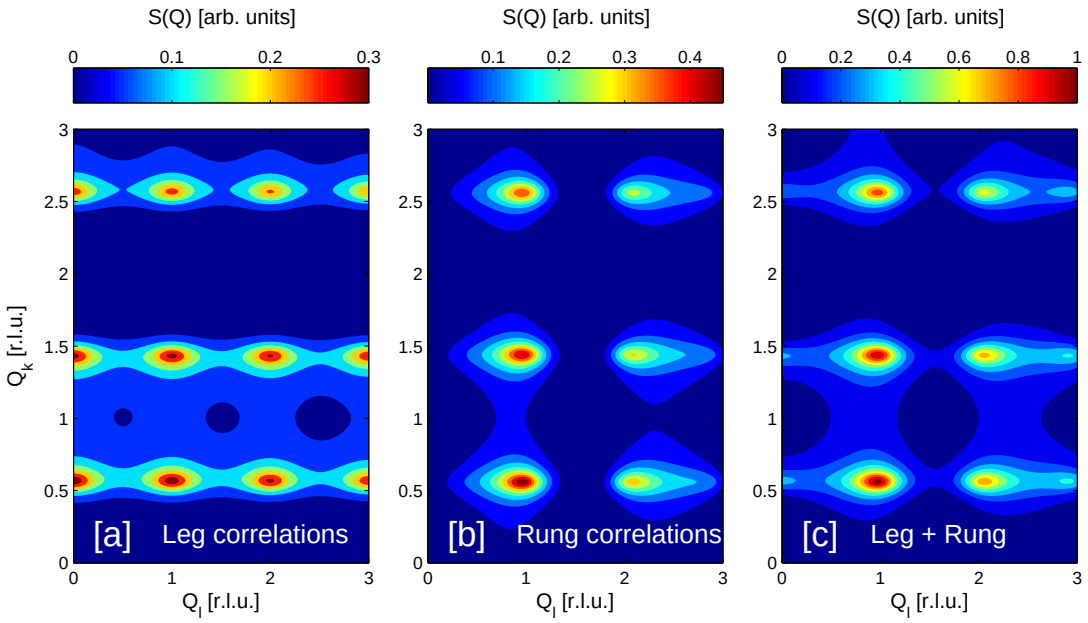

Figure 5.29: Contour plots of the structure factor contributions for $\vec{Q} = (0\ Q_k\ Q_l)$ r.l.u. **[a]** Structure factor contribution from correlations along J_{leg}; **[b]** Structure factor contribution from correlations along J_{rung}; **[c]** Addition of structure factor contributions from J_{leg} and J_{rung}, where a value $J_{rung}/J_{leg} = 2.0$ has been taken. All three have been corrected for the $\vec{Q}$-dependent form factor of the Cu^{2+} ion.

In Figure 5.28, panels [a] and [b] show the different excitations present in the unit cell for the Q_k and Q_l directions respectively. The dashed black line gives the dispersion that describes both ω_-^1 and ω_-^2, and the solid green line describes both ω_+^1 and ω_+^2. The structure factors in units of $[J/\omega]$ are given in [c] and illustrate the lack of spectral weight in the ω_-^1, ω_-^2 modes, and the dominant spectral weight for the leg and rung couplings in the ω_+^1, ω_+^2 modes. The structure factor for dispersion in the Q_l direction is similarly illustrated in [d].

The calculated structure factor for the two exchange couplings are presented in Figure 5.29. In these figures, the intensity plotted at $(Q_k,\ Q_l)$ is inclusive of the $1/\omega$ prefactor, and as such is given for appropriate excitation energy of the excitation considered, with [a] giving the structure factor from the leg correlations, [b] from the rung correlations and [c] the added total of these contributions weighted by the relative exchange energies, taking the fitted parameters from §5.5: $J_1 = 6.5$ meV, $J_4 = 13$ meV.

In Figure 5.30 the total calculated structure factor, with contributions from the leg and rung exchange, is compared to the data collected in scans in Q_k and Q_l. In these plots, the energy-integrated scattering intensity and the fitted single-mode integrated scattering intensity are plotted in Figure 5.30 [a] for Q = (0 1.45 Q_l) r.l.u. and [b] for Q = (0 Q_k 2) r.l.u.

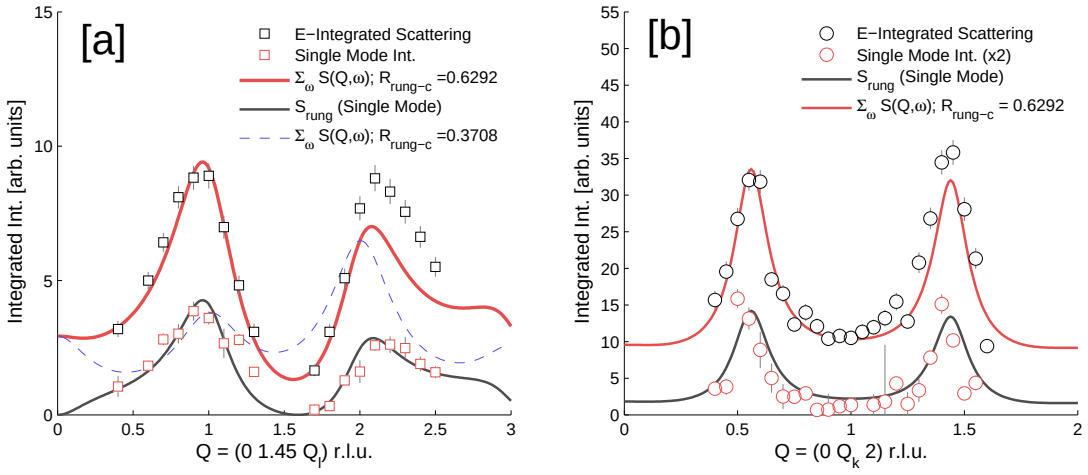

Figure 5.30: Comparison of the calculated structure factor to experimental results. **[a]** $\vec{Q}$ = (0 0.55 Q_l) r.l.u.; **[b]** $\vec{Q}$ = (0 Q_k 2) r.l.u. The total integrated INS scattering intensity for these directions is given by the black bordered squares (Q_l direction) and black bordered circles (Q_k direction). Integrated scattering intensity for a fitted single mode contribution is given by red bordered squares (Q_l) and red bordered circles (Q_k). The black line in [a] and [b] denotes the calculated structure factor for an individual mode, and the red line in [a] and [b] denotes the total integrated calculated structure factor. In [a], the calculation for total scattering intensity is also given for $\mathbf{R}_{rung-c}$ = 0.3708 f.l.c. (blue dashed line).

The red solid lines are the calculated structure factors given by Equation 5.14 assuming the magnon dispersions fitted in §5.5, where the contributions from all magnon branches, weighted for their respective excitations energies, have been integrated. The black solid lines are the calculated rung contribution to the structure factor in Q_k and Q_l for a single mode. Both of the calculated descriptions well describe the data, leading one to conclude that the rung correlations are indeed dominant.

It is to be noted that the NNN exchange couplings have not been considered in the implemented RPA solution, and as such are not included in this calculation which would introduce a renormalisation of the leg contribution to the calculated structure factor. Therefore any assumed ratios of leg to rung correlations cannot be exactly modeled, and an accurate fit awaits a complete RPA treatment of the frustrated ladder geometry of $BiCu_2PO_6$.

The dispersion calculations from the SO-PSR method [42] do not relate to the specific structure of $BiCu_2PO_6$, stating only the relative magnitudes of the exchange interactions. Their correspondence to real lattice geometry is not implicit, in particular they make no distinction over which atoms the exchange interactions exist. In Ref. [41] the exchange model was concluded to consist of the strong rung exchange existing on the J_4 with a connection vector $\mathbf{R}$ = [±0.0176 0.000 0.6292] f.l.c., with the inter-

ladder exchange corresponding to J_3 with a connection vector [±0.0176 0.000 0.3708] f.l.c. This result is confirmed through the Q-dependence of the dynamical structure factor, as illustrated in Figure 5.30 [a] by comparing the blue dashed line ($\mathbf{R}_{rung-c}$ = 0.3708 f.l.c.) and the solid red line ($\mathbf{R}_{rung-c}$ = 0.6292 f.l.c.), from which it can be seen that the connection vector with c-component $\mathbf{R}_{rung-c} = 0.6292$ is that which reproduces the data.

The observed structure factor is seen to peak at the values Q = (0, 1 ± 0.44, 1) r.l.u. and (0, 1 ± 0.44, 1) r.l.u. In absolute units, these maxima occur at $|Q| \sim 1$ Å^{-1} and $|Q| \sim 2$ Å^{-1}, the values previously observed to exhibit maximum INS intensity for powder samples of $BiCu_2PO_6$ measured by Mentre *et al.* in Ref. [41].

5.6.1 Two-Magnon Continuum

The triplet excitations observed and modeled in $BiCu_2PO_6$ near the spin gap minimum are well-defined quasi-particles, existing as coherent states of fundamental quanta of energy and momentum. The coherence of quasi particles across reciprocal space can be precluded beyond a certain threshold at which decay channels can be allowed by conservation laws and significant damping of the excitation can exist, leading to quasi-particle breakdown. This property has been investigated for quantum spin liquid materials made of dimers with triplet quasiparticle excitations, where breakdown occurs when a coherent excited state merges with its two-particle continuum [101].

Two-magnon continuum states in a gapped quantum magnet are simply composed of two single-magnon excitations [120]. For two magnons with $\vec{Q}_1$ and $\vec{Q}_2$, the energy Ω of the two-magnon particle with total momentum $\vec{Q} = \vec{Q}_1 + \vec{Q}_2$ is

$$\Omega(\vec{Q}) = \omega_0(\vec{Q}_1) + \omega_1(\vec{Q}_2), \tag{5.15}$$

where $\vec{Q}$ obeys the crystal momentum constraints. If a fixed two magnon momentum transfer is considered, a range of possible energies can be extracted by varying $\vec{Q}_1$ and constraining $\vec{Q}_2 = \vec{Q} - \vec{Q}_1$, demonstrated in Figure 5.31 for the extracted dispersion in $BiCu_2PO_6$. The range of excitations within the upper and lower boundaries are the aforementioned $S = 1$ continuum states. The black circles are given examples of two-magnon states formed from the single-magnon excitations given by the red circles.

The coexistence of continuum scattering with single triplon scattering with similar energy scales can be evidenced from the high energy scattering data presented in Figure 5.24 and presented again in Figure 5.32, plotted with a line of best fit to the total scattering intensity and with the contiuum contribution highlighted. Figure 5.32 illustrates a large amount of magnetic scattering extending to high energies. The lower

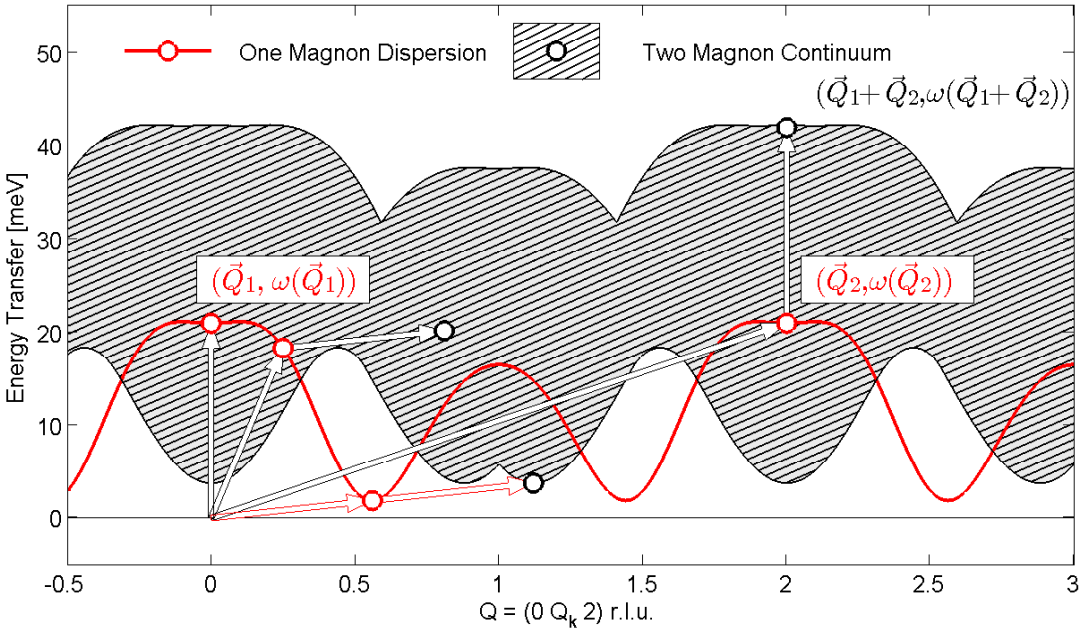

Figure 5.31: Formation of the two-magnon continuum from addition of two triplet excitations. The addition of the two ($\vec{Q}$, ω) values for the two magnons is shown by the vector-addition of the two black bordered arrows, resulting in a state lying within the continuum. The boundaries of the continuum are given by the solid black lines; an example of the contributing magnons are given by the red bordered arrows.

lying excitations have been identified as phonons due to their persistence and increased intensity at higher temperature.

The phonon excitations give the expected energy FWHM for a coherent excitation convolved with the resolution ellipsoid, allowing one to infer that the high energy magnetic scattering is not a coherent mode, but rather that of a two magnon continuum. The boundaries of the continuum at $\vec{Q}$= (0 2 2) r.l.u. can be deduced from the figure to be 7 meV and 42 meV, a consistent result with that plotted in Figure 5.31.

The lower continuum boundary shown is consistent with the observed INS intensities, where the majority of intensity is contained near the spin gap minimum and outisde the continuum region, as can be seen in Figure 5.33. As the one-triplon mode dispersion enters the two-particle continuum, decay channels become possible. The mode is thus damped and difficult to observe inside the continuum.

5.6.2 Two Magnon Bound States

These continuum states are delocalised excitations, and correspond to the formation of two $S = 1$ excitations that are sufficiently separated such as to experience min-

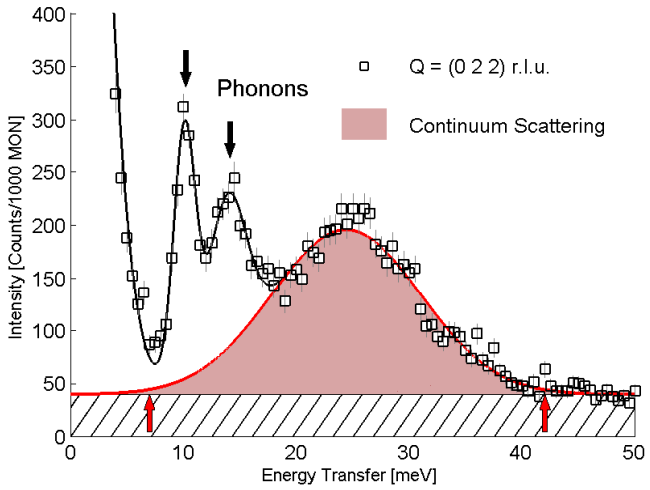

Figure 5.32: The high energy INS data presented in Figure 5.24, collected with the lower resolution at $k_f = 3.884$ Å^{-1}. The black line is the total fitted intensity, with the red shaded area the conjectured two-magnon continuum contribution. The two red arrows indicate the onset of the scattering and are consistent with the continuum boundaries given in Figure 5.31.

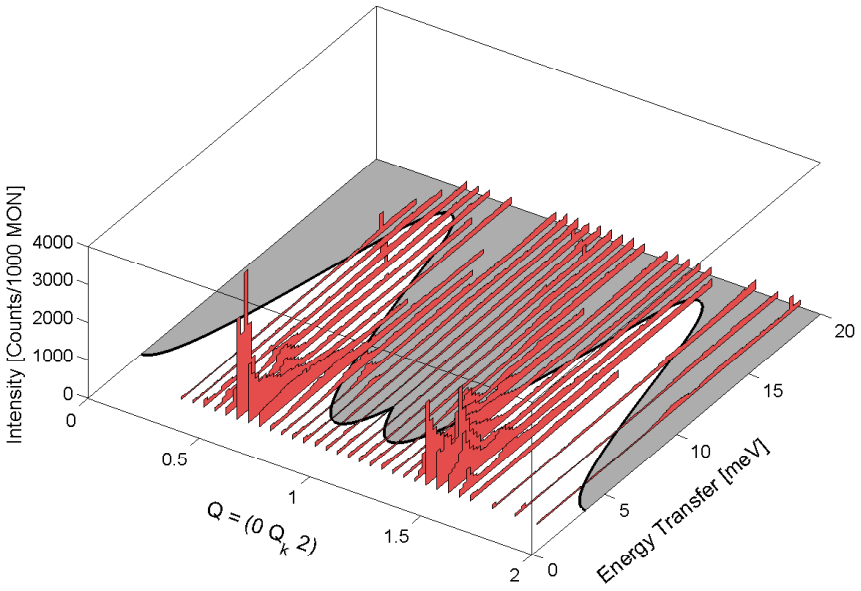

Figure 5.33: INS intensity as a function of $\vec{Q} = (0\ Q_k\ 2)$ r.l.u. and energy, compared to the continuum boundary. The shaded region in the basal plane is the area where continuum scattering is predicted to occur, with the black solid line the boundary. The red bars are the measured INS scans with the height indicating the intensity. The majority of the scattering is contained in the region outside the predicted continuum.

imal interaction. As the distance between the excited dimers decreases, the energy of the magnon excitation is lowered through an effective exchange interaction, with the maximum interaction occurring when the two-magnon excitation occupy adjacent

dimers.

The two-triplon creation matrix element in the INS cross-section that gives rise to the continuum of two-magnon scattering described in the previous section also allows the possibility of a coherent two particle excitation corresponding to a bound state of two single-triplet excitations. It may occur with a dispersion with an energy Δ_B below the lower continuum boundary, where Δ_B is the binding energy between the two excited one-particles states. This is referred to as a two-magnon bound state, and is a general feature of all gapped quantum spin systems [121], albeit only actually observed in a few systems [122].

Analysis of possible bound states of the unfrustrated S =1/2 quantum spin ladder has predicted the existence of an $S = 0$ and an $S = 1$ bound state [123]. Introducing frustration into the system complicates the description, but a multitude of bound states are predicted to exist with large binding energies [124].

Taking the model where the bound state occurs with the excitation of two triplets on adjacent rungs on a ladder, then two different bound states can be formed, corresponding to a binding mediated through the leg exchange J_1 or through the NNN exchange $J_2(J_2')$. The former would correspond to a bound state described by the addition of two modes located on equivalent rungs, and the latter on inequivalent rungs.

The bound state from addition of equivalent rung momenta is given by the boundary in Figure 5.31, and from the addition of inequivalent rung momenta in Figure 5.34 [a]. A comparison of the two boundaries to the as yet unfitted highest excitation branch (the white circles in Figure 5.19) is given in Figure 5.34 [b].

The structure factor for two magnon bound states differs from that of the single-magnon bound states, taken to leading order as $[1 + \cos(\vec{k} \cdot \vec{R})]$ [125, 126] and exists in antiphase with the single magnon excitation.

The calculated structure factors for the connection vectors of two exchange interactions present on the ladder, $\mathbf{R}_{NNN}$ and $\mathbf{R}_{leg}$ are presented in Figure 5.34 [c], given by the red and blue lines.

From the results presented in [b] and [c] it can be seen that the band dispersion given may be consistent with a two-magnon boundstate. However, these excitations could merely correspond to the continuum boundary, with the distinction between the two lying in the magnitude of the binding energy, an unknown quantity. To determine the correspondence of the above excitations to any continuum excitations, further experimental studies must be performed in combination with a formulation of a full theoretical treatment of two-magnon excitatons within $BiCu_2PO_6$.

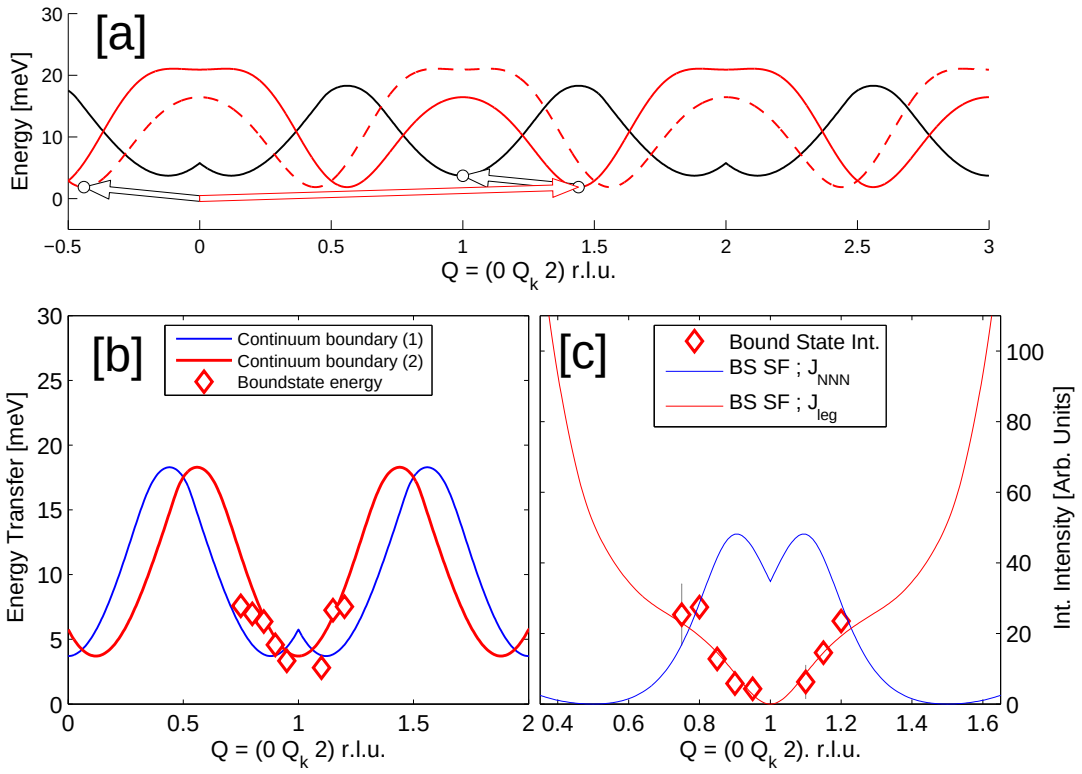

Figure 5.34: Summary of the proposed boundstate properties. **[a]** The formation of the lower continuum boundary (black line) with the two contributing triplons from inequivalent rungs (red solid and red dashed lines). **[b]** A comparison of fitted excitation energies to the lower continuum boundaries, given by the blue and red lines. **[c]** The integrated scattering intensity for the modes presented, compared to calculated structure factors.

5.7 Discussion and Outlook

As has been demonstrated in the preceding sections, the magnon excitation spectrum can reveal significant information about the Hamiltonian of a system subject to study. Specific to the case of $BiCu_2PO_6$, and drawing on the work presented, conclusions can be made about the exchange interaction geometry and dimensionality, the scattering weight and dispersion of single and two triplon excitations, spin-spin correlation terms in the dynamic structure factor and the effect of any anisotropic terms.

For an ideal spin dimer system, the excitations correspond to propagation of degenerate triplet excitations that are described by the standard Heisenberg Hamiltonian with isotropic exchange terms. The dispersion spectrum of $BiCu_2PO_6$ is a departure from this case, with a plurality of excitation branches with zero-field energy splitting that exhibit non-linear and mode-dependent coupling with the applied magnetic field for $\mathbf{H} \parallel \mathbf{a}$. These effects can be successfully parameterised through the combination of single-ion anisotropy and Dzyaloshinskii-Moriya interactions added to the isotropic

Hamiltonian.

The presence of anisotropic terms in the Hamiltonian is expected; in any real magnetic system there will always exist anisotropy[127] albeit sometimes on an energy scale too low as to make it experimentally indistinguishable from the isotropic case. The effect of anisotropic interactions in quantum magnets is an important topic of experimental investigation and theoretical discussion due to the significant effect on the ground state and low-energy excitations of such systems[128, 129, 130].

The contributing terms within $BiCu_2PO_6$ can be split into those present on the rungs, described by an effective single-ion term and a DM term, and those present on the legs, described by a DM term. The rung single-ion anisotropy is used to parameterise the observed behaviour through the implementation of an easy axis through the terms E^x and E^z. These terms only hint as to the consequence of the anisotropy and not its origin, with the assumption of a relation between the anisotropy and the local crystal field. The DM anisotropy terms are sourced from the allowed DM interaction terms that come from non-centrosymmetric leg and rung connection vectors; this term results in the mixing of triplet excited states which, on the level of the three lowest excitations, reproduce the data with one field-independent excitation and two non-linear excitations with differing field dependence.

It is to be noted that this can be used to qualitatively describe the data only; the values of the quoted parameters reproduce behaviour seen in the data but neglect key important features that are important in the magnitude of the spin gap. Quantitative analysis requires the application of a more comprehensive model that accounts for NNN exchange, multiple linked clusters and momentum-resolved excitation energies. A full theoretical extension of the bond operator theory or ED calculations could help elucidate the magnon dispersion relation upon implementation of the allowed anisotropies.

Analysis of the structure factor observed from the powdered samples in Ref. [41] yielded results for the exchange geometry that necessitated strong NNN exchange $J_2 > 0.5J_1$ to reproduce the observed double peak structure of maximum scattering intensity, with a predicted value in the range 0.7 - 1 J_1. Furthermore, it was shown that the range of J_2/J_1 that reproduces the split intensity is relatively narrow compared to the J_4/J_1 range. This suggests that it is the NNN exchange that is largely responsible for the incommensurate nature of the material, and the strength of said interaction must be on the same scale as the rung and leg exchange. For example, an un-frustrated ladder system such as $La_4Sr_{10}Cu_{24}O_{41}$ shows commensurate dispersion [112].

This supports the results that find the excitation energies described by the MFBO and SO-PSR dispersion representations, in which the incommensurate minima is pro-

duced from the NNN exchange J_2 (and J_2'). A specific J_2 value can be fixed for the MFBO solution (in which $J_2/J_2' = 1$), but a range of values for J_2 and J_2' result from consideration of the SO-PSR theory.

The exact determination of the exchange value(s) is then dependent on the validity of the assumption of a dominant rung coupling regime, the requirement that $J_2 \neq J_2'$ and the relative suitability of the MFBO approach to describe the system. For the case $J_2 = J_2'$, the SO-PSR result for the NNN exchange is that of the MFBO fit, but with a different resulting J_4 that fails to describe the high energy scattering at $Q_k = 2$.

At present, information is lacking to distinguish the validity of the two models, with both producing reasonable descriptions of the data. The assertion of $J_2 \neq J_2'$ is made with numerous structural arguments and numerical studies [42] and an estimate from a LSDA + U approach indicates $J_2' \simeq 0.5J_2$, but the input of these values into the SO-PSR description does not yield a satisfactory result. While ED calculations have been performed to test the validity of the MFBO approach for a set of parameters within the incommensurate strong coupling regime ($J_2 = 0.6J_1$, $J_4 = 3J_1$), further calculations are required to confirm the results for the exchange values extracted from the data. Indeed, ED calculations across all derived exchange values would be sufficient to distinguish the two cases and confirm the values of the exchange interactions.

The formulation of the theoretical representations have been made upon the assumption of dominant rung correlations. This would seem to be counter to the observation that $BiCu_2PO_6$ demonstrates a larger ratio of band width to band gap than would be typically expected of a strongly-coupled system, and the determined exchange interactions $J_1 + J_2 \simeq J_4$ are those inconsistent with a typical formulation of strong-rung coupling. However, it could be reconciled by the observation that the leg-connection vectors are not ones that are preserved by the symmetry operations of the lattice. Therefore, excitations of triplets on the legs could therefore be rendered untenable by the same symmetry operations, resulting in the rung excitation being preferable despite the lack of a dominant rung coupling term.

The validity of assuming dominant rung correlations is confirmed through the $S(\vec{Q}, \omega)$ representations presented in §5.6, in which the fitted triplet mode intensities and integrated scattering intensities were compared to the calculated structure factor, and were seen to be well described by the leading interference term [1 - cos($\vec{Q} \cdot \vec{R}_{rung}$)].

The intensity of the scattering from the two-magnon continuum has been studied for similar cases of spin ladder geometries with single runged unit cells, where bound states and continuum states are formed from the additive momenta of identical excitations on the ladder units. The low energy scattering in $BiCu_2PO_6$ observed near $Q_k = 1$ r.l.u. follows the evolution of the lower boundary of two-magnon excitations formed

by additive momentum of excitations with the weak intensity typical of two-magnon boundstates.

Theoretical models have been applied with some success to account for elements of the observed magnetic excitations. However, further work is needed to provide a complete and self-consistent model to describe the properties of $BiCu_2PO_6$. In particular, a full model should include: magnon dispersion relations for a full frustrated exchange geometry for different exchange interaction ratios; the inclusion of aniostropic terms within the Hamiltonian, such as Dzyaloshinksii-Moriya interactions; and a full theoretical treatment for the one-magnon and two-magnon terms of the structure factor of $BiCu_2PO_6$.

In conclusion, the frustrated two-leg spin ladder system $BiCu_2PO_6$ has been investigated through INS along the main symmetry directions. Coherent magnon excitations have been observed and fitted, with the excitation energies extracted and analysed with theoretical models for the dispersion from first order strong-rung perturbations, MFBO theory and second-order strong-rung perturbations, resulting in an estimate for the exchange parameters given in Table 5.7.

The fitted INS intensity is found to be in excellent agreement with the calculated structure factor formulated for a strong-rung coupling model, albeit with additional scattering observable in the integrated scattering intensity across the measured energy range, which has been argued to originate from appreciable continuum scattering.

Summary

$BiCu_2PO_6$ is a frustrated quasi-1D two-leg spin ladder system with a plurality of dispersive magnetic excitations. Neutron scattering studies have been performed to investigate these excitations, including a comparison to theory, an investigation into anisotropy and a study of the applied field dependence.

- The dispersion of the magnetic excitations along the ladder (crystallographic b direction) is incommensurate with the lattice, with a spin gap minimum occurring for $Q_m \simeq$ (0 0.56 2) r.l.u.
- The dispersion is commensurate in the crystallographic c direction. There appears to be no or minimal dispersion in the crystallographic a direction.
- A first estimate of the exchange interactions have been produced, from fits to expressions from perturbative expansions, and mean-field bond operator theory. The dispersion appears to be dominated by the rung correlations.

- A region of magnetic scattering exists at high energy transfers, corresponding to a continuum of two-magnon excitations, with a possible two-magnon boundstate occurring in the region $\vec{Q} = (0\ 1\ 2)$ r.l.u.
- Sources of anisotropy appear to be present, resulting in zero-field splitting of the excitation energies and non-linear applied magnetic field dependence.

Additional theoretical contributions are required to formulate a satisfactory model that captures the essential features highlighted above. In particular, expressions with full consideration of both the frustrated leg couplings and the contributions of anisotropy into the Hamiltonian are necessary.

6

$BiCu_{2(1-x)}Zn_{2x}PO_6$ - Impurity-induced Antiferromagnetism

In this chapter I will outline the experimental studies of the magnetic properties of the impurity-doped two leg spin ladder $BiCu_{2(1-x)}Zn_{2x}PO_6$ (BCZnPO), created through Zn doping of the $BiCu_2PO_6$ spin ladder system discussed in the previous chapter. Large single crystal samples have been investigated for doping concentrations x = 0.01, 0.03 and 0.05 by INS and neutron diffraction to determine the properties of the observed antiferromagnetic order.

A background of $BiCu_{2(1-x)}Zn_{2x}PO_6$ and other impurity doped spin gapped systems will be presented, followed by a summary of the field and temperature dependence of the emergent long-range magnetic order, a magnetic structure determination from the reciprocal space distribution of measured Bragg scattering, analysis of the coherence of the ground state and an investigation of the effect of doping on the spin gap. A discussion of the salient points will follow with an outlook for further work.

6.1 Background

The introduction of magnetic order by non-magnetic impurities is a phenomenon that has sparked much interest in the field of gapped low-dimensional quantum magnets [131]. In such magnets, the ground state is separated from excited states by a finite gap that is due to quantum effects e.g. dimerisation of $S = 1/2$ moments. Thus, the magnetic correlations are characterised by the energy scale of the gap and are dynamical in nature. Below these energy values all spin degrees of freedom vanish [132].

When non-magnetic impurities are introduced onto a lattice with a dimerised ground state, each acts to break a singlet resulting in the creation of one spin-1/2 degree of freedom. This kind of induced spin is typically referred to as a Local Moment (LM) due to its tendency to remain highly localised around the impurity [133, 134]. While the moments are considered localised, they can exhibit long-range interactions mediated by intermediate spin sites. The energy scale of these interactions dominate the low-energy region, with their magnetic properties determined by an effective coupling J_{eff} between LMs and correlation length ξ_{LM}, which are in turn dictated by the exchange, geometry and dimensionality of the parent compound [131].

Properties of the magnetism arising from impurity-doping has been the focus of much experimental and theoretical work, with a range of exchange geometries being investigated. Examples include the spin-Peierls chains $Cu_{(1-x)}(Zn \text{ or } Ni)_xGeO_3$ [135, 136], the 1-D Haldane chains $Pb(Ni_{1-x}Mg_x)_2V_2O_8$[137, 138], $Y_{(2-x)}Ca_xBaNiO_5$ [139], the quasi-1-D isolated spin ladder $Sr(Cu_{(1-x)}(Zn \text{ or } Ni)_x)_2O_3$ [140, 141], and the 3-D coupled spin dimer $TlCu_{(1-x)}Mg_xCl_3$ [142]. Only recently has work been done on impurity-induced magnetism on a parent insulator that possessed incommensurate magnetic correlations.

As an inorganic spin ladder $BiCu_2PO_6$ is an excellent candidate for Zn-substitution, allowing for the growth of large crystal samples for a range of concentrations that is typically more difficult for inorganics or metallic systems. The resultant compound, $BiCu_{2(x-1)}Zn_{2x}PO_6$, can be investigated considering the above outlined approach of liberated LMs interacting on a fluctuating rung-singlet ground state with frustration effects. The magnetic correlation between and within the LMs will help elucidate the properties of the Hamiltonian.

Susceptibility measurements conducted on a SQUID magnetometer result in an observed susceptibility smaller than expected from a free $S = 1/2$ moment (corresponding to an effective paramagnetic moment of $S \sim 0.3$) [143]. This can be understood by a spin not being localised on a single site, but instead developing an induced, extended alternating cloud as illustrated in Figure 6.1. The properties of this cloud have been extensively studied with NMR [144], indicating the extension of the paramagnetic cloud over multiple lattice units. Furthermore, it was indicated that the distance over which the moment is extended, ξ_{LM}, is independent of impurity content, an assertion supported in Ref. [111] by QMC simulations.

At low enough temperatures, the LMs from spin impurities can exhibit long-range order or spin freezing [145, 146]. This is an observed property of the system when there is a sufficiently strong effective exchange interaction that allows for the long-range correlation of impurity induced spins, and has been observed in $BiCu_{2(1-x)}Zn_{2x}PO_6$

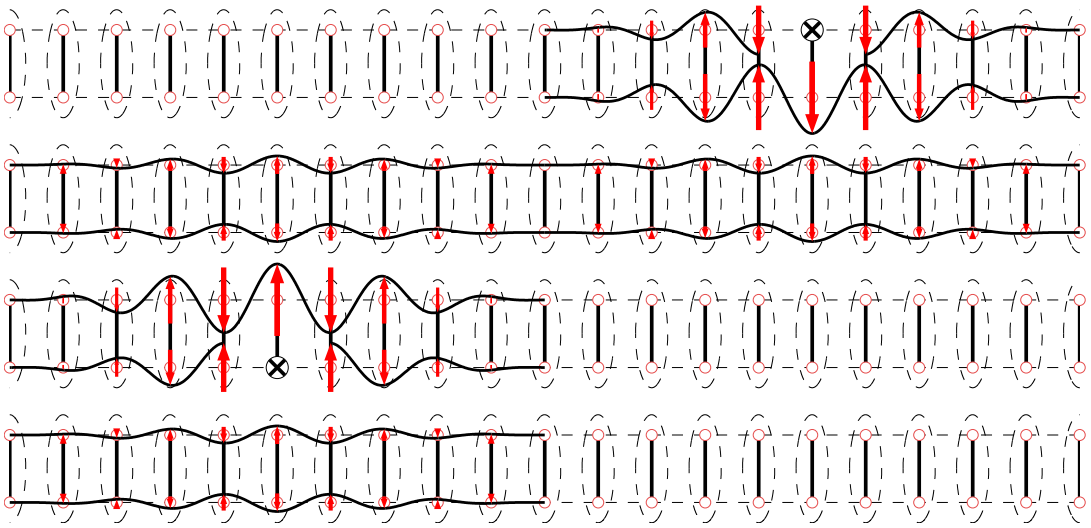

Figure 6.1: The effect of non-magnetic impurity doping on a ladder system. The red bordered circles illustrate the Cu sites which couple into dimers, indicated by dashed ellipses. Replacing a Cu site with a Zn impurity (white circle with black cross) breaks a dimer bond and liberates a free spin. This LM induces a finite size extended magnetic moment with reduced moments located on adjacent spins. The LMs can correlate with each other through the intermediate, undoped dimers.

[111, 144]. Furthermore, Bobroff *et al.* [111] present evidence that the observed spin freezing is a universal observation of impurity-induced magnetism that results from an extended magnetic moment that is similar in all systems that lie far from a QCP, resulting in a linear dependence of the freezing temperature T_g on x (Figure 6.2).

In addition, while coherent magnetic ordering has been observed, recent theoretical work has predicted the existence of a spin glass (SG) type magnetic ordering within site-diluted incommensurate gapped magnets [147]. This is supported by recent DC-susceptibility measurements on $x = 0.05$ single crystals, which indicate the presence of SG-like behaviour existing within $BiCu_{2(1-x)}Zn_{2x}PO_6$. This is evidenced by an onset of irreversibility that is not typically a feature found within long-range ordered anti-ferromagnets, but occurs within the doped compounds alongside an AFM transition at $T_N \sim 4.2$K [148]. Upon application of field $\mathbf{H}||\mathbf{b}$, the onset of irreversibility moves to lower temperatures (Figure 6.3). It has been argued that the ground state of the doped compound has features both from spin glass and long-range magnetic order, an assertion supported by muon spin resonance [111], and that the glassiness is lost under application of applied fields. It has been hypothesised that this is a result of interacting, finite-sized clusters as seen in $Sr(Cu_{(1-x)}Zn_x)_2O_3$ [149].

The impurity concentrations required to achieve spin freezing are small, but even small amounts of substitution have been seen to have a drastic effect on the inelas-

Figure 6.2: The dependence of the transition temperature T_g on impurity concentration for some spin systems. The symbols refer to the coupled ladders $BiCu_{2(1-x)}$(Zn or Ni)$_{2x}PO_6$, isolated ladders $Sr(Cu_{(1-x)}$(Zn or Ni)$_x)_2O_3$, the Haldane chain $Pb(Ni_{1-x}Mg_x)_2V_2O_8$ and the spin-Peirels chains $Cu_{(1-x)}$(Zn or Ni)$_xGeO_3$. The figure on the right is the same data, scaled relative to the value at 3%. The T_g values exhibit similar impurity dependence at low concentrations. Figure 4 from [111].

tic spectrum of many of the spin compounds under investigation, as can be seen in the work on the Spin-Peirls compound $CuGeO_3$ with Zn-doping [150], the 3D coupled spin dimer $TlCuCl_3$ under Mg-doping [151] and the two-leg spin-ladder compound $Sr(Cu_{1-x}Zn_x)_2O_3$ [140]. In these examples it is found that drastic changes of the system Hamiltonian occur upon the introduction of even small quantities of non-magnetic impurities into the lattice, a result confirmed through numerical calculations [152, 153].

In this chapter, experiments will be outlined that investigate the onset of long-range, impurity induced magnetic order in $BiCu_{2(x-1)}Zn_{2x}PO_6$. Neutron scattering studies will be outlined in an attempt to discern the static magnetic correlation lengths, the phase diagram in temperature and applied field, a magnetic structure determination and investigations of the renormalisation of the excitations.

6.2 Single-Crystal Samples

The doped single crystal samples used for the detailed experiments were grown in the same fashion as those described in §5.2.1, by S.Wang *et al.*, LDM (PSI) [114]. Single crystal samples of $BiCu_{2(1-x)}Zn_{2x}PO_6$ were grown with the concentrations $x = 0.01$, 0.03 and 0.05. The homogeneity of the samples was measured through Micro-X-ray-Fluorescence (Micro-XRF), and the doping concentration of the samples measured at

Figure 6.3: The phase diagram for $BiCu_{2(1-x)}Zn_{2x}PO_6$, from susceptibility measurements [148]. Magnetic field is applied such that $\mathbf{H}||\mathbf{b}$, with the transition between a region of coexisting spin glass and antiferromagnetism (SG + AFM) to the AFM region indicated by the red circles. The black circles denote the transition from a state of AFM to a state of disorder (Quantum Paramagnetism, or QPM). With increasing field, the SG transition moves to lower temperatures.

Compound	a ($\AA$)	b ($\AA$)	c ($\AA$)
$BiCu_2PO_6$	11.7768(1)	5.1729(0)	7.7900(1)
$Bi(Cu_{0.99}Zn_{0.01})_2PO_6$	11.7800(1)	5.1742(1)	7.7924(1)
$Bi(Cu_{0.95}Zn_{0.05})_2PO_6$	11.7822(1)	5.17770(1)	7.7969(1)

Table 6.1: Lattice parameters of $BiCu_{2(1-x)}Zn_2PO_6$, taken from [114], measured at room temperature.

different positions in each crystal.

The samples were found to have a good level of homogeneity, with concentrations varying little throughout the sample. There is some radial variance in concentration in the single crystal rods, but within about 5% of the prescribed x value [154].

The samples were analysed with X-ray/Neutron Laue diffraction to discern their main crystallographic axes, and were cut for use in neutron scattering studies. They were mounted inside custom sample holders such that they were typically aligned in the **b-c** scattering plane. The $x = 0.03$ and $x = 0.05$ samples are shown in Figure 6.4, with the lattice parameters for $x = 0.01$ and $x = 0.05$ given in Table 6.1.

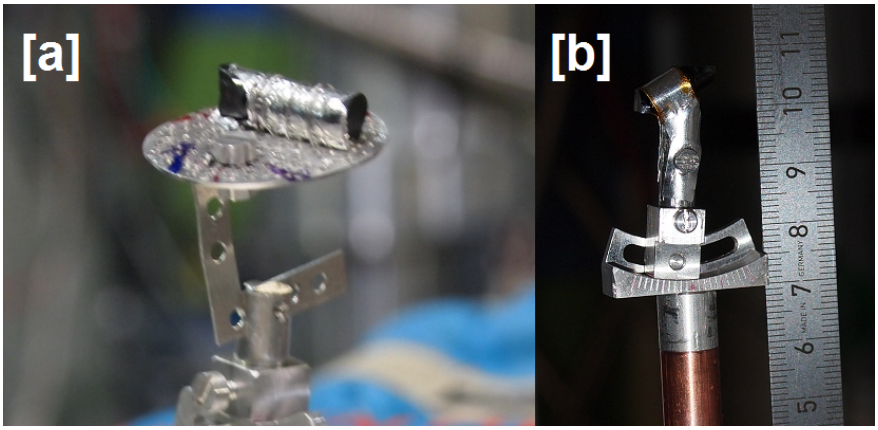

Figure 6.4: Single crystal samples for use in Neutron Diffraction and INS experiments. **[a]** $x = 0.03$ sample. **[b]** $x = 0.05$ sample. In both cases, sample mounts are used that include a small goniometer for high-precision alignment.

6.3 Magnetic Order

6.3.1 Neutron Diffraction Study

Initial studies to investigate the onset of impurity-induced magnetic ordering in the $x = 0.01$ and $x = 0.05$ samples were conducted in an experiment in October 2010 on the RITA-II spectrometer at SINQ, PSI. The single crystals were oriented in the **b-c** scattering plane on a regular sample stick ($x = 0.05$) and a dilution stick ($x = 0.01$) mounted inside an Oxford Instruments 15 T cryomagnet. This allowed for an operational temperature range down to 100 mK. The cryomagnet allowed for the setting of stable fields $H < 15$ T, running in persistent current mode.

RITA-II [155] is a cold neutron triple-axis spectrometer and is located on the beam guide system RNR13 at SINQ, PSI. A monochromator is placed before the sample consisting of a combination of vertical and horizontally focusing PG(002) crystals, with a mosaicity of $40'$ in both directions. A Be-filter was placed between the sample and the analyser. The analyser consists of nine separate PG 'blades', mounted on vertical axes. Scattered neutrons are measured on a position-sensitive detector that can separately count scattered contributions from each of the blades. Confining the experiment to a narrow $\vec{Q}$ region in diffraction mode, only intensity from the central blade may be considered.

The instrument was operated without additional collimation, and the motors of electronically controlled slits before and after the sample were removed due to the application of large magnetic fields.

At a temperature of $T = 1.5$ K, magnetic ordering was observed through the measurement of significant Bragg peak intensity at $\vec{Q} = (0\ 0.56\ 2)$ r.l.u., shown in

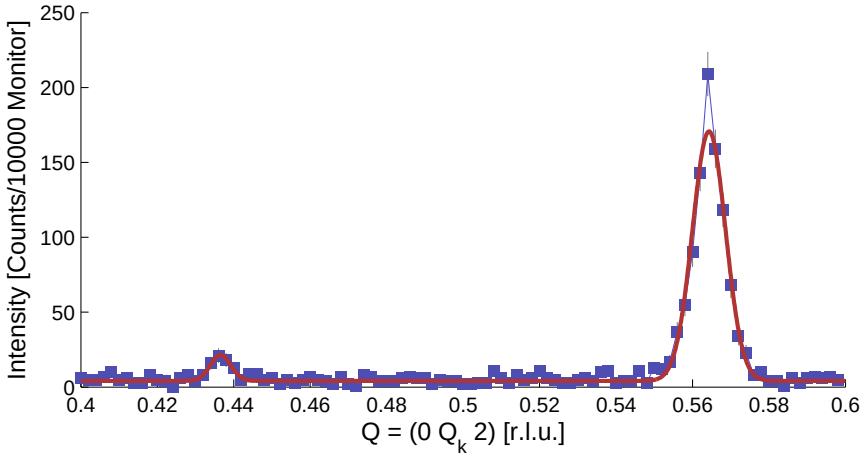

Figure 6.5: Long-range magnetic order in $BiCu_{2(1-x)}Zn_xPO_6$, $x = 0.05$. Q-scan for $\vec{Q} = (0\ Q_k\ 2)$ r.l.u. Two magnetic Bragg peaks are observed at $Q_k = 0.44$ and 0.56 r.l.u. at $T = 1.5$ K

Figure 6.5. It can also be seen in the figure that a second Bragg peak is also present at a second incommensurate wavevector $\vec{Q} = (0\ 0.44\ 2)$ r.l.u., albeit of significantly lower scattering intensity (integrated intensity $I_{Q_k=0.44} \sim 0.064\ I_{Q_k=0.56}$).

The magnetic peak at $\vec{Q} = (0\ 0.56\ 2)$ r.l.u. was systematically investigated as a function of field and temperature. Initial high-resolution Bragg scans along Q_k were conducted at $T = 1.5$ K for a range of applied field values $H < 13.5$ T, and at $H = 0$ T for a range of temperatures 1.5 K $< T <$ 6 K. Contour plots summarising the intensity as a function of Q_k are presented in Figure 6.6, for [a] applied field dependence and [b] temperature dependence. In panels [c] and [d], the peak position is plotted for the indicated variables, and illustrates that the magnetic Bragg peak centre does not show any change as a function of temperature and field.

Similar studies were performed on the $x = 0.01$ sample, mounted in the Cryomagnet with a base temperature $T \sim 100$ mK. Figure 6.7 illustrates the magnetic Bragg peak intensity for scans in temperature and field illustrating the constant incommensurate ordering wavevector, $Q = (0\ 0.554\ 2)$ r.l.u. The critical temperature is seen to be lower than that in $x = 0.05$, with a lower Bragg scattering intensity.

In a separate neutron diffraction experiment on TASP at SINQ, PSI, the $x = 0.03$ sample with sample mass 2.0 g was measured alongside the same $x = 0.05$ sample used on RITA-II. There was no applied field, with the crystal oriented in the **b-c** scattering plane inside a standard orange cryostat. A PG(002) monochromator was used with the analyser operated at zero curvature. No additional collimation was used, but manual slits placed between the sample and monochromator and between the sample and

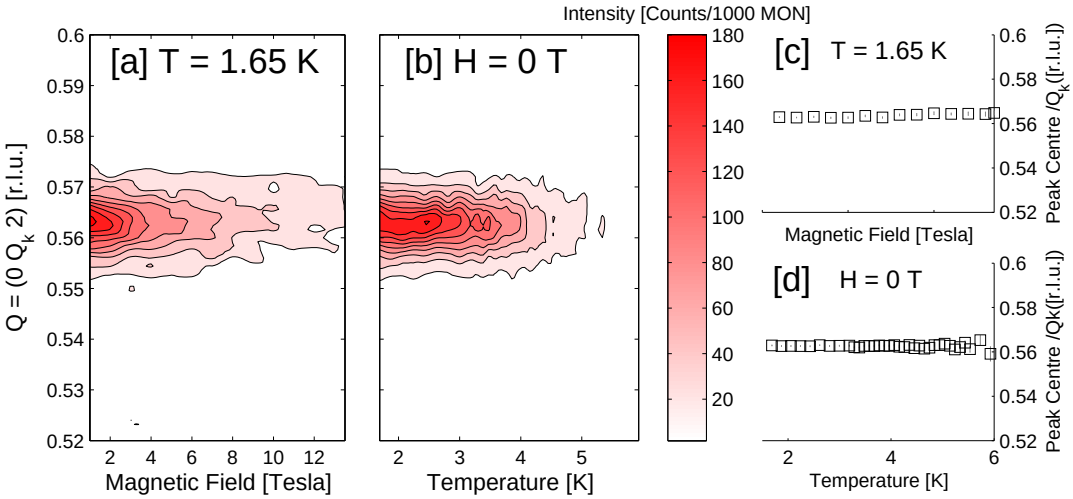

Figure 6.6: Field and temperature dependence of the Bragg peak centred at Q_m = (0 0.563 2) r.l.u. **[a]** Contour plot of scattering intensity for $\vec{Q}$ = (0 Q_k 2) r.l.u. at T = 1.65 K and $H < 13.5$ T; **[b]** Contour plot of scattering intensity for $\vec{Q}$ = (0 Q_k 2) r.l.u. at H = 0 T and $T < 6$ K; **[c]** The Bragg peak centre for T = 1.65 K and $H < 13.5$ T; **[d]** The Bragg peak centre for H = 0 T and $T < 6$ K. It can be seen that the Bragg peak remains centred at Q_m for all given temperatures and applied fields.

analyser were optimised for maximum background reduction. A Be-filter was placed between the sample and the analyser.

A magnetic Bragg peak was observed for this setup at $\vec{Q}$ = (0 0.56 2) r.l.u. and is plotted in Figure 6.8, alongside the same scan conducted for an identical setup on TASP for x = 0.05 at T = 1.55 K. The higher temperature values T = 3, 4 and 5 K are also shown for the x = 0.03 sample. The peak centre is at $\vec{Q}$ = (0 0.56 2) r.l.u. and the magnetic Bragg intensity has been removed entirely at T = 5 K. The minimum operational temperature was T = 1.5 K and for this reason a comparable scan for x = 0.01 for $T < T_N(x = 0.01)$ was not possible.

6.3.2 Field-Temperature Phase Diagram

The constant peak position in temperature and field in the doped samples allowed for systematic determination of the Bragg peak intensity as a function of temperature and field without the requirement to measure full $\vec{Q}$-scans at each point in (H, T); a count of the scattering intensity at the peak maximum is sufficient to estimate the magnetic Bragg intensity scattered by the sample. In the case when the magnetic field is applied in a direction orthogonal to the magnetic order, the magnetic field does not alter the spin structure factor and the Bragg intensity is proportional to the square of the order parameter.

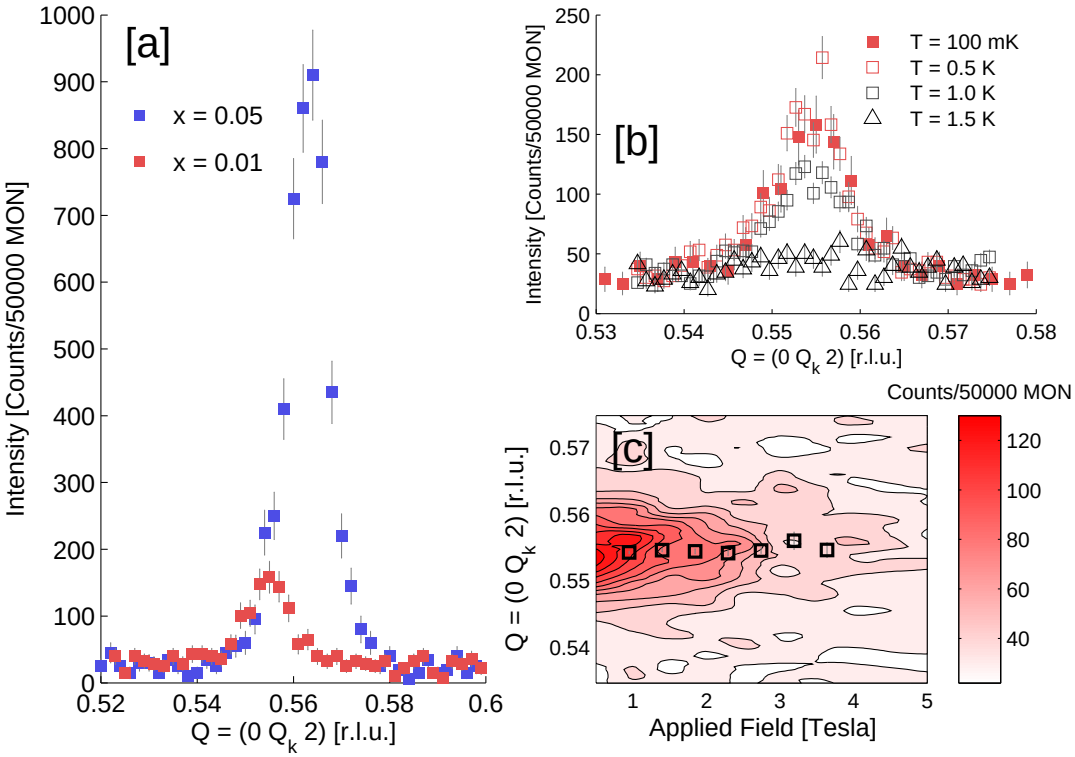

Figure 6.7: Bragg peak properties for $x = 0.01$. **[a]** $\vec{Q} = (0\ Q_k\ 2)$ r.l.u. for $x = 0.01$ and $x = 0.05$. **[b]** $\vec{Q} = (0\ Q_k\ 2)$ r.l.u. for $x = 0.01$ at $T = 100$ mK, 0.5 K, 1.0 K and 1.5 K. **[c]** $\vec{Q} = (0\ Q_k\ 2)$ r.l.u. for $0 < H < 5$ T. The scattering intensity is shown by the contour plot, and fitted peak centres are shown by the black open squares. For comparative purposes, $x = 0.01$ data in this figure has been multiplied by a scaling factor (1.87/1.3) to account for the larger $x = 0.05$ sample mass.

For $x = 0.05$, the RITA-II spectrometer was oriented in a fixed geometry at the peak maximum $\vec{Q}_m = (0\ 0.563\ 2)$ r.l.u. Then, without varying the momentum wavevector, the field and temperature dependence of the scattering intensity at the peak maximum was investigated through systematic sweeps in temperature at set applied fields and sweeps in applied field at set temperatures.

An identical methodology was used for $x = 0.01$, but with the spectrometer centred at the peak maximum $\vec{Q}_m = (0\ 0.555\ 2)$ r.l.u., for set fields and varying temperature. The temperature-dependence of the $x = 0.03$ sample was measured in the same fashion on TASP, but with no field dependence due to the lack of a cryomagnet.

The temperature-dependent magnetic Bragg peak intensity for $x = 0.05$ is given in Figure 6.9 [a]. In this figure the continuous removal of magnetic ordering can be seen, with a critical temperature separating the region of long-range magnetic order for $T < T_N$ and magnetic disorder at $T > T_N$. A fit to a typical power-law is difficult due to the large amount of critical scattering around T_N (Figure 6.9 [c]).

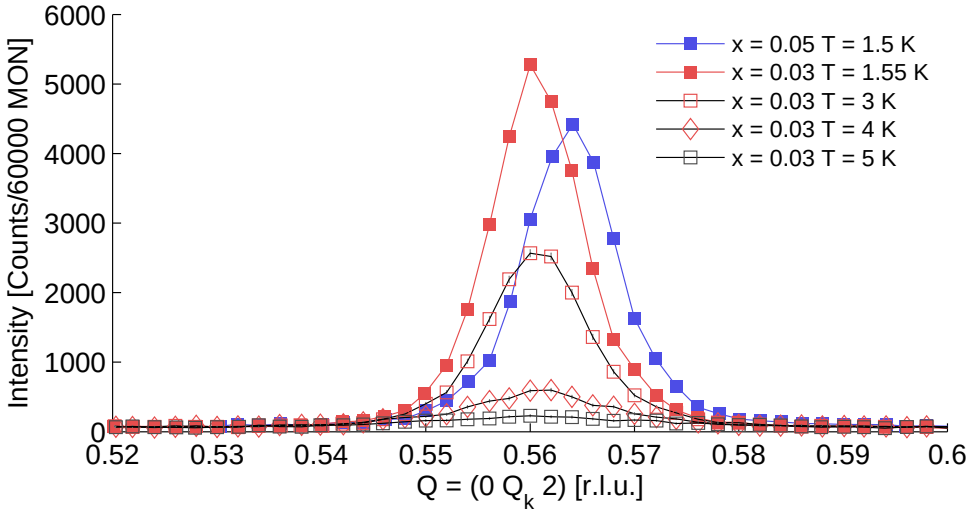

Figure 6.8: Measured Bragg peaks for $x = 0.03$ and $x = 0.05$, as measured on TASP (SINQ). The intensity of the $x = 0.05$ peak has been multiplied by a scaling factor (2/1.87) to account for the different sample mass. The magnetic Bragg peak is centred at Q = (0 0.56 2) and intensity is removed with raising the temperature.

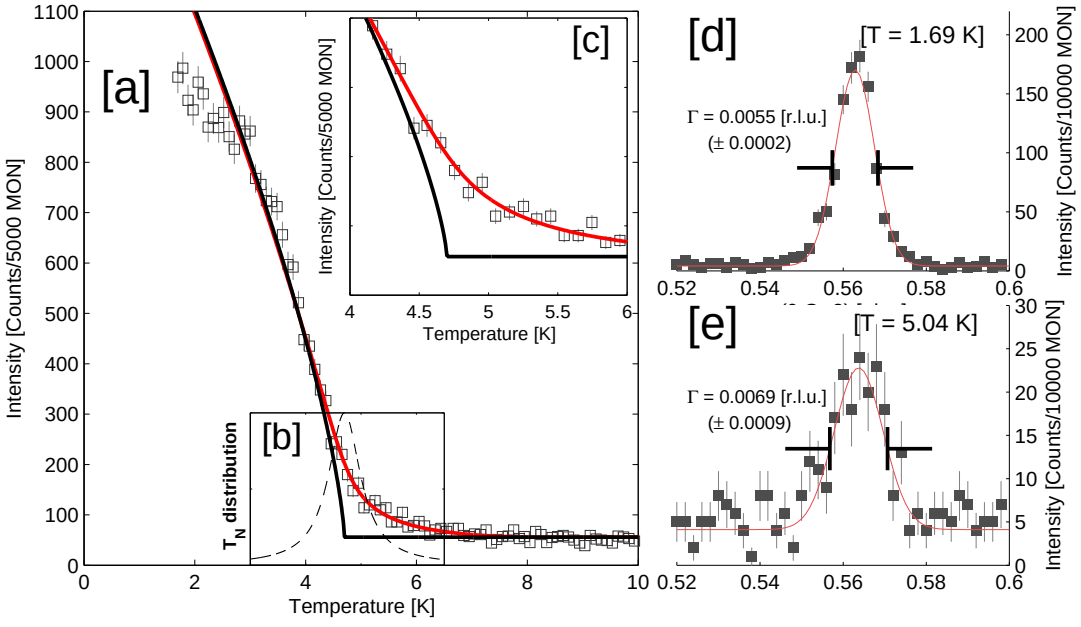

Figure 6.9: Fits of the temperature-dependent peak intensity at $\vec{Q} = (0\ 0.56\ 2)$ r.l.u.. **[a]** The fitted intensity for $H = 0$ T, assuming a generic power law $I = I_0[T - T_N]^\beta$ (black line), and for the same power law convolved with a Lorentzian distribution of T_N given by equation 6.1 (red line). **[b]** Distribution of T_N. **[c]** The fit shown in [a] for the region near the Néel temperature. **[d]** $\vec{Q} = (0\ Q_k\ 2)$ r.l.u. at $T = 1.69$ K. **[e]** $\vec{Q} = (0\ Q_k\ 2)$ r.l.u. at $T = 5.04$ K. In panels [d] and [e], the fitted Gaussian lineshapes are given by the red lines, and associated FWHM (Γ) values are given by the bounding bars.

Critical scattering in magnetically ordered crystals is typically a manifestation of short-range correlations between magnetic moments persisting above T_N; the correlation length is greatly decreased and the magnetic signal is no longer described by a resolution-limited Bragg peak, but by a signal that is broadly distributed in reciprocal space and energy.

However, magnetic Bragg peaks may persist above T_N in impurity-doped magnetic systems because of the inhomogeneity of the sample. In any doped sample the impurities are not perfectly homogeneously distributed, and there will exist regions of the crystal with different concentrations. As such it is possible for T_N to vary across the sample. In this case the magnetic signal is still from Bragg diffraction, but will have greatly reduced intensity. It is difficult to distinguish this effect from critical scattering, but we may assume the latter to be wider in momentum space.

In Figure 6.9 [c] and [d], two Q scans are given for magnetic Bragg intensity for the ordered region (T = 1.69 K) and the critical region (T = 5.04 K). Gaussian lineshapes are fitted to the data and given the by red lines. The FWHM are given by the bounding black bars and are 0.0055 ($\pm$ 0.0002) r.l.u. and 0.0069 ($\pm$ 0.0009) r.l.u., respectively. Diffuse scattering would be evidenced in a significantly larger FWHM than is observed and it can therefore be read from the data that the persistent scattering above T_N is from weak Bragg scattering as described above.

The data can then be fitted with the assumption of a distribution in T_N due to a distribution in doping concentration, x. This is achieved by convolving a power-law function with an assumed function for the T_N distribution, $P(T_N)$, and fitting the resultant intensity with additional fitting parameters that determine the centre and FWHM of the T_N distribution. The precise nature of a real-space distribution of doping concentration is not known and as such no preferred model for the distribution of T_N is obvious; however, a Lorentzian distribution has been assumed rather than a Gaussian distribution for T_N in consideration of a possibility of outliers in doping concentration, and because the resulting fit from the convolution better describes the data. The T_N distribution is plotted panel [b] of Figure 6.9 in which a T_N occurs with a probability

$$P(T_N) = P_0[\frac{\Gamma_{T_N}}{(T_N - T_N^{cen})^2 + \Gamma_{T_N}^2}], \tag{6.1}$$

where T_N^{cen} is the centre of the distribution, P_0 a normalisation prefactor and Γ_{T_N} the FWHM. This distribution is convolved with the standard power law for Heisenberg antiferromagnets $I = A|T - T_N|^{2\beta}$ where $\beta = 0.367$, the value for a 3-D Heisenberg system [2, 156]. The resultant fit is given by the red line in Figure 6.9. The black line

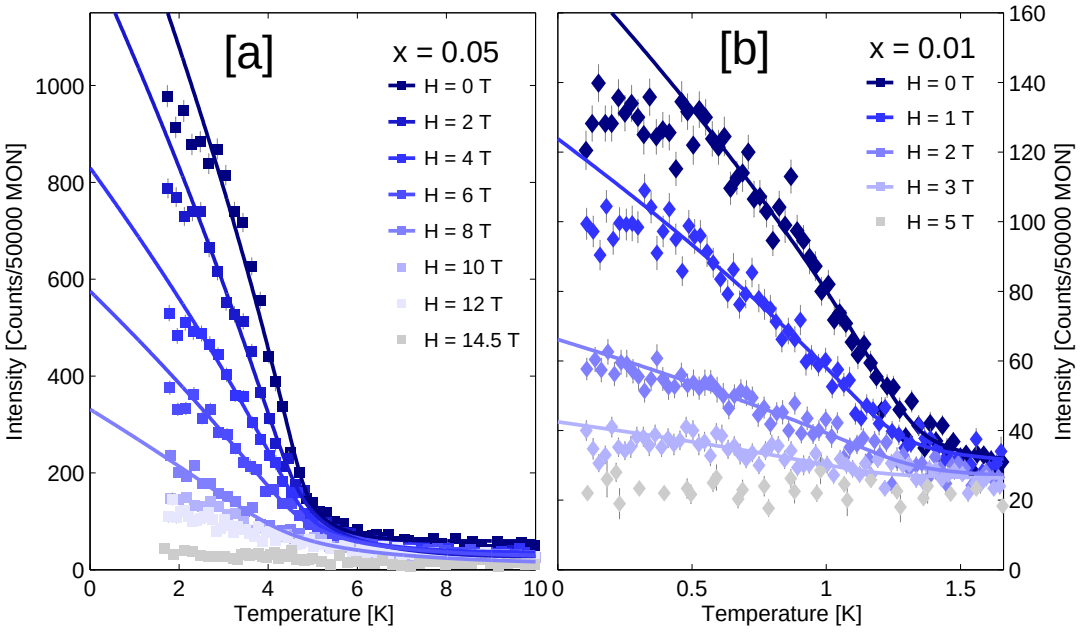

Figure 6.10: Temperature dependence of the magnetic Bragg peak intensity, with lines of best fit. **[a]** $x = 0.05$. **[b]** $x = 0.01$. The solid lines are lines of best fit assuming the distributed T_N formalism illustrated in Figure 6.9, and taking the 3D Heisenberg exponent $\beta = 0.37$.

is the corresponding unconvolved power law for the fitted T_N. For the example shown, $T_N = 4.7$ (± 0.05) K, $\Gamma_{T_N} = 0.35 \pm 0.05$ K.

From the homogeneity of the crystal samples, it can be estimated that one would expect a T_N distribution of $\sim 5\%$. It is to be noted that the FWHM of the fitted T_N distribution is $\sim 7\%$ of the fitted value for T_N and as such represents a larger broadening that would be expected. This can be reconciled with the observation that the function $T_N(x)$ is not exactly linear, some diffuse scattering will also be present, and the assumed critical exponent value is that of a classical Heisenberg system and may not accurately correspond to the dimensionality of the spin-coupling present in the sample.

The same fitting routine was applied to all temperature dependent scans of the Bragg peak intensity that were collected on RITA-II, and are shown in Figure 6.10. Panel [a] shows the peak intensity data for $x = 0.05$ in the temperature range 1.5 K$< T <$ 10 K, measured for the field values $H = 0$, 2, 4, 6, 8, 10, 12 and 14.5 T. Figure 6.10 [b] shows the fitted data for $x = 0.01$, where the temperature range 0.1 K $< T <$ 1.6 K for $H = 0$, 1, 2, 3 and 5 T.

Figure 6.11 demonstrates the field-dependence of the intensity of the magnetic Bragg peak maximum for temperature values $T = 1.6$, 2.8, 3.5 and 4.0 K. The data

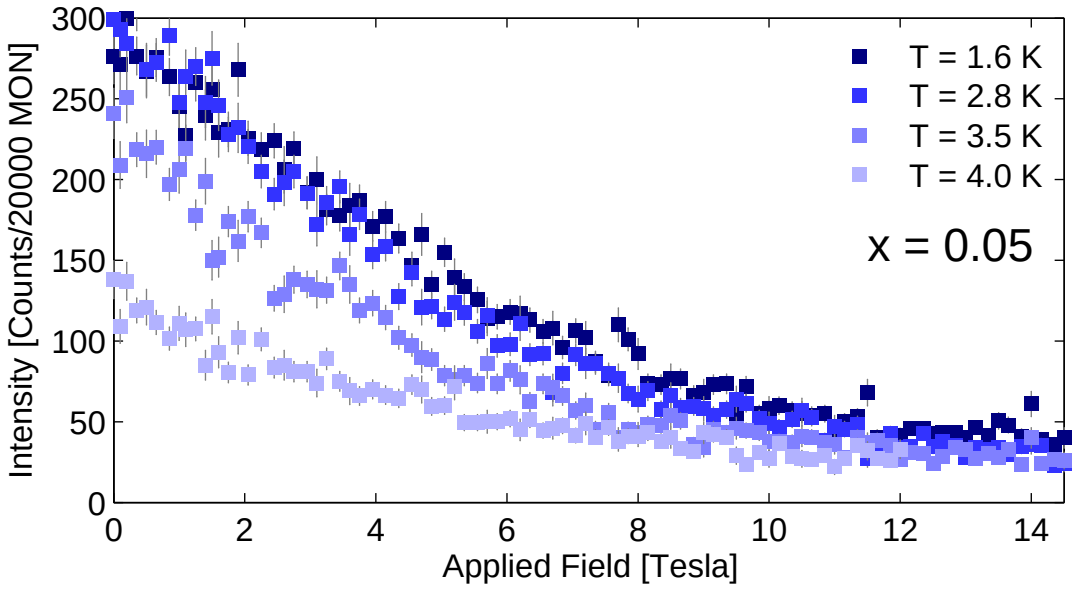

Figure 6.11: Applied field dependence of the peak magnetic Bragg intensity for $x = 0.05$ and $T = 1.6$ K, 2.8 K, 3.5 K and 4.0 K. It is not possible to discern any critical value of applied field separating a phase of long-range order and disorder; the data shows a continuous reduction of scattered intensity.

cannot be described by any critical exponent and there is no obvious value of critical magnetic field beyond which long-range order is suppressed. Instead, a continuous reduction of intensity is observed at all temperatures. This can be qualitatively understood by the impurity-induced, antiferromagnetically aligned magnetic moments coupling to the magnetic field and being continuously rotated out of the scattering plane into the $H(||\mathbf{a})$ direction. In this case, between 0 T and the saturation value ($\sim$ 14 T, the point where the impurity induced spins are ferromagnetically aligned along H), the observed antiferromagnetic intensity would be observed to gradually decrease rather than demonstrate a discontinuity. Further studies in applied fields with different crystal orientations or with a horizontal cryomagnet are required for quanitative analysis.

The phase diagram in temperature and applied field for $x = 0.05$ and 0.01 is plotted in Figure 6.12, with the contour intensity and colour gradient illustrating the peak magnetic Bragg intensity at the respective incommensurate ordering wavevectors. The amplitude for $x = 0.01$ has been multiplied such as to present it on the same scale as $x = 0.05$ for comparison. The fitted T_N values are plotted by the open black squares ($x = 0.05$) and diamonds ($x = 0.01$), with the higher field values omitted due to the impracticality of fitting a critical exponent to the measured data. The critical values appear to be approximately constant in field, with $T_N(x = 0.05) \sim 4.6$ K and

$T_N(x = 0.01) \sim 1.2$ K at zero field. An additional point for the $H = 0$ T Néel temperature for $x = 0.03$ is also included in the plot, given by the triangular symbol.

The fitted peak intensity for $x = 0.03$ is shown in Figure 6.12 [b], and the extracted T_N value at $H = 0$ T is shown alongside the corresponding values for $x = 0.01$ and 0.05 [c]. The dotted line is not a fit and provides a guide to the eye only; from this it can be seen that the $T_N(x)$ is approximately linear. Taking this relationship, the sample homogeneity required to produce the fitted T_N distribution results in a concentration FWHM Δx given by $\Delta x/x \sim 0.07$.

6.4 Spin Structure Determination

From an experimental perspective, the critical temperature $T_N = 4.37$ K for $x = 0.05$ is a convenient result; typical cryostat operational temperatures do not go below $T = 1.5$ K, with values as low as 1.2 K only reachable through simultaneous operation of efficient root pumps. The magnetic intensity for $x = 0.05$ can be readily identified and measured without specialist equipment (e.g. dilution), increasing the scope and range of data that can be collected.

This prompted an experimental study where a multitude of magnetic Bragg peaks were measured across reciprocal space. With a systematic study of Bragg peak intensities, FWHM and reciprocal lattice vectors a theoretical structure factor can be fitted to match the data and from it a model for the structure of the ordered impurity-induced spins inferred.

6.4.1 Experimental Setup

For this study, a diffraction experiment on the $x = 0.05$ sample was performed on thermal neutron single crystal diffractometer TriCS [157] located at SINQ, PSI. TriCS is on the thermal beamline R42, and was operated with two focusing monochromators, Ge(311) with wavelength $\lambda = 1.17$ Å, and PG(002) with $\lambda = 2.32$ Å. The instrument was operated in conjunction with an orange cryostat with an operational temperature range 1.5 K $< T <$ 200 K, and operated in tilting mode.

After the sample there is a ^{3}He-tube detector, with $80'$ collimation between the detector and the sample. Cd slits were attached to reduce the vertical beam aperture to optimise the signal strength. The $x = 0.05$ sample was mounted in the **b-c** scattering plane and cooled to $T = 1.5$ K. With the tilt geometry setup, access to finite Q_h was possible. The diffractometer setup includes a UB matrix defined from the observation of known Bragg peaks and formulated with Busing-Levy angle definitions [158].

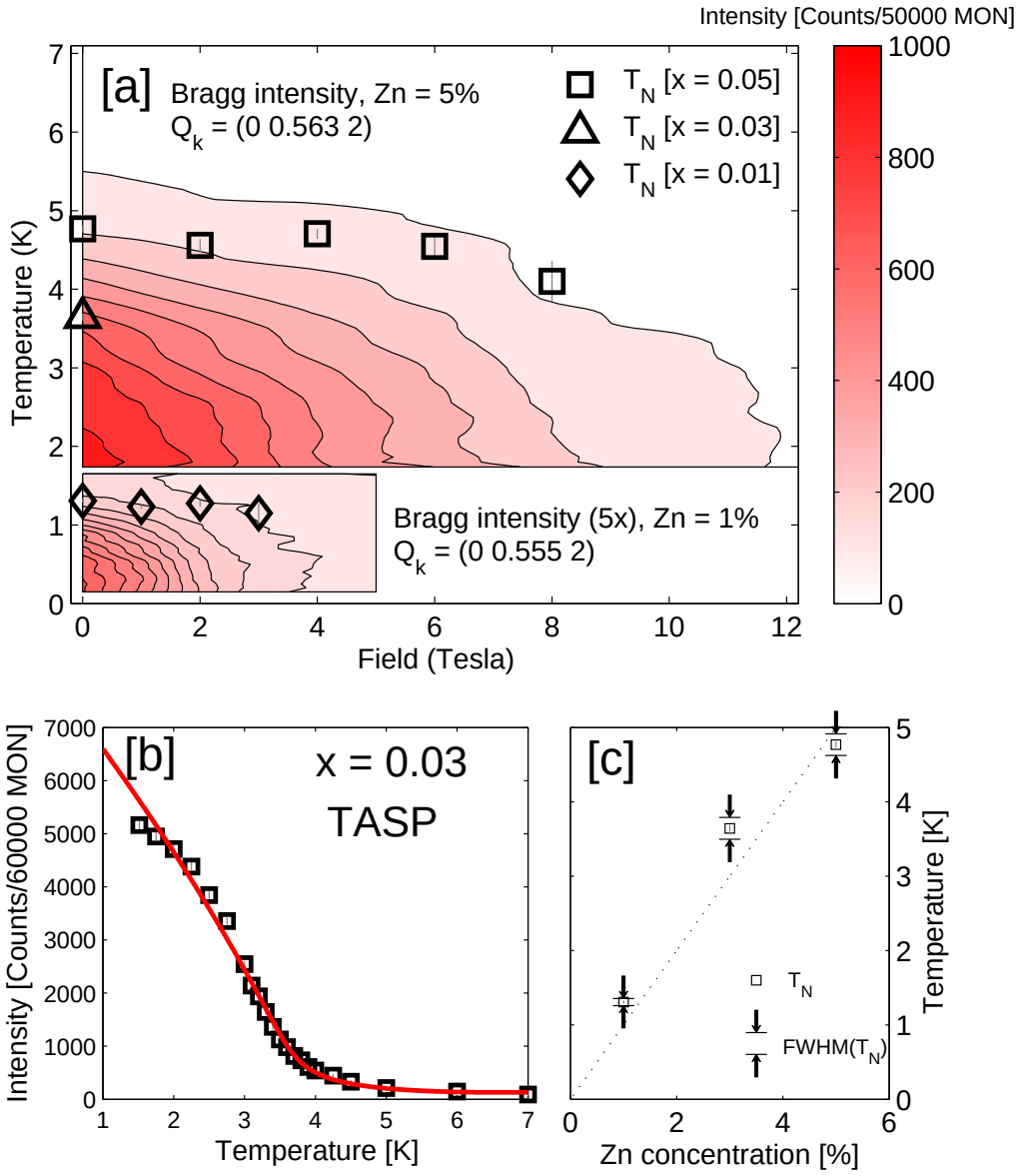

Figure 6.12: Phase diagram and fitted T_N values in $BiCu_{2(1-x)}Zn_{2x}PO_6$ for $x = 0.01$; 0.03; 0.05. **[a]** The Field-Temperature phase boundary for x= 0.05 and $x = 0.01$, with T_N given for each concentration by the open squares and open diamonds respectively. The intensity for $x = 0.01$ has been multiplied by 5 to allow for illustrative purposes. The intensity has not been normalised for mass. **[b]** Fit of the temperature dependent peak Bragg intensity for $x = 0.03$ from the data collected on TASP. **[c]** T_N at $H = 0$ T for all measured concentrations x. The fitted T_N distribution is given by the bounding arrows. A dashed line for $T_N(x)$ is provided as a guide to the eye, and corresponds to a linear relationship between x and T_N.

6.4.2 Bragg Peak Distribution

Scans in ω, the sample rotation, were performed for the reciprocal lattice vectors $\vec{Q} = (Q_h\ [Q_k \pm 0.44]\ Q_l)$, for all attainable Miller indices within the scattering geometry. Figure 6.13 illustrates the measured points within the Q_k-Q_l plane for different Q_h values. Green square markers indicate where there was no observed Bragg intensity, and red square markers where intensity was measured. The green lines indicate the aluminium 'powder' lines, measured due to the aluminium present within the neutron beam from equipment components (e.g. sample holder). The 2θ values are constant because of the nature of the aluminium used; the holder is manufactured from an aluminium liquid which has solidified. The scattering is the same as from a powder and thus has no ω dependence. The open circles are measured nuclear Bragg peaks that are necessary for the structure determination.

Magnetic Bragg intensity was observed to be present in all Q_k-Q_l planes, albeit for different values. For $Q_h = 0$ and 2, the intensity occurs for even $Q_l = 0$, 2, 4 r.l.u.; for $Q_h = 1$ r.l.u., intensity is seen at odd $Q_l = 1$, 3 r.l.u. A selection of data illustrating this is shown in Figure 6.14. The strongest Bragg peak is that measured on RITA-II and TASP in the previous section and is shown in Figure 6.14 [g]. Despite the $x = 0$ sample possessing a comparable spin gap at $\vec{Q} = (0\ 0.56\ 1)$ r.l.u., there does not appear to be any magnetic ordering in the doped sample at this point for $Q_h = 0$. However, significant scattering intensity comparable to [g] is observed for the peak at $\vec{Q} = (1\ 0.56\ 1)$ r.l.u. and is shown in [e].

Because of the scattering geometry, an additional scaling factor must be applied to the observed intensities, and is given as

$$L = \sin(\Gamma)\cos(\nu), \tag{6.2}$$

where L is the *Lorentz factor* [159] and is a function of the scattering angles θ and ν (where θ is the angle in plane and ν is the angle out of plane) for the case of an incident beam angle $\mu = 0$. Its origin is in consideration of the intersection of the Ewald sphere and magnetic Bragg point not being constant in (θ, ν) and instead having a geometry-dependent overlap.

A summary of the collected intensities after the Lorentz correction is given in Figures 6.15, 6.16 and 6.17 for $Q_h = 0$, 1 and 2 respectively. In all figures, measured points that lack Bragg intensity are given by the green bars, and the Al 'powder' lines are given by green lines in the basal plane. In Figure 6.15, the red bars indicate points where intensity was measured, with the height of the bar indicating the intensity of the Bragg peak. In Figure 6.16, the Bragg peak intensity is indicated by the blue bars

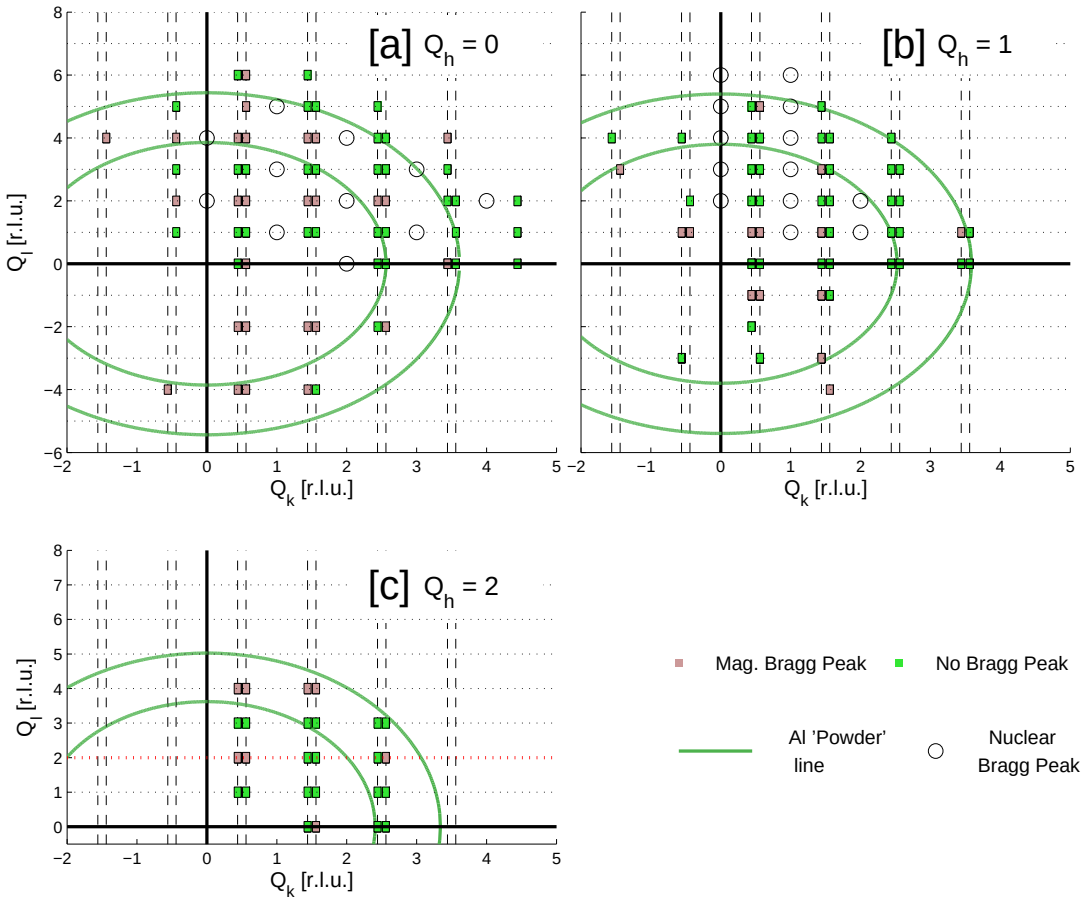

Figure 6.13: The measured points in reciprocal space for the diffraction study on TriCS (SINQ). **[a]** $\vec{Q} = (0\ Q_k\ Q_l)$ r.l.u. **[b]** $\vec{Q} = (1\ Q_k\ Q_l)$ r.l.u. **[c]** $\vec{Q} = (2\ Q_k\ Q_l)$ r.l.u. Green markers indicate no Bragg intensity, red markers indicate measured intensity and green lines indicate the region where coherent elastic scattering from aluminium is observed. Open circles are the measured nuclear Bragg peaks, included for the structure determination.

for $Q_h = 1$ r.l.u., and the cyan bars for $Q_h =$ -1 r.l.u. In Figure 6.17, the orange bars indicate Bragg peak intensity for $Q_h = 2$ r.l.u.

6.4.3 Magnetic Structure Determination

The reciprocal space distribution of magnetic Bragg intensities is determined by the magnetic structure factor, as given by Equation 2.18. As with nuclear diffraction where the positions of the atoms define the structure factor, magnetic neutron diffraction is dependent on the size, orientation and wavevector of the magnetic moments in the system. This results in a momentum dependent structure factor that can be used to compare to the data and test the quality of a specific model for the magnetic ordering.

A modeling of the magnetic ordering in $BiCu_{2(x-1)}Zn_{2x}PO_6$ is then possible through

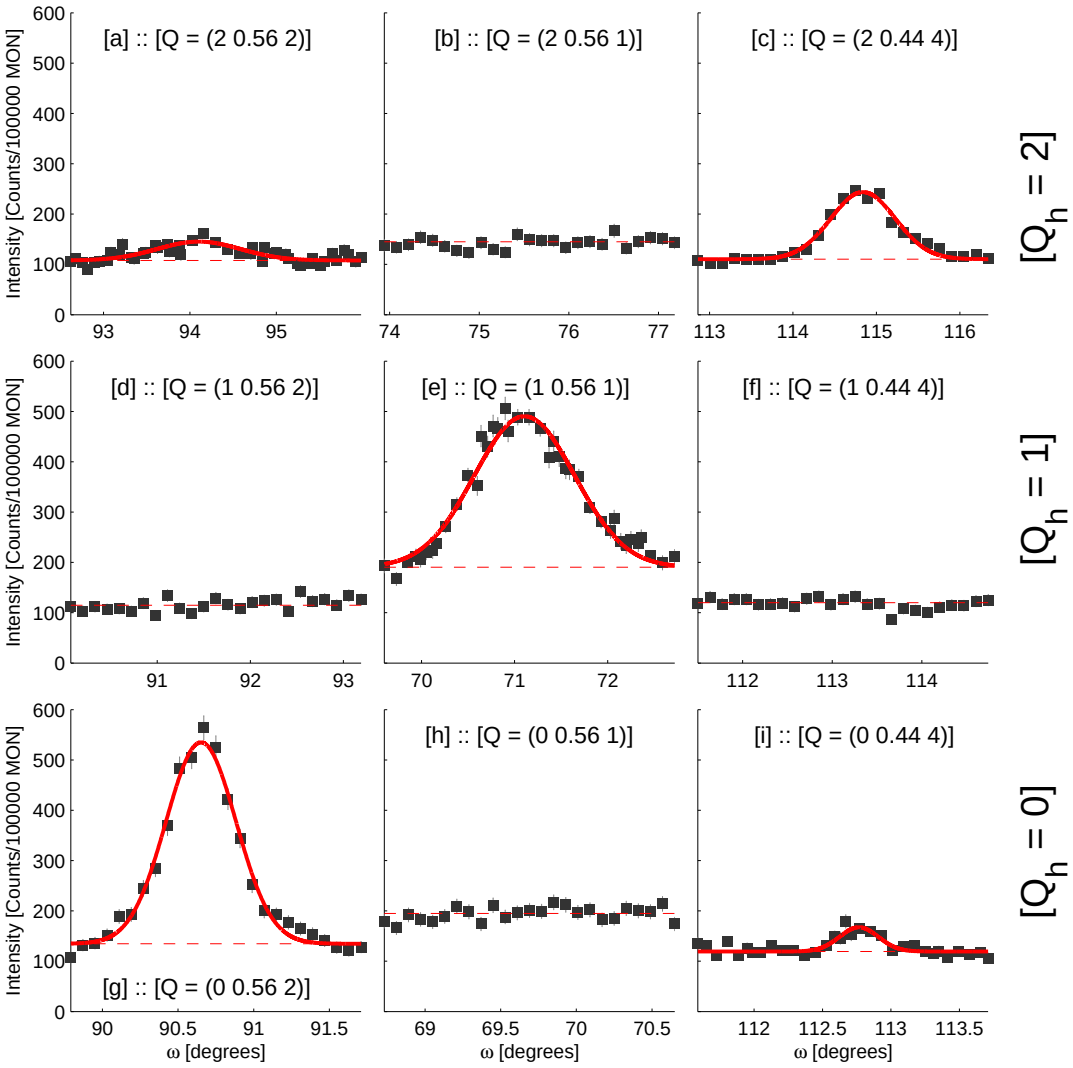

Figure 6.14: A selection of the scans presented in Figure 6.13, measured in ω. **[a]** $\vec{Q}$ = (2 0.56 2) r.l.u. **[b]** $\vec{Q}$ = (2 0.56 1) r.l.u. **[c]** $\vec{Q}$ = (2 0.44 4) r.l.u. **[d]** $\vec{Q}$ = (1 0.56 2) r.l.u. **[e]** $\vec{Q}$ = (1 0.56 1) r.l.u. **[f]** $\vec{Q}$ = (1 0.44 4) r.l.u. **[g]** $\vec{Q}$ = (0 0.56 2) r.l.u. **[h]** $\vec{Q}$ = (0 0.56 1) r.l.u. **[i]** $\vec{Q}$ = (0 0.44 4) r.l.u. The horizontally aligned data are arranged in ascending order for Q_h = 0, 1 and 2 r.l.u. with vertically aligned data illustrate Q_l = 2, 1, 4 r.l.u. from left to right.

a magnetic structural refinement process, where simulated structure factors from various models are compared to the extracted data. The FullProf software package [160] was employed to analyse the data summarised in the previous section. The package operates on a least-squares (LS) fitting routine where multiple parameters can be simultaneously varied including the magnitude, direction, the phase and the real and imaginary components of the magnetic moment.

The structure factor is calculated by considering the magnetic moment on each

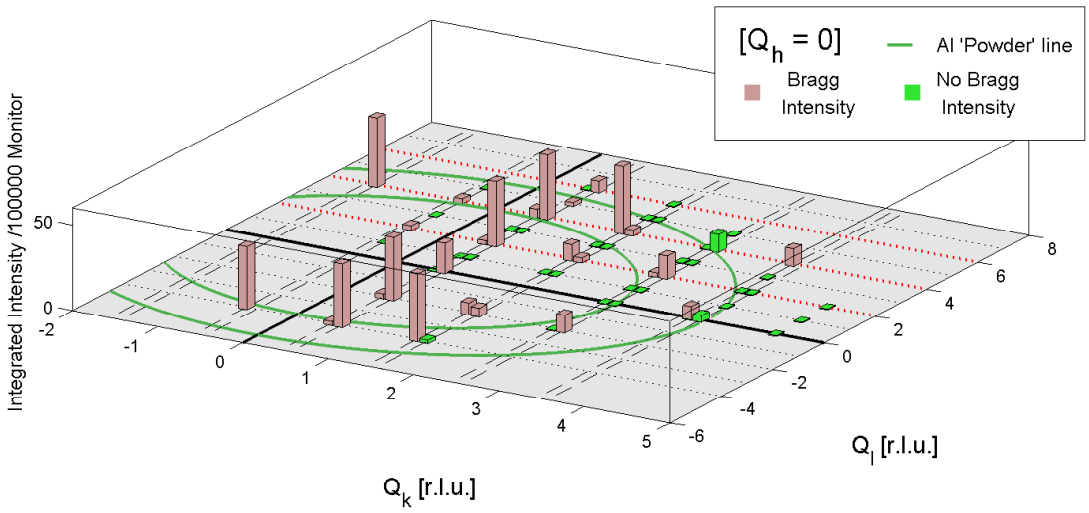

Figure 6.15: Fitted Bragg peak intensities for $Q_h = 0$. Green bars indicate no measured Bragg intensity, red bars at reciprocal points of observed peaks with the height indicating the scattering intensity. The green line indicates the region where elastic scattering from aluminium occurs.

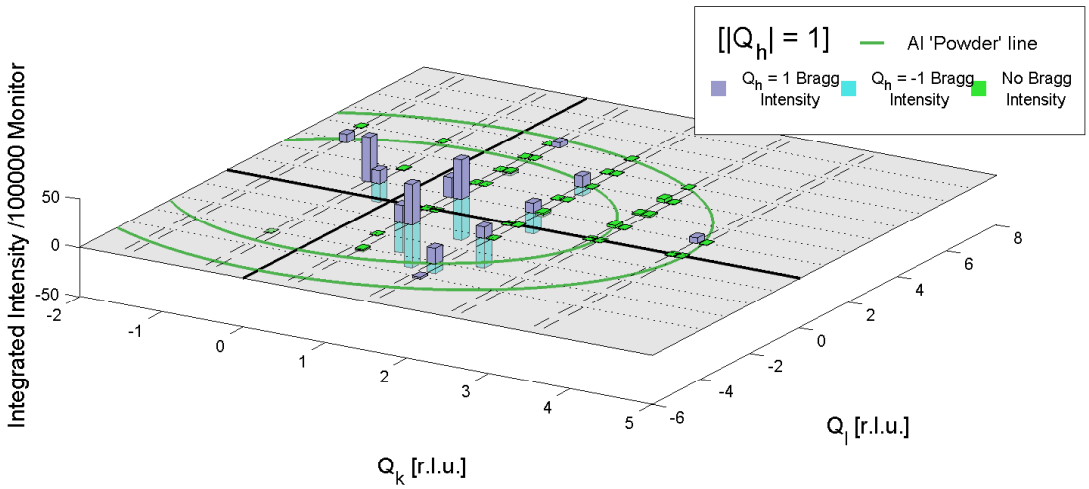

Figure 6.16: Fitted Bragg peak intensities for $|Q_h| = 1$. Green bars indicate no measured Bragg intensity, blue bars at reciprocal points of observed peaks with the height indicating the scattering intensity, with $Q_h = 1$. Cyan bars indicate the complementary scans at Q_h = -1. The green line indicates the region where elastic scattering from aluminium occurs.

lattice site within the unit cell

$$\mathbf{m}_j = \mathbf{S}_j \exp(\phi_j) \tag{6.3}$$

where $\mathbf{S}_j = (S_j^x \quad S_j^y \quad S_j^z)$ is a complex spin vector and ϕ_j is the relative phase at site j. By considering the real and imaginary components of S, the spin structure can be

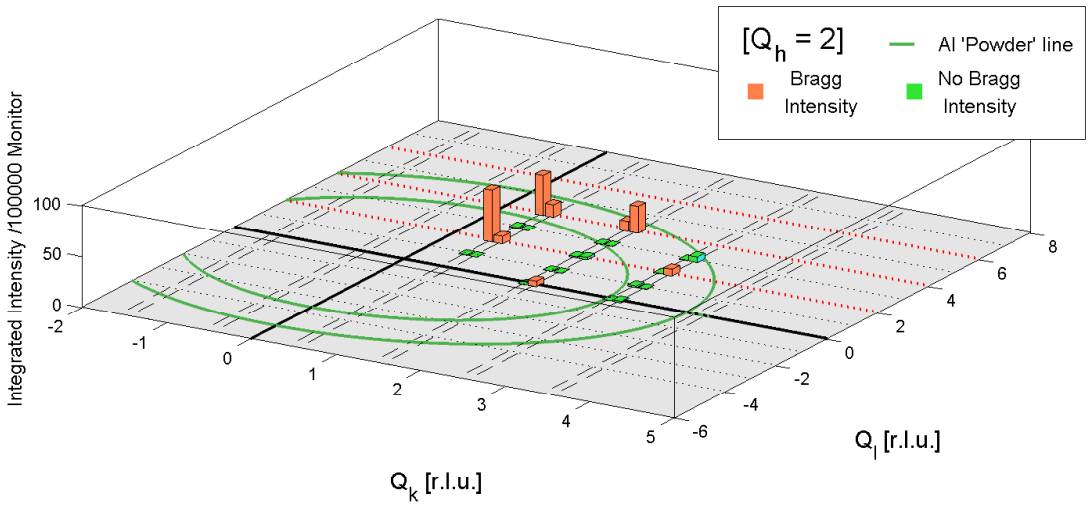

Figure 6.17: Fitted Bragg peak intensities for Q_h =2. Green bars indicate no measured Bragg intensity, orange bars at reciprocal points of observed peaks with the height indicating the scattering intensity. The green line indicates the region where elastic scattering from aluminium occurs.

fitted to be amplitude or phase modulated.

Taking the magnetic ordering wavevector to be k = (0 0.44 0) r.l.u., a general, unconstrained initial set of parameters was implemented into the software and simulated annealing (SA) [161] was performed on the parameter space, where all parameters are allowed to vary with a finite stepsize and the solution converges to an optimum set as the stepsize is continuously reduced. The entire dataset is normalised to an intensity prefactor that was obtained by performing a structural refinement on 21 nuclear peaks. This allows for the signal to be normalised to the sample mass and ultimately provides magnetic moments in absolute units of μ_B.

Implementing parameter variation constraints that assume the spins to be constant magnitude but varying with relative orientation (i.e. a phase modulated structure), SA was performed that produced a best fit to the data given by Figure 6.18. The observed peaks with higher intensity match the resultant model closely, shown by their proximity to the line $F_{obs} = F_{calc}$ in Figure 6.18 [c], but shows large discrepancies for low intensity peaks.

Taking an amplitude modulated structure, in which the spin vector modulates in magnitude and not in orientation, SA resulted in a spin model that had zero contribution along S^x and S^z. Setting these parameters to zero, and taking the refinement parameters as the S^y component and the relative phases of the eight Cu atoms within the unit cell, a LS fit was produced and is summarised in Figure 6.19.

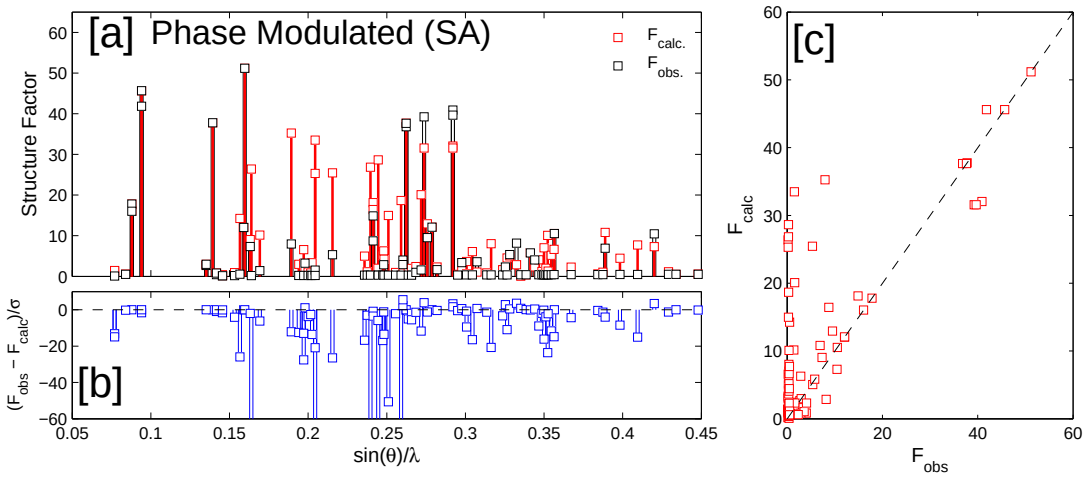

Figure 6.18: The least squares fit with Fullprof of the magnetic Bragg peak intensities to the calculated structure factor for a phase modulated spin structure fitted through simulated annealing. **[a]** The difference in the observed and calculated structure factor. **[b]** The value $((F_{obs} - F_{calc})/\sigma$, the difference between the two divided by the standard deviation of the measured intensity. **[c]** Plot of F_{obs} against F_{calc}.

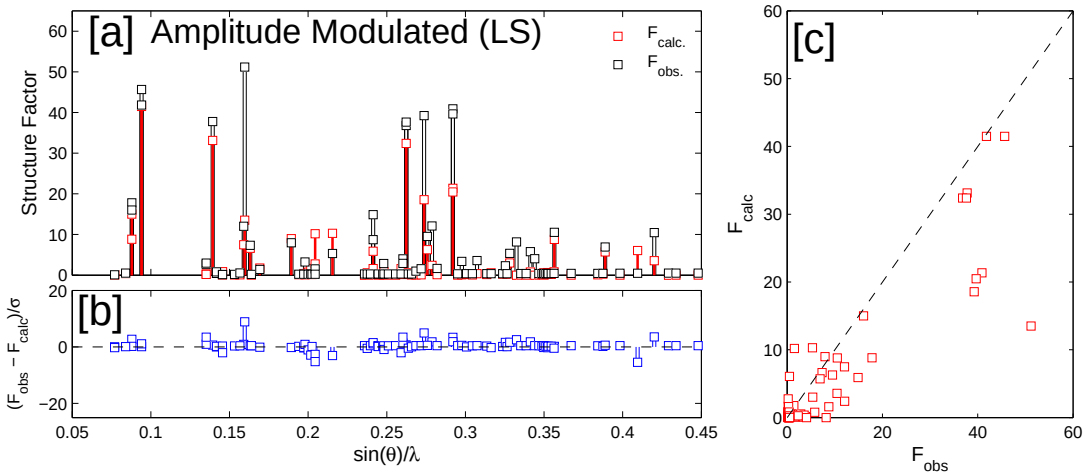

Figure 6.19: The least squares fit with Fullprof of the magnetic Bragg peak intensities to the calculated structure factor for an amplitude modulated spin structure fitted through least squares. **[a]** Illustrates the difference in the observed and calculated structure factor, **[b]** The value $((F_{obs} - F_{calc})/\sigma$, the difference between the two divided by the standard deviation of the measured intensity. **[c]** Plot of F_{obs} against F_{calc}.

The quality of fit is greater than that of the phase modulated model, producing low $(F_{obs} - F_{calc})/\sigma$ values as seen in panel [b] of Figure 6.19. The plot of F_{obs} against F_{calc} illustrates that the highest lying peaks have lower observed intensities than predicted, but the model sucessfully accounts for the weaker observed intensities.

An amplitude modulated structure is then taken as the best description of the magnetic ordering within $BiCu_{2(x-1)}Zn_{2x}PO_6$. However, the relative orientation of the magnetic moments of the atoms within the unit cell given by a magnetic structure must conform to the permitted symmetry operations of the lattice that relate the copper sites. Therefore the fitted model must match a possible structure allowed by symmetry.

The magnetic order occurs alongside a breaking of the symmetry of the lattice. The symmetry operations that remain are those that, when applied, still generate the atomic sites within the unit cell but no not change the orientation of the ordering wavevector. It is these elements that dictate the magnetic structure and for the observed ordering wavevector k = (0 0.44 0) r.l.u. are given by those in column 2 of Table 6.2.

The relative phases and magnitudes of each Cu spin determined by the symmetry are given, and have four possible solutions. These solutions are a result of four possible spin structures for the prescribed symmetry elements and are defined as *Irreducible Representations* (IReps).

The predicted magnetic moment orientation for each IRep, assuming an amplitude modulated structure, is given in Table 6.3, with the generalised fitted parameters included for comparison. It can be seen that the first IRep is that which reproduces the previously fitted results.

This can be confirmed and a final model extracted by performing a least squares fit on the amplitude modulated structure for each of the four IRep models. The results are given in Figures 6.20, 6.21, 6.22 and 6.23. IReps(2 - 4) do not provide an adequate description of the magnetic ordering that reproduces the observed data; IRep(1) provides the greatest consistency between F_{obs} and F_{calc}. This model is plotted in Figure 6.24.

The amplitude modulated structure fitted by the Fullprof software operates under the assumption of a homogeneous spin distribution. The delocalisation of the spins induced from site-dilution is not encoded in the software. The fitted moments of Figure 6.24 are an observed average, and the modulation corresponds to that shown schematically in Figure 6.25 [a]. This is an approximation to the real structure in which the magnetic order originates from the correlation of regions of impurity induced AFM order. The fitted amplitude modulated order is then the order present within each correlated region localised around the impurity. The long-range order is an effect of the effective exchange interaction J_{eff}, mediated via the Cu atoms between the impurities. This is illustrated in Figure 6.25 [b]. The difference between the real model and the homogeneous model implemented by Fullprof can be identified as the

$\mathbf{m}_j$	Symm. Element	IRep(1)	IRep(2)	IRep(3)	IRep(4)
$\mathbf{S}_1$	(x, y, z)	(+ + +)	(+ + +)	(+ + +)	(+ + +)
ϕ_1		0	0	0	0
$\mathbf{S}_2$	(-x, y+$\frac{1}{2}$, -z)	(- + -)	(- + -)	(+ - +)	(+ - +)
ϕ_2		$\xi_{0.44}$	$\xi_{0.44}$	$\xi_{0.44}$	$\xi_{0.44}$
$\mathbf{S}_3$	(x+$\frac{1}{2}$, y, $\frac{1}{2}$-z)	(- - +)	(+ + -)	(- - +)	(+ + -)
e_3^{ϕ}		0	0	0	0
$\mathbf{S}_4$	($\frac{1}{2}$-x, y+$\frac{1}{2}$, z+$\frac{1}{2}$)	(+ - -)	(- + +)	(- + +)	(+ - -)
ϕ_4		$\xi_{0.44}$	$\xi_{0.44}$	$\xi_{0.44}$	$\xi_{0.44}$

Table 6.2: Tabular representation of the symmetry elements that preserve the ordering wavevector k = (0 0.44 0) r.l.u. and the four possible representations of relative spin orientation. Here (+) and (-) refer to the sign of the {x y z} components of the spin vector given in column 1. $\xi_{0.44}$ is the resultant phase difference, given by exp(-0.22(2π i)). The same operations are applied to the second basis atom which has no explicit dependence on the moment of the first basis atom.

	$\mathbf{m}_j$	$\lvert m\rvert(\mu_B)$	Fit param.	IRep(1)	IRep(2)	IRep(3)	IRep(4)
[Cu1]	$\mathbf{S}_1$	0.1521	$(+)M_Y$	$(+)M_Y$	$(+)M_Y$	$(+)M_Y$	$(+)M_Y$
	ϕ_1		0	0	0	0	0
[Cu1]	$\mathbf{S}_2$	- 0.0138	$(+)M_Y$	$(+)M_Y$	$(+)M_Y$	$(-)M_Y$	$(-)M_Y$
	ϕ_2		0.2645 ± 0.0619	0.22	0.22	0.22	0.22
[Cu1]	$\mathbf{S}_3$	- 0.1447	$(-)M_Y$	$(-)M_Y$	$(+)M_Y$	$(-)M_Y$	$(+)M_Y$
	ϕ_3		0.0498 ± 0.1096	0	0	0	0
[Cu1]	$\mathbf{S}_4$	0.0398	$(-)M_Y$	$(-)M_Y$	$(+)M_Y$	$(+)M_Y$	$(-)M_Y$
	ϕ_4		0.2921 ± 0.1224	0.22	0.22	0.22	0.22
[Cu2]	$\mathbf{S}_5$	-0.1521	$(-)M_Y$	$(-)M_Y$	$(-)M_Y$	$(-)M_Y$	$(-)M_Y$
	ϕ_5		0	0	0	0	0
[Cu2]	$\mathbf{S}_6$	-0.0134	$(-)M_Y$	$(-)M_Y$	$(-)M_Y$	$(+)M_Y$	$(+)M_Y$
	ϕ_6		0.2360 ± 0.0649	0.22	0.22	0.22	0.22
[Cu2]	$\mathbf{S}_7$	0.1521	$(+)M_Y$	$(+)M_Y$	$(-)M_Y$	$(+)M_Y$	$(-)M_Y$
	ϕ_7		0 ± 0.1266	0	0	0	0
[Cu2]	$\mathbf{S}_8$	0.0647	$(+)M_Y$	$(+)M_Y$	$(-)M_Y$	$(-)M_Y$	$(+)M_Y$
	ϕ_8		0.1801 ± 0.1100	0.22	0.22	0.22	0.22

Table 6.3: A tabular representation of the fitted magnetic moment on each spin site, with each spin denoted in the first column by the site number and the Cu atom to which it belongs. The magnitude $|m|$ is given in the second column and represented by the absolute magnitude M_Y and a site-dependent phase ϕ_i in the third column, where M_Y = 0.1521 ± 0.0126 μ_B. The predicted spin sign and phase from each Irep is given in the final four columns, from which it can be seen that IRep(1) is that which matches the fitted model.

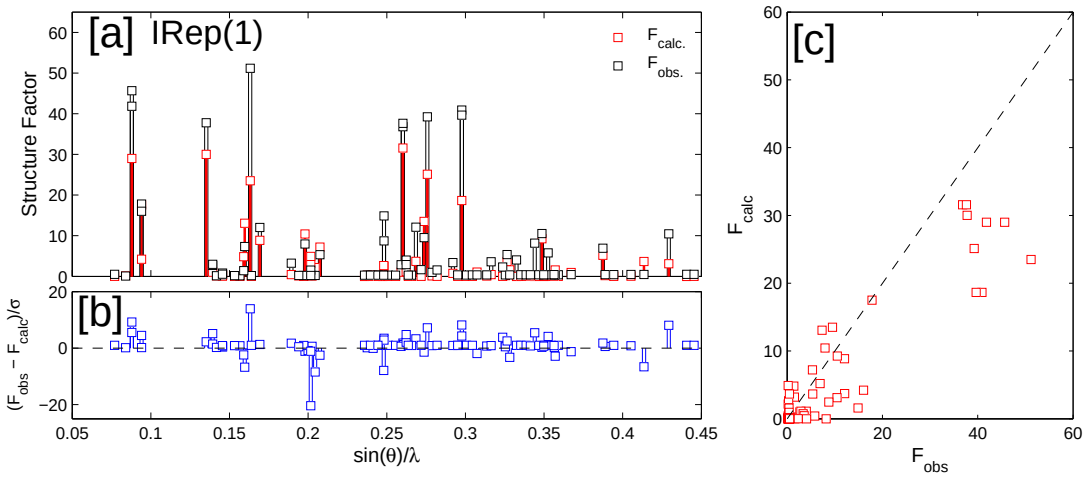

Figure 6.20: The least squares fit with Fullprof of the magnetic data to the calculated structure factor for IRep(1). **[a]** The difference in the observed and calculated structure factor, **[b]** The value $((F_{obs} - F_{calc})/\sigma$, the difference between the two divided by the standard deviation of the measured intensity. **[c]** Plot of F_{obs} against F_{calc}.

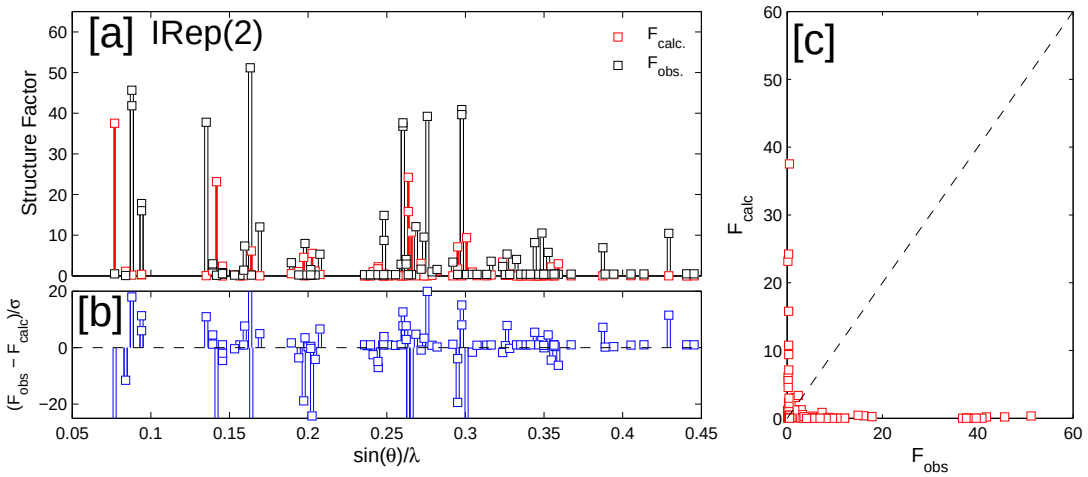

Figure 6.21: The least squares fit with Fullprof of the magnetic data to the calculated structure factor for IRep(2). **[a]** The difference in the observed and calculated structure factor, **[b]** The value $((F_{obs} - F_{calc})/\sigma$, the difference between the two divided by the standard deviation of the measured intensity. **[c]** Plot of F_{obs} against F_{calc}.

source of the deviation of the F_{obs}/F_{calc} values away from unity in the fit assuming IRep(1). Nevertheless, the correspondence of the magnetic order with IRep(1) is a robust result, and from it a level of confidence can be assumed about the measured magnetic ordering wavevector and the dominant magnetic moment direction being that of the y direction.

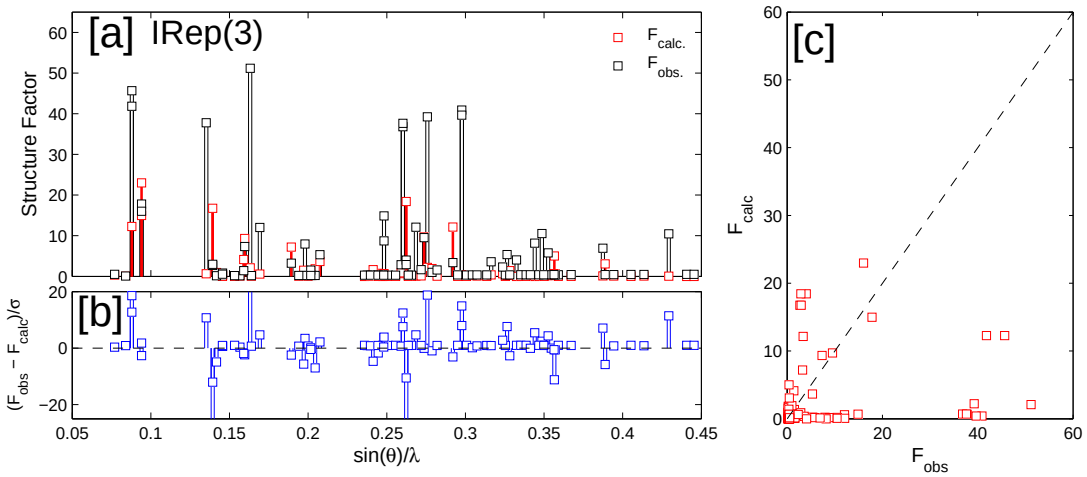

Figure 6.22: The least squares fit with Fullprof of the magnetic data to the calculated structure factor for IRep(3). **[a]** The difference in the observed and calculated structure factor, **[b]** The value $((F_{obs} - F_{calc})/\sigma$, the difference between the two divided by the standard deviation of the measured intensity. **[c]** Plot of F_{obs} against F_{calc}.

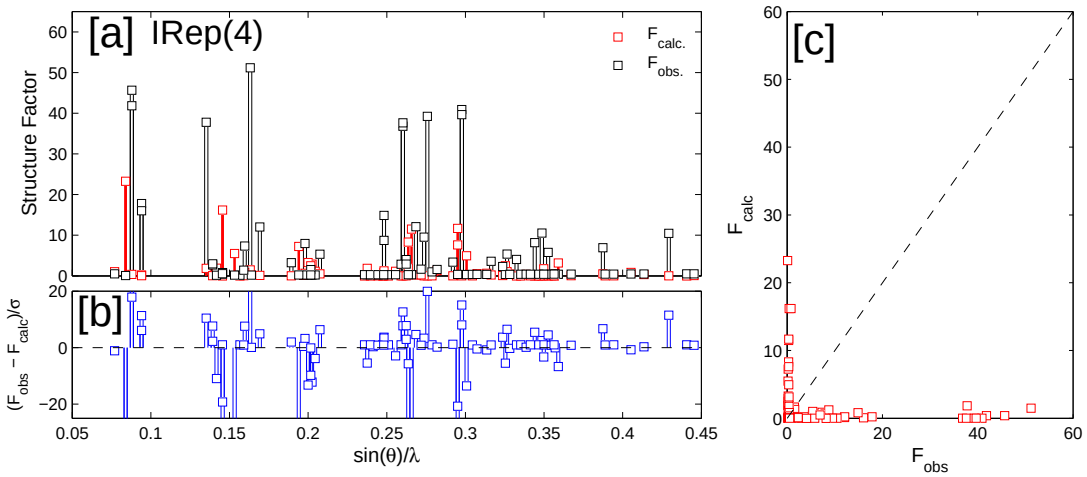

Figure 6.23: The least squares fit with Fullprof of the magnetic data to the calculated structure factor for IRep(4). **[a]** The difference in the observed and calculated structure factor, **[b]** The value $((F_{obs} - F_{calc})/\sigma$, the difference between the two divided by the standard deviation of the measured intensity. **[c]** Plot of F_{obs} against F_{calc}.

6.5 Coherence of the ground state

The occurence of magnetic Bragg scattering is evidence of a state of long-range magnetic order within $BiCu_{2(x-1)}Zn_{2x}PO_6$, with the observation of significant intensity even for small ($x = 0.01$) impurity concentrations. The ordered state is a consequence of a sizeable interaction between impurity induced LMs, mediated via the intermediate

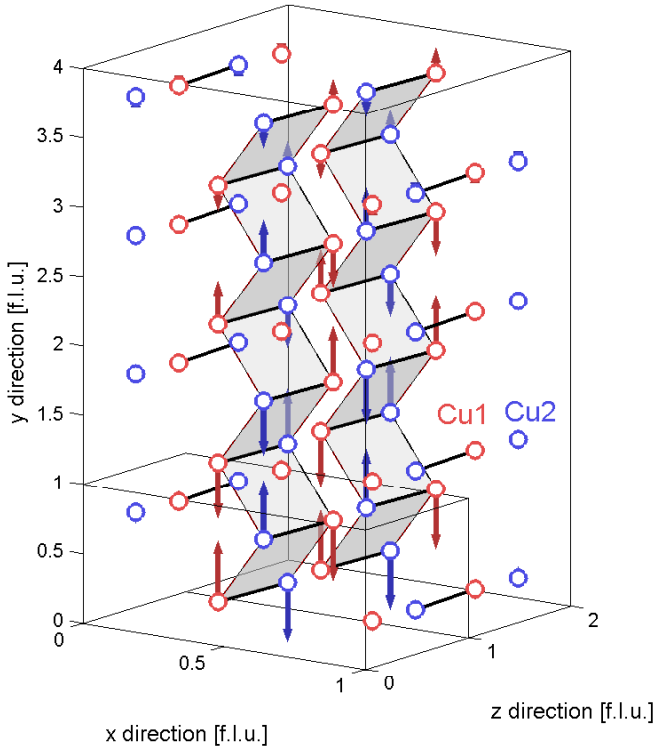

Figure 6.24: A schematic of the magnetic order in $BiCu_{2(1-x)}Zn_{2x}PO_6$ as determined through a least squares fit to IRep(1). The red and blue arrows illustrate the amplitude modulated moment when plotted on top of the lattice. The vertical direction is the direction of the ordering wavevector.

dimer states and denoted by the effective exchange interaction J_{eff}.

A ground state of long-range magnetic order is one where the order persists over infinite length and time scales. The length scales of the magnetic order detailed previously cannot be thought to be infinite, as evidenced by the appreciable FWHM observed in the Bragg peaks, and the observed susceptibility measurements indicating a phase of co-existing spin glass and long-range magnetic order.

A state of long-range magnetic order has a reciprocal space distribution described by a delta function centred at the Bragg scattering wavevector, $\delta(\vec{Q} - \vec{Q}_m)$. Any reduction of the correlation length to a finite value results in a broadening in the FWHM of the Bragg peak and therefore the extent to which the coherence of the ground state is constrained can be quantified with neutron diffraction experiments by considering the FWHM of the observed Bragg peaks.

Taking a perfectly ordered crystal, the broadening from a finite magnetic correlation length would simply be the experimentally observed profile deconvolved with the instrumental resolution. However, crystal imperfections can introduce systematic

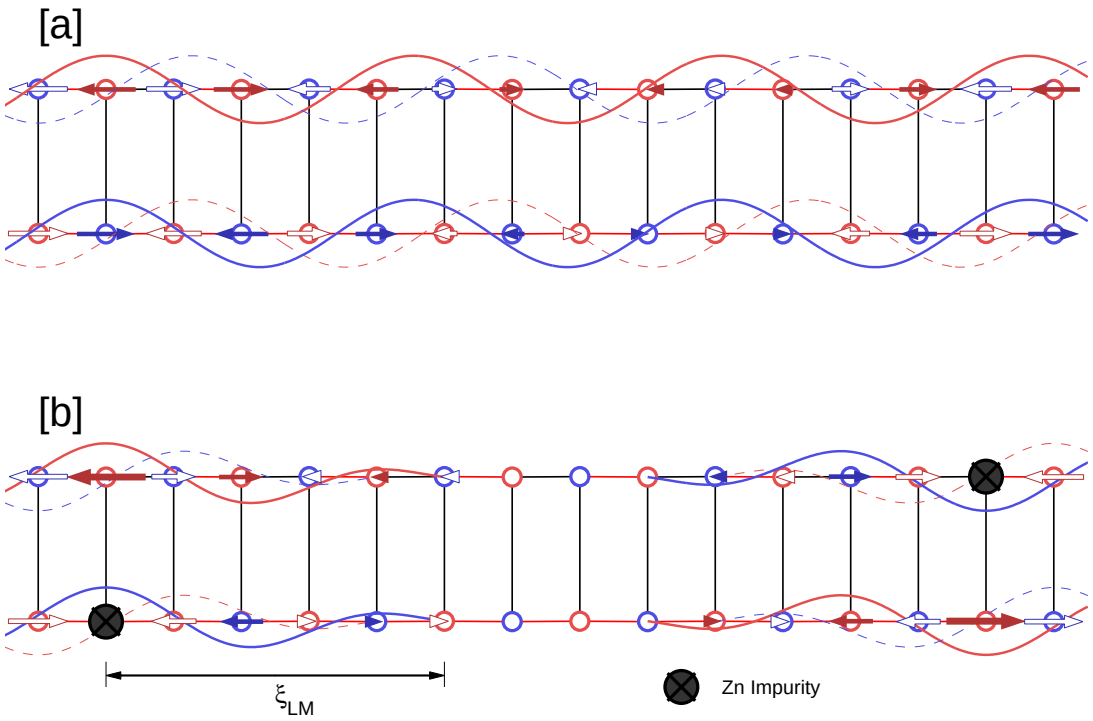

Figure 6.25: The proposed amplitude modulated spin structure. **[a]** The spin structure fitted from the TriCS data, assuming a homogeneous magnetic system where the amplitude modulates with the ordering wavevector k = (0 0.44 0) r.l.u. **[b]** A proposed model for the real magnetic ordering within the system, where Zn impurities introduce magnetic moments on the lattice. The ordering around each impurity is the fitted amplitude modulation with propagation vector k that correlates with other impurity-induced moments across the lattice.

error in such a determination.

Localised impurities such as point defects or crystallographic dislocations manifest as diffuse nuclear scattering across a broad reciprocal space distribution, which is observed in conjunction with the coherent Bragg lineshape. Long-range imperfections such as finite mosaicity in the crystal sample result in a finite broadening of the Bragg lineshape. The long-range magnetic correlations are constrained by the ordered nature of the crystal, and structural deformities are propagated to the magnetic profile.

The observed magnetic Bragg peak is therefore a convolution of all systematic forms of broadening with the instrumental resolution, and an observed nuclear peak is a result of the convolution of structural broadening with the instrumental resolution. The effect of finite magnetic correlation length can then be decoupled by deconvolving the observed magnetic Bragg profile with the observed profile of an adjacent nuclear Bragg peak.

With the assumption that these effects can both be described by Gaussians, the

resultant lineshape is also a Gaussian

$$\begin{aligned} F_{\text{tot}} &= \hat{F}_{\text{nuc}} * F_{\text{mag}} \\ &= \left[\frac{I_n}{(\sigma_n\sqrt{2\pi})}\exp\left(\frac{-Q^2}{2\sigma_n^2}\right)\right] * \left[\frac{I_m}{(\sigma_m\sqrt{2\pi})}\exp\left(\frac{-(Q-Q_m)^2}{2\sigma_m^2}\right)\right] \\ &= \left[\frac{I_n I_m}{(\sqrt{2(\sigma_n^2+\sigma_m^2)\pi})}\exp\left(\frac{-(Q-Q_m)^2}{2(\sigma_n^2+\sigma_m^2)}\right)\right] \end{aligned} \tag{6.4}$$

where $\hat{F}_{\text{nuc}}$ is the zero-centred nuclear distribution. The magnetic FWHM (and hence inverse correlation length) is given by $\Gamma_m = 2\sigma_m\sqrt{2\ln 2}$ and can then be extracted from the two measured peaks, through $\sigma_m = \sqrt{\sigma_t^2 - \sigma_n^2}$. Recalling that a delta function in reciprocal space corresponds to infinite length in real space, a finite reciprocal space distribution corresponds to a finite length scale in real space; thus from a FWHM in a reciprocal space direction, the correlation length in the corresponding real-space direction can be calculated (e.g. $\xi_m(a) = a/\Gamma_m(a)$ for the x direction, where $\Gamma_m(a)$ is given in reciprocal lattice co-ordinates). In a similar fashion, the convolution of two Lorenzian lineshapes is also a Lorenzian.

6.5.1 Experimental Setup

The orthorhombic structure of $BiCu_{2(1-x)}Zn_{2x}PO_6$ allows for the study of the correlation lengths along the three crystallographic directions by direct measurement of the magnetic Bragg peak intensity along the three reciprocal lattice directions Q_h, Q_k and Q_l.

Q-resolved magnetic Bragg intensity scans were performed for all three available single crystals $x = 0.01$, $x = 0.03$ and $x = 0.05$. The experiments were performed as a part of previously described experimental setups on TASP (§6.3.2), with $x = 0.03$ and 0.05 oriented in a **b-c** scattering plane and measured at a stable temperature $T \simeq 1.5$ K, and on TriCS (§6.4.1), with the $x = 0.05$ crystal mounted in a scattering geometry with a 5° offset to the **b-c** scattering plane.

TASP was operated with a flat (non-focusing) analyser, allowing for higher-resolution determination, but was constrained within the **b-c** plane; only momentum scans in Q_k and Q_l were possible. TriCS was operated with 20' collimation. The tilting geometry allows for a determination in all three lattice directions.

It is to be noted that the resolution ellipsoid for both instruments varies as a function of reciprocal space (and energy). This constrains the measurement such that the nuclear Bragg peak chosen for comparison must be chosen such that it possesses the same $\vec{Q}$ resolution. For investigations on the magnetic Bragg peak $\vec{Q} = (0\ 0.56\ 2)$ r.l.u., the best nuclear Bragg peak for such an analysis was identified as $\vec{Q} = (0\ 0\ 2)$

r.l.u. However, the resolution is not identical and as such introduces an unavoidable, but small error.

6.5.2 Correlation Lengths

The observed magnetic and nuclear Bragg profiles are given in Figure 6.26 for TASP and TriCS for $x = 0.03$ and $x = 0.05$. The minimum possible temperature on the instruments used in this study was $T = 1.5$ K, which lies above the $x = 0.01$ T_N value, and as such comparative scans for $x = 0.01$ are not available.

The magnetic and nuclear profiles were fitted assuming Gaussian lineshapes as given in Equation 6.4 to decode the structural contribution to the observed line widths. However, while the nuclear peaks are well defined Gaussian peaks, this approach is less successful for the magnetic peaks and it is observed they can be better described by a Lorentzian. This is most evident in the Q_h distribution given in Figure 6.26 [g].

The line of best fit results from the assumption of a nuclear Gaussian lineshape convolved with a Lorentzian magnetic broadening. The FWHM of two convolved Gaussians or two convolved Lorentzian is a trivial calculation upon application of the convolution theorem, but the FWHM of the convolution of a Gaussian and a Lorentzian function, referred to as a Voigt profile [162], is a problem that is solveable through numerical methods only.

Taking a Voigt profile as the assumed magnetic profile, the independent FWHM values can be extracted from a simultaneous fit of the nuclear and magnetic intensities. The fitted lineshapes are those shown in Figure 6.26, and the extracted parameters are summarised in Figure 6.27.

From the extracted values, there is a notable discrepancy observed in the values for $x = 0.05$ taken from the TriCS experiment and that of the TASP experiment. This difference is not a cause of instrument or sample misalignment; each instrument operated without error within functional parameters and within prescribed limits and at a stable temperature. The only obvious cause is the discrepancy in scattering geometry. The comparison to the nuclear Bragg peak was implemented to allow for a consistent comparison, but the $Q_k = 0.56$ r.l.u. difference in reciprocal lattice vector will be manifest in different ways between the two instruments, but the scale of the discrepancy is surprising. Discussion of this point must be deferred until the structure can be validated with further experimental work. Another possible source of the discrepancy is that the magnetic order may be affected by different rates of cooling.

However, it can be seen from the TriCS data that the spin-spin correlations are largely confined within the **b-c** plane. This is evident due to the large FWHM in the Q_h direction, over 10 times the magnitude of the other two directions. Taking

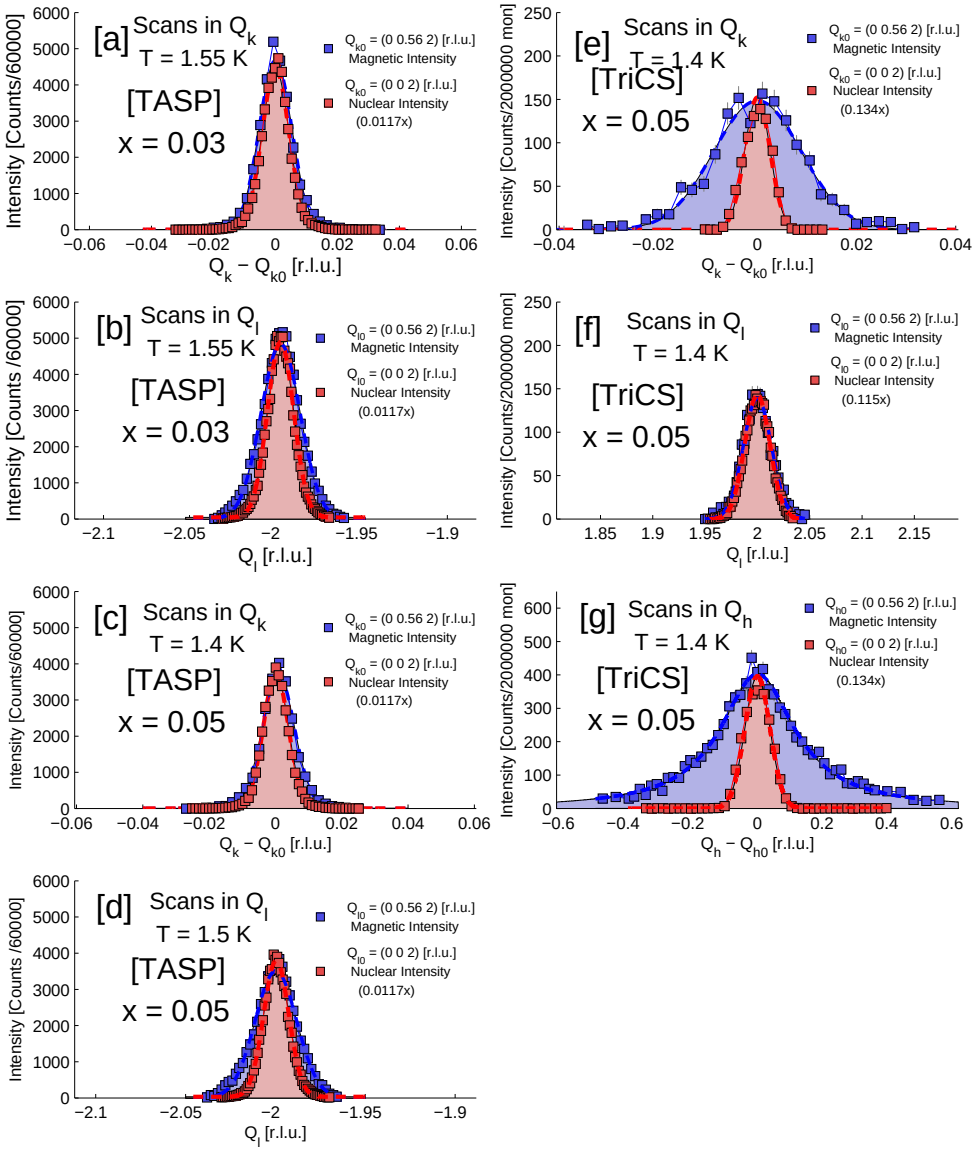

Figure 6.26: Comparison of nuclear and magnetic scattering intensity on TASP and TriCS. **[a]** TASP scans for $\vec{Q} = (0\ Q_k\ 2)$ r.l.u. for $x = 0.03$. **[b]** TASP scans for $\vec{Q} = (0\ 0.56\ Q_l)$ r.l.u. (magnetic) and $\vec{Q} = (0\ 0\ Q_l)$ r.l.u. (nuclear) for $x = 0.03$. **[c]** TASP scans for $\vec{Q} = (0\ Q_k\ 2)$ r.l.u. for $x = 0.05$. **[d]** TASP scans for $\vec{Q} = (0\ 0.56\ Q_l)$ r.l.u. (magnetic) and $\vec{Q} = (0\ 0\ Q_l)$ r.l.u. (nuclear) for $x = 0.05$. **[e]** TriCS scans for $\vec{Q} = (0\ Q_k\ 2)$ r.l.u. for $x = 0.05$. **[f]** TriCS scans for $\vec{Q} = (0\ 0.56\ Q_l)$ r.l.u. (magnetic) and $\vec{Q} = (0\ 0\ Q_l)$ r.l.u. (nuclear) for $x = 0.05$. **[g]** TriCS scans for $\vec{Q} = (Q_h\ 0.56\ 2)$ r.l.u. (magnetic) and $\vec{Q} = (Q_h\ 0\ 2)$ r.l.u. (nuclear)for $x = 0.05$. The magnetic Bragg scans are centred around the magnetic Bragg peak centre ($\vec{Q} = (0\ 0.56\ 2)$ r.l.u.) and the nuclear Bragg scans are centred around the nuclear Bragg peak centre ($\vec{Q} = (0\ 0\ 2)$ r.l.u.). The functional form of the observed magnetic Bragg intensity is the convolution of the two constituent lineshapes from finite magnetic correlation and instrumental resolution.

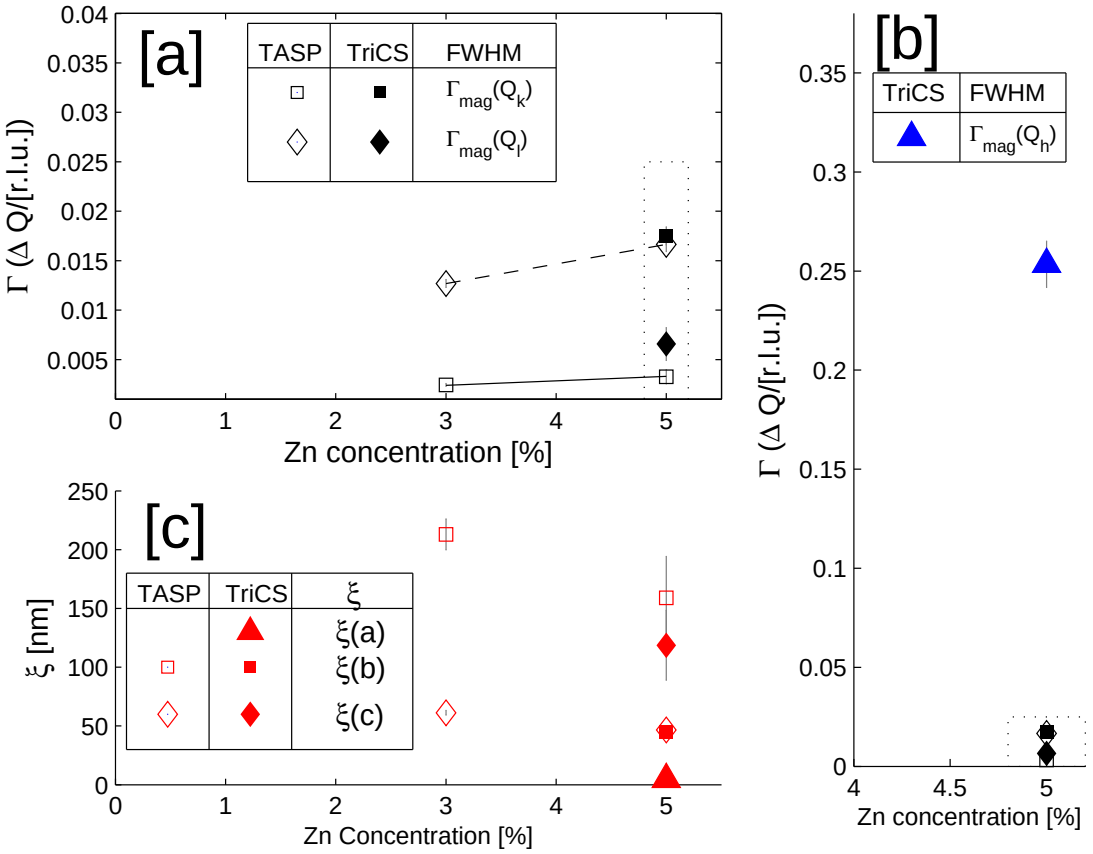

Figure 6.27: The fitted reciprocal space FWHM and correlation length ξ for $x = 0.05$ and $x = 0.03$ in all three crystallographic directions for the deconvolved magnetic Bragg intensities. **[a]** Black symbols denote the FWHM of the Lorenzian magnetic Bragg peaks, with squares for the Q_k direction and diamonds for Q_l. Open and filled squares correspond to parameters extracted from TASP and TriCS, respectively. **[b]** The blue symbol denotes the FWHM for the magnetic Bragg peak measured in the Q_h direction on TriCS. The black dotted square denotes the same region as in [a], included for a scalar comparison. **[c]** The extracted correlation lengths for the three crystallographic directions, denoted by the red markers with identical notation to that of [a] and [b].

the TASP data to be self-consistent, it can be further concluded that an increase of Zn-doping from $x = 0.03$ to $x = 0.05$ results in a decrease in spin-spin correlations, principally in Q_l, but also evident in Q_k.

This is indicative of the strongest correlations lying within the ladder structure. Counter-intuitively, increasing the Zn-doping results in shorter spin-spin correlations. This can be reconciled with the fact that a large spin correlation length results in an overlap of the paramagnetic clouds, but without overlap with the impurities themselves. Increasing the density raises the probability of an incommensurately ordered spin structure terminating at an impurity, reducing the correlation length.

The extracted correlation lengths for the measured data is shown in Figure 6.27 [c] by the red symbols; the shapes denote the instrument on which they were measured and the direction in reciprocal space and is detailed in the figure. The large FWHM seen in Q_h results in a correlation length of $\xi_a = 46.47 \pm 2.15$ Å^{-1}, indicating correlations across only ~ 4 unit cells. In comparison, the extracted Q_l correlation length from TriCS is $\xi_c = 1186.62 \pm 298$ Å^{-1}, which corresponds to correlations over 150 unit cells.

6.6 Inelastic Scattering Intensity

The introduction of impurity induced-local moments liberate spin degrees of freedom with characteristic energy scales below that of the spin gap. However, the gapped nature of the excited state can still persist in conjunction with the antiferromagnetically ordered state, with the dynamical properties of the triplet excitations characterised at and above the gap energy. While the gapped state persists, significant doping can affect the dynamical properties and quantum coherence of the ground state, and the extent to which this occurs depend on the exchange interaction geometry, the distribution of impurities and the coherence length in relation to that distribution.

Due to the observation of long-range magnetic order upon doping, one would expect the emergence of a Goldstone mode corresponding to transverse fluctuations of the impurity-induced magnetic moments (spin waves). However, in regions far from these magnetic moments, the dimerised groundstate of the undoped structure persists, with excitations described by propagating triplets. This therefore raises the possibility of the simultaneous observation of both types of excitation at different energy scales.

The spin gap as a function of Zn-doping x was measured for $BiCu_{2(x-1)}Zn_{2x}PO_6$ for $x = 0.0$, 0.01, 0.03 and 0.05. The crystals were oriented in the **b-c** scattering plane and the experimental setup was that of TASP outlined in §6.3.2. The analyser was oriented in a focusing condition and for $k_f = 1.3$ Å^{-1}, scattering in energy transfer ΔE was measured at the incommensurate minimum $\vec{Q} = (0\ 0.56\ 2)$ r.l.u. for 0 meV $< \Delta E <$ 6.5 meV.

The results are shown in Figure 6.28. In panels [a] - [d], the fitted intensities for x = 0.01, 0.03 and 0.05 are compared to $x = 0.00$, with each case highlighted separately, and the $x = 0.05$ intensity rescaled in [d]. An asymmetric Gaussian lineshape, as given in Chapter 5, is assumed to fit the data to account for the resolution effects. The extracted spin gap energies are shown in Figure 6.28 [e] with the FWHM of the asymmetric lineshape described by the bounding bars.

It can be seen that the introduction of Zn impurities has a drastic effect on the inelastic spectrum. The spin gap Δ is shown to increase with x, and the observed

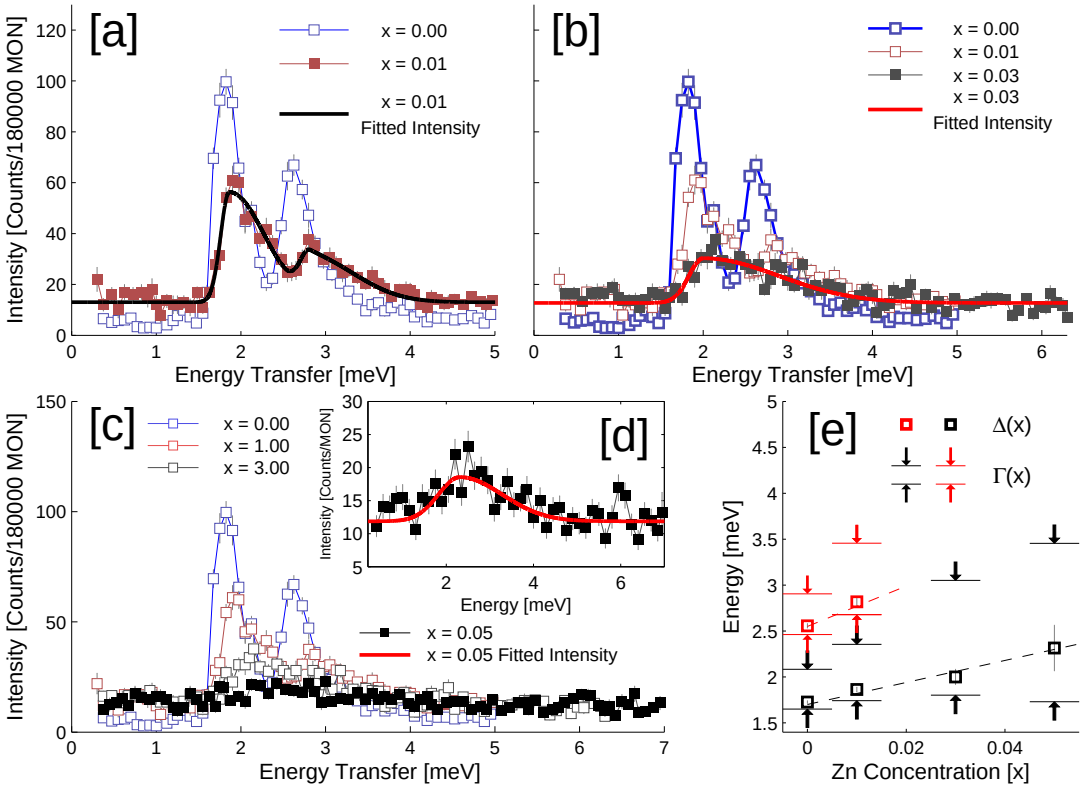

Figure 6.28: The effect of non-magnetic impurity doping upon the inelastic scattering intensity at $\vec{Q} = (0\ 0.56\ 2)$ r.l.u. **[a]** Line of best fit to the $x = 0.01$ INS data (red squares), compared to the $x = 0.0$ INS data (blue bordered squares) **[b]** Line of best fit to the $x = 0.03$ INS data (grey squares), compared to the $x = 0.0$ INS data and $x = 0.01$ INS data (red bored squares). **[c]** Comparison of the $x = 0.05$ INS data (black squares) to the $x = 0.0$ INS data, the $x = 0.01$ INS data and $x = 0.03$ INS data (grey bordered squares). **[d]** Inset panel showing line of best fit to the $x = 0.05$ INS data. **[e]** Summary of the fitted excitation energies and FWHM for $x = 0.0$, 0.01, 0.03 and 0.05. It can be seen from the figure that by introducing non-magnetic impurities, the value of the spin gap increases with a significant reduction of coherent scattering intensity.

coherent scattering intensity decreases. Additionally, a significant energy-broadening is realised that results in an almost complete removal of coherent scattering intensity at $x = 0.05$. A notable feature of the data is an increase of scattering intensity to energies below that of the original spin gap ($\Delta E < 1.5$ meV) for all Zn-impurities, with registered intensity well above the measured background for $x = 0.0$. This feature is not a result of incoherent scattering or instrumental effects, and a real result of impurity doping.

The renormalisation of the spin gap energy under increased impurity doping can have two origins. First, the perturbation of the lattice by the impurities can result in different exchange interactions and the excitation energy change is then a result of a

renormalised Hamiltonian. The validity of this explanation can be examined through the comparison of the measured lattice parameters of the Zn-doped samples, given in Table 6.1, from Ref. [114], which change only by $\sim 0.08\%$. This confirms that the lattice is not significantly altered by the substitutions and therefore the spin gap shift is unlikely to be a result of perturbed exchange interactions. However, we note that in the immediate vicinity of the impurity induced spins, the exchange parameters may be altered by the different radius of the Zn^{2+} ion.

Instead it is likely the renormalised gap energy and spectral distribution arises from the second consideration - the effect of decoherence of the gapped triplet excitations from the introduction of impurities onto the lattice.

A coherent wavefunction is one that is perfectly periodic in time and in space, and is typically constrained by classical order within the system e.g. the renormalisation and damping of spin wave excitations with the removal of long-range magnetic order. However, coherent magnetic excitations can be observed in the absence of long-range order in spin-gapped systems and are those described by propagating triplet excitations, or triplons. The triplons can propagate across the lattice and are mediated via the localised spin couplings, and scatter upon encountering a defect within the system. The introduction of impurities reduce the number of sites to which a triplet can propagate; this reduces the mobility, resulting in a band narrowing and therefore an increase in the spin gap. In addition, lifetime broadening occurs due to damping effects from additional scattering processes within the crystal.

The effect of the defect is to prevent the occupation of a site by the triplet excitation and can occur via site dilution, where an impurity removes spins from the lattice, or through bond-dilution which can introduce holes into the ground state. This is analagous to the situation where a site is already occupied by a thermally excited triplet [34].

An example of this effect can be seen in the effect of thermal population on the quantum coherence of excitations in the 1-D Haldane chain Y_2BaNiO_5, which demonstrates dispersing coherent $S = 1$ excitations from a disordered ground state [163]. It was shown that the FWHM and spin gap energy Δ renormalise upwards upon the raising of temperature and is consistent with presented theory of reduction of the mean-free path from increased defect density.

This is in contrast to the case of the Zn-doped two-leg ladder $Sr(Cu_{(1-x)}Zn_x)_2O_3$, which contains a very large spin gap due to the strong exchange coupling. While observing significant spectral damping and the removal of the spin gap intensity for $x \sim 4\%$, the overall magnitude of the spin gap does not change with increasing Zn-concentration [164].

The discussion for Y_2BaNiO_5 is presented for the case of a 1-D $S = 1$ chain, but is useful in consideration of the S= 1 excitations of the quasi-1D geometry of BCPO and the effect of thermal defects can be compared to impurities leading to site dilution. The increase in spin gap and FWHM is strongly indicative of persistent short-range triplon correlation upon doping, albeit resulting in an decrease of mean-free path within the system and therefore quantum decoherence of the gapped excitations upon increase of x.

In Ref. [165], through the consideration of the spin ladder geometry as a finite-size two-dimensional antiferromagnet, the zero temperature properties were obtained from the finite-sized (2+1)-dimensional nonlinear σ model. In this fashion it was possible to obtain estimates for the correlation lengths and spin gaps in spin ladders [166]; taking this approach a general model can be taken where one can assume a correlation length ξ is given by

$$\xi = \frac{\hbar c}{\Delta}, \tag{6.5}$$

where Δ is the spin gap and c is a velocity of the excitation. The precise value of the dynamical correlation length cannot be calculated without knowledge of the velocity of the magnon excitation within the frustrated ladder geometry. However, the proportionality $\xi \propto 1/\Delta$ can be applied and, assuming the velocity of the excitation remains unchanged, it can be deduced that the correlation length has decreased by $\sim 25\%$.

The other key observation of the x dependence of the inelastic intensity is the shift in spectral weight of the excitations as x increases. This result is consistent with the total sum rule [167] and the reduced intensity can be explained by the emergent scattering weight at the magnetic Bragg peaks and related dynamics at energies below the original spin gap.

6.7 Discussion and Outlook

$BiCu_{2(x-1)}Zn_{2x}PO_6$ provides a unique opportunity to study three cases of spin-spin correlation effects in a spin gapped system with non-magnetic impurities: the case of weakly coupled spins; the case of strongly coupled spins in a frustrated geometry and the study of strongly coupled spins in an unfrustrated geometry. Due to the nature of the exchange interactions these three cases can be decoupled and studied simultaneously through independent investigation of the three directions in reciprocal space.

It has been observed that long-range magnetic order is clearly observable upon the introduction of the smallest available Zn doping $x = 0.01$, indicating a finite effective J_{eff} exchange interaction between LMs, with a correlation length ξ_M at least on the order of magnitude of the Zn-Zn separation. Assuming a picture of a spin-spin interaction term that is exponentially decreasing with the spin separation distance [147], increasing the LM concentration results in an increase in the average LM interaction term. This is the behaviour observed in $BiCu_{2(x-1)}Zn_{2x}PO_6$, where the strength of the exchange interaction can be estimated by the temperature required to remove the order, namely the Néel temperature, which is observe to increase roughly proportionally to x.

However, while the increase in LM coupling is evident, the crystallographic direction-dependence of the LM correlation length is unresolved. While the weakly coupled nature of the spins from the weak magnetic exchange in the crystallographic **a**-direction is clear, the magnitude of the correlation length in **b** and **c** is an open question due to the significantly different magnetic portraits as seen in the experimental data. The influence of instrumental parameters and geometry is something that must be tested experimentally. The weaker inter-ladder coupling along **c** and the frustrated coupling along **b** are both potential reasons for the observed effect on the correlation length.

The non-magnetic impurities, rather than inducing an isolated spin, induce paramagnetic clouds made of alternating moments within their vicinity. In the rung singlet pictures of $BiCu_2PO_6$, the induced spins can create a local mixture of singlet and triplet states that results in an attenuated moment on each dimer with a magnitude that decays with increasing distance from the impurity. Taking the average fitted moment from the Fullprof structure analysis, a total of 1 μ_B results from the integration of the magnetic moments of merely seven nearest neighbours, supporting the argument that the length scale of this induced magnetism, ξ_{LM}, is on the order of a few lattice sites.

It is the correlation of these clouds that gives rise to the long-range magnetic order, and it is postulated that the observed 'glassiness' previously discussed is a result of the difficulty in forming a long-range ordered, incommensurate structure involving randomly placed clouds [147]. The coherence in one crystallographic direction and incoherence in another is a possible explanation of the coexistence of the two states.

The reduction of correlation lengths in different crystallographic directions from persistent spin-glass properties is a realistic expectation. The presence of the spin-glass nature is inferred from the susceptibility measurements, but is as yet unconfirmed with neutron scattering results. A full study of the correlation lengths in **a**, **b** and **c** under a range of applied fields is the next logical step; an observation of the renormalisation

of the magnetic Bragg peak width under the proposed SG+AFM to AFM transition would confirm its existence, and further be an indication of the origin of the spin-glass behaviour.

This work would further complement the current phase diagram in temperature and field. While this has been succesfully investigated for $x = 0.01$ and 0.05, the work is still incomplete. The field was applied along **a**, the direction of weakest magnetic exchange coupling. A continuous reduction of magnetic moment was observed, and it would be desirable to compare this to different directions of applied field, namely **H**||**b** and **H**||**c**. The determination of and the observation of field-dependence of critical saturation values would yield further information on the orientation of the magnetic moment and provide a useful comparison to the observed transition from SG+AFM to AFM which was observed with the field applied **H**||**b**.

The temperature dependence of the magnetic Bragg peak intensity was shown to demonstrate significant critical scattering. A fit to the scattering intensity in the region of T_N was managed assuming a distribution of critical temperatures that corresponds to the distribution of impurity concentration within the sample. The fitted T_N distribution was broader than would be expected from a distribution in Zn impurity concentration, which is indicative of either an overly optimistic concentration distribution or additional effects within the critical regime. While the fitted momentum Bragg peak widths are not indicative of a broad diffuse scattering in the Q_k direction, a systematic and detailed determination of the Bragg peak widths in all three reciprocal space directions would allow one to infer what diffuse scattering effects are present near the phase boundary.

The magnetic structure investigation resulted in the data best described by a model for magnetic order that is amplitude modulated with the magnetic moments directed along the crystallographic **b**-direction. The lack of a perfect correspondence to an Irreducible Representation is likely a result of the attenuated distribution of impurity-induced spins in regions localised around the impurity. In addition, due to the relatively large crystal samples that are being used there is the possibility that the observed scattering intensity is reduced due to extinction effects [168]. This would mean that the observed scattering intensity would not be proportional to square of the structure factor; to retain such a relationship one must work with much smaller crystal samples. Unfortunately, because of the relatively low doping concentration, the small magnetic moment present in the sample necessitates the use of large single crystals. Therefore these effects in diffraction experiments on $BiCu_{2(1-x)}Zn_xPO_6$ such as the one conducted on TriCS are, lamentably, unavoidable.

This aspect of the magnetic structure is complicated and there is not an obvious model that can be assumed, especially considering the frustrated nature of the spin couplings and possible glass-like behaviour. Nevertheless, the resulting fit assuming a homogeneous spin distribution provides a robust result; this can be seen by the comparatively poor levels of agreement that models assuming other Irreducible Representations have with the magnetic Bragg peak intensities. As such, a high level of confidence can be ascribed to the key results, namely the ordering wavevector and the existence of magnetic order described by an amplitude modulated structure with the spin direction predominantly oriented such that it lies in the crystallographic **b**-direction.

However, small S^x and S^z contributions cannot be excluded because they are either not resolvable or they have no preferential spin ordering direction. The precise magnetic structure remains an open question and necessitates further experimental work.

In conclusion, through the use of neutron diffraction experiments, it was observed that $BiCu_{2(x-1)}Zn_{2x}PO_6$ shows long-range magnetic order for $x \geq 0.01$, with an $x-$ dependent critical temperature. The magnetic structure and low-energy excitations coexist with higher-energy dynamical correlations up to and including $x = 0.05$, albeit with significantly reduced INS intensity. The dominant structural ordering exists as an amplitude modulated spin moment oriented along the **b**-direction, with weaker magnetic correlations along the **a** direction. The propagation vector is exactly that of the minimum spin gap for $x = 0$.

Summary

$BiCu_{2(x-1)}Zn_xPO_6$ is an impurity doped frustrated spin ladder system that has been shown to exhibit magnetic order below a critical temperature. Bragg peaks are observed in all measured doping concentrations ($x = 0.01$, $x = 0.03$ and $x = 0.05$), a result of long-range correlations of the liberation of spins from an introduction of non-magnetic impurities. Neutron scattering studies were performed to elucidate the properties of this system, and to perform a comparison to the undoped compound, $BiCu_2PO_6$.

- Bragg peaks were observed at incommensurate ordering wavevectors for all doping concentrations.
- The ordering wavevector is identical to the spin gap minimum for $x = 0$.

- A field-temperature phase diagram has been investigated, with critical temperatures determined for different values of applied field.
- A spin structure was determined, and found to be amplitude modulated with an incommensurate ordering wavevector.
- The local moments exhibit varying levels of coherence across reciprocal space, with minimal correlations between ladder units in the crystallographic a direction, where the exchange is weak.
- A comparison of the inelastic spectra revealed an upward renormalisation and damping of the spin gap for increasing impurity concentration and new low-energy dynamics associated with magnetic order.

Further experimental work is required to build upon the results presented in this chapter. In particular, further high-resolution measurements are required to investigate the coherence of the ground state in all three directions in reciprocal space for all sample concentrations. In addition, the field-dependence of the magnetic Bragg peak intensity for different directions of applied field would provide further information about the direction of the ordered moment. Further work on the region of low-energy inelastic scattering would also be desirable to investigate the possible Goldstone modes, i.e. transverse excitations of the impurity-induced ordered moment.

7

Conclusions and Outlook

The compounds investigated and discussed are a selection of model magnetic systems that can be used to experimentally investigate theoretical ideas of magnetism. Notably $TlCuCl_3$ provides the unique opportunity to investigate excitations near a pressure-induced QCP, and $BiCu_2PO_6$, doped and undoped, gives an exciting insight into the properties of frustrated spin ladder geometries. The work that constitutes this thesis contributes toward a larger body of ongoing research that seeks further understanding of quantum magnetism through investigation and deduction of the properties of the various ground states of experimentally accessible systems.

The range of work presented above consists of investigations of such ground states, with the systems presented above existing as different models of quantum magnetism. Studies on $BiCu_2PO_6$ constitute consideration of the excitations of a model magnet with no observed long-range order; investigations on the magnetic structure of the impurity-induced long-range ordered doped spin ladder $BiCu_{2(1-x)}Zn_{2x}PO_6$, and studies of $TlCuCl_3$ yielding further understand of a material where one can continuously tune between states of order and disorder by applying hydrostatic pressure, and through increasing/decreasing temperature through the pressure-dependent Néel temperature.

The work on $TlCuCl_3$ has successfully extended the previous work, which constituted an investigation across the QPT, into a consideration of the experimental case of interplay between quantum and thermal fluctuations by investigation of excitations across the phase boundary. Theoretical models were successfully applied in conjunction with neutron scattering techniques to allow for a determination of the elementary excitations across the phase boundary. The amplitude fluctuations of the ordered moment were found to persist up to $P = 3.4$ kbar, with an excitation energy that continuously reduced to zero as the system was driven through the thermal phase transition at

constant pressures. In this sense, the dynamics for the case of 'thermal melting' were found to be similar to the case for 'quantum melting'.

Theoretical arguments have been made to explain the behaviour of the longitudinal mode, but a systematic description up to finite temperatures is still lacking. The outlook for future work on $TlCuCl_3$ is therefore largely theoretical; the self-consistent MFBO discussed in Chapter 4 reproduces some of the features of the experimental data, but does not reproduce the pressure-dependent Néel temperature nor make reliable estimates about the parametric description of the excitations across the phase boundary. With the addition of adjustments to the existing theory, such as log corrections to the scaling factors, a description could be shown to reproduce the data.

The experiments on $BiCu_2PO_6$ constitute a large body of data collected on the first single crystals of this compound. Significant progress has been made toward discerning the dispersion of magnon excitations across reciprocal space, revealing a 2-D dispersion with excitations propagating along the ladder and rung lattice directions. The application of magnetic field perpendicular to both these directions revealed a non-linear field dependence of the excitations, qualitatively described by anisotropic terms within the system Hamiltonian.

Attempts to describe the measured INS intensity with theoretical descriptions from perturbative and bond-operator methods were made with a level of success; the dispersion was shown to be reproduced by the analytical descriptions. Further numerical simulations by exact diagonalisation would help to determine if the parameterisation is accurate. In addition to ongoing theoretical considerations, further experimental work is vital to connect the currently disparate elements of a much larger picture; in particular, INS studies must be continued to determine the proposed two-magnon boundstate and to elucidate the contribution of Dzyaloshinskii-Moriya splitting on the inter-ladder dispersion. Further data on the field-dependence of the observed multiplicity of excitations near the spin gap minimum is also desirable for a more quantitative treatment of the proposed anisotropic terms.

It is hypothesised that the spin degrees of freedom from impurity-doping order with Néel temperatures that are independent of parent lattice composition. The work on $BiCu_{2(x-1)}Zn_{2x}PO_6$ detailed above supports this hypothesis, and work on this compound is presented as an investigation of the emergent long-range order of site dilution on a frustrated spin-ladder geometry. Systematic investigations of the Bragg peak intensities have allowed a determination of the field-temperature phase diagram, coherence of the ground state and a first estimate of the magnetic structure.

The work on $BiCu_{2(x-1)}Zn_{2x}PO_6$ detailed in this thesis serves as a foundation upon which future experimental studies will build. Further work on the field-dependence of

the magnetic ordering will complete the phase diagram in three field directions, also extending the studies to include investigations of the 3% compound, at present only measured at $H = 0$ T. Additional diffraction studies will allow for further refinement of the proposed magnetic order, and confirmation of the coherence of the ground state by repeat measurements of magnetic Bragg peak intensity and possible diffuse scattering. The effect of doping upon the excitations is to be probed in depth with further high resolution neutron scattering experiments near the spin gap minimum. This will help to determine the redistribution of magnetic intensity to coherent Bragg peaks, the renormalisation of the spin gap and the possible emergence of a Goldstone mode, required by the observation of long-range order.

It is my hope that the work I have completed and outlined above will contribute in no small part toward not only the future work on these model quantum magnets and the specific questions they pertain to, but to the field of quantum magnetism as a whole and the general scope of scientific understanding.

Bibliography

[1] É. d-Lacheisserie, D. Gignoux and M. Schlenker, *Magnetism: Fundamentals*, Springer (2005). 15

[2] S. Blundell, *Magnetism in Condensed Matter*, Oxford University Press (2001). 17, 20, 90, 160

[3] P. Fazekas, *Lecture Notes on Electron Correlation and Magnetism*, World Scientific Publishing Co. (1999). 18

[4] N.D. Mermin, H. Wagner, Phys. Rev. Lett. **17**, 1133 (1966). 18

[5] S. Sachdev, Nature Physics **4**, 173 (2008). 19

[6] H.- J. Mikeska and A. K. Kolezhuk , Lect. Notes Phys. **645**, 1-83 (2004). 19

[7] J. Richter, J. Schulenburg and A. Honecker, Lect. Notes Phys **645**, 85 - 153 (2004). 19

[8] S. Sachdev, Lect. Notes Phys **645**, 381 (2004). 19

[9] S. Sachdev, *Quantum Phase Transitions*, Cambridge University Press (1999). 20

[10] J. Goldstone, A. Salam, and S. Weinberg, Phys. Rev. **127**, 965 (1962). 20, 39

[11] P. W. Anderson, Phys. Rev. **79**, 350 (1950). 20

[12] B. Thielmann, PhD. Thesis, ETH Zürich (2009). 21, 137

[13] G.L. Squires, *Introduction to the Theory of Thermal Neutron Scattering*, Cambridge University Press (1978). 24, 25, 26, 29

[14] S. W. Lovesey, *Theory of Neutron Scattering from Condensed Matter: Volume 1, Nuclear Scattering*, Clarendon Press (1984). 24

[15] S. W. Lovesey, *Theory of Neutron Scattering from Condensed Matter: Volume 2, Polarization effects and Magnetic Scattering*, Clarendon Press (1984). 24

[16] G. Shirane, S. M. Shapiro and J. M. Tranquada, *Neutron Scattering with a Triple-Axis Spectrometer: Basic Techniques*, Cambridge University Press (2002). 24

[17] ILL website, http://www.ill.eu 24

[18] SINQ website, http://www.psi.ch/sinq/ 24, 30, 31

[19] M. J. Cooper and R. Nathans, Acta Cryst, **23**, 357 (1967). 32

[20] M. Popovici, Acta Cryst. A, **31**, 507 (1975). 32

[21] G. K. White and P. J. Meeson, *Experimental Techniques in Low Temperature Physics*, Oxford University Press (2002). 34

[22] A. T. Holmes, G. R. Walsh, E. Blackburn, E. M. Forgan and M. S-. Bennet, Rev. Sci. Instr **83**, 023904 (2012). 35

[23] M. Ermets, *High Pressure Experimental Methods*, Oxford University Press (1996). 36

[24] W. B. Holzapfel and N. S. Isaacs, *High Pressure Techniques in Chemistry and Physics: A Practical Approach*, Oxford University Press (1997). 36

[25] D. W. J. Langer, J. Phys. Chem. Solids **21**, 123 (1961). 37

[26] B. Normand, Ch. Rüegg, Phys. Rev. B **83**, 054415 (2011). 38, 46, 98

[27] S. P. Bayrakci, T. Keller, K. Habicht and B. Kiemer, Science **312**, 1926 (2006). 39

[28] A. Tucciarone, H.Y. Lau, L.M. Corliss, A. Delapalme, and J.M. Hastings. Phys. Rev. B **4**, 3206 (1971). 39

[29] J. An, C-.D. Gong and H-.Q Lin, J. Phys. Condens. Matter **13**, 115-122 (2001). 39

[30] S. Sachdev and R. N. Bhatt, Phys. Rev. B **41**, 9323 (1990). 39

[31] M. Matsumoto, B. Normand, T. M. Rice, and M. Sigrist, Phys. Rev. B **69**, 054423 (2004). 39, 40, 41, 44, 56, 57, 66, 69

[32] M. Matsumoto, B. Normand, T. M. Rice, and M. Sigrist, Phys. Rev. B **89**, 077203 (2002). 39

[33] Ch. Rüegg, A. Furrer, Th. Strässle, K. W. Krämer, H.-U. Güdel and L. Mélési, Phys. Rev. Lett. **93**, 257201(2005). 42, 59, 60, 64

[34] Ch. Rüegg B. Normand, M. Matsumoto, Ch. Niedermayer, A. Furrer, K. W. Krämer, H.-U. Güdel, Ph. Bourges, Y. Sidis and H. Mutka, Phys. Rev. Lett. **95**, 267201 (2005). 45, 51, 70, 87, 90, 183

[35] S. Gopalan, T. M. Rice and M. Sigrist, Phys. Rev. B **49**, 8901 (1994). 46, 50, 51, 130

[36] B. Normand and T. M. Rice, Phys. Rev. B **54**, 7180 (1996). 46

[37] B. Normand and T. M. Rice, Phys. Rev. B **56**, 8760 (1997). 46

[38] C. K. Majumdar and D. K. Ghosh, J.Math. Phys **10**, 1388 (1969). 47

[39] A. Lavarélo, G. Roux and N. Laflorencie, Phys. Rev. B **84**, 144407 (2007). 47, 48, 50, 51, 101, 130

[40] B. Koteswararao, S. Salunke, A. V. Mahajan, I. Dasgupta and J. Bobroff, Phys. Rev. **76**, 052402 (2007). 49, 101

[41] O. Mentré, E. Janod, P. Rabu, M. Hennion, F. Leclercq-Hugeux, J. Kang, C. Lee, M.-H. Whangbo and S. Petit, Phys. Rev. B **80**, 180413 (R) (2009). 49, 101, 140, 141, 146

[42] A. Tsirlin, I. Rousochatzakis, D. Kasinathan, O. Janson, R. Nath, f. Weickert, C. Geibel, A. M. Läuchli and H. Rosner, Phys. Rev. B **82**, 144426 (2010). 47, 49, 50, 51, 101, 115, 128, 129, 137, 140, 147

[43] W. Meyerhoffer, Z. Physik. Chem., **3**, 185 (1889). 52

[44] R.D. Willett, C. Dwiggins, R.F. Kruh and R.E. Rundle, J. Chem. Phys. **38**, 2429 (1963). 52

[45] P. H. Vossos, L. D. Jennings and R. E. Rundle, J. Chem. Phys, **32**, 1590 (1960). 52

[46] G.J. Maass, B.C. Gerstein and R. D. Willett, J. Chem. Phys. **46**, 401 (1966). 53

[47] J. E. Hynes, B. B. Garrett and W. G. Moulton, J. Chem. Phys., **52**, 2671 (1970). 53

[48] H. Tanaka, K. Takatsu, W. Shiramura and T. Ono, J. Pys. Soc. Jpn, **65**, 1945 (1996). 53

[49] K. Takatsu, W. Shiramura and H. Tanaka, J. Phys. Soc. Jpn. **66**, 1611 (1997). 53, 54

[50] M. Troyer, H. Tsunetsugu, and D. Würtz, Phys. Rev. B. **50**, 13515 (1994). 53, 90

[51] W. Shiramura, K. Takatsu, H. Tanaka, K. Kamishima, M. Takahashi, H. Mitamura, T. Goto, J. Phys. Soc. Jpn. **66** 1900 (1997). 54, 55

[52] Ch. Rüegg, PhD Thesis, ETH Zurich (2005). 54, 60, 64, 70

[53] N. Cavadini, G. Heigold, W. Henggeler, A. Furrer, H-U. Güdel, K. Krämer and H. Mutka, J. Phys. Condens. Matter **12**, 5463 (2000). 54, 57

[54] J. H. M. Thornley, N. E. Magnum, J. H. E. Griffiths and J. Owe, Proc. Phys. Soc. bf 78, 1263 (1963). 54

[55] D. Harker, Z. Kristallogr. **93**, 136 (1936). 54

[56] J. D. Dunitz, Acta Crystallogr. **10**, 307 (1957). 54

[57] K. Takeda, S. Matsukawa and T. Haseda, J. Phys. Soc. Jpn. **30**, 1330 (1971). 54

[58] T. Nakamura and K. Okamoto, Phys. Rev. B., **58** 2411 (1998). 54

[59] R. A. Cowley, B. Lake and D. A. Tennant, J. Phys. Condens. Matter. **8**, L179 (1996). 55

[60] J. Eckert, D. E. Cox, G. Shirane, S. A. Friedberg, H. Kobayashi, Phys. Rev. B. **20**, 4596 (1979). 55

[61] M. B. Stone, Y. Chen, J. Rittner, H. Yardimci, D. H. Reich, C. Broholm, D. V. Ferraris and T. Lectka, Phys. Rev. B **65**, 064423 (2002). 55

[62] T. Kato, A. Oosawa, K. Takatsu, H. Tanaka, W. Shiramura, K. Nakajima, K. Kakurai, J. Phys. Chem. Solids, **60**, 1125 (1999). 55

[63] N. Cavadini, W. Henggeler, A. Furrer, H. U. Güdel, K. Kämer, and H. Mutka. Physica B **276**, 540 (2000). 55

[64] N. Cavadini, G. Heigold, W. Heggler, A. Furrer, G.-U. Güdel, K. Krämer and H. Mutka, Phys. Rev. B **63**, 172414 (2001). 55, 57, 58, 70, 137

[65] N. Cavadini, W. Henggeler, A. Furrer, H.-U. Güdel, K. Krämer and H. Mutka, Eur. Phys. J. B **7**, 519-522 (1999). 56

[66] N. Cavadini, Ch. Rüegg, W. Henggeler, A. Furrer, H.-U. Güdel, K. Krämer and H. Mutka, Eur. Phys. J. B **18**, 565 (2000). 57

[67] F. London, Nature **141**, 643-644 (1938). 58

[68] M Jaime, V. F. Correa, N. Harrison, C. D. Batista, N. Kawashima, Y. Kazuma, G. A. Jorge, R. Stern, I. Heinmaa, S. A. Zvyagin, Y. Sasago and K. Uchinokura, Phys. Rev. Lett. **93**, 087203 (2004). 58

[69] B. Grenier, Y. Inagaki, L. P. Regnault, A. Wildes, T. Asano, Y. Ajiro, E. Lhotel, C. Paulsen, T. Ziman and J. P. Boucher, Phys. Rev. Lett **92**, 177202 (2004) 58

[70] B. Grenier, J. P. Boucher, J. Y. Henry, L. P. Regnault and T. Ziman, J. Magn. Magn. Mater **310**, 1269 - 1271 (2007) 58

[71] V. O. Garlea, A. Zheludev, T. Masuda, H. Manaka, L. P. Regnault, E. Ressouche, B. Grenier, J.-H. Chung, Y. Qiu5, K. Habicht, K. Kiefer, and M. Boehm, Phys. Rev. Lett. **98**, 167202 (2007) 58

[72] T. Giamarchi, Ch. Rüegg, O. Tchernyshyov, Nature Physics **4**, 198 (2008). 59

[73] Ch. Rüegg, N. Cavadini, A. Furrer, H.-U. Güdel, K. Krämer, H. Mutka, A. Wildes, K. Habicht and P. Vorderwisch, Nature (London) **423** 62 (2003). 59

[74] H. Tanaka, K. Goto, M. Fujisawa, T. Ono and Y. Uwatoko, Physica B **329 -333**, 697 (2003) 59

[75] K. Goto, M. Fujisawa, T. Ono, H. Tanaka and Y. Uwatoko, J. Phys. Soc. Jpn. **73** 3254 (2004). 59

[76] A. Taketani, T. Sakurai, M. Kodama, S. Okubo, H. Ohta, H. Tanaka and Y. Uwatoko, *et al.* Progress of Theoretical Physics Supplement **159**, 407 (2005). 59

[77] V. N. Glazkov, A. I. Smirnov, H. Tanaka and A. Oosawa, Phys. Rev. B **69**, 184410 (2004). 60

[78] Ch. Rüegg, B. Normand, M. Matsumoto, A. Furrer, D. F. McMorrow, K. W. Krämer, H.-U. Güdel, S. N. Gvasaliya, H. Mutka and M. Boehm, Phys. Rev. Lett. **100**, 205701(2005). 61, 64, 66, 67, 71, 83, 88, 89, 91

[79] H. B. Callen and E. Callen, J. Phys. Chem. Solids **27**, 1271 (1966). 63

[80] M. G. Cottam and R. B. Stinchcombe, J. Phys. C: Solid State Phys. **3**, 2305 (1970) 63

[81] P. Martel, R. A. Cowley and R. W. H. Stevenson, J. Appl. Phys. **39** 1116 (1968) 63

[82] P. A. Fleury, Phys. Rev **180**, 591 (1968). 63

[83] K. Krämer, Department of Chemistry and Biochemistry, University of Bern. 63

[84] A. Oosawa, K. Kakurai, T. Osakabe, M. Nakamura, M. Takeda and H. Tanaka, J. Phys. Soc. Jpn **73**, 1446 (2004). 67

[85] A. Oosawa, M. Fujisawa, T. Osakabe, K. Kakurai and H. Tanaka, J. Phys. Soc. Jpn **72**, 1026 (2003). 67

[86] E. F. Talbot, H. R. Glyde, W.G. Stirling, E.C. Stevenson, Phys. Rev. B **38**, 112299 (1988). 70

[87] B. Fak and B. Dorner, Physica B **234-236**, 1107 (1997). 70

[88] A. Oosawa, T. Kato, K. Kakurai, M. Müller and H.-J. Mikeska, Phys. Rev. B **65**, 094426 (2002). 70

[89] M. G. Cottam and R. B. Stinchcombe, J. Phys. C: Solid State Phys. **3**, 2305 (1970). 85

[90] A. Zheludev, K. Kakurai, T. Masuda, K Uchinokura and K. Nakajima, Phys. Rev. Lett. **89**, 197205(2002). 88

[91] B. Lake, D.A. Tennant and S. E. Nagler, Phys. Rev. B **71**, 134412 (2005). 88

[92] Z. Tun, W. J. L. Buyers, A. Harrison, and J. A. Rayne, Phys. Rev. B **43**, 13331 (1991). 88

[93] M. Enderle, Z. Tun, W. J. L. Buyers, and M. Steiner, Phys. Rev. B **59**, 4235 (1999). 88

[94] N. Johannsen, A. Vasiliev, A. Oosawa, H. Tanaka and T. Lorenz, Phys. Rev. Lett. **95**, 017205 (2005). 91

[95] E. Ya. Sherman, P. Lemmens, B. Busse, A. Oosawa and H. Tanaka, Phys. Rev. Lett. **91**, 057201 (2003). 91

[96] B. Normand, Private Communication. 94

[97] S. Jin and A. W. Sandvik, Phys. Rev. B **85**, 020409(R) (2012). 92, 93

[98] Y. Kulik and O. P. Sushkov, Phys. Rev. B **84**, 134418 (2011). 94

[99] I. Affleck and G. F. Wellman, Phys. Rev. B **46**, 8934 (1992). 95

[100] M. A. Stephanov, Phys Rev. D **52**, 3746 (1995). 95

[101] M. Stone, I. A. Zaliznyak, T. Hong, C. L. Broholm and D. H. Reich, Nature **440**, 187 (2006). 95, 141

[102] B. R. Patyal, B. L. Scott and R. D. Willett, Phys. Rev. B **41**, 1657 (1990). 98

[103] B. C. Watson, V. N. Kotov, M.W. Meisel, D. W. Hall, G. E. Granroth, W. T. Montfrooij, S. E. Nagler, D. A. Jensen, R. Backov, M. A. Petruska, G. E. Fanucci and D. R. Talham, Phys. Rev. Lett. **86**, 5168 (2001). 98

[104] P. W. Anderson, Mater. Res. Bull **8**, 153 (1973). 98

[105] S. R. White, R. M. Noack and D. J. Scalapino, Phys. Rev. Lett. **73**, 886 (1994). 98

[106] E. Dagotto and T. M. Rice, Science **271**, 618 (1996). 98

[107] Ch. Rüegg, K. Kiefer, B. Thielemann, D. F. McMorrow, V. Zapf, B. Normand, M. B. Zvonarev, P. Bouillot, C. Kollath, T. Giamarchi, S. Capponi, D. Poilblanc, D. Biner, and K. W. Krämer, Phys. Rev. Lett. **101**, 247202 (2008). 99

[108] C. J. Calzado, C. de Graaf, E. Bordas, R. Caballol and J-P. Malrieu, Phys. Rev. B **67**, 132409 (2003). 99

[109] S. Nishimoto and M. Arikawa, Phys. Rev. B **79**, 113106 (2009). 99

[110] O. Mentré, E-.M. Ketatni, M. Colmont, M. Huvé, F. Abraham and V. Petricek, J. Am. Chem. Soc. **128**, 10857 (2006). 99

[111] J. Bobroff, N. Laflorencie, L. K. Alexander, A. V. Mahajan, B. Koteswararao and P. Mendels, Phys. Rev. Lett **103**, 047201 (2009) 101, 151, 152, 153

[112] Y. Mizuno, T. Tohyama, S. Maekawa, T. Osafune, N. Motoyama, H. Eisaki and S. Uchida, Phys. Rev. B **57**, 5326 (1998). 101, 146

[113] C. K. Majumdar and D. K. Ghosh, J. Math. Phys **10**, 1388 (1969). 101

[114] S. Wang, E. Pomjakushina, T. Shiroka, G. Deng, N. Nikseresht, Ch. Rüegg, H. M. Rønnow and K. Conder, J. Cryst. Growth **313**, 51 (2010). 99, 102, 153, 154, 183

[115] S. Miyahara, J.-B. Fouet, S. R. Manmana, R. M. Noack, H.Mayaffre, I. Sheikin, C. Berthier, and F. Mila, Phys. Rev. B **75**, 184402 (2007). 115

[116] J. T. Haraldsen, T. Barnes and J. L. Musfeldt, Phys. Rev. B **71**, 064403 (2005). 116, 117

[117] O. Cépas, K. Kakurai, L. P. Regnault, T. Ziman, J. P. Boucher, N. Aso, M. Nishi, H. Kageyama and Y. Ueda, Phys. Rev. Lett. **87**, 167205 (2001). 124

[118] B. Leuenberger, A. Stebler, H.U. Güdel, A. Furrer, R. Feile and J. K. Kjems, Phys. Rev. B **30**, 6300 (1984). 136

[119] B. Leuenberger, H.U. Güdel, R. Feile and J. K. Kjems, Phys. Rev. B **28**, 5368 (1983). 136

[120] T. Barnes, Phys. Rev. B **67**, 024412 (2003). 141

[121] P. Lemmens, G. Güntherodt and C. Gros, Physics Reports **357**, 1 (2003). 144

[122] D. A. Tennant, C. Broholm, D. H. Reich, S. E. Nagler, G. E. Granroth, T. Barnes, K. Damle, G. Xu, Y. Chen and B. C. Sales, Phys. Rev. B **67**, 054414 (2003). 144

[123] O. P. Sushkov and V. N. Kotov, Phys. Rev. Lett **81**, 1941 (1998). 144

[124] V. N. Kotov, O. P. Sushkov and R. Eder, Phys. Rev. B **59**, 6266 (1999). 144

[125] S. Notbohm, Ph.D. Thesis, University of St. Andrews (2007). 144

[126] S. Notbohm, P. Ribeiro, B. Lake, D. A. Tennant, K. P. Schmidt, G. S. Uhrig, C. Hess, R. Klingeler, G. Behr, B. Büchner, M. Reehuis, R. I. Bewley, C. D. Frost, P. Manuel and R. S. Eccleston, Phys. Rev. Lett. **98**, 027403 (2007). 144

[127] E. Čižmár, M. Ozerov, J. Wosnitza, B. Thielemann, K. W. Krämer, Ch. Rüegg, O. Piovesana, M. Klanjšek, M. Horvatić, C. Berthier and S. A. Zvyagin, Phys. Rev. B **82** 054431 (2010). 146

[128] V. N. Glazkov, A. I. Smirnov, J. P. Sanchez, A. Forget, D. Colson and P. Bonville, J. Phys. Condens. Matter **18**, 2285 (2006). 146

[129] E. Orignac and T. Giamarchi, Phys. Rev. B **57**, 5812 (1998). 146

[130] R. Citro and E. Orignac, Phys. Rev. B **65**, 134413 (2002). 146

[131] H. Alloul, J. Bobroff, M. Gabay and P. J. Hirschfeld, Rev. Mod. Phys. **81**, 45 (2009). 150, 151

[132] M. Sigrist, A. Furusaki, J. Phys. Soc. Jpn **65**, 2385 (1996) 150

[133] R. Yu, O. Nohadani, S. Haas and T. Roscilde, Phys. Rev. B **82**, 134437 (2010). 151

[134] T. Nakamura, Phys. Rev. B **59**, R6589 (1999). 151

[135] B. Grenier, J.-P. Renard, P. Veillet, C. Paulsen, G. Dhalenne and A. Revcolevschi, Phys. Rev. B **58**, 8202 (1998). 151

[136] V. Simonet, B. Grenier, F. Villain, A.-M. Flank, G.. Dhalenne, A. Revcolevschi and J.-P. Renard, Eur. Phys. J. B **53**, 155-167 (2006). 151

[137] Y. Uchiyama, Y. Sasago, I. Tsukada, K. Uchinokura, A. Zheludev, T. Hayashi, N. Miura and P. Böni, Phys. Rev. B **83**, 631 (1999). 151

[138] S. Imai, T. Masuda, T. Matsuoka and K. Uchinokura, arXiv:cond-mat/0402595v1. 151

[139] G.Xu, G. Aeppli, M. E. Bisher, C. Broholm, J. F. DiTusa, C. D. Frost, T. Ito, K. Oka, R. L. Paul, H. TAgaki and M. M. J. Treacy, Science **289**, 419 (2000). 151

[140] H. Azuma, Y. Fujishiro, M. Tanako, M. Nohora and H. Tagaki, Phys. Rev. B **55**, R8658 (1997) 151, 153

[141] S. Ohsugi, Y. Tokunaga, K. Ishida, Y. Kitaoka, M. Azuma, Y. Fujishiro and M. Takano, Phys. Rev. B **60**, 4181 (1999). 151

[142] A. Oosawa, T. Ono and H. Tanaka, Phys. Rev. B **66**, 020405(R) (2002). 151

[143] B. Koteswararao, A. V. Mahajan, L. K. Alexander and J. Bobroff, J Phys: Condens. Matter **22**, 035601 (2010). 151

[144] L. K. Alexander, J. Bobroff, A. V. Mahajan, B. Koteswararao, N. Laflorencie and F. Alet, Phys. Rev. B **81**, 054438 (2010). 151, 152

[145] M. Hase, I. Terasaki, Y. Sasago and K Uchinokura, Phys Rev. Lett **71**, 4059 (1993) 151

[146] E. F. Shender and S. A. Kivelson, Phys. Rev. Lett **66**, 2384 (1991). 151

[147] E. C. Andrade and M. Vojta, EPL **97**, 37007 (2012). 152, 185

[148] Krunoslav Prša, private communication. 152, 154

[149] M. I. Larkin, Y. Fudamoto, I. M. Gat, A. Kinkhabwala, K. M. Kojima, G. M. Luke, J. Merrin, B. Nachumi, Y. J. Uemara, M. Azuma, T. Saito and M. Takano, Phys. Rev. Lett. **85**, 1982 (2000). 152

[150] T. Masuda, A. Fujioka, Y. Uchiyama, I. Tsukada and K. Uchinokura, Phys. Rev. Lett. **80**, 4566 (1998). 153

[151] M. Fujisawa, T. Ono, H. Fujiwara, H. Tanaka, V. Sikolenko, M. Meissner, P. Smeibidl, S. Gerischer and H. A. Graf, J. Phys. Soc. Jpn. **75**, 033702 (2006). 153

[152] M. Imuda and Y. Iino, J. Phys. Soc. Jpn. **66**, 568 (1997). 153

[153] C. Yasuda, S. Todo, M. Matsumoto and H. Takayama, Phys. Rev. B **64**, 092405 (2001). 153

[154] S. Wang, private communication. 154

[155] K. Lefmann, D.F. McMorrow, H.M. Rønnow, K. Nielsen, K.N. Clausen, B. Lake, G. Aeppli: Physica B **283**, 343 (2000); 155

[156] A. Sabba Stefanescu and P -J Becker 1981 J. Phys. C: Solid State Phys. **14**, L737 (1981). 160

[157] TriCS website http://http://trics.web.psi.ch/ 163

[158] W.Busing and H.A. Levy, Acta Cryst. **22**, 457-464 (1967). 163

[159] D-.M. Smilgies, Rev. Sci. Instrum. **73**, 1706 (2002). 165

[160] Fullprof website: http://www.ill.eu/sites/fullprof/ 167

[161] S. Kirkpatrick, C. D. Gelatt, Jr. and M. P. Vecchi, Science **220**, 671 (1983). 169

[162] J. J. Olivero ad R. L. Longbothum, J. Quant. Spectrosc. Radiat. Transfer **17**, 233 (1977). 178

[163] G. Xu, C.Broholm, Y-A. Soh, G.Aeppli, J. F. DiTusa, Y. Chen, M. Kenzelmann, C. D. Frost, T. Ito, K. Oka and H. Takagi, Science **317**, 1049 (2007). 183

[164] M. Azuma, M. Takano and R. S. Eccleston, J. Phys. Soc. Jpn. **67** 740 (1998). 183

[165] S. Chakravarty, Phys. Rev. Lett. **77**, 4446 (1996). 184

[166] O. F. Syljuåsen, S. Chakravarty and M. Greven, Phys. Rev. Lett. **78**, 4115 (1997). 184

[167] J. Lorenzana, G. Seibold and R. Coldea, Phys. Rev. B **72**, 224511 (2005). 184

[168] G. E. Bacon and R. D. Lowde, Acta. Cryst. **1** 303 (1948). 186